NOTICE

The quality of this microform is heavily dependent upon the quality of the original thesis submitted for microfilming. Every effort has been made to ensure the highest quality of reproduction possible.

If pages are missing, contact the university which granted the degree.

Some pages may have indistinct print especially if the original pages were typed with a poor typewriter ribbon or if the university sent us an inferior photocopy.

Reproduction in full or in part of this microform is governed by the Canadian Copyright Act, R.S.C. 1970, c. C-30, and subsequent amendments.

AVIS

La qualité de cette microforme dépend grandement de la qualité de la thèse soumise au microfilmage. Nous avons tout fait pour assurer une qualité supérieure de reproduction.

S'il manque des pages, veuillez communiquer avec l'université qui a conféré le grade.

La qualité d'impression de certaines pages peut laisser à désirer, surtout si les pages originales ont été dactylographiées à l'aide d'un ruban usé ou si l'université nous a fait parvenir une photocopie de qualité inférieure.

La reproduction, même partielle, de cette microforme est soumise à la Loi canadienne sur le droit d'auteur, SRC 1970, c. C-30, et ses amendements subséquents.

MULTINUCLEAR MAGNETIC RESONANCE APPROACH

TO THE STUDY OF

ADENOSINE TRIPHOSPHATE–ALUMINUM INTERACTIONS

By

CLAUDE ROGER DUPRESSOIR

A thesis submitted to the School of Graduate Studies
in partial fulfillment of the requirements for the degree of

DOCTOR OF PHILOSOPHY

Department of Chemistry,
University of Ottawa,
Ottawa, Canada.

ISBN 0-315-53782-5

J'ai pétri de la boue,
et j'en ai fait de l'or.
Glorifier le culte des images
(ma grande, mon unique, ma primitive passion).

Charles Baudelaire

I have travelled around the globe.
I have seen the Canadian and American Rockies,
the Andes and the Alps and the highlands of Scotland;
But for simple beauty, Cape Breton outrivals them all.

Alexander Graham Bell

ACKNOWLEDGEMENTS

I wish to express my sincere gratitude to my thesis director, Dr. Christian Detellier, for his patience and support during the course of this work, and for always being willing to give freely of his time.

It is a pleasure to acknowledge Dr. Alfred Delville from Liège (Belgium), for the valuable discussions which took place during his stay in Ottawa. His help in solving important theoretical questions to be considered in this work is most gratefully appreciated.

The journey through graduate studies has not been without its rough moments, and I am grateful to my colleagues, especially Dr. Harald Stöver, for providing such enjoyable company.

I wish to thank my parents for their continued guidance and interest throughout my studies.

Finally I am indebted to my wife Anita for her constant help and encouragement.

Unfortunately, my friend Mrs. Henock from France, who inspired me with her strength and wisdom, did not have the joy of sharing the completion of my student life.

It is to my parents and to her everlasting memory that I dedicate this endeavor.

ABSTRACT

The interactions taking place in aqueous solution at pH = 7.4 between adenosine 5′ triphosphate (ATP) and aluminum were studied by multinuclear magnetic resonance. As an introduction to the ATP–Al system, a phosphorus–31 spin relaxation study of ATP alone permitted the sorting out of the different dynamic contributions to the overall relaxation rate. A solvation model for the triphosphate chain was also proposed.

ATP–Al interactions were studied by ^{1}H, ^{13}C, ^{31}P, and ^{27}Al NMR spectroscopies. Qualitative ^{31}P NMR measurements showed the existence of a unique 4:3 ATP:Al aggregate present in solution. In this complex, there is the equivalent of one "free" ATP molecule which is taking part in the aggregate but not directly implicated in aluminum complexation. For the three remaining aggregated ATP molecules, all three phosphates were equally engaged in aluminum complexation. The overall complexation phenomenon was not dependent upon the total ATP concentration in solution. The observed ^{31}P linewidth field dependencies of the complexed phosphates resulted from a scalar relaxation of the second kind with the ^{27}Al nucleus and permitted the determination of the complex correlation time of 2.8 ns.

^{1}H and ^{13}C chemical shifts and spin-lattice relaxation studies permitted the proposition of an overall geometry for the adenosine bases of the aggregate. In this complex, each aggregated adenosine base is partially stacked and skewed by an angle of about 120° from the other bases. ^{1}H chemical shifts and ^{31}P T_1 experiments showed the existence of rapid exchange between a free ATP molecule in solution and a surface ATP molecule of the aggregate confined in a pre-aggregated state. Two-dimensional NMR exchange spectroscopy revealed the presence of a chemical exchange between

aggregated and pre-aggregated ATP molecules as well as giving a value of 0.8 s^{-1} for the pseudo first-order rate constant.

^{27}Al NMR spectra confirmed that the cation was complexed by the triphosphate side chain of ATP. It also indicated two different aluminum complexation sites with a ratio of 2:1. Finally, the qualitative and quantitative descriptions of ATP Al interactions were combined to propose a model of the ATP_4Al_3 aggregate.

Contents

List of Figures

List of Tables

List of Symbols

CSA	Chemical Shift Anisotropy
D	Translational diffusion coefficient
DFS	Dynamic Frequency Shift
eQ	Electric quadrupole moment
eq	Electric field gradient
efg	The electric field gradient
FID	Free Induction Decay
$F(t)$	Random perturbation function
$G(\tau)$	Autocorrelation function
$g(\tau)$	Reduced autocorrelation function
h	The Plank constant divided by 2π
$\mathcal{H}$	The Hamiltonian
H_0	Static magnetic field
H_1	Perturbating radio frequency field

H_{eff}	The effective magnetic field in the rotating frame of reference
ΔH_1	The offset from exact resonance
$< I_z >$	The expectation value of the longitudinal magnetization
$< I_0 >$	The expectation value of the equilibrium magnetization
Im	Imaginary part of a complex function
J	Spin-spin coupling constant
$J(\omega)$	Spectral density function
$j(\omega)$	Reduced spectral density function
k	The exchange rate constant
M_{xy}	Macroscopic magnetization in the xy plane
M_z	Macroscopic magnetization along the z axis
M_0	Macroscopic magnetization at equilibrium
NOE	Nuclear Overhauser Effect
PD	Preparation Period
Q	The quadrupole moment
$q(\omega)$	Reduced imaginary spectral density function
QQC	Quadrupole Coupling Constant

QSR	Quasi-Spin Rotation
R(obs)	Observed relaxation rate
R(CSA)	Chemical shift anisotropy relaxation rate
R(trans)	Translational relaxation rate
R(left)	Leftover relaxation rate
R(QSR)	Quasi-spin rotation relaxation rate
R(SR)	Spin rotation relaxation rate
Re	Real part of a complex function
r.f	Radio frequency
S/N	Signal over Noise ratio
T_1	Spin-lattice relaxation time
T_2	Spin-spin relaxation time
t_1	The evolution period
t_2	The detection period
u	The component of the magnetization in phase with r.f field
v	The component of the magnetization out of phase with r.f field
x_A, x_B	The mole fractions of A and B respectively
α	The spectrometer dead time

β	Bohr magneton
γ	Gyromagnetic ratio
δ	Chemical shift
δ_{int}	Intrinsic chemical shift
η	The asymmetry parameter
η_{obs}	The Nuclear Overhauser Effect factor
μ	Magnetic moment
$\mathcal{V}$	Resonance frequency
$\mathcal{V}_{1/2}$	Linewidth value at half height
σ	Standard deviation
$\Delta\sigma$	Chemical shift anisotropy term
τ_A, τ_B	Lifetime in the environment A and B
τ_c	Isotropic rotational correlation time
τ_e	Water molecule residence time
τ_m	Mixing time
τ_r	Quasi-rotation jump time
τ_R	Correlation time for over-all rotational reorientation
τ_G	Correlation time for internal motion

τ_w	Duration of the electronic current pulse
χ	Quadrupole coupling constant
ω_0	Larmor frequency
ω_{DS}	Dynamic frequency shift value

Nucleus:	Resonance frequencies used in MHz:
^{1}H	299.944
^{13}C	75.429
^{27}Al	20.722, 78.157
^{31}P	32.198, 80.962, 121.421

Chapter 1

INTRODUCTION

Representing 8.1% of the total earth's crust, aluminum is the most abundant metal and generally considered to be an inactive biological cation. The interaction of aluminum with cellular components has recently aroused interest [1] because it has been implicated in a number of toxic pathological and biological processes. Abnormally high concentrations of aluminum have been detected in the gray matter of the brain of patients submitted to hemodialysis treatment [2,3] and in a progressive form of senile dementia often called Alzheimer's disease [4,5,6,7]. The accumulation of aluminum in the nuclear chromatin of brain cells [8] is believed to be responsible for a progressive encephalopathy characterized by neurofibrillary degeneration [4,5]. The toxicity of aluminum [21] is now widely recognized and the volume of literature on the subject is expanding. Aluminum has been shown to interact strongly with DNA [28,29], producing three distinguishable complexes in solution, in which the metallic cation binds to the phosphate groups or produces intrastrand cross-links [28]. In the blood, aluminum is mainly bound and transported by plasma proteins such as transferrin and hemoglobin [24,25,26,27]. The interactions of aluminum in model membrane systems [30,31,32] show that aluminum binds strongly to the phosphate head groups of the membrane. The effect of aluminum is to increase the fluidity or even induce a

phase separation of the membrane [31,32]. This event could constitute the first step to the neuro-degenerative process, as the highly selective nature of the membrane has been diminished. The neurotoxicity of aluminum is manifested by inhibiting a number of enzymes, such as acetylcholine esterase [33], choline acetyltransferase [21] and Na^+-K^+ ATPase [34]. It has also been shown that aluminum inhibits the function of hexokinase in the brain [10,11,22,23]. The toxic effects of aluminum are thought to be due to the binding of aluminum to adenosine 5′-triphosphate (ATP) and the consequent inhibition of reactions which require ATP participation. Indeed, the substrate for most ATP utilizing enzymes in the cell is a complex of ATP and magnesium, and the possibility of competition with aluminum deserved some attention [10]. For these reasons, interactions between ATP and aluminum are of significance.

ATP–Aluminum interactions are part of the more general family of metal complexes of nucleotides. This subject has resulted in considerable research activity. Many approaches and techniques have been combined to elucidate metal binding in solution [12,13,14,16] and have been compared to solid state studies [12,15]. Nucleotides are made of three subunits, each one possessing some possible chelation sites. In the case of ATP (see Figure 1.1), the three nitrogen atoms N–1, N–3 and N–7 of the adenine base, the two hydroxyl groups of the ribose sugar and the triphosphate side chain represent an impressive series of potential binding sites. Among many spectroscopic techniques available [17] to study metal complexes of nucleotides, nuclear magnetic resonance spectroscopy presents the advantage of looking directly at the sites of complexation with a great nuclei selectivity. Chemical shifts, linewidths, spin-lattice and spin-spin relaxation times, and Nuclear Overhauser Effects contribute some powerful NMR parameters which, combined with a wide range of available pulse sequences [154], makes multinuclear NMR spectroscopies an attractive tool for studies

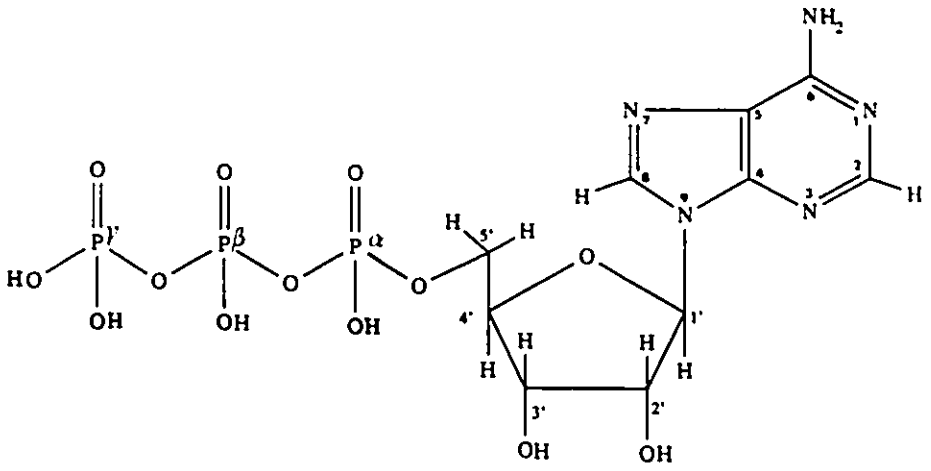

Figure 1.1: Structure and numbering of the adenosine 5′–triphosphate molecule.

of this nature.

ATP–Aluminum interactions were first studied by ^{31}P and ^{27}Al NMR spectroscopies at different pH values and for equimolar mixtures of ATP and aluminum [18]. Qualitative interpretation of the obtained results supported the existence of two complexes in solution.

During the course of our research, two detailed multinuclear (^{1}H, ^{13}C, ^{31}P and ^{27}Al) spectroscopic studies appeared in the literature [19,20]. In the first study [19], by varying the pH values from 3 to 10 and for different Al/ATP ratios, the presence of two species in slow exchange with the free ATP in solution was established. For an equimolar mixture of ATP and aluminum, only a dimer $(ATP)_2Al_2$ species was present. For solutions in which the ATP concentration was in excess, an $(ATP)_2Al$ species was formed. The formation of the two different species was found to be pH independent. The data obtained supported the conclusion that binding occured at the γ and β phosphates of ATP.

In the second study [20], by varying the pH from 1 to 12 but only for equimo-

lar ATP:Al mixtures, the combination of NMR results suggested that at least four different ATP–Aluminum complexes were formed in solution. Their existence was found to be pH dependent and, under any set of conditions, there was generally more than one complex in solution. Around neutral pH, a stacking of nucleotides in a 1:1 ratio was proposed in which the γ and β phosphates were involved in aluminum complexation.

It seems that these two publications contain some clear contradictory results regarding the nature of ATP–Aluminum complexes formed in solution.

We studied the interactions occurring between ATP and aluminum at physiological pH, focusing the work on concentration studies using multinuclear magnetic resonance spectroscopies of dipolar (^{1}H, ^{13}C, ^{31}P) and quadrupolar (^{27}Al) nuclei. Since many aspects of this work relied on relaxation studies, the general concepts of nuclear spin relaxation are outlined in the second chapter. As well, general expressions for the spin-lattice and spin-spin relaxation times were grouped and presented for dipolar and quadrupolar nuclei. Chapters 4, 5, 6, 7, and 8 will deal with the investigation of ATP–Aluminum interactions using dipolar nuclei, while in the final chapter, the ^{27}Al quadrupolar nucleus will be used to probe the environment of the cation.

Chapter 2

NUCLEAR SPIN RELAXATION

2.1 Description of Spin-Lattice and Spin-Spin Relaxation Phenomena

In Fourier transformed NMR an excitation pulse is applied, resulting in a tipping of the macroscopic magnetization M_0 of 90° or 180° . This process is very rapid and, in most cases, excludes significant relaxation during the pulse excitation [42]. After each 180° pulse, leading to the inversion of the M_0, the restoration of the equilibrium of spin population begins immediately due to spin-lattice interactions. The time scale for M_z to regain an equilibrium value M_0 is a measure of the spin-lattice relaxation time, T_1. On the other hand, immediately following a 90° excitation pulse, which causes M_0 to coincide with the y axis, each microscopic component of the total magnetization M_{xy} tends to get out of phase again due to interactions with fluctuating local fields. The time scale for this loss of phase coherence is the spin-spin relaxation time, T_2 , which corresponds to the relaxation of M_{xy} in the xy plane. M_{xy} decays to zero as the nuclear spins resume a random precession around H_0 without any phase coherence between them. The signal detected by the NMR spectrometer is the decay of M_{xy} as a function of time which is called the Free Induction Decay (FID) [43]. Fourier transformation of the FID results in an NMR spectrum as a

function of the frequency. However, M_z may or may not be equal to M_0 depending on whether the spin-lattice relaxation process is completed. Bloch [38] viewed both of these magnetic processes as first-order decays:

$$\frac{dM_z}{dt} = -\frac{M_z - M_0}{T_1} \qquad M_z(t) = M_0\,[1 - \exp(-t/T_1)] \tag{2.1}$$

$$\frac{dM_{xy}}{dt} = -\frac{M_{xy}}{T_2} \qquad M_{xy}(t) = M_0 \exp(-\frac{t}{T_2}) \tag{2.2}$$

In most cases these simple equations provide a correct description of relaxation phenomena in the liquid phase.

2.2 Origin of Nuclear Relaxation

Nuclei are isolated from their surroundings by electron clouds and are therefore insensitive to molecular collisions. Furthermore, the probability of spontaneous emission (W) in NMR is very small and is given by the following equation [35]:

$$W = \frac{2}{3}\frac{\gamma^2}{c^3\hbar^2}\Delta E \qquad \text{with} \qquad \Delta E = \hbar\omega_0 \tag{2.3}$$

For a proton at 300 MHz, the spontaneous emission of a photon is 10^{-24} $\sec^{-1}$. Therefore, neither of the above mechanisms is responsible for nuclear relaxation. In general, two conditions are necessary for a successful relaxation mechanism. There must be some interaction, electric or magnetic in nature, acting directly upon the spin system, and it must be time dependent. In order to know if at $\omega = \omega_0$ the interaction leads to efficient relaxation, the variation of the strength of the interaction over a frequency distribution is needed. If a random function $F(t)$ represents a fluctuation interaction, around a mean value of zero, a measure of its strength is given by the mean square average $\overline{F^*(t+\tau)F(t)}$. The autocorrelation function of $F(t)$ is defined

by:

$$G(\tau) = \overline{F^*(t+\tau)F(t)} \tag{2.4}$$

This function represents a measure of the persistence of the fluctuations after a time τ. Normalization of $G(\tau)$ introduces a reduced autocorrelation function:

$$g(\tau) = \frac{G(\tau)}{G(0)} = \frac{\overline{F^*(t+\tau)F(t)}}{\overline{F^*(t)F(t)}} \tag{2.5}$$

$g(\tau)$ is large for a short time because the correlation is important but then decreases to zero when τ increases as there is a loss of information. It is usually a good approximation to consider that $g(\tau)$ drops off exponentially with a time decay τ_c called the correlation time:

$$g(\tau) = \exp(-\tau/\tau_c) \tag{2.6}$$

This has been shown to be the case for random Brownian motion of molecules as they rotate and diffuse through a fluid [37]. The power spectrum of $F(t)$ is the Fourier transform of the autocorrelation function:

$$J(m\omega) = \int_{-\infty}^{+\infty} G(\tau)\exp(-im\omega\tau)d\tau \tag{2.7}$$

It is usually more convenient to work with the reduced autocorrelation functions:

$$J(m\omega) = \int_{-\infty}^{+\infty} \overline{F^*(t)F(t)}g(\tau)\exp(-im\omega\tau)d\tau \tag{2.8}$$

If $g(\tau)$ follows an exponential decay the spectral density functions or power spectrum are obtained:

$$J(m\omega) = \overline{F^*(t)F(t)}\frac{2\tau_c}{1+(m\omega\tau_c)^2} \tag{2.9}$$

As well the reduced spectral density functions are defined as:

$$j(m\omega) = \frac{J(m\omega)}{\overline{F^*(t)F(t)}} = \frac{2\tau_c}{1+(m\omega\tau_c)^2} \tag{2.10}$$

Consider a nuclear spin system characterized by two eigenstates $|\alpha>$ and $|\beta>$, and a perturbation acting on these states represented by a random time dependent Hamiltonian $\mathcal{H}(t)$ (for example the dipolar coupling between two spins in Brownian motion). The transition probability $W_{\alpha\beta}$ between these two eigenstates is found using time dependent perturbation theory [37]:

$$W_{\alpha\beta} = \int_{-\infty}^{+\infty} G_{\alpha\beta}(\tau) \exp(-im\omega_{\alpha\beta}\tau) d\tau \tag{2.11}$$

where $G_{\alpha\beta}(\tau)$ is the autocorrelation function of the random function $\mathcal{H}(t)$:

$$G_{\alpha\beta}(\tau) = \overline{<\alpha|\mathcal{H}^*(t+\tau)\mathcal{H}(t)|\beta>}$$

In most cases $\mathcal{H}(t)$ can be written as [35]:

$$\mathcal{H}(t) = A \cdot F(t)$$

where A is an operator acting on the nuclear spins and $F(t)$ a random function. Then equation (2.11) becomes:

$$W_{\alpha\beta} = <\alpha|A|\beta>^2 J(\omega_{\alpha\beta}) \tag{2.12}$$

where $<\alpha|A|\beta>$ represents the matrix element of the operator A (see Appendix A). An essential requirement for relaxation in liquids is that the molecular motion has a suitable time scale. Interactions which fluctuate with a distribution of frequencies much higher or lower than the Larmor frequency ω_0 will be inefficient in relaxing nuclear spins. Thus, electronic motions and molecular vibrations are unimportant in liquid NMR [39]. On the other hand, any interaction which fluctuates strongly at the resonance frequency ω_0 will cause transitions between the $|\alpha>$ and $|\beta>$ spin states and produce powerful nuclear spin relaxation. The time scale for magnetic resonance is slow, so that diffusion, rotation and torsional motions are important

sources of relaxation in liquids. So are some chemical exchange processes. The expressions for the spin-lattice and spin-spin relaxation times of a dipolar nucleus in the case of dipole-dipole, chemical shift anisotropy, and scalar coupling interactions will now be reviewed. As well, the effects of nuclear transfer on relaxation rates will be outlined. Finally, quadrupolar relaxation conditions both in the extreme and non-extreme narrowing conditions will be discussed.

2.3 Relaxation Mechanisms for Dipolar Nuclei

2.3.1 Dipole-Dipole

The prime source of spin relaxation in most diamagnetic liquids arises from local magnetic fields produced by intramolecular nuclear dipole-dipole interactions. The magnetic field produced at the nucleus j by any nucleus i ($I \neq 0$) is given by:

$$H_{loc} = \sum_i \pm\mu_i \left(\frac{3\cos^2\theta_{ij} - 1}{r_{ij}^3} \right) \tag{2.13}$$

Molecular rotational Brownian motion introduces a time dependence in equation (2.13) through θ_{ij} and causes these random local fields to fluctuate with a characteristic time scale, τ_c , the correlation time. Intermolecular contributions via translational motion are usually ignored because of the r^{-6} distance dependence of the relaxation times T_1 and T_2. It should be noted that, if the spins I and S are "like" spins (two protons for example), only the sum $< I_z + S_z >$ proportional to the macroscopic magnetization is observed; whereas, if the spins are unlike $< I_z >$ and $< S_z >$ are observed separately ($< I_z >$ represents the expectation value of the macroscopic magnetization along the z axis, at time t and for the nuclear spins I). In the case of like spins, the macroscopic equations of motion for the longitudinal and transverse

magnetizations are of the type [35]:

$$\frac{d < I_z + S_z >}{dt} = -\frac{1}{T_1^I}[< I_z + S_z > - < I_z + S_z >_0] \tag{2.14}$$

$$\frac{d < I_y + S_y >}{dt} = -\frac{1}{T_2^I}[< I_y + S_y >] \tag{2.15}$$

where the dipolar contribution of the nucleus S to the spin-lattice and spin-spin relaxation time is given by:

$$\frac{1}{T_1^I} = \frac{1}{5}\frac{\hbar^2\gamma_I^4 I(I+1)}{r^6}[j(\omega_I) + j(2\omega_I)] \tag{2.16}$$

$$\frac{1}{T_2^I} = \frac{1}{10}\frac{\hbar^2\gamma_I^4 I(I+1)}{r^6}[3j(0) + 5j(\omega_I) + 2j(2\omega_I)] \tag{2.17}$$

It should also be noted that equations (2.14)(2.15) and (2.1)(2.2) derived from Bloch's equations are equivalent. However, in the case of unlike nuclei, the macroscopic longitudinal equation of motion for $< I_z >$ and $< S_z >$ are coupled in the following manner [35]:

$$\frac{d < I_z >}{dt} = -\frac{1}{T_1^{II}}[< I_z > - < I_z >_0] - \frac{1}{T_1^{IS}}[< S_z > - < S_z >_0] \tag{2.18}$$

$$\frac{d < S_z >}{dt} = -\frac{1}{T_1^{SI}}[< I_z > - < I_z >_0] - \frac{1}{T_1^{SS}}[< S_z > - < S_z >_0] \tag{2.19}$$

where

$$\frac{1}{T_1^{II}} = \frac{1}{15}\frac{\hbar^2\gamma_I^2\gamma_S^2 S(S+1)}{r^6}[j(\omega_I - \omega_S) + 3j(\omega_I) + 6j(\omega_I + \omega_S)] \tag{2.20}$$

$$\frac{1}{T_1^{IS}} = \frac{1}{15}\frac{\hbar^2\gamma_I^2\gamma_S^2 I(I+1)}{r^6}[6j(\omega_I + \omega_S) - j(\omega_I - \omega_S)] \tag{2.21}$$

On the other hand the macroscopic transverse equation of motion is not coupled but simply given by:

$$\frac{d < I_y >}{dt} = -\frac{1}{T_2^I} < I_y > \tag{2.22}$$

where

$$\frac{1}{T_2^I} = \frac{1}{30}\frac{\hbar^2\gamma_I^2\gamma_S^2 S(S+1)}{r^6}[4j(0) + 3j(\omega_I) + 6j(\omega_S) + 6j(\omega_I + \omega_S) + j(\omega_I - \omega_S)] \quad (2.23)$$

Similar equations hold for T_1^{SS}, T_1^{SI} and T_2^S by interchanging the indices I and S. A very important feature appears in equation (2.18). The polarizations of the spins S and I are coupled so that an r.f field applied at say ω_I will affect $< S_z >$ while acting upon $< I_z >$. The second terms in equations (2.18) and (2.19) are due to cross relaxation effects between spins S and I. Cross-relaxation can be cancelled by irradiating the spins S at ω_S, making $< S_z > = < S_z >_0 = 0$, while observing the spins I at ω_I. Equation (2.18) then reduces to:

$$\frac{d < I_z >}{dt} = -\frac{1}{T_1^{II}}[< I_z > - < I_z >_0] \quad (2.24)$$

Thus, the solution of the equation of motion for the longitudinal magnetization is a mono-exponential with a time decay of $\frac{1}{T_1^{II}}$.

In the case of extreme narrowing conditions, that is when $\omega_0\tau_c \ll 1$, the spectral density functions are no longer frequency dependent and $j(0) = j(\omega_0) = j(2\omega_0) = 2\tau_c$. Under these conditions, normally met for samples of reasonable molecular weight (say < 1000 MW) in non-viscous solutions, the dipolar spin-lattice and spin-spin relaxation times for like spins are equal and:

$$\frac{1}{T_1^I} = \frac{1}{T_2^I} = \frac{\hbar^2\gamma_I^4 I(I+1)}{r^6}2\tau_c \quad (2.25)$$

2.3.2 Chemical Shift Anisotropy

The magnetic field experienced by a nucleus depends upon its electronic shielding. The existence of anisotropic electronic shielding around the nucleus results in a shield-

ing tensor σ, written in the Laboratory frame L(x, y, z) as:

$$\sigma = \begin{pmatrix} \sigma_{xx} & \sigma_{yx} & \sigma_{zx} \\ \sigma_{xy} & \sigma_{yy} & \sigma_{zy} \\ \sigma_{xz} & \sigma_{yz} & \sigma_{zz} \end{pmatrix} \tag{2.26}$$

If the screening tensor is symmetric $\sigma_{ij} = \sigma_{ji}$ $(i \neq j)$, σ can be diagonalized into a new set of cartesian coordinate axes (x', y', z') known as the principal axis of this diagonal tensor:

$$\sigma'_{diagonal} = \begin{pmatrix} \sigma'_{xx} & 0 & 0 \\ 0 & \sigma'_{yy} & 0 \\ 0 & 0 & \sigma'_{zz} \end{pmatrix} \tag{2.27}$$

By definition $|\sigma'_{xx}| \leq |\sigma'_{yy}| \leq |\sigma'_{zz}|$ represent the principal directional components of this tensor. They are bound to the molecular frame and undergo modulation because of reorientational molecular motion in solution. The induced magnetic fields also fluctuate and represent therefore a source of spin relaxation. The spin-lattice and the spin-spin relaxation times are given by [35]:

$$\frac{1}{T_1} = \frac{1}{15}\omega_0^2(\Delta\sigma)^2\left(1+\frac{\eta^2}{3}\right)j(\omega_0) \tag{2.28}$$

$$\frac{1}{T_2} = \frac{1}{90}\omega_0^2(\Delta\sigma)^2\left(1+\frac{\eta^2}{3}\right)[4j(0)+3j(\omega_0)] \tag{2.29}$$

where η is the asymmetry parameter ($\eta = \frac{\sigma'_{xx}-\sigma'_{yy}}{\sigma'_{zz}}$) and represents the deviation from axial symmetry in which case:

$$(\Delta\sigma)^2\left(1+\frac{\eta^2}{3}\right) = (\sigma_{\parallel}-\sigma_{\perp})^2$$

$\Delta\sigma$ is the chemical shift anisotropy term and is defined [103] as:

$$\Delta\sigma = \sigma'_{zz} - \left(\frac{\sigma'_{xx}+\sigma'_{yy}}{2}\right)$$

2.3.3 Scalar Relaxation

If there is spin-spin (scalar) coupling between the nuclei I and S, their NMR resonance lines will be split into multiplets with a coupling constant J. Scalar coupling can be a source of relaxation for I if the spin S relaxes rapidly. Such a situation may be found when S relaxes via a quadrupolar relaxation mechanism. The spin I will be relaxed by virtue of its coupling with S and the multiplet splitting of I will collapse. This relaxation mechanism was termed the "scalar relaxation of the second kind" [35] and:

$$\frac{1}{T_1^I} = \frac{8\pi^2 J^2 S(S+1)}{3}\left[\frac{T_{2,S}}{1+(\omega_I-\omega_S)^2(T_{2,S})^2}\right] \tag{2.30}$$

$$\frac{1}{T_2^I} = \frac{4\pi^2 J^2 S(S+1)}{3}\left[T_{1,S}+\frac{T_{2,S}}{1+(\omega_I-\omega_S)^2(T_{2,S})^2}\right] \tag{2.31}$$

2.3.4 Influence of Nuclear Transfer

2.3.4.a The General Two-Site Case

A simple chemical exchange can be considered in which reversible transfer of a nucleus X is taking place between two different molecular environments A and B. To study the influence of such a nuclear transfer on both the spin-lattice and spin-spin relaxation times, the starting point is to use the set of Block's equations in the rotating frame of reference [38]. Using Bloch notations, u, v and M_z denote respectively the components of the nuclear magnetizations which are in phase with the r.f field H_{1x}, out of phase with H_{1x}, and in the direction of the static magnetic field H_0. In pulsed NMR, where the magnetization components can be observed in the absence of the r.f field ($\omega_1 = \gamma H_{1x} = 0$), the modified Block's equations [44] including chemical

exchange are:

$$\dot{u}_A = -(\omega - \omega_A)v_A - \frac{u_A}{T_{2A}} - \frac{u_A}{\tau_A} + \frac{u_B}{\tau_B} \tag{2.32}$$

$$\dot{u}_B = -(\omega - \omega_B)v_B - \frac{u_B}{T_{2B}} - \frac{u_B}{\tau_B} + \frac{u_A}{\tau_A} \tag{2.33}$$

$$\dot{v}_A = +(\omega - \omega_A)u_A - \frac{v_A}{T_{2A}} - \frac{v_A}{\tau_A} + \frac{v_B}{\tau_B} \tag{2.34}$$

$$\dot{v}_B = +(\omega - \omega_B)u_B - \frac{v_B}{T_{2B}} - \frac{v_B}{\tau_B} + \frac{v_A}{\tau_A} \tag{2.35}$$

$$\dot{M}_z^A = \frac{M_z^A - M_0^A}{T_{1A}} - \frac{M_z^A}{\tau_A} + \frac{M_z^B}{\tau_B} \tag{2.36}$$

$$\dot{M}_z^B = \frac{M_z^B - M_0^B}{T_{1B}} - \frac{M_z^B}{\tau_B} + \frac{M_z^A}{\tau_A} \tag{2.37}$$

where T_{1A} and T_{2A} are the longitudinal and transverse relaxation times for nuclei in the environment A with a lifetime τ_A and an equilibrium magnetization M_0^A in the z direction. Similar definitions apply for the state B. Equations (2.32) and (2.34), (2.33) and (2.35) can be added by using the following short notation:

$$F_{A,B} = u_{A,B} + iv_{A,B}$$

and written as follows:

$$\begin{aligned} \dot{F}_A &= -\alpha_2 F_A + \tfrac{1}{\tau_B} F_B \\ \dot{F}_B &= -\beta_2 F_B + \tfrac{1}{\tau_A} F_A \end{aligned} \tag{2.38}$$

$$\begin{aligned} \dot{M}_0^A - \dot{M}_z^A &= -\alpha_1 (M_0^A - M_z^A) + \tfrac{1}{\tau_B}(M_0^B - M_z^B) \\ \dot{M}_0^B - \dot{M}_z^B &= -\beta_1 (M_0^B - M_z^B) + \tfrac{1}{\tau_A}(M_0^A - M_z^A) \end{aligned} \tag{2.39}$$

with:

$$\alpha_1 = \frac{1}{T_{1A}} + \frac{1}{\tau_A} \tag{2.40}$$

$$\alpha_2 = \frac{1}{T_{2A}} + \frac{1}{\tau_A} + i(\omega - \omega_A) \tag{2.41}$$

Similar definitions apply for β, the B state. Equations (2.38) and (2.39) represent two sets of two simultaneous equations of the form:

$$\begin{aligned} \dot{m} &= -\alpha m + bn \\ \dot{n} &= -\beta n + am \end{aligned} \tag{2.42}$$

the solutions of this set (2.42) of simultaneous equations are of the form [45]:

$$m(t) = A_+ \exp(-\Phi_+ t) + A_- \exp(-\Phi_- t) \tag{2.43}$$

$$n(t) = B_+ \exp(-\Phi_+ t) + B_- \exp(-\Phi_- t) \tag{2.44}$$

where $\Phi_\pm$, $A_\pm$ and $B_\pm$ are evaluated with the aid of initial conditions and related by [45,46]:

$$\frac{B_\pm}{A_\pm} = \frac{(\Phi_\pm - \alpha)}{b}$$

$$2\Phi_\pm = (\alpha + \beta) \pm \sqrt{[(\alpha - \beta)^2 + 4ab]}$$

Φ_+ or Φ_- represent either the longitudinal or transverse relaxation time contribution from site A and B to $m(t)$ and $n(t)$, α and β being chosen accordingly from equations (2.40) and (2.41). $m(t)$ and $n(t)$ then represent the evolution of the transverse magnetization of each site, the Free Induction Decay (FID), as well as the evolution of the longitudinal magnetization along the z axis. Equations (2.43) and (2.44) show that, in the general case, the magnetization decay in each site is no longer described by a single exponential. The magnetization evolution of each chemical site $m(t)$ and $n(t)$ is now governed by two different modes of relaxation due to chemical exchange between two different molecular environments. A mono-exponential treatment of the

FIDs would lead to erroneous relaxation data. Two component relaxation behavior has already been observed for water vapor absorbed on silica gel [48,49] and benzene molecules absorbed on silica gel [50].

2.3.4.b Approximate Solutions

Equations given for $m(t)$ and $n(t)$ represent the exact solutions of a system in which a nucleus is undergoing chemical exchange between two different molecular environments. However, it is possible to derive, under particular physical conditions, approximate solutions for both the longitudinal and transverse relaxation times [47].

Slow Exchange: The slow exchange approximation will be valid when the rate of exchange between the two environments is much slower than the difference between the two relaxation rates:

$$k \ll \left|\frac{1}{T_{1A}} - \frac{1}{T_{1B}}\right| \qquad \text{and} \qquad k \ll \left|\frac{1}{T_{2A}} - \frac{1}{T_{2B}}\right|$$

In this case, two unique resonances will be observed with respective transverse and longitudinal relaxation times:

$$\begin{array}{cc} \textit{Site } A & \textit{Site } B \\ \frac{1}{T_1} = \frac{1}{T_{1A}} + x_B k & \frac{1}{T_1} = \frac{1}{T_{1B}} + x_A k \\ \frac{1}{T_2} = \frac{1}{T_{2A}} + x_B k & \frac{1}{T_2} = \frac{1}{T_{2B}} + x_A k \end{array} \tag{2.45}$$

There are no restrictions on the relative values of the chemical shift difference $\Delta\omega_{AB}$ and the exchange rate k, nor on the relative values of $\Delta\omega_{AB}$ and $\left|\frac{1}{T_{2A}} - \frac{1}{T_{2B}}\right|$. Under slow exchange conditions two unique resonances will always be observed, regardless of whether these resonances are resolved or not. If the resonances are not resolved,

the observed spectrum will be the overlap of two resonances with their respective characteristic linewidth and longitudinal relaxation rate.

Fast Exchange: The fast exchange approximations are valid when the rate of exchange between the two environments A and B is much faster than the difference between the two relaxation rates:

$$k \gg \left|\frac{1}{T_{1A}} - \frac{1}{T_{1B}}\right| \qquad \text{and} \qquad k \gg \left|\frac{1}{T_{2A}} - \frac{1}{T_{2B}}\right|$$

If the rate of exchange satisfies $k \gg \Delta\omega_{AB}$, then the resonances are "exchange narrowed" and a single resonance will be observed and centered at:

$$\omega = \omega_A x_A + \omega_B x_B \tag{2.46}$$

with a transverse relaxation time given by [45]:

$$\frac{1}{T_2} = \frac{x_A}{T_{2A}} + \frac{x_B}{T_{2B}} + x_A x_B k^{-1} \Delta\omega_{AB}^2 \tag{2.47}$$

On the other hand, if $k \ll \Delta\omega_{AB}$ then the resonances are not "exchange narrowed" but separated by $\Delta\omega_{AB}$ and the two resonances will be observed with respective transverse relaxation times:

$$\begin{aligned} \frac{1}{T_2} &= \frac{1}{T_{2A}} + x_B k \\ \frac{1}{T_2} &= \frac{1}{T_{2B}} + x_A k \end{aligned} \tag{2.48}$$

Whether the resonances are exchange narrowed or not, a single averaged longitudinal relaxation time is observed:

$$\frac{1}{T_1} = \frac{x_A}{T_{1A}} + \frac{x_B}{T_{1B}} \tag{2.49}$$

It should be noted that the fast exchange condition for the longitudinal relaxation times does not necessarily imply the exchange narrowed conditions for the transverse

relaxation times. In fact, it is possible to observe two different resonances for the A and B environments with different respective transverse relaxation times but with the same averaged longitudinal relaxation time.

2.4 Quadrupolar Relaxation

2.4.1 Quadrupolar Relaxation Under the Extreme Narrowing Conditions

Nuclei with a spin $I > 1/2$ possess a nuclear electric quadrupole moment eQ. The existence of an asymmetric electronic environment creates an electric field gradient eq around the nucleus causing pure electrical interactions between the electric quadrupole moment and the electric field gradient. Modulation of these interactions by rotational motion induces transitions between nuclear quadrupole levels. Thus, while the effect is electrical in nature, it does provide a means for magnetic spin relaxation. If the fluctuations of the electric field gradient, characterized by a correlation time τ_c are fast enough so that $\omega_0\tau_c \ll 1$ (called the extreme narrowing conditions), then nuclear quadrupole relaxation can be described [35] by:

$$\frac{1}{T_1} = \frac{1}{T_2} = \frac{3\pi^2}{10}\frac{2I+3}{I^2(2I-1)}\left(1+\frac{\eta^2}{3}\right)\left(\frac{e^2qQ}{h}\right)^2\tau_c \qquad (2.50)$$

where η is the asymmetric parameter that measures the departure of the nuclear environment from axial symmetry ($\eta = \frac{\eta_{xx}-\eta_{yy}}{\eta_{zz}}$). $\chi = \left(\frac{e^2qQ}{h}\right)$ is the quadrupole coupling constant. Unless the electric field gradient is very small or zero due to molecular symmetry, this mechanism dominates the relaxation of most quadrupolar nuclei.

2.4.2 Quadrupolar Relaxation Under the Non-Extreme Narrowing Conditions

In studies of ion complexation with biological macromolecules like DNA, proteins or other macromolecular systems like molecular aggregates, the extreme narrowing condition usually applies for the free ion in the bulk solution. However, the extreme narrowing conditions are often violated for the bound site, as a result of the slow motion of these macromolecules. In the latter case, the concept of relaxation time has to be revised for spins $I \geq 3/2$ as the longitudinal and transverse magnetization decays are multi-exponential [51]. This is in contrast with spins $I = 1$ like Deuterium, for which the longitudinal and transverse magnetization decays are still governed by a single exponential [35]. For spins 3/2 (^{23}Na, ^{39}K, ^{87}Rb) the longitudinal and transverse magnetizations evolve as a weighted sum of two exponentials [51] and analytical equations were derived [52] and expressed as:

$$M_z(t) = M_z(0)\left\{1 - \left[\frac{4}{5}\exp(-\frac{t}{T_{11}}) + \frac{1}{5}\exp(-\frac{t}{T_{12}})\right]\right\} \tag{2.51}$$

$$M_{xy}(t) = M_{xy}(0)\left[\frac{2}{5}\exp(-\frac{t}{T_{21}}) + \frac{3}{5}\exp(-\frac{t}{T_{22}})\right] \tag{2.52}$$

The spin-lattice and spin-spin relaxation times corresponding to the single quantum transition $m = 1/2 \rightarrow m = -1/2$ are:

$$\frac{1}{T_{11}} = \frac{\pi^2}{5}\left(1 + \frac{\eta^2}{3}\right)\chi^2 j(2\omega_0) \tag{2.53}$$

$$\frac{1}{T_{21}} = \frac{\pi^2}{10}\left(1 + \frac{\eta^2}{3}\right)\chi^2[j(\omega_0) + j(2\omega_0)] \tag{2.54}$$

while for the $m = \pm 3/2 \rightarrow m = \pm 1/2$ transitions:

$$\frac{1}{T_{12}} = \frac{\pi^2}{5}\left(1 + \frac{\eta^2}{3}\right)\chi^2 j(\omega_0) \tag{2.55}$$

$$\frac{1}{T_{22}} = \frac{\pi^2}{10}\left(1+\frac{\eta^2}{3}\right)\chi^2[j(0)+j(\omega_0)] \qquad (2.56)$$

Equation (2.51) shows that the evolution of the longitudinal magnetization is composed of two distinct modes of relaxation [53]: a slow relaxation component ($\frac{1}{T_{11}}$) with 80% weight and a fast relaxation component ($\frac{1}{T_{12}}$) with a weight of 20% of the total magnetization M_z^0. A similar situation holds for the transverse magnetization which is composed of a narrow component ($\frac{1}{T_{21}}$) with 40% weight and a broad component ($\frac{1}{T_{22}}$) with a weight of 60% of the total transverse magnetization M_{xy}^0. Fourier transformation of the transverse magnetization does not yield a single Lorentzian line shape but the overlap of two Lorentzians composed of a broad (equation (2.56)) and a narrow (equation (2.54)) component. Deviations from a simple exponential decay are not exceptional and non-Lorentzian line shapes have already been observed, for example, with ^{23}Na [54,55,56].

For a 5/2 nuclear spin (like ^{25}Mg, ^{27}Al, ^{67}Zn) the relaxation behavior of these nuclei is more complicated and it will be dealt with in detail in Chapter 9.

Chapter 3

MATERIALS AND METHODS

3.1 Introduction

Spin-lattice relaxation time determination has increasingly become an indispensable tool for solving chemical problems and understanding solution dynamics [57]. Fourier transformed NMR has made simultaneous spin-lattice relaxation time determination possible for each nucleus of a complex molecule [58]. During the 70's there has been a proliferation of pulse sequences [61,62,63,64,66,67,68,81] for measuring longitudinal relaxation times leaving the NMR spectroscopist with a wide choice of pulse sequences. The choice of a method depends on many factors: the specific nuclei and chemical problems under investigation, the accuracy of T_1 values to be achieved and, finally, the amount of spectrometer time available.

It is important to realize that there are two main sources of measurement errors associated with T_1 determination. The use of a specific pulse sequence sometimes depends upon the availability of the appropriate hardware on the spectrometer but, once the choice is made, it is associated with the inherent limitations of the pulse sequence which generates *systematic measurements errors*. The experimentalist can do little to minimize them. On the other hand, the adequate choice of an optional set of experimental parameters [70,71,72,73], like the initial evolution time, the pulse

delay, the spacing and the number of evolution times contributes toward the minimization of *random measurement errors* on T_1 determinations. The selection of a method [69] is of considerable importance for minimizing experimental and instrumental uncertainties, as well as the length of time spent on the spectrometer, to determine spin-lattice relaxation times.

The different techniques commonly used for T_1 measurements can be divided into two classes. The first class includes pulse sequences that perturb the magnetization M_0 from its equilibrium value, and then acquire the nuclear magnetization after various different evolution times τ. This method is commonly used in Saturation Recovery (SR) [63], Inversion Recovery (IR) [58], Fast Inversion Recovery (FIR) [61], and Modified Fast Inversion Recovery (MFIR) [62] pulse sequences. The other technique is to prepare the magnetization in a series of different steady-states before sampling takes place. This is achieved in Progressive Saturation (PS) [64,66] and Variable Nutation Angle (VNA) [67,68] pulse sequences.

When signal averaging is needed and the T_1 is not too long, IR is the most commonly used pulse sequence for T_1 determination because it is the best experimental approach to yield accurate T_1 results [69,72]. However, the system must be allowed to relax back to its equilibrium state before the pulse sequence can be repeated. Typical pulse delays (PD) range from 5 to 7 T_1 [60]. For low sensitivity nuclei like ^{31}P,^{13}C, or ^{15}N with long T_1 values, the need for this lengthy pulse delay at the end of each pulse sequence, can be time consuming and is an obvious limitation to this pulse sequence. In such cases, a better choice would be to use the FIR or MFIT pulse sequences in which typical PD values are in the order of 2 T_1 [61,62]. In order to reduce systematic T_1 error when using the IR method, the spectroscopist has to be aware that these pulse sequences are sensitive to off resonance effects, due to the finite pulse power

available, but has the advantage of tolerating pulse angle missetting by a few degrees [70,71].

The selection of the saturation method [63,64,66] represents an alternative for measuring spin-lattice relaxation times. The danger of this method lies in the possible formation of echoes [59] which necessitate the application of field gradients [64], not always appreciated by the spectroscopist. As well, the method is quite sensitive to 90° pulse angle missetting [70] and does not possess the attractive dynamic range (sensitivity) of the inversion method [66,69]. All these features make the saturation method less prone to be used in T_1 measurements, unless the relaxation time becomes too long (typically longer than 5 sec). In such cases the SR pulse sequence is preferred over the PS pulse sequence for accuracy reasons [69].

3.2 NMR Spectrometers

Two different NMR spectrometers were used to study the T_1 field dependency. The resonance frequencies of ^{31}P were 121.421 MHz (XL-300 Varian spectrometer) and 32.198 MHz (FT-80 Varian spectrometer) using quadrature and single phase detection, respectively. NMR tubes (Wilmad Glass Co.) were 10 mm on the FT-80 as opposed to 5 mm on the XL-300 (the probe used on the XL-300 was a 5 mm broadband). For both fields a 20% D_2O solution was used to catch the internal field lock, and the sample temperature was kept constant at 22 ± 1 °C throughout the studies. The pulse width calibration was done on a solution of ATP 100 mM at pH 7.3 with 20% D_2O. The 90° pulse widths determined by the 360° method (null method) were 47 μs and 14.5 μs on the FT-80 and XL-300 respectively. Chemical shifts were referenced to an 85% H_3PO_4 solution with a coaxial tube filled with D_2O.

An important instrumental requirement for the inversion recovery experiment is

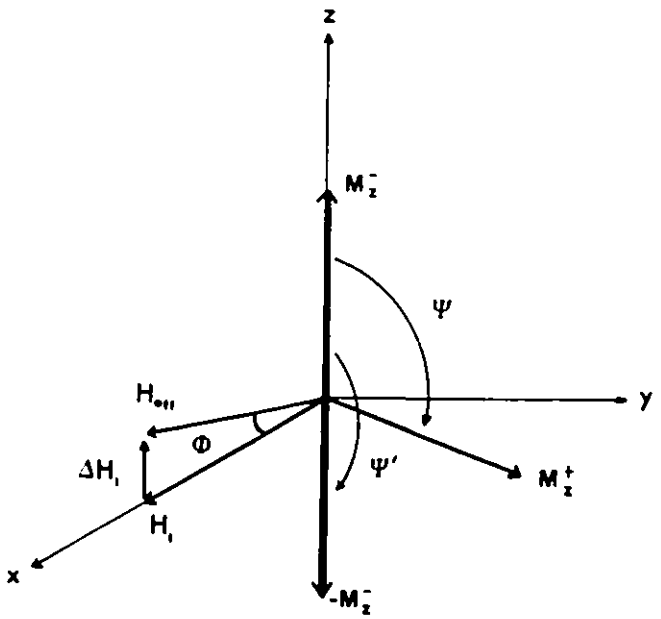

Figure 3.1: Offset resonance effects and definition of the angles Φ, Ψ and Ψ' in the rotating frame of reference.

a sufficient r.f pulse power H_1 to irradiate the spins throughout the spectral window of interest ΔH_1 [70]. In practice however, because of the finite radio frequency pulse power available on the spectrometer, resonance offset effects may arise. This refers to the magnetization which, away from the exact resonance frequency γH_1 , does not tip about the applied r.f field H_1 but rather about an effective field H_{eff} [66] as shown in Figure 3.1. The angles Φ, Ψ and Ψ' (corresponding to a 90° and a 180° tipping of the z magnetization respectively) are defined by:

$$\tan \Phi = \frac{\Delta H_1}{H_1} \qquad \Psi = \gamma H_{eff} t_{90} \qquad \Psi' = \gamma H_{eff} t_{180}$$

in which ΔH_1 represents the offset from exact resonance. The effective field H_{eff} is given by:

$$H_{eff} = \sqrt{H_1^2 + \Delta H_1^2}$$

	H_1	ΔH_1	k	k′	k′
	(gauss)		(theoretical)		(experimental)*
FT–80	3.1	0.4	0.01	- 0.97	- 0.96 ± 0.01†
XL–300	10.0	1.5	0.01	- 0.96	- 0.95 ± 0.01†

Table 3.1: ^{31}P field strength, spectral window and pulse imperfection values at 32 and 121 MHz. (*) The experimental values represent the average over 39 k′ values on the FT–80 and 35 on the XL–300 NMR spectrometers. (†) The experimental k′ values are reported with the error as twice the standard deviation.

For a 90° pulse, the residual longitudinal component of magnetization immediately after the pulse (M_z^+) in terms of the longitudinal component before the pulse (M_z^-) can be written as [66]:

$$M_z^+ = kM_z^- \qquad \text{with} \qquad k = \sin^2\Phi + \cos^2\Phi\cos\Psi$$

or for a 180° pulse as :

$$M_z^+ = k'M_z^- \qquad \text{with} \qquad k' = \sin^2\Phi + \cos^2\Phi\cos\Psi'$$

These k factors reflect the imperfections of the r.f pulse throughout the spectral window due to the finite pulse power available. In the case of perfect 90° and 180° pulses $k = 0$ and $k' = -1$. Deviation from these ideal values results in erroneous signal intensity measurements leading to systematic errors [69,70,71] in T_1 determination. Determination of the pulse power and frequency offsets at both fields allowed the theoretical k and k' factors to be calculated (see Table 3.1). With regards to the form of the equation of $M_z(t)$ taken in a non-linear regression analysis (see equation (3.1)) only the experimental k' could be determined. We report this experimental

value obtained from a curve fitting to the experimental data sets and there is excellent agreement between the theory and the experiment. At a frequency effect corresponding to the resonance of the β phosphorus of ATP, we observe minor deviations from ideal values of $k' = -1$ and $k = 0$ which still fully satisfy the criterion of ideal experimental condition at both fields [70].

3.3 Phosphorus-31 Spin-Lattice Relaxation Time Measurements

Each sample in this study was oxygen degassed by bubbling argon through the solution for 15 minutes. The solution was then allowed to reach thermal equilibrium in the spectrometer probe head (typically 10 to 15 minutes).

The inversion recovery pulse sequence was used to obtain all T_1 values without proton decoupling. The pulse delay (PD) was always greater than 5 $(T_1)_{max}$ [60]. In order to obtain accurate T_1 measurements we have used at least 7 to 10 different τ values, generally linearly spaced from 0.1 T_1 to 2 T_1 [71,72]. For the most accurate results, the increment chosen between two successive τ values satisfied $0.3\ T_1 \leq \tau \leq 1\ T_1$ [72]. For the ATP-H_2O system the reported average $\hat{T}_1$ values for each phosphate at both fields represented at least three to five T_1 measurements on the same solution. In the case of the ATP-Al(III) system, we were only able to determine one T_1 value per sample because of sample decomposition, typically four hours after the solutions were prepared.

Taking into account systematic errors due to resonance offset [71] and random errors arising from the experimental parameter set [72] for these experiments, the standard deviation obtained $\sigma(\hat{T}_1)$ is about 2 to 3% of the $\hat{T}_1$ (see equation (3.2)). It is important to note that these calculated standard deviations do not include errors

due to sample preparation which could introduce a 5% error in the T_1 data. Because all of the T_1 and NOE measurements have been determined at both fields on the same sample, we consider our data to be "free" of sample preparation errors, and these errors will not be taken into consideration in further calculations.

Typical accumulation time was 4 sec over 1000 Hz (FT–80) and 4000 Hz (XL–300) sweep width. Signal averaging was performed until a signal to noise ratio of at least 100 was achieved. Each FID was then Fourier transformed, without any weighting function unless indicated, using the full 8K (FT–80) and 32K (XL–300) data tables.

3.4 ^{31}P–{^{1}H} NOE Factor Measurements

Nuclear Overhauser Effects were measured by using a gated decoupling technique with the pulse delay equal to 10 times $(T_1)_{max}$ [60,78]. This fastidious waiting period results from the non-exponential recovery rate of the M_z magnetization [78]. The decoupler utilized on the XL–300 was a Waltz–16, a broadband heteronuclear decoupler, which offers substantial improvement in decoupling efficiency [77] while using considerably less decoupling power (0.5 Watt) and preventing sample heating problems. Experiments on the FT–80 were performed by using a pseudo-random noise decoupling power of 2.5 Watts spread over a noise band width of 1000 Hz. The frequency of the decoupler offset was set in the middle of the proton spectrum at both fields. The NOE enhancement factor η was measured [57] using:

$$\eta + 1 = I(on)/I(off)$$

where $I(on)$ and $I(off)$ refer to the peak heights when the decoupler is turned *on* or *off*, respectively. Reported η values at both fields represent the average of typically four successive measurements on the same sample used to determine T_1 values, while

σ values represent twice the standard deviation.

In order to measure NOE factors with a degree of confidence better than 10% [79], signal averaging was performed until a signal to noise ratio better than 100 was achieved. Special care was given to phasing spectra in view of minimizing intensity errors resulting from a poor phasing [80]. Because sharp peak intensities are influenced by field inhomogeneities, the NOE factors measured by intensities have been compared, in a few cases, with a more time consuming peak area measurement method [80] (the product of the peak height times the width of the peak at one half peak height). The results by the peak area method were in very good agreement (within two σ of our original measurements).

3.5 Data Analysis

Longitudinal relaxation times were evaluated using a non-linear three parameter least square procedure which minimizes the following quantity:

$$Q = \sum_i [y_i - f(t_i, k', M_0, T_1)]^2$$

where y_i are the measured intensity peak heights and f represents the three parameter (k', M_0, T_1) relaxation function. In the case of the inversion recovery sequence the evolution of the longitudinal magnetization for different recovery times t_i is given by [69]:

$$M_z(t) = M_0 \frac{\left[(1 - e^{-t/T_1}) + k'(1 - e^{-PD/T_1})e^{-t/T_1}\right]}{\left[1 - kk'e^{-PD/T_1}e^{-t/T_1}\right]}$$

A few justified approximations can be made. Keeping the pulse delay (PD) greater than 5 $(T_1)_{max}$ makes the exponential term e^{-PD/T_1} negligible. As well, the theoretical product $kk' \approx 10^{-3}$ is very small (see Table 3.1) and under these conditions:

$$M_z(t) = M_0 \left[1 - (1 - k')e^{-t/T_1}\right] \tag{3.1}$$

Equation (3.1) represents the three parameter relaxation function in which field inhomogeneities and pulse imperfections are being considered. At this point, there are basically two reliable methods for determining T_1 from experimental signal intensities $M_z(t)$, by using a linear regression analysis [75] or a non-linear least square minimization with two [82,74] or three [83] parameters. There is also the use of a semi-logarithmic method but, apart from its simplicity, it does not provide any other advantage. In fact, this technique is considered to be imprecise and time consuming because it requires an accurate measurement of the equilibrium magnetization M_0 [71]. Both disadvantages can be avoided by fitting the experimental values to an exponential function of the type given in equation (3.1). We have chosen the non-linear three parameters least square fitting procedure because it does not entail the precise additional experimental determination of the r.f inhomogeneity factor k' for each resonance line [84], which is needed in the case of linear [75] or non-linear [82] analysis with two parameters.

For each phosphorus longitudinal relaxation time of the triphosphate chain of ATP the precision of our measurements is reported as twice the standard deviation $\sigma(\hat{T}_1)$ calculated from [73]:

$$\frac{\sigma(\hat{T}_1)}{T_1} = \left(\frac{S}{N}\right)^{-1} \left[\frac{\sum_i u_i^2 + (\sum_i u_i v_i)^2}{(\sum_i u_i^2)^2}\right]^{\frac{1}{2}} \tag{3.2}$$

in which u_i and v_i are the dimensionless functions:

$$u_i = 2\frac{\tau_i}{T_1} e^{-\tau_i/T_1}$$

and

$$v_i = 1 - 2e^{-\tau_i/T_1}$$

S/N is the signal to noise ratio, T_1 the spin-lattice relaxation time and τ_i the different recovery times in the IR pulse sequence.

3.6 Sample Preparation

It is well known that phosphorus spin-lattice relaxation times are extremely sensitive to paramagnetic impurities. It is therefore crucial to remove every trace of paramagnetic ions in the sample. Throughout this work, the pH of the solution was kept constant at 7.40 ± 0.05 (20% D_2O solution). The pH meter reading (Corning pH/ion meter 155) was always corrected for the deuterium isotope effect. The Corning pH electrode was filled with saturated ultrapure KCl (Alfa Products) dissolved in triply distilled water, and standardized using a pH = 7 buffer solution (Fischer Scientific Company). A cation exchange resin (Amberlite IR–120 analytical reagent 20–50 mesh) was loaded on a column, treated with HCl (2M), rinsed with triply distilled water and then converted into the sodium salt by passing through 2M ultra pure sodium hydroxide (Alfa Products). The pH of the column was then adjusted to pH = 8 by rinsing it with triply distilled water. The 20% D_2O solution used to prepare all sample solutions was passed twice through the column. The water bed was then removed by blowing nitrogen through the column.

ATP stock solutions (0.2M, 25 ml) were prepared as follows. In a volumetric flask, ATP (Sigma Company) was dissolved in 20% D_2O solution and then adjusted to pH = 6 with ultra pure solid sodium hydroxide pellets, handled with teflon coated tweezers. Paramagnetic ions in ATP were then removed by adding and stirring 2 g of the dry treated resin into the ATP stock solution. The total exchange capacity was 5.0 meq/g corresponding to a potential removal of approximately 3 mmol of Fe^{3+} ions.

Hexahydrated aluminum chloride (99.999%) gold label (Aldrich Company) was used without further purification. The stock solution was (0.2M, 50 ml) in 20% D_2O

solution and used without any pH adjustment.

Aluminum–ATP samples were prepared by mixing, in the following order the appropriate amount of ATP, 20% D_2O solution and the aluminum solution using micropettor syringes (Scientific Manufacturing Industries).

At this stage, typically 0.1 mM of solid $EDTANa_4$ was added to the 4 ml sample solution, and then the pH adjusted to 7.4 using ultra pure pellets of sodium hydroxide previously dried under vacuum (120 °C overnight). Removal of oxygen was carried out in the NMR tube by argon bubbling for 15 min. Every sample was then sealed with parafilm.

Every piece of glassware used throughout for sample preparation (pipettes, beakers, vials, syringes, caps) was carefully washed in a basic EDTA (50 ml) solution bath, rinsed three times with triply distilled water and then dried in the oven. Spatulas and tweezers were all teflon coated. NMR tubes were soaked in concentrated HCl, washed at least twice in an EDTA bath, thoroughly rinsed with triply distilled water and finally dried in the oven.

Chapter 4

PHOSPHORUS-31 SPIN-LATTICE RELAXATION OF ADENOSINE TRIPHOSPHATE IN AQUEOUS SOLUTIONS

4.1 Introduction

There is an extensive variety of important biological compounds containing phosphorus atoms. Moreover, this nucleus is easily detectable due to a relatively high gyromagnetic ratio $\gamma = 10.8289$ rd. T^{-1}. sec^{-1}, a natural abundance of 100% and a receptivity of 377 compared to ^{13}C [114]. These NMR properties makes it a convenient and popular tool to probe molecular dynamics in solution, by means of relaxation studies and there is already a great deal of data present in the literature for phosphorus–proton NOE and phosphorus spin-lattice relaxation times of orthophosphates [85,86,87,88,89,90,130], mononucleotides [101] and polynucleotides [91,92,93,102] solutions.

In the early studies on aqueous orthophosphate solutions, several investigations have shown that the variation of the relaxation rate of phosphorus was strongly

affected by the pH [85,86,87]. The trend of the T_1–pH profile for such molecules generally showed several minima for T_1 values close to the pK_a of the different ionic species present in solution. However, large relaxation rate discrepancies were observed in orthophosphate solutions. For example, at pH = 7, the ^{31}P relaxation rate can vary from $R = 1.0\ sec^{-1}$, corresponding to a maximum relaxation rate for non-purified samples [86], $R = 0.2\ sec^{-1}$ for samples treated with a Chelex resin [87], to $R = 0.065\ sec^{-1}$ for highly purified samples [90]. There has been a clear demonstration [90] that the T_1 was almost independent of the pH in rigorously purified samples and the observed minima T_1 values from previous studies were erroneously attributed to different ionic species in solution [85]. In fact, differences in T_1 values were largely dominated by paramagnetic impurities in solution [87,90] . In the case of orthophosphate solutions it has been possible to separate the different relaxation rate contributions to the overall spin-lattice relaxation rate and to analyze the dynamics of orthophosphate ions as well as to propose a solvation model for this compound in solution [90].

The influence of paramagnetic impurities present in aqueous solution samples were also studied for different nucleotides [87]. For ATP in the presence of paramagnetic ions in solution, all three phosphorus relaxation times were very similar regardless of the solution pH. A clear distinction between relaxation rates for each phosphate occurred when paramagnetic ions were removed by Chelex or EDTA treatment and longitudinal relaxation times generally followed the trend $T_1(P_\gamma) > T_1(P_\beta) > T_1(P_\alpha)$. In this study [87], the T_1–pH profiles were still tainted by minima, showing the presence of paramagnetic impurities left in solution. Although there are phosphorus spin-lattice relaxation data available for nucleotides [87,92,93,115], different contributions to the overall T_1 were not clearly resolved. Relaxation parameters like chemical shift

anisotropy values, correlation times and spin-rotation coupling constants were not unambiguously determined. As well, no detailed solvation model presently exists for the phosphate side chain of nucleotides.

In this work, we have resolved the different dynamic contributions to the overall spin-lattice relaxation rate for the three different phosphorus atoms of the triphosphate chain of ATP. As well, we have determined the correlation times and chemical shift anisotropy values of the α, β and γ phosphorus atoms. A solvation model was also proposed for the triphosphate chain that is compatible with our results at a pH of biological importance (pH = 7.4).

4.2 Results of Phosphorus-31 and Carbon-13 Measurements

Previous reports have clearly shown the dependence of phosphorus T_1 values on paramagnetic contamination. Only a few research groups have been able to extract valuable information from orthophosphate, mono and polynucleotides solutions via phosphorus spin-lattice relaxation [90,113,133] or NOE measurements [100,101,102] because of careful sample preparations. Any comparisons to literature data should be done cautiously.

A typical example of erroneous T_1 value determinations is given in Table 4.1, case (1). No special treatment of the sample solution was done and we observe quite similar relaxation times for the γ and β phosphorus atoms of ATP (T_1 = 1.0 sec). Substantial improvement was achieved by use of distilled water and ultra pure NaOH, as the P_γ and P_β relaxation time values were double and became clearly distinctive (see case (2)). Finally, erroneous T_1 data (case (1)) can be compared with reliable T_1 values when sample preparation is appropriately and carefully done (cases (3), (4)

Case	Sample Preparation	$T_1(P_\gamma)$ (sec)	$T_1(P_\alpha)$ (sec)	$T_1(P_\beta)$ (sec)
(1)	No special treatment	1.06	1.42	0.96
	σ	0.04	0.05	0.04
	ATP used as is			
(2)	Distilled water	2.19	1.81	1.77
	Ultra pure NaOH			
	σ	0.05	0.04	0.04
(3)	As case (2) + 3 mM EDTA	3.97	1.91	2.72
	σ	0.06	0.04	0.05
	ATP treated on resin			
(4)	Distilled water	4.02	1.97	2.65
	Ultra pure NaOH			
	σ	0.06	0.04	0.05
(5)	As case (4) + 3 mM EDTA	3.87	1.89	2.69
	σ	0.06	0.04	0.05
	$\hat{T}_1$	3.95	1.92	2.69
	$2\sigma(\hat{T}_1)$	0.06	0.04	0.05

Table 4.1: ^{31}P longitudinal relaxation times as a function of sample preparation at 121 MHz. Experimental T_1 values are reported with the error as twice the standard deviation (see Section 3.5). Experimental conditions were: pH = 7.4, 20% D_2O, T = 22 °C, [ATP] = 100 mM, $S/N > 100$ at 121 MHz.

	P_γ	P_α	P_β
T_1^* (sec)	7.34	5.55	7.80
$T_1^\dagger$ (sec)	6.2	4.5	7.0

Table 4.2: ATP phosphorus-31 longitudinal relaxation times at 32 MHz. (*) This work, 32 MHz, 20% D_2O, 22 °C; (†) from reference [104] 40 MHz, 10% D_2O and 4 °C.

and (5)). An upper limit plateau is reached for each phosphorus atom which then takes its own true T_1 value.

Figure 4.1 shows a typical phosphorus-31 T_1 inversion recovery experiment corresponding to the case (4) of Table 4.1. It has been difficult to compare our results with published data because experimental conditions often differ from one work to another (frequency of observation, D_2O content, pH and temperature of the solution), or simply because of a lack of confidence in published T_1 data of free ATP [87,103] which are generally too short. As well, studies of the pH–T_1 profile [87] closely resemble those found for inorganic phosphates, indicating in both cases sample contamination by paramagnetic impurities. Among available T_1 data on mononucleotides [87,92,93,115], we have only found one example of published relaxation times of ATP [104] which agree closely with our results (see Table 4.2). In that study, we have to consider that the measurements were made at 4 °C and at 40 MHz. Under these conditions, the contributions of both CSA and dipolar mechanisms to the overall T_1 data will be smaller in magnitude, resulting in a lower overall T_1 for all three phosphate groups.

The overall relaxation rates for each phosphorus atom γ, β and α are presented

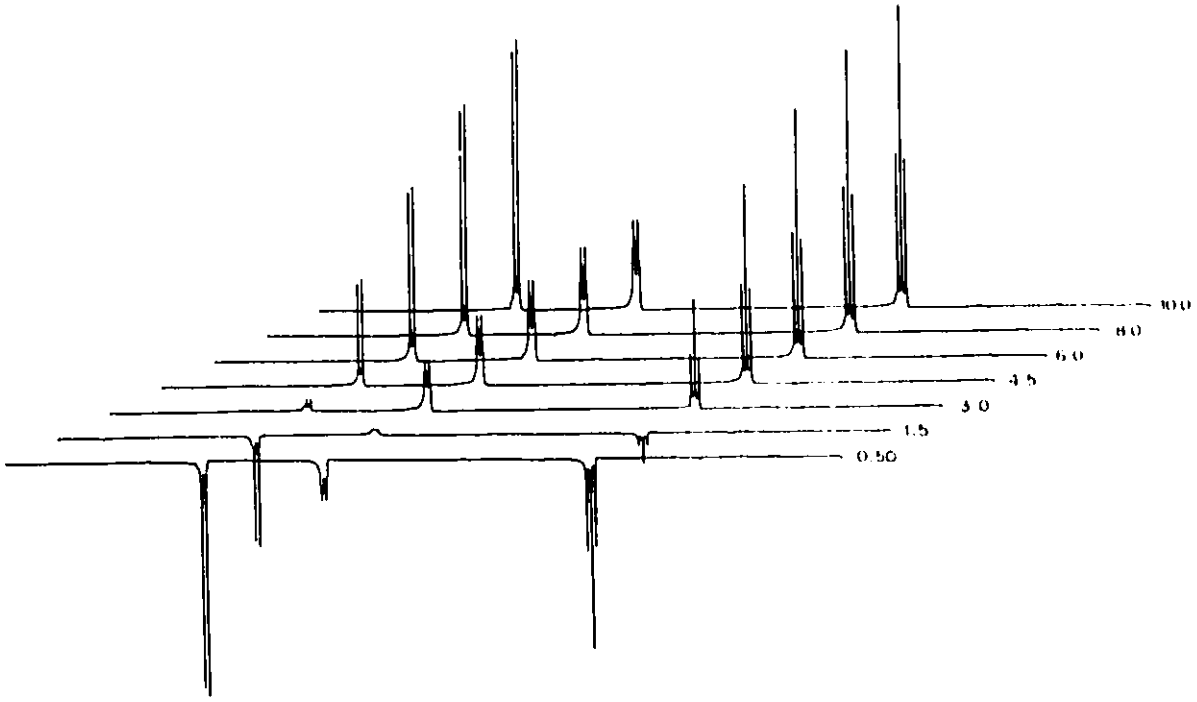

Figure 4.1: Display of a phosphorus-31 inversion recovery nmr experiment of ATP at 121 MHz. For experimental conditions see Table 4.1. Instrumental conditions were: spectral width of 4000 Hz, acquisition time of 5 sec, pulse delay of 20 sec, no proton decoupling and 40 transients in 5 mm tube. Recovery times in seconds are shown near each spectrum.

in Table 4.3, at two different magnetic field strengths, in 20% D_2O solution and at T = 22 ± 1 °C. From our experimental relaxation rates at two different magnetic fields, and for each of the three individual phosphates of the triphosphate chain of ATP, we observed a clear field dependency upon the relaxation rate efficiency. This means that relaxation by chemical shift anisotropy was definitely one of many possible sources of relaxation contributing to the observed overall relaxation rates of phosphorus nuclei in ATP molecules. For example, the α phosphorus at 121 MHz had a relaxation rate of $R(\text{obs}) = 0.521\ \text{sec}^{-1}$ compared with $R(\text{obs}) = 0.180\ \text{sec}^{-1}$ at 32 MHz (see Table 4.3). Chemical Shift Anisotropy (CSA) only becomes an efficient relaxation mechanism at high magnetic field strengths, as it is dependent upon the square of the magnetic field (see Section 2.3.2). Contribution of CSA to the overall relaxation rates has to be calculated. Consider the observed relaxation rates at ω_1 and ω_2:

$$R(\text{obs},\omega_1) = R(\text{CSA},\omega_1) + R(\text{left},\omega_1) \tag{4.1}$$

$$R(\text{obs},\omega_2) = R(\text{CSA},\omega_2) + R(\text{left},\omega_2) \tag{4.2}$$

Assuming that for each phosphorus nucleus the leftover relaxation rate $R(\text{left})$ is not dependent upon the frequency of observation, equations (4.1) and (4.2) can be subtracted and rearranged to obtain:

$$R(\text{CSA},\omega_1) = \left[1 - \frac{R(\text{CSA},\omega_2)}{R(\text{CSA},\omega_1)}\right][R(\text{obs},\omega_1) - R(\text{obs},\omega_2)] \tag{4.3}$$

The ratio $R(\text{CSA},\omega_2)/R(\text{CSA},\omega_1)$ is evaluated by expressing the CSA relaxation equation at two different pulsations (see equation (2.28)). Equation (4.3) becomes:

$$R(\text{CSA},\omega_1) = \frac{\omega_1^2 j(\omega_1)}{\omega_1^2 j(\omega_1) - \omega_2^2 j(\omega_2)}[R(\text{obs},\omega_1) - R(\text{obs},\omega_2)] \tag{4.4}$$

	P_γ		P_α		P_β	
	ν_1	ν_2	ν_1	ν_2	ν_1	ν_2
$\hat{R}$(obs) (sec^{-1})	0.253	0.136	0.521	0.180	0.372	0.128
2σ	0.004	0.002	0.008	0.003	0.007	0.002
R(CSA) (sec^{-1})	0.125	0.008	0.365	0.024	0.261	0.017
$\pm$	0.005	0.0003	0.010	0.001	0.008	0.001
R(left) (sec^{-1})	0.128	0.128	0.156	0.156	0.111	0.111
$\pm$	0.007	0.007	0.007	0.009	0.005	0.008
$\hat{\eta}_{obs}$	0.26	0.55	0.19	0.72	0.13	0.53
2σ	0.04	0.05	0.03	0.08	0.02	0.05
R(P–H) (sec^{-1})	0.054	0.061	0.082	0.105	0.040	0.055
$\pm$	0.009	0.006	0.014	0.013	0.010	0.006
R(other) (sec^{-1})	0.074	0.067	0.074	0.051	0.071	0.056
$\pm$	0.016	0.010	0.016	0.010	0.015	0.010

Table 4.3: Decomposition of the ^{31}P overall relaxation rates into the different operating sources of relaxation. Experimental conditions were: ν_1 = 121 MHz, ν_2 = 32 MHz, 20% D_2O, T = 22 °C, pH = 7.4, [ATP] = 100 mM.) The reported observed relaxation rates $\hat{R}$(obs) and NOE factors $\hat{\eta}_{obs}$ represent the average of at least three measurements on the same sample and at two different fields. All experimental values are reported with an error of twice the standard deviation (see Section 3.5). Calculated relaxation rate values are reported with their respective uncertainty which was calculated using a rigorous error calculation.

in which $j(\omega_i)$ represents the spectral density function at ω_i (see Section 2.2). The contribution of R(CSA) at the pulsation ω_2 is identical to equation (4.4) by interchanging the indices 1 and 2.

The contribution of CSA at a pulsation ω_1 (equation (4.4)) to the overall relaxation rate can be calculated if two T_1 measurements at two different pulsations, ω_1 and ω_2, have been measured and if the rotational correlation time τ_c of the phosphorus atom considered is known. For our purposes it will be assumed that the rotational correlation time of the three phosphorus atoms is identical to that of an ATP molecule. This assumption will be justified in the discussion section.

The contribution of CSA mechanism to the overall relaxation rate is reported in Table 4.3, and is preponderant at 121 MHz $R(\mathrm{CSA}, \mathrm{P}_\alpha) = 0.365\ \mathrm{sec}^{-1}$ but negligible at 32 MHz $R(\mathrm{CSA}, \mathrm{P}_\alpha) = 0.024\ \mathrm{sec}^{-1}$, as expected. Its efficiency to relax the three phosphorus atoms of the triphosphate chain is different and occurs in the following order: $\mathrm{P}_\alpha > \mathrm{P}_\beta > \mathrm{P}_\gamma$. Note that even though the spectral density functions $j(\omega_i)$ are very weakly frequency dependent, neglecting them in equation (4.4) would introduce some error to the third significant figure. For example, at 121 MHz, $R(\mathrm{CSA}, \mathrm{P}_\gamma) = 0.122\ \mathrm{sec}^{-1}$ when calculated with the approximate equation (4.4) in which $j(\omega_1) = j(\omega_2)$, instead of $0.125\ \mathrm{sec}^{-1}$ as indicated in Table 4.3.

We also report in Table 4.3 a leftover relaxation rate defined as:

$$R(\mathrm{left}) = R(\mathrm{obs}) - R(\mathrm{CSA})$$

due to other relaxation mechanisms. It was immediately observed that, for each of the three phosphorus atoms, the leftover relaxation rates were not dependent upon the frequency of observation, which justifies our previous assumption used to derive equation (4.3). Furthermore, for each phosphorus atom at two different fields the

results were identical, providing confidence about the reliability of the measured T_1 data.

We have determined the phosphorus Nuclear Overhauser Effects (NOE) upon broadband proton irradiation for samples containing 20% D_2O (at 121 MHz and 32 MHz, see Table 4.3) and 70% D_2O (121 MHz only, see Table 4.4).

Figure 4.2 gives an example of NOE spectra obtained at 32 MHz. The experiments consisted of applying a strong r.f field at the proton resonance frequency ω_H so that the proton longitudinal magnetization becomes zero. The phosphorus magnetization was then enhanced by a factor [208]:

$$\eta_{obs} = \frac{\gamma_H}{\gamma_P} \frac{\sigma_{PH}}{\rho_{PH} + \rho_P^*} \tag{4.5}$$

where γ_H and γ_P are the gyromagnetic ratio of proton and phosphorus respectively and σ_{PH} represents the cross-relaxation rate between phosphorus and proton nuclei (see Section 2.3.1). ρ_{PH} is the phosphorus heteronuclear dipolar relaxation rate while ρ_P^* represents other relaxation mechanisms contributing to relaxation of phosphorus. If the extreme narrowing condition applies then $\rho_{PH} = 2\sigma_{PH}$ (see equation (2.20) and (2.21)) and the observed NOE factor equation (4.5) becomes:

$$\eta_{obs} = \frac{\gamma_H}{2\gamma_P} \frac{\rho_{PH}}{\rho_{PH} + \rho_P^*} \tag{4.6}$$

If the relaxation of phosphorus nuclei is not purely dipolar, the observed NOE will be smaller than the expected theoretical maximum value of:

$$\eta_{max} = \frac{\gamma_H}{2\gamma_P} = 1.235$$

in the case of pure dipolar relaxation ($\rho_P^* = 0$) in the extreme narrowing conditions. Otherwise, the theoretical maximum NOE factor becomes frequency dependent and,

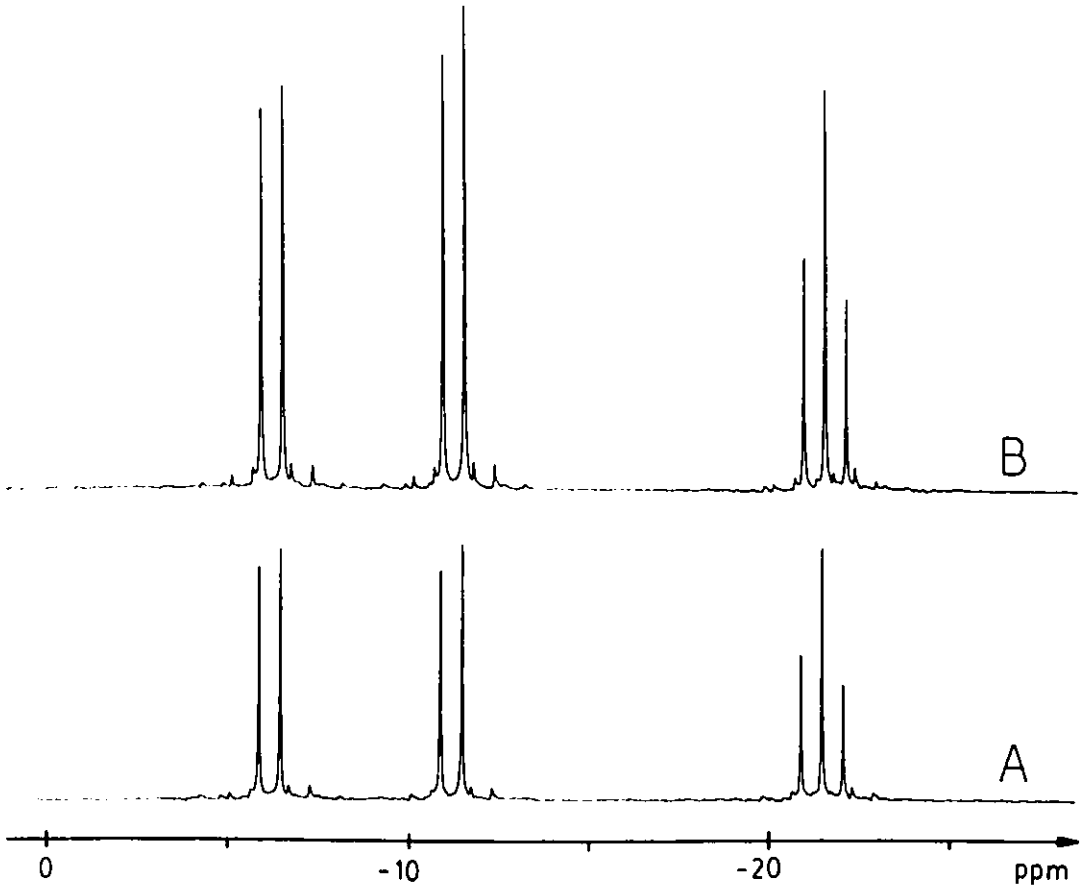

Figure 4.2: Proton decoupled phosphorus-31 Nuclear Overhauser Effects of ATP at 32 MHz. For experimental conditions see Table 4.3. Instrumental conditions were: sweep width of 1000 Hz, acquisition time of 4 sec, pulse delay of 40 sec and 40 transients in 10 mm tube. For spectrum (A), proton decoupling during the accumulation only. For spectrum (B), full proton decoupling.

expressing the dipolar and cross-relaxation rates (see equation (2.20) and (2.21)), equation (4.5) becomes:

$$\eta_{max} = \frac{\gamma_H}{\gamma_P} \frac{6j(\omega_P + \omega_H) - j(\omega_P - \omega_H)}{6j(\omega_P + \omega_H) + 3j(\omega_P) + j(\omega_P - \omega_H)} \tag{4.7}$$

From experimental NOE value at both fields, the theoretical maximum NOE factor $\eta_{max} = 1.235$ was not observed (see Table 4.3 and 4.4) confirming that heteronuclear proton-phosphorus dipolar interactions are not the only mode of relaxation. A short qualitative note on the conformational analysis of the triphosphate side chain of ATP [104] via phosphorus-proton nuclear overhauser effects has already indicated this. However, the published NOE values cannot be compared quantitatively with our values because of magnetic field strength and D_2O content differences between the two studies.

Comparison of NOE values at 121 MHz and 20% D_2O or 70% D_2O solutions (see Table 4.4) shows a clear dependency upon the deuterium content of the solvent. For example, the observed NOE values for the γ phosphate were 0.26 with 20% D_2O but only 0.12 with 70% D_2O. As well, the observed NOE values at 121 MHz were all smaller than those observed at 32 MHz (see Table 4.3). These results can be explained using equation (4.6). Since relaxation by CSA becomes efficient at high magnetic field strengths, the contribution of other relaxation mechanisms ρ_P^* is more important at high field (121 MHz) than at low field (32 MHz). The resulting observed NOE factors are therefore smaller $\eta_{obs}(P_\alpha) = 0.19$ at121 MHz as compared to $\eta_{obs}(P_\alpha) = 0.72$ at 32 MHz.

In the expression of the observed NOE factor (equation (4.5)), the observed relaxation rate $R(\text{obs}) = \rho_{PH} + \rho_P^*$ while the proton-phosphorus dipolar relaxation $R(\text{P–H}) = \rho_{PH}$. By rearranging equation (4.6) and using equation (4.7) we find the

	P_γ		P_α		P_β	
	20%	70%	20%	70%	20%	70%
$\hat{R}$(obs) (sec^{-1})	0.253	0.245	0.521	0.520	0.372	0.394
2σ	0.004	0.004	0.008	0.008	0.007	0.006
$\hat{\eta}_{obs}$	0.26	0.12	0.19	0.13	0.13	0.05
2σ	0.04	0.03	0.03	0.02	0.02	0.02
R(P–H) (sec^{-1})	0.054	0.024	0.082	0.055	0.040	0.016
$\pm$	0.009	0.006	0.014	0.009	0.007	0.007

Table 4.4: Dependence of the ^{31}P Nuclear Overhauser Enhancement upon D_2O in solution at 121 MHz. See Table 4.3 for experimental conditions and the significance of reported values.

following expression:

$$R(\text{P–H}) = R(\text{obs})\frac{\eta_{obs}}{\eta_{max}} \tag{4.8}$$

The NOE experiments provided direct access to the heteronuclear dipolar relaxation contributions to phosphorus nuclei due to solvent and intramolecular protons. The dipolar relaxation rates R(P–H) reported in Table 4.3 and 4.4 were calculated using equation (4.8). The theoretical maximum NOE factor detectable η_{max} was calculated by means of equation (4.7). At 32 MHz and for a correlation time of τ_c = 72 ps, the spectral density functions were not frequency dependent so that η_{max} = 1.235. However, at 121 MHz, the spectral density function $j(\omega_I + \omega_S)$ became frequency dependent and the maximum NOE detectable was lowered to η_{max} = 1.212. At both fields and in 20% D_2O solution (Table 4.3), the calculated dipolar relaxation rates for the γ phosphate, R(P–H, $\mathcal{V}_1$) = 0.054 sec^{-1} and β phosphate R(P–H, $\mathcal{V}_1$) = 0.040 sec^{-1} were smaller than the rate observed for the α phos-

	P_γ		P_α		P_β	
	$\mathcal{V}_1$	$\mathcal{V}_2$	$\mathcal{V}_1$	$\mathcal{V}_2$	$\mathcal{V}_1$	$\mathcal{V}_2$
R(CSA) %	50	6	70	13	70	13
R(P-H) %	21	45	16	58	11	43
R(other) %	29	49	14	29	19	44

Table 4.5: Expression of each ^{31}P relaxation mechanism as a percentage of the total relaxation rate at $\mathcal{V}_1 = 121$ MHz and $\mathcal{V}_2 = 32$ MHz.

phate $R(\text{P–H}, \mathcal{V}_1) = 0.082$ sec^{-1}. A similar situation existed at 121 MHz in 70% D_2O solution (Table 4.4) where $R(\text{P–H}, P_\gamma) = 0.024$ sec^{-1} and $R(\text{P–H}, P_\beta) = 0.016$ sec^{-1} compared to $R(\text{P–H}, P_\alpha) = 0.055$ sec^{-1} for the α phosphate.

After subtraction of the CSA and dipole-dipole relaxation rate contributions from the overall observed rate R(obs) for each of the three phosphorus atoms, a residual relaxation rate remains called R(other) which is due to the sum of several other rates. The source of these residual relaxation rates will be discussed in detail in the next section. Each relaxation mechanism contribution to the overall rate is expressed as a percentage in Table 4.5. These residual relaxation rates are far from negligible as for each phosphorus γ, β and α they account for 49%, 44% and 29% of the observed rate at 32 MHz respectively, in comparison with smaller residual relaxation rates of 29%, 19% and 14% at 121 MHz.

Very often in this study, the rotational correlation time value of an ATP molecule in solution was necessary so that relaxation rates and structural parameters could be determined. For this reason, the carbon-13 spin-lattice relaxation times of ATP

	C-2	C-8	C–1′	C–2′	C–3′	C–4′	CH_2
T_1(obs) (sec)	0.42	0.40	0.50	0.48	0.40	0.53	0.24
2σ	0.03	0.03	0.04	0.04	0.04	0.04	0.02
η_{obs}	1.20	1.45	1.34	1.44	1.40	1.55	1.73
2σ	0.05	0.06	0.06	0.07	0.07	0.08	0.08
T_1(C–H) (sec)	0.69	0.54	0.73	0.65	0.68	0.67	0.27
$\pm$	0.08	0.06	0.09	0.09	0.09	0.08	0.03
τ_c(ps)	67	86	63	70	67	69	85
$\pm$	8	10	8	9	9	9	11

Table 4.6: Carbon-13 spin-lattice relaxation times of ATP Experimental conditions were: [ATP] = 100 mM, pH = 7.4, 20% D_2O, 75 MHz, T = 22 °C. The observed spin-lattice relaxation times T_1(obs) and NOE factors η_{obs} are reported with an error of twice the standard deviation (see Section 3.4 and 3.5). The calculated dipolar spin-lattice relaxation times T_1(C–H) and correlation times τ_c are reported with an error which has been rigorously calculated.

(100 mM, pH = 7.4, 20% D_2O) with their respective Nuclear Overhauser factors (see Table 4.6) were determined allowing the rotational correlation time of an ATP molecule in solution to be calculated. Figures 4.3 and 4.4 present the spectra obtained for the inversion recovery and NOE experiments, respectively. From the experimental results of the carbon-13 spin-lattice and NOE factors, the rotational correlation time of ATP was calculated using equations (4.7) and (4.8) and by expressing the proton-carbon dipolar relaxation rate[1] using equation (4.10). For each protonated carbon the resulting correlation time value is summarized in Table 4.6, and an average value

[1]The proton carbon internuclear distance chosen in (4.10) was dependent upon the type of carbon [121] used in the calculations: r(aliphatic) = 1.070 ± 0.007 Å and r(aromatic) = 1.084 ± 0.006 Å.

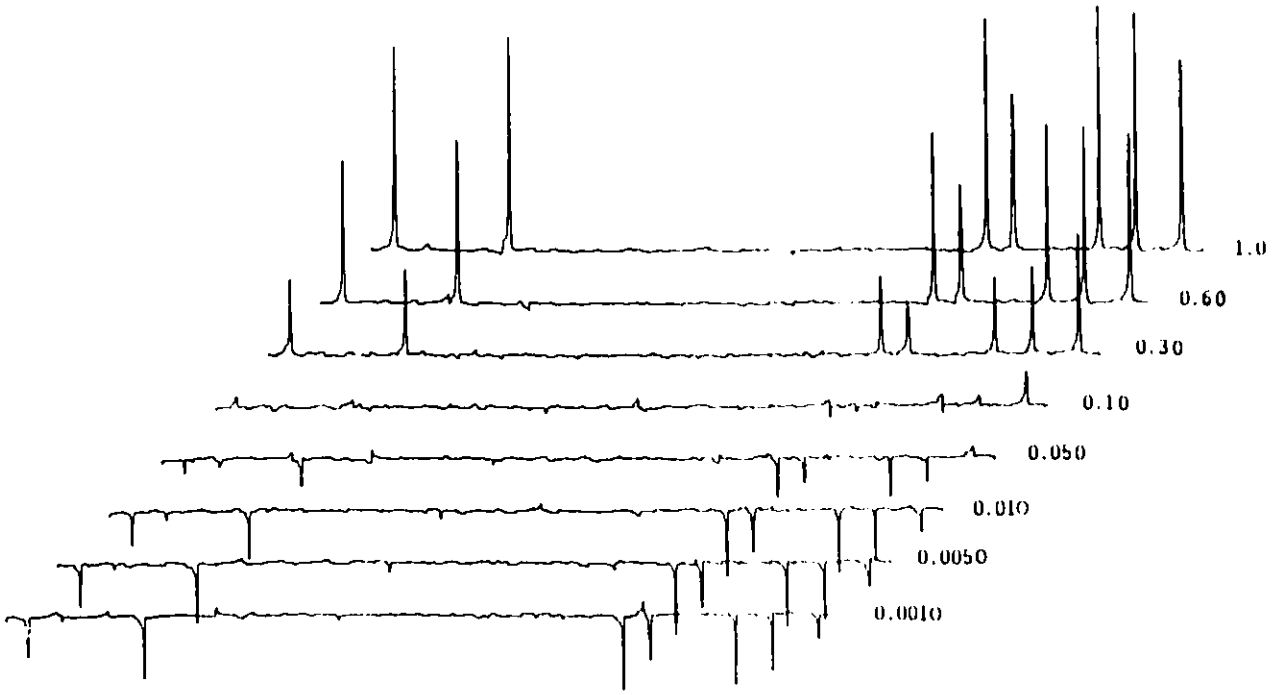

Figure 4.3: Proton decoupled carbon-13 spectral display of an inversion recovery experiment of ATP at 75 MHz. For experimental conditions see Table 4.6 Instrumental conditions were: sweep width of 9000 Hz, acquisition time of 1.5 sec, pulse delay of 1 sec, full proton decoupling and 1000 transients in 10 mm tube. Recovery times are shown in seconds near each spectrum.

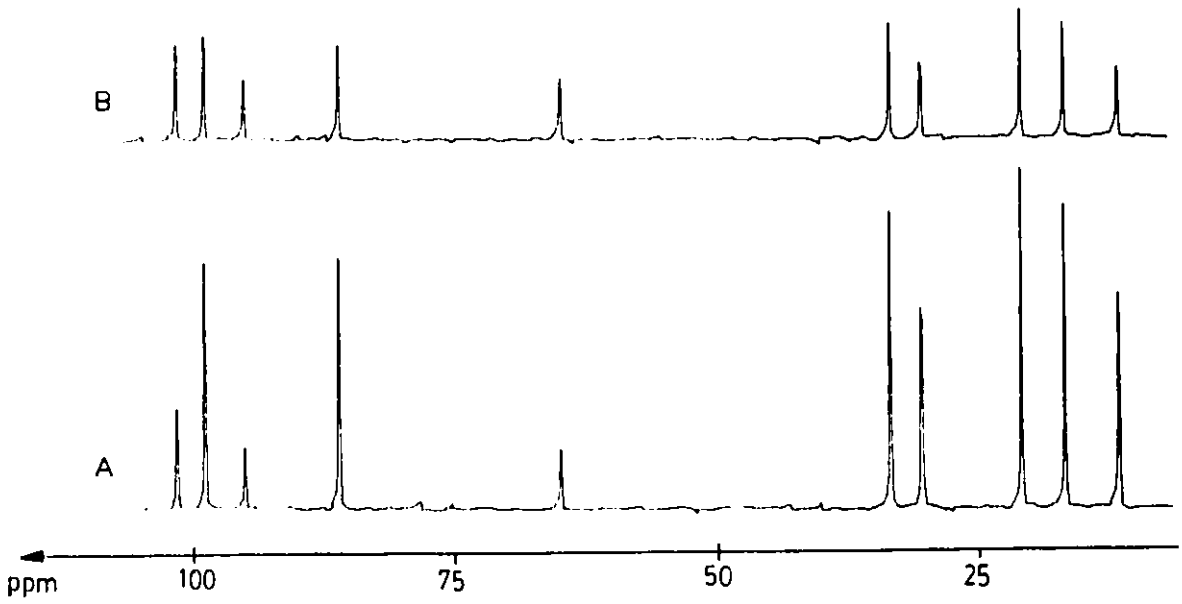

Figure 4.4: Proton decoupled ^{13}C Nuclear Overhauser Effects of ATP at 75 MHz. For experimental conditions see Table 4.6. Instrumental conditions were: sweep width of 9000 Hz, acquisition time of 1.5 sec, pulse delay of 3 sec and 1500 transients in 10 mm tube. For spectrum (A) full proton decoupling. For spectrum (B) proton decoupling during the acquisition only.

of 72 ± 9 ps was calculated.

4.3 Discussion

In this discussion, the following points will be examined:

- What is the nature of an ATP molecule in solution under our experimental conditions ?
- What are the different conformations of the triphosphate chain ?
- After a short presentation of the various possible relaxation mechanisms of a phosphorus nucleus, the pertinent mechanisms operating in this case will be sorted out along with the information these mechanisms give about the ATP molecule.

A pK_a of 6.42 for ATP in water corresponds to the deprotonation of the γ phosphorus, as compared to $pK_a = 6.96$ in D_2O accounting for a deuterium isotope effect [95]. From these values, it can be shown that 88% of the ATP in solution is in the fully deprotonated form ATP^{4-} (for these calculations, a linear variation of the pK_a with deuterium content in solution was considered). It is well known that nucleotides have a tendency to form aggregates in solution [94,119,120,131]. In the case of ATP, the stacking equilibrium constant using an indefinite isodesmic model is $K^{st} = 1.3 \pm 0.2\ M^{-1}$ [94] or $K^{st} = 0.9 \pm 0.3$ [106]. Assuming this model and using an averaged stacking equilibrium constant of $K^{st} = 1.1\ M^{-1}$, the proportions of ATP present as a monomer, dimer and trimer in solution are 83%, 15% and 2% respectively. As a result, for this discussion, only the presence of a fully deprotonated monomer ATP molecule (ATP^{4-}) will be considered.

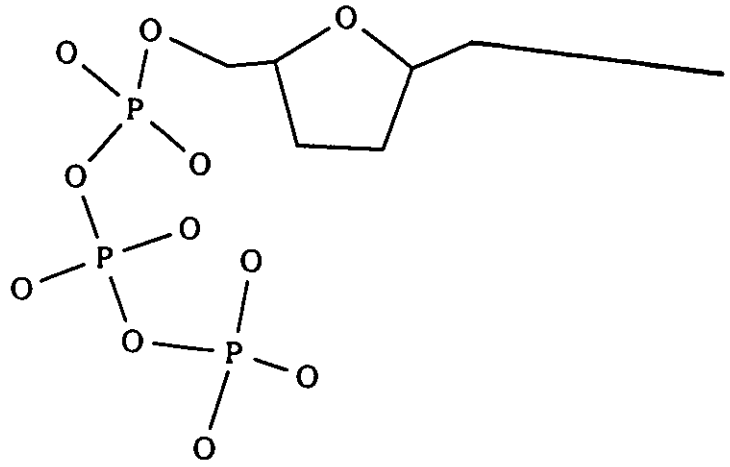

Figure 4.5: Schematic representation of an ATP molecule in the A form. The triphosphate side chain shows a left-handed helix conformation. The adenine base is perpendicular to the plane of the paper.

The conformation of the triphosphate chain of ATP has been studied by means of X-Ray crystallography [96,97,116], molecular orbital calculations [98], phosphorus-proton Nuclear Overhauser Effects [104] and by using the Lanthanide probe method [99].

In the solid state [96,97,116], two ATP molecules, four sodium ions and six water molecules constitute the unit cell of the crystal. In the two crystallographically different ATP molecules (A and B), the triphosphate chain is folded backwards toward the adenine base (see Figure 4.5 and 4.6). In molecule (A) the triphosphate chain shows a typical left-handed helix conformation (Figure 4.5), while the other molecule (B), shows a right-handed helix conformation (Figure 4.6). Two sodium ions are imbedded into this dimer, representing the fundamental structural unit. For both

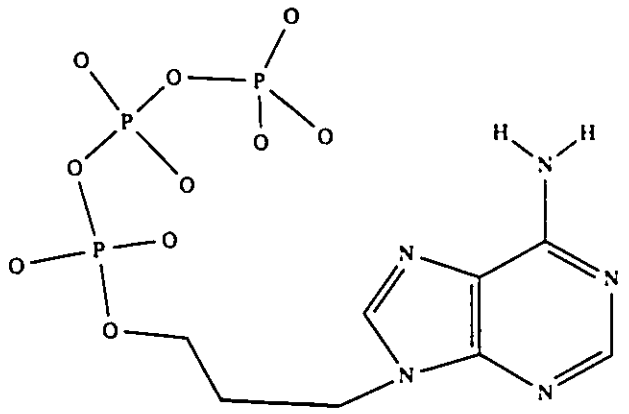

Figure 4.6: Schematic representation of an ATP molecule in the B form. The triphosphate chain shows a right-handed helix conformation. The ribose sugar ring is perpendicular to the plane of the paper.

molecules (A and B) of this dimer, each sodium ion coordinates to the phosphate oxygens and the nitrogen N-7 of the base. The remaining sodium ions and water molecules serve to build up the three dimensional crystal structure.

The folded conformation of the triphosphate chain of ATP could be due to the influence of the metallic cation, and give stability to the chelated form. Molecular orbital calculations [98] for a free ATP molecule have confirmed that this folded crystallographic conformation is more stable than any other selected folded or extended ones. This result suggests that this folding is an intrinsic tendency of the molecule, the interaction of the adenine base with the terminal phosphate having a stabilizing effect. The role of the metallic cation is to give additional stability to the complex. Phosphate side chain folding geometry has been investigated using lanthanides [99] and manganese probes [105] and the overall structure obtained resembles closely the

ATP B form in the solid state.

The decomposition of the overall relaxation rate into different contributions as well as the interpretation of each relaxation rate for a phosphorus nucleus is complicated by many possible sources of relaxation. The overall relaxation rates could be written as:

$$R(\text{obs}) = R(\text{CSA}) + R(\text{P–H}) + R(\text{P–D}) + R(\text{P–P}) + R(\text{trans}) + R(\text{SR}) \qquad (4.9)$$

where $R(\text{CSA})$ represents relaxation by Chemical Shift Anisotropy, $R(\text{P–H})$ and $R(\text{P–D})$ are due to heteronuclear dipolar interactions arising between a phosphorus nucleus and protons or deuterons. In fact these heteronuclear dipolar interactions can be intermolecular, in the case of a solvent-solute interactions, or intramolecular. $R(\text{P–P})$ is derived from homonuclear dipolar interactions while $R(\text{trans})$ represents the contribution of the translational relaxation rate arising from molecular diffusion through the medium. Finally one has to consider the spin-rotation mechanism $R(\text{SR})$.

As a classical approach to proton-phosphorus dipolar relaxation rates it could be considered that dipolar relaxations occur via translational and rotational interactions. The heteronuclear rotational dipolar interaction between a phosphorus atom and protons introduces a relaxation rate given by [35] (see equation (2.20)):

$$R(\text{P–H}) = n\hbar^2\gamma_H^2\gamma_P^2 r^{-6}\tau_c \qquad (4.10)$$

in which h and γ have their usual meanings, n is the number of protons, r the proton-phosphorus internuclear distance, and τ_c the rotational correlation time. Assuming a non-solvated fully deprotonated triphosphate chain, there is no dipolar relaxation arising from the solvent. However, the intramolecular P–H interactions must be considered. By examination of an ATP molecular model in a B conformation (see

Figure 4.6) as it is thought to exist in solution [99,105], the protons H–4′ and H-2′ are too far away ($r \geq 3.5$ Å) from any phosphorus α, β or γ of the chain to create any significant intramolecular relaxation contributions and the calculated rate, using equation (4.10), is smaller than 7×10^{-3} sec^{-1}. The only potential dipolar relaxation could be from the CH_2 group and the H–3′ proton, both close enough to the α phosphate group. Considering an average internuclear distance value of $r = 2.8$ Å, found in models for DNA backbone motions [132] or used in the interpretation of internal molecular motions in deoxyoligonucleotides [133], the corresponding calculated relaxation rate using equation (4.10) was $R(\text{rot}) = 42 \times 10^{-3}$ sec^{-1}.

In the following section the translational dipolar relaxation contributions are considered assuming Brownian diffusion through a homogeneous viscous medium. The translational rate is given by [35]:

$$R(\text{trans}) = \hbar^2 \gamma_H^2 \gamma_P^2 \left(\frac{2N}{15r\overline{D}}\right) \tag{4.11}$$

where N is the density of protons in the medium ($N = 5.4 \times 10^{22}$ cm^{-3} in 20% D_2O solution), r is the closest internuclear distance approach for a P–H interaction, and $\overline{D}$ the average of water and ATP molecules translational diffusion coefficients. For water at 23 °C, the diffusion coefficient is 2.30×10^{-5} cm^2.sec^{-1} [107]. The ATP diffusion coefficient may be estimated from [35]:

$$D = \frac{kT}{6\pi\eta r} \tag{4.12}$$

η being the macroscopic viscosity of 0.1 M ATP solution ($\eta \approx 1.00$ cp at 27 °C [106]). r, the apparent radius of an ATP molecule, can be estimated by a water volume displacement technique [117]. A parafilm wrapped ATP molecule was immersed in a water bath and the resulting water displacement was measured. This method has previously given satisfactory results for a variety of different molecular shapes

and sizes [117,118]. Idealizing an ATP molecule to a rigid sphere we find $r = 4.2 \pm 0.1$ Å. This result was tested by calculating the resulting correlation time from the Stoke-Debye-Einstein formula:

$$\tau_c = \frac{4\pi}{3}\frac{\eta r^3}{kT} \tag{4.13}$$

and the value, $\tau_c = 75 \pm 6$ ps is in excellent agreement with $\tau_c = 72 \pm 9$ ps obtained by carbon-13 NMR. Using the value $r = 4.2$ Å, a diffusion coefficient was calculated from equation (4.12) $D = 0.5 \times 10^{-5}$ cm^2.sec^{-1} giving $\overline{D} = 1.4 \times 10^{-5}$ cm^2.sec^{-1}. The phosphorus-proton with the closest internuclear distance approach in equation (4.11) was estimated[2] to be $r = 2.77$ Å for the ATP $\cdots$ H_2O system in the solid state. Under these conditions $R(\text{trans}) = 1.7 \times 10^{-3}$ sec^{-1}. The sum of translational and rotational dipolar components for phosphorus β and γ is in the order of $R(\text{tot}) \approx 2 \times 10^{-3}$ sec^{-1} while for the α phosphate group $R(\text{tot}) \approx 44 \times 10^{-3}$ sec^{-1}. These calculated values are far from the observed rates $R(\text{P–H}, \text{P}_\gamma) = 0.061$ sec^{-1}, $R(\text{P–H}, \text{P}_\beta) = 0.055$ sec^{-1}, or $R(\text{P–H}, \text{P}_\alpha) = 0.105$ sec^{-1} at 32 MHz (see Table 4.3). In the previous section we considered a naked negatively charged triphosphate chain (ATP^{4-}) in an aqueous medium, without being preoccupied by the triphosphate chain moiety hydration. A simple model was tested in which the translational and rotational dipolar relaxations would explain our experimental results. This simple solution dynamics model clearly did not agree with our observed relaxation rate values for all three phosphorus atoms.

A more elaborate solution dynamics model is to consider in the first hydration sphere n water molecules, hydrogen bonded to the triphosphate chain of ATP and in rapid exchange with the bulk solvent. This model has previously been treated

[2]The P $\cdots$ H internuclear distance was estimated by using averaged structural values from ATP in the solid state [96,116], P-O = 1.50 Å, PO $\cdots$ OH_2 = 2.74 Å (which compares very well with an average oxygen-oxygen distance of 2.66 Å in different phosphate compounds [110]) and $\text{P} - \widehat{\text{O}\cdots\text{OH}_2} = 119°$. From phosphate ester values [110] the $\text{PO}\cdots\widehat{\text{H}} - \text{OH}$ bond angle was calculated to be 168°. The bond distance HO-H was taken as 1.05 Å [90].

theoretically [107,108,122]. If the residence time (τ_e) of water molecules in the first hydration sphere, before exchanging with the bulk solvent, is greater than the structural relaxation time for the bulk water molecules (typically 2 ps) [107,109] then the system is described as a positive hydration.

It is possible that each phosphate ion is hydrated, by n water molecules in the first coordination sphere, through hydrogen bonding to the free oxygen atoms of the phosphate group. It will be shown that this solvation model accounts for our observed heteronuclear phosphorus-proton dipolar relaxatior. data. The relaxation data are in principle complicated by cross-relaxation terms [111,134] as the heteronuclear dipolar interaction between a phosphorus nucleus and a surrounding proton must be written as a set of coupled differential equations (see Section 2.3.1). The spin-lattice relaxation of the ^{31}P nucleus can be described as a sum of two spin interactions [113] by the following equation:

$$\frac{dI_z}{dt} = -(\rho_{PH} - \rho_P^*)(< I_z > - < I_0 >) - \sigma_{PH}(< S_z > - < S_0 >) \qquad (4.14)$$

where $< I_z >$ and $< S_z >$ represent the expectation values of the longitudinal magnetizations of the phosphorus and proton nuclei while $< I_0 >$ and $< S_0 >$ are the corresponding magnetizations at equilibrium. ρ_{PH} and σ_{PH} are the dipolar and cross-relaxation rates respectively while ρ_P^* represents other relaxation mechanisms contributing to relaxation of the ^{31}P nucleus. It will be shown that the triphosphate chain is surrounded by a solvation sphere of water molecules in rapid exchange with the bulk solvent. On the M_z recovery time scale of the experiment, the proton spin reservoir will always remain close to equilibrium ($< S_z > - < S_0 > \approx 0$, and the cross relaxation term $\sigma_{PH}(< S_z > - < S_0 >)$ can therefore be safely neglected in equation (4.14). The evolution of the longitudinal ^{31}P magnetization will there-

fore follow a single exponential recovery characterized by a relaxation rate given by $(\rho_{PH} - \rho_P^*)$. This rapid dynamic exchange of water molecules is equivalent to the application of a r.f field, at the resonance frequency ω_H. We are dealing with an internally self-decoupled system. In the case of the CH_2 group or the H–3′ proton, these heteronuclear P–H spin systems are too weakly coupled to create any significant errors due to cross-relaxation terms [112]. Furthermore, the smaller γ_P relative to γ_H means that relaxation of these protons by a phosphorus nucleus will be much less efficient than proton-proton interactions.

The examination of a molecular model of the triphosphate chain of ATP in the B form leads to the reasonable assumption that the α and β phosphates are solvated by two water molecules and the γ phosphate by three water molecules. This assumption was made by taking into consideration the conformation of the chain as well as steric hindrance factors.

This solvation model is also supported by other studies. A gravimetric study on DNA [123] shows that two molecules of water are strongly bound to each phosphate group. This result was confirmed by NMR [124,125] which detected the water molecules as being bound to the phosphate groups. Phosphorus-31 spin-lattice relaxation times of orthophosphate ions [90] in aqueous solution were analyzed by using a solute-solvent interaction model in which the phosphate ions were hydrogen bonded to four water molecules. As well, recently, rationalization of the dipolar proton-phosphorus spin-lattice relaxation rates of phosphoglucomutase [126], during the conversion of glucose 1–phosphate to glucose 6–phosphate, led to the identification of an enzymatic phosphate solvated by three water molecules.

The proton-phosphorus dipolar relaxation rate for this model can be expressed, using equation (4.10), as:

$$R(\text{P–H}) = 2n\hbar^2\gamma_H^2\gamma_P^2 r^{-6}\tau_c \tag{4.15}$$

in which n represents the number of water molecules in the first hydration shell of the triphosphate chain, r the internuclear P–H vector distance between the phosphorus atom and the hydrogen of a water molecule (r = 2.77 Å), while τ_c represents the correlation time characteristic of the P–H vector reorientation in solution. In 20% D_2O solution $2n$ = 4.8 for the γ and β phosphorus atoms and 3.2 for the α phosphorus atoms, while the dipolar relaxation rate values R(P–H) are taken from Table 4.3. Under these conditions the calculated correlation time using equation (4.15) is $\tau_c = 65 \pm 11$ ps. This value represents a time characteristic for the reorientation of the P–H vector and is comparable to the rotational correlation time of an ATP molecule measured by carbon-13 (72 ± 9 ps). However, this calculated τ_c is not representative of a water molecule residence time in the first hydration shell of the ATP triphosphate chain. The fast molecular tumbling of ATP in solution prevents the detection of a water molecule residence time longer than the rotational correlation time of ATP. The residence time τ_e is therefore at least $\tau_e \geq \tau_c$. It is much longer than the structural relaxation time for water molecules in the bulk solvent (2 ps) meaning that there is a strong well developed hydrogen bonding network surrounding the triphosphate chain.

The solvation model described above, in which seven water molecules solvate the triphosphate chain, has been tested by increasing the deuterium content of the solvent. The experimental NOE's listed in Table 4.4, in the case of a 70% D_2O solution, are much less intense than those observed in 20% D_2O content, supporting our solva-

tion model. The resulting correlation time, using equation (4.15), of 67 ± 16 ps is in excellent agreement with the study made with 20% D_2O for which $\tau_c = 65 \pm 11$ ps.

It should be emphasized that these correlation times were only calculated from the experimental proton-phosphorus dipolar relaxation rates of the γ and β phosphates, as the α phosphorus relaxation data arise from three contributions: dipolar relaxation from the first hydration sphere composed of two water molecules (identical to the β phosphate) and relaxation from the CH_2 group and H-3′ proton of the sugar. It is possible to extract the overall α phosphorus intramolecular proton-phosphorus relaxation contribution arising from the CH_2 group and the H-3′ proton by assuming that the relaxation rate due to water molecules in the solvation sphere are the same for the β and α phosphates. Using Table 4.3 and 4.4 one finds $R(\text{P-CH}_2 + \text{H-3}') = 0.050$ sec^{-1} (at 32 MHz) and 0.042 sec^{-1} (at 121 MHz) in 20% D_2O solutions while $R(\text{P-CH}_2 + \text{H-3}') = 0.039$ sec^{-1} (at 121 MHz) in 70% D_2O. Using equation (4.10), an average proton-phosphorus internuclear distance was calculated as 2.79 ± 0.10 Å which is in excellent agreement with reported values in DNA [132] or structural parameters used in the interpretation of NMR relaxation experiments with DNA [137] or RNA [136].

The following calculation will be made under the assumption that the correlation times of each phosphorus atom are identical to those of the carbon atoms of ATP, calculated by carbon-13 NMR, $\tau_c = 72$ ps (see Table 4.6). To support the validity of this important assumption it is necessary to consider the nature of internal and overall motions of nucleotides. The mobility of nucleotides is usually described by three modes of internal motion [135]:

- Rotation of the base around the glycosidic bond represented by a syn-anti equilibrium, in the proportion of 75:25 for ATP.

- A ribose puckering characterized by a conformational equilibrium between two states called the S type (C–2′ endo) or N type (C–3′ endo) in the proportion of 60:40 for ATP.

- Internal rotation about the (C–4′)-(C–5′) carbon bond of the ribose side chain giving rise to a distribution of rotamers gg, gt or tg in favor of the gg conformation (55%).

Activation energies for the rotation around the glycosidic [138] bond and the pseudo-rotation of the furanose ring [139] in adenosine have been determined: E_a = 26 kJ.mol^{-1} and E_a = 20 kJ.mol^{-1} respectively, while activation energies of 18 to 25 kJ.mol^{-1} for the motion of the phosphate backbone unit were evaluated by ^{31}P NMR for deoxyoligonucleotides [133] and poly(inosinic acid) [113]. The insertion of these activation energies into the Boltzmann equation yields the result that, at room temperature (RT = 2.5 kJ mol^{-1}), the majority (99.9%) of molecules are locked into a fixed conformation. This indicates that the transitions between the syn and anti states for the base and S or N states for the sugar will be too infrequent to contribute to relaxation. The purine base and sugar backbone of ATP should therefore reorient as a whole rigid molecule in solution giving rise to identical ^{13}C dipolar spin-lattice relaxation times. This was what occurred, and the results are recorded in Table 4.6, showing the average dipolar T_1 for the protonated carbons of the sugar and base moieties of 0.66 ± 0.06 sec.

Internal rotation around the side chain carbon-carbon bond has been treated theoretically [140]. Depending upon the isotropic rotational correlation time τ_H of the molecule and the value of the internal rotational correlation time τ_G of a group undergoing internal rotation, the carbon-13 dipolar spin-lattice relaxation times could

be significantly affected. In the case of an ATP molecule, rapid internal rotation about the (C-4')-(C-5') bond would be expected to increase the effective motion for the carbon C-5' and hence increase its T_1 value. The experimental data show that the NT_1 of C-5' and C-8 are the same (T_1 = 0.54 sec.) and a little shorter than the average T_1 for all protonated carbons ($\hat{T}_1$ = 0.66 $\pm$ 0.06 sec.). Therefore, internal rotational motion about the (C-4')-(C-5') bond in 5'-ATP does not affect the T_1 values, allowing the conclusion that internal motions cannot be as fast as $\tau_r = 10^{-10}$ sec [140].

What is happening to the triphosphate chain of ATP ? According to our model, the triphosphate side chain of ATP is solvated by seven water molecules hydrogen bonded to the non-bridging phosphate oxygens. Each phosphate ion is locked into a structural network of water molecules whose residence time is at least equal to the re-orientational correlation time of an ATP molecule (72 ps). From this solvation model and equation (4.8) and (4.15), the rotational correlation time responsible for the P $\cdots$ H_2O vector re-orientation in solution was calculated to be τ_c = 65 ps, identical to those of the sugar and adenine base carbons. For similar experimental conditions, analysis of the ^{23}Na NMR linewidth gave a correlation time of 109 ps for a sodium ion bound to the phosphate group of guanosine 5'-monophosphate (GMP) [120]. Finally, the intrinsic folding property of the triphosphate chain of ATP [98], folded backwards to the adenine base, gives an extra stability to the conformation of the whole chain-sugar-base assembly.

All of these arguments allow the safe assumption that the ATP molecule reorients in solution as a rigid body and, as a consequence, the phosphorus rotational correlation time is identical to those of the carbons. The contribution of the spin-rotation relaxation mechanism to the overall observed relaxation rate (see equation (4.9)) will

now be discussed.

In order to be consistent with the spin-rotation theory [127,128], a model must be devised in which very fast molecular rotation of small groups are interrupted by frequent molecular collisions. Typical spin-rotational correlation times τ_{SR}, at room temperature, lie in the range of $10^{-14} - 10^{-12}$ sec [129] and, as a consequence, this solvation model will not allow for the spin-rotation relaxation mechanism to contribute effectively to the overall observed relaxation rates of equation (4.9).

The magnetic fields experienced by a nucleus depend upon its electronic shielding. Anisotropic shielding of the nucleus results in a shielding tensor $\Delta\sigma$ which can induce spin-lattice relaxation (see Section 2.3.2). This mechanism is very well known for phosphorus-31 and is described by the following equation (see equation (2.28)):

$$R(\text{CSA}) = \frac{2}{15}\omega_0^2(\Delta\sigma)^2\left(1+\frac{\eta^2}{3}\right)\tau_c \tag{4.16}$$

where η represents the asymmetry parameter, τ_c the phosphorus rotational correlation time estimated by carbon-13 and ω_0 the spectrometer pulsation. As shown in Table 4.3, this mechanism is mostly effective at high field because of the square field dependence. For example, $R(\text{CSA}) = 0.365$ sec^{-1} at 121 MHz compared to $R(\text{CSA}) = 0.024$ sec^{-1} at 32 MHz for the α phosphate. From the calculated relaxation rate due to CSA (see Table 4.3) and equation (4.16), chemical shift anisotropy values $\Delta\sigma\left(1+\frac{\eta^2}{3}\right)^{1/2}$ can be estimated for each phosphorus atom γ, β and α (see Table 4.7). Average values for the γ, β and α phosphates were 147 $\pm$ 12 ppm, 212 $\pm$ 18 ppm and 252 $\pm$ 21 ppm respectively. The calculated shielding constants in Table 4.7 support the general trend that, for phosphate monoesters, chemical shift anisotropies (typically 80 – 140 ppm) are smaller than their diester counterparts (160 – 175 ppm) [103]. The chemical shift anisotropy of the γ phosphate (147 $\pm$ 12 ppm) falls into

	P_γ		P_α		P_β	
	ν_1	ν_2	ν_1	ν_2	ν_1	ν_2
$\Delta\sigma(1+\frac{\eta^2}{3})^{\frac{1}{2}}$ (ppm)	150	143	256	247	216	208
$\pm$	12	12	20	21	17	19

Table 4.7: ^{31}P chemical shift anisotropy values of ATP at $\nu_1 = 121$ MHz and $\nu_2 = 32$ MHz.

the typical range for monoesters while values for the β (212 $\pm$ 12 ppm) and α phosphates (252 $\pm$ 20 ppm) are higher than would be expected for phosphate diesters. This may indicate that the electronic structure of the β and α phosphate of ATP have triester-like characteristics as their chemical shift anisotropy values are closer to a phosphate triester compound like phosphorus pentoxide P_4O_{10} (265 ppm) [141]. Principal values of the chemical shift tensor for ATP or ADP have not yet been determined but similar triester-like characters for the β and α phosphates have already been reported for an ATP molecule bound to G-actin [103]. It may well indicate a general structural property of ATP.

At the beginning of the discussion the phosphorus-31 overall relaxation rates (Table 4.3) have been sorted out into possible sources of relaxation (see equation (4.9)). So far, the CSA and proton-phosphorus relaxation rates have been analyzed. As well, it was concluded that solvation of the ATP triphosphate chain did not allow for the spin rotation relaxation mechanism to be effective under these conditions. The calculated translational relaxation rate component $R(\text{trans}) = 1.7 \pm \times 10^{-3}$ sec^{-1} (equation (4.11)) is too small to account for the residual relaxation rates $R(\text{other})$ tabulated in Table 4.3. The last two relaxation rates to be considered are the homonu-

clear dipolar relaxation between phosphorus nuclei R(P–P) and the heteronuclear dipolar relaxation between the solvent deuterons and a phosphorus nucleus R(P D).

Relaxation by homonuclear dipolar interactions between phosphorus nuclei are expected to be negligible due to the length of the P–P average internuclear distance of r = 2.95 Å, (P–O = 1.61 Å and P $-\widehat{\text{O}}-$ P = 133° are average values by X-Rays [96,116]). The homonuclear dipolar rotational relaxation rate for a molecule undergoing isotropic rotation is given by:

$$R(\text{P–P}) = \frac{3}{2} n \hbar^2 \gamma_P^4 r^{-6} \tau_c \qquad (4.17)$$

r being the spatial internuclear distance between two phosphorus atoms, n the number of phosphorus involved in the interaction and τ_c the rotational correlation time of the phosphorus nucleus. Relaxation rates of 2.5 × 10^{-3} sec^{-1} for the α and γ phosphorus atoms and 5.0 × 10^{-3} sec^{-1} for the β phosphorus atoms were calculated using equation (4.17).

For an equal number of nuclei, dipole-dipole relaxation due to solvent deuterons is 6.3% as fast as relaxation from protons: R(P–D) = 6.3% R(P–H). Applying equation (4.15) to our solutions we estimate:

$$R(\text{P–D}) = 0.063 \times \frac{1}{4} R(\text{P–H}) = 0.016\ R(\text{P–H}) \qquad \text{for 20\% } D_2O$$

$$R(\text{P–D}) = 0.063 \times \frac{3.5}{4} R(\text{P–H}) = 0.055\ R(\text{P–H}) \qquad \text{for 70\% } D_2O$$

the 1/4 and 3.5/4 factors reflect the deuterium/hydrogen concentration ratios. For 20% and 70% D_2O solution samples, these relaxation rates contribute to 10^{-3} sec^{-1} or less of the overall relaxation rate for each of the three different phosphorus atoms.

The observed overall relaxation rate R(obs) of equation (4.9) cannot be dissected any further and, as a result, the sum of the following relaxation rates R(trans),

R(P D) and R(P–P) is $\approx 4 \times 10^{-3}$ sec^{-1} for the α and γ phosphates and $\approx 7 \times 10^{-3}$ sec^{-1} for the β phosphate. These calculated rates are far too small to account for the residual relaxation rates R(other), tabulated in Table 4.3 at two different fields, and is defined by:

$$R(\text{other}) = R(\text{obs}) - R(\text{CSA}) - R(\text{P–H}) \tag{4.18}$$

As can be seen from Table 4.3, these residual relaxation rates R(other) are far from negligible as the average of $\hat{R}$(other) = 0.073 ± 0.016 sec^{-1} at 121 MHz and $\dot{R}$(other) = 0.058 ± 0.010 sec^{-1} at 32 MHz were calculated. Within experimental error, these residual relaxation rates are also identical at both fields. Similar residual relaxation rates have also been reported by ^{31}P spin-lattice relaxation of aqueous orthophosphate solutions [90]. It was suggested that this residual rate arises from a Quasi-Spin Rotation (QSR) mechanism. This relaxation process results from the rotation of an electric charge around the PO_4 group. The net effect being the creation of a pulse of electronic current through the ions which generates an electromagnetic field capable of relaxing the nuclear spin. The QSR relaxation rate was expressed as [90]:

$$R(\text{QSR}) = \frac{1}{3}\gamma_P^2 H^2 \tau_w^2 \tau_r^{-1} \tag{4.19}$$

in which H represents the magnetic field strength generated by the pulse electron current, τ_w the duration of the pulse and τ_r the quasi-rotation jump time. According to the hydrogen bonded solvation model developed earlier for the triphosphate chain of ATP, each PO_4 unit is locked into a sphere of water solvent molecules. However, the departure of a solvent molecule of the phosphate solvation sphere is associated with an electronic charge redistribution along the P–O bond. The continuous exchange of solvent molecules between the phosphate solvation sphere and the bulk solvent has the

net effect of rotating the electronic charge around the PO_4 unit, without physically rotating the PO_4 group. This overall process leads to nuclear spin relaxation via the QSR mechanism expressed by equation (4.19). The following calculation shows that the QSR relaxation mechanism accounts for the residual relaxation rates of Table 4.3. The rotating electronic charge creates a magnetic field equivalent to one Bohr magneton (β) at a distance r from the ^{31}P nucleus [90]:

$$H = \frac{\beta}{r^3} \tag{4.20}$$

where the pulse duration of the magnetic field pulse is given by the oscillation time of a hydrogen bonded water molecule ($\tau_w = 10^{-14}$ sec). τ_r may be identified with the average residence time of a water molecule in the first phosphate solvation sphere ($\tau_c = 65$ ps, see earlier discussion and Section 8.4). Then the only unknown of equation (4.20) is the distance r for the ^{31}P nucleus. Using the different values of R(other) from Table 4.3 an average distance of 0.7 $\pm$ 0.1 Å was calculated. This value is in close agreement with the distance of 1 Å taken for the calculation of R(QSR) for orthophosphate solutions [90], which yielded a relative rate of 3×10^{-2} sec^{-1}, in the same order of magnitude ($\hat{R}$(QSR) = 6×10^{-2} sec^{-1}) for each phosphate group of the triphosphate side chain of ATP.

4.4 Conclusion

phosphorus-31 spin-lattice relaxation rates and Nuclear Overhauser Effects were measured for ATP aqueous solutions at two magnetic field strengths and two solvents differing in their deuterium content. It was shown that relaxation rates may be easily dominated by paramagnetic impurities. In purified samples, proton-phosphorus dipolar interactions, chemical shift anisotropy, and leftover components represent

the different contributions to the observed overall relaxation rate of each phosphate group. A solvation model of the triphosphate side chain of ATP was supported by proton -phosphorus dipolar interactions. Finally, a quasi-spin rotation mechanism introduced for aqueous orthophosphate solutions accounted for the leftover relaxation rates.

Chapter 5

QUALITATIVE AND QUANTITATIVE DESCRIPTIONS OF ATP–ALUMINUM INTERACTIONS

5.1 Introduction

Aluminum is generally considered to be an inactive biological metallic cation. In the past few years, interactions between aluminum and ATP have however aroused interest because aluminum was suspected to be responsible for a number of toxic biological processes (see Chapter 1).

In the first study [18], the interaction between Al(III) and adenosine triphosphate was investigated by means of ^{27}Al and ^{31}P nuclear magnetic resonance. Results were obtained by varying the pH ($4.4 \leq \text{pH} \leq 10.2$) of an equimolar ATP:Al mixture in aqueous solution. For acidic or neutral conditions ($4.4 \leq \text{pH} \leq 7.5$) it was suggested that aluminum was coordinated to the β and γ phosphates of ATP in a 1:1 ATP:Al complex. In mildly acidic conditions, infrared spectroscopy qualitatively confirmed the existence of an aluminum complexed to a γ phosphate. In basic solution, a second

complex was speculated to be $(ATP)_2$:Al_2 or $(ATP)_2$:Al in which aluminum would be coordinated to the β or α phosphates. More recently, a detailed ^{31}P, ^{27}Al and ^{1}H multinuclear NMR study on Al(III) complexes of ATP showed the presence of at least four different 1:1 ATP:Al complexes, whose existence was dependent upon the pH of the solution [20] . In all of them, aluminum was bound to the β and γ phosphates, or only to the γ phosphate, but never was the α phosphate implicated in aluminum complexation. Under any set of conditions, there was generally more than one complex in solution.

In this chapter, the interactions between aluminum and ATP at various concentrations are reported at a physiological pH (7.4) by means of phosphorus-31 NMR spectroscopy. ^{31}P spectra were recorded at three different magnetic fields (32, 81 and 121 MHz) and for three different ATP concentration (25, 50 and 100 mM). For each series, the Al/ATP ratio was varied from 0 to 1.0.

5.2 Qualitative Description of ATP–Aluminum Interactions

Figure 5.1 displays a set of phosphorus-31 NMR spectra of ATP (100 mM, pH = 7.4) at 32 MHz in which the Al/ATP ratio was varied from 0 to 1. From previous studies [135,143], the three resonances centered at – 6.5, – 11.2 and – 21.5 ppm in spectrum A of Figure 5.1 were assigned to the γ, α and β phosphate resonances of ATP in solution respectively. The apparent triplet resonance for the β phosphate is due to the similar spin-spin coupling constant values of the β phosphate with the α and γ phosphates (^2J(P–P) = 18–19 Hz).

By increasing the aluminum concentration (Figure 5.1 spectra B, C, D, E and F) ATP and aluminum formed complexes in slow exchange on the NMR time scale

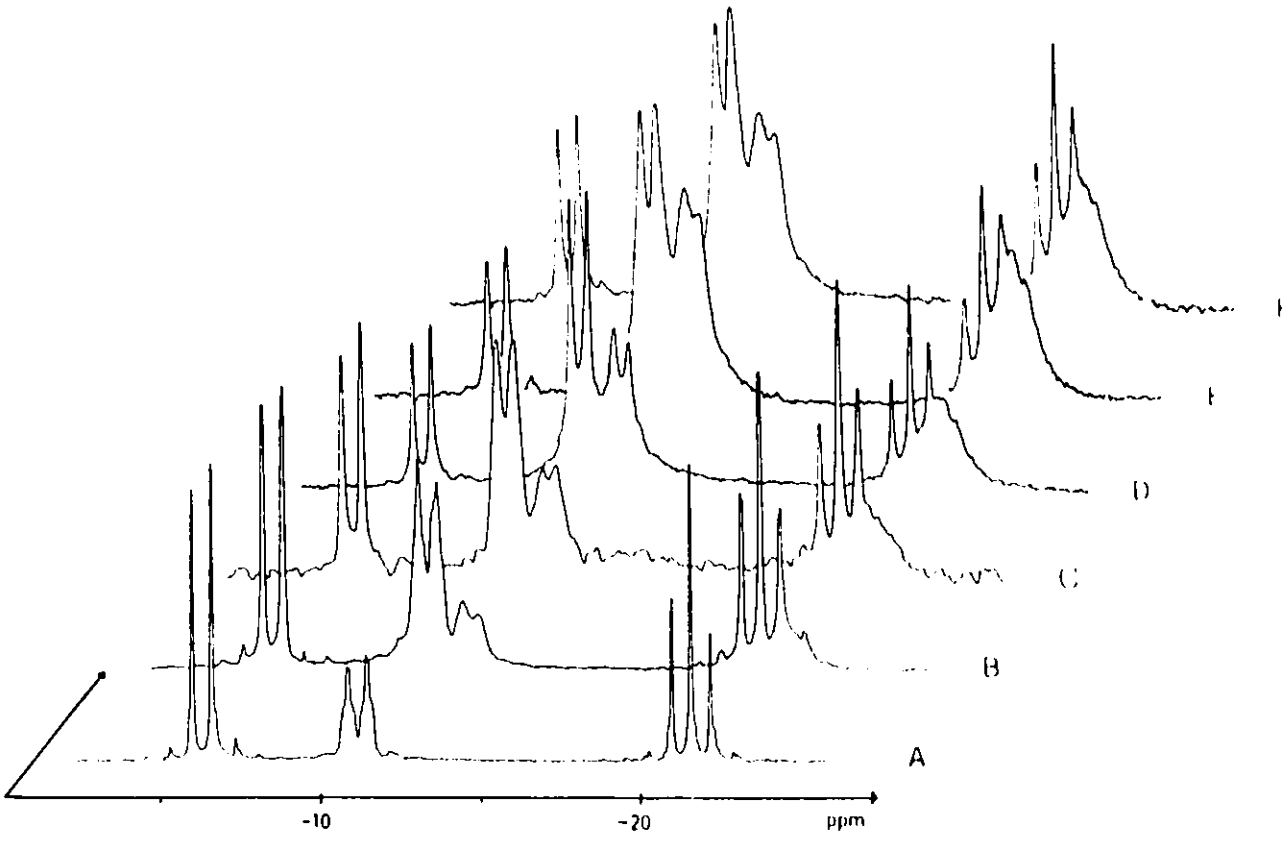

Figure 5.1: A series of ^{31}P NMR spectra of ATP–Al aqueous solutions at 32 MHz. The Al/ATP ratios were: A) 0; B) 0.33; C) 0.50; D) 0.75; E) 0.90 and F) 1.0. The instrumental and experimental conditions were as follows: spectral width of 1000 Hz, acquisition time of 4 sec, pulse delay of 10 sec, 0.5 Hz line broadening, typically 600 transients, no proton decoupling, [ATP] = 100 mM, pH = 7.4, 22 °C and 20% D_2O.

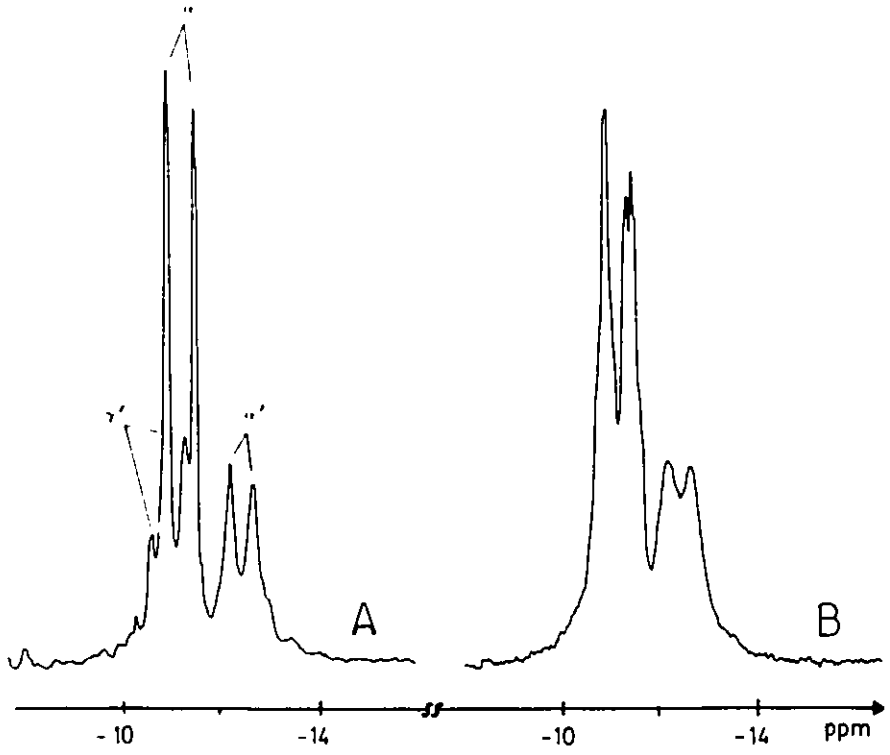

Figure 5.2: Display of an ATP spectral region between – 8 and – 16 ppm recorded under full proton decoupling (A) as compared to no proton decoupling applied (B) for which the Al/ATP ratio was 0.50 (see text for peak attributions). Same instrumental and experimental conditions as in Figure 5.1.

giving rise to the appearance of new resonances.

The resonance shifted upfield from the β phosphate resonance of ATP was attributed to a β phosphate complexed by aluminum as it behaved as a triplet (see spectrum E of Figure 5.1). This attribution is in agreement with previous studies [20] and will be called a β' resonance.

Spectrum A of Figure 5.2 shows part of an ATP spectrum between – 10 and – 14 ppm under full proton decoupling. Spectrum B of Figure 5.2 shows the same chemical shift region but recorded without proton decoupling. Under the latter con-

ditions, the phosphorus α is spin coupled to the two methylene protons and to the H–4′ proton of the ribose sugar. Phosphorus-proton spin-spin coupling constants for ATP in solution were reported [135] to be $^{3}J(P\text{–}CH_2)$ = 10 Hz and $^{4}J(P\text{–}CH\text{–}4')$ = 2 Hz giving rise to a broad multiplet resonance. For a total ATP concentration of 100 mM at pH = 7.4 and no added aluminum the proton decoupled α phosphate line width at half height was measured to be 10 Hz broader than its equivalent proton decoupled resonance. The use of proton decoupling removed scalar magnetic couplings and an intense doublet of narrow lines was expected for the α phosphate and observed in spectrum A of Figure 5.2. The removal of heteronuclear spin-spin couplings, yielding a better spectral resolution, also permitted the appearance of a new doublet centered at – 10.9 ppm. This spectral region was then composed of three doublets, one of which was the α phosphate resonance of ATP .

Examination of a full spectral integration (see Section 5.3.3) showed that the two new resonances always had an equal weight in the total spectrum integration. Furthermore, the sum of their respective integrals was always twice that of the β' resonance. These results suggested that the two new resonances were representative of two different complexed phosphates. Upon addition of aluminum in ATP solution, complexation occurred resulting in the appearance of two new resonances in the α region, attributed to complexed γ and α phosphates of ATP. They will be called γ' and α' respectively.

Assignment of the α' and γ' resonances was done by comparing two spectra of the same solution for which different decoupling parameters were applied (see Figure 5.2). For the broad doublet, shifted upfield from the α resonance of ATP and centered at – 12.6 ppm, the increase of the line width at half height between the proton decoupled spectrum (spectrum A) and the normal spectrum (without proton decou-

pling, spectrum B) was measured as 10 Hz. This increase in line width value for the complexed resonance doublet was identical to the one observed for the α phosphate of ATP (10 Hz) and suggested that this broad resonance corresponded to an aluminum complexed α phosphate, henceforth called α'. The remaining resonance was therefore attributed to a complexed γ phosphate, called γ'. Under normal conditions, (for a spectrum recorded without proton decoupling at pH = 7.4) this γ' resonance will not be observed as it is hidden underneath the α resonance of ATP (see spectrum B of Figure 5.1).

This set of three resonances (α', β', γ') was already clearly observed in ATP-Aluminum aqueous solution (at pH = 6.3) but peak assignments were omitted [143]. This work is in agreement, with a recent study [20], for the β' phosphate resonance attribution but, at the same time, in direct contrast with this same work as only one complexed resonance in the α region was reported at pH = 7.5.

Throughout the variation of the Al/ATP ratio, the ^{31}P chemical shifts of the free α, β and γ phosphate resonances of ATP, as well as the α', β' and γ' complexed species, did not seem to be dependent upon the aluminum concentration. This qualitative observation will be discussed in more detail in the following section, based upon quantitative results.

For an equimolar mixture of aluminum and ATP (see spectrum F of Figure 5.1) relatively sharp resonances, attributed to the free ATP resonances in the absence of aluminum, (spectrum A) are still observed. As the aluminum concentration is increased beyond an Al/ATP ratio of approximately 0.8 (spectra E and F), the intensities of the free and aluminum complexed ATP resonances remain unchanged. For Al/ATP $\geq$ 0.8 no further complexation occurs for the remaining free ATP resonances and, for an Al/ATP ratio greater than 1.7 precipitation occurs in solution

at pH = 7.4. Although association constants are not known at pH = 7.4, reported values [20] in acidic solution (pH = 2) were greater than 10^5 M^{-1} and a quantitative complexation of ATP with aluminum will be assumed. In the case of other cations, stability constants of binary complexes $M(ATP)^{2-}$ between metallic cations like Mn^{2+}, Co^{2+}, Ni^{2+}, Cu^{2+}, Zn^{2+}, Mg^{2+}, or Ca^{2+} and ATP^{4-} were determined and they are all greater than 10^4 M^{-1} [144,146]. The observation of free ATP phosphate resonances in these spectra for which Al/ATP $\geq$ 0.8 then suggests that they could be due to uncomplexed ("free") phosphate resonances involved in an ATP–Al complex. In this species, they would not directly participate in aluminum complexation.

Figure 5.3 displays a similar set of ^{31}P spectra of ATP at 121 MHz (pH = 7.4, 100 mM) as compared with Figure 5.1 at 32 MHz under similar conditions. The same overall qualitative features present at 32 MHz were observed at 121 MHz: the existence of free α, β and γ ATP resonances in slow exchange with three α', β' and γ' complexed resonances also appear in this set of spectra.

In the case of the two resolvable α' and β' resonances, we observed a linewidth field dependency which increased with the field. As a result of this linewidth broadening, detection of their respective spin-spin coupling constants, detected at 32 MHz (see Figure 5.1), were not observed at 121 MHz. The broad lines observed at both fields for the ATP–Al complex resonances may be due to aggregation. Modulation of the spin-spin relaxation time by Chemical Shift Anisotropy (CSA) (see Section 2.3.2) in an aggregate is a plausible hypothesis for the interpretation of the linewidth field dependency. This phenomenon could also be rationalized by a scalar relaxation of the second kind (see Section 2.3.3) due to a spin-spin coupling between a quadrupolar nucleus, ^{27}Al, and a phosphorus nucleus involved in an aggregate. In any case, the small correlation time (about 100 ps) of an ATP–Al monomer could not be responsible

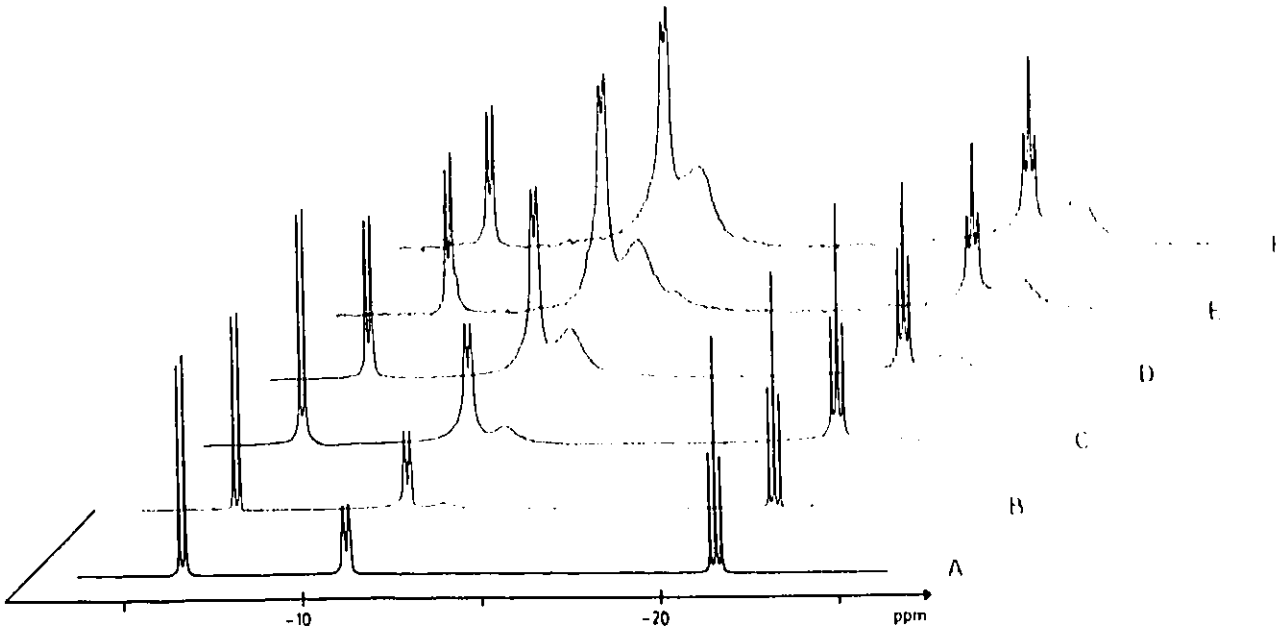

Figure 5.3: A series of phosphorus-31 NMR of ATP–Al aqueous solutions at 121 MHz. The Al/ATP ratios were: A) 0; B) 0.33; C) 0.50; D) 0.75; E) 0.90 and F) 1.0. The instrumental and experimental conditions were as follows: spectral width of 4000 Hz, acquisition time of 3.8 sec, pulse delay of 8 sec, 0.5 Hz line broadening, typically 400 transients, no proton decoupling, [ATP] = 100 mM, pH = 7.4, 20 °C and 20% D_2O.

for such linewidth variations as the spin-spin CSA relaxation mechanism would not be field dependent enough (see equation (2.29)). The increase of the linewidth with the field suggests that we are dealing with an aggregate whose correlation time τ_c is long enough, i.e. a few nanoseconds, so that both spin-spin relaxation times described above are field dependent, and become efficient enough to substantially contribute to the linewidth . For example, similar linewidth values (29 $\pm$ 3 Hz at 81 MHz) and field dependencies were reported for the three complexed phosphates of an ATP molecule bound to G-actin [103]. The long correlation time (τ_c = 40 ns) of this protein allowed the CSA relaxation mechanism to be the main source of spin-spin relaxation.

The influence of chemical exchange, between the free (α, β, γ) and complexed (α', β', γ') species, as a plausible explanation for the observed linewidth field dependency of these complexed resonances can be eliminated for the following reasons. A spin-spin relaxation time which is dependent upon the square of the magnetic field strength (see Figure 5.16) requires a fast exchange between the two species and, a single resonance would be detected (see Section 2.3.4.b), in contradiction with our experimental spectra (see Figure 5.1 and 5.3). As well, chemical shifts and linewidth variations would be observed in disagreement with experimental results (see Section 5.3.2). Finally, homonuclear dipolar spin-spin relaxation in an aggregate could not account for such observed linewidths of the complexed species. The maximum contribution of the nuclear spin relaxation mechanism to the linewidth would account for only 0.02 Hz at 32 MHz, for a rotational correlation time of 5 ns.

Figure 5.4 presents a series of phosphorus-31 NMR spectra at 32 MHz. For each spectrum, the Al/ATP ratio was kept constant at 0.4, and the total ATP concentration varied from 25 mM (spectrum A) to 100 mM (spectrum C). It is interesting to notice that the qualitative overall appearance of the three spectra was identical,

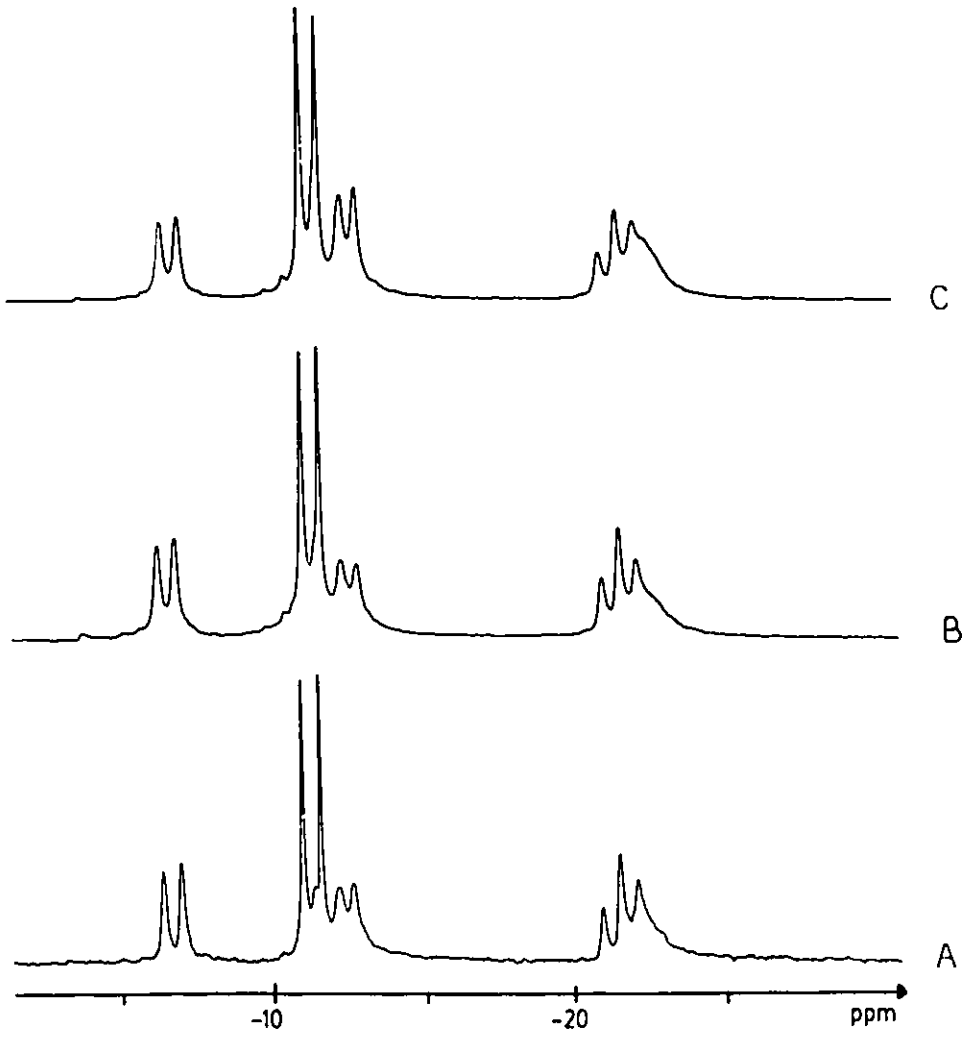

Figure 5.4: A series of proton decoupled phosphorus-31 NMR spectra of ATP–Al aqueous solutions at 32 MHz. The Al/ATP ratio was kept constant at 0.40 while the total ATP concentration was A) 25 mM; B) 50 mM to C) 100 mM. For further instrumental and experimental conditions see Figure 5.1.

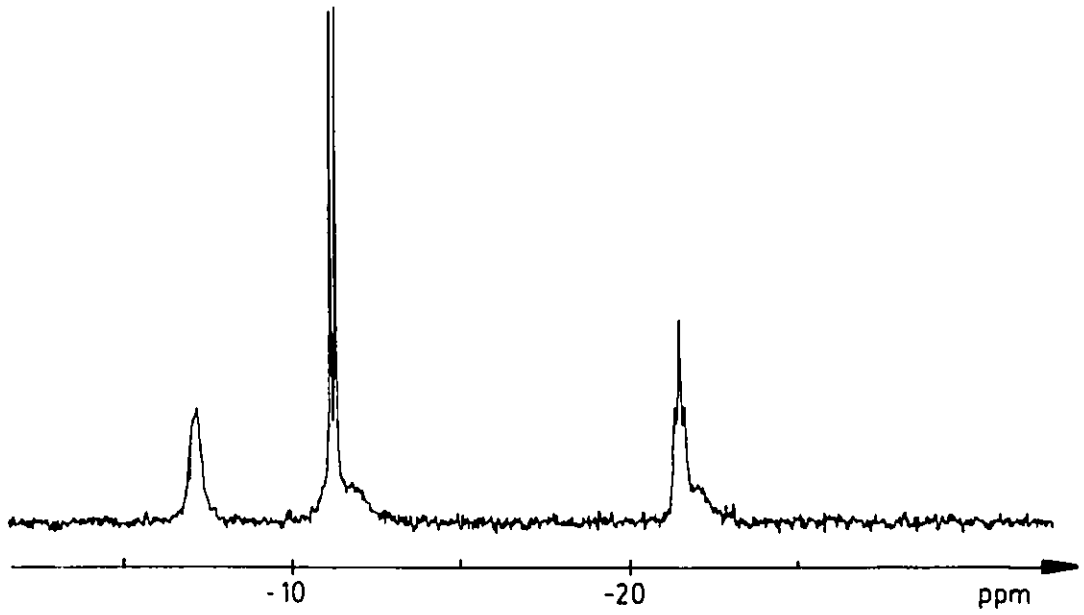

Figure 5.5: Proton decoupled phosphorus-31 NMR spectrum of an ATP–Al aqueous solution at 121 MHz. The Al/ATP ratio was 0.30 and the total ATP concentration present in solution lowered to 1.33 mM. The total experiment accumulation time was 20 hours. For further instrumental and experimental conditions see Figure 5.3.

suggesting that the ATP complexation phenomenon was not dependent upon the total ATP concentration. These qualitative results were supported by experiments performed at 121 MHz, pH = 7.4, in which the Al/ATP ratios were 0.30 and 0.50 and the total ATP concentration present in solution lowered to 1.33 mM (see Figure 5.5). At around pH = 7.4, the resonance frequency of the γ phosphate is very sensitive to the solution pH [145]. The β phosphate exhibits the same behavior but to a lesser extent. Contrary to this, the resonance frequency of the α phosphate does not have any pH dependence. These different behaviors explained the apparent increase in linewidth for the γ and β phosphates which resulted from pH variations within the sample due to the lengthy experiment time of 20 hours. As expected, the α phosphate linewidth was not affected. These experimental conditions (pH and

ATP concentration) can be thought to mimic the interaction of aluminum with ATP in cellular components. Under these conditions, the recorded spectra were identical to those observed with 25, 50 or 100 mM in total ATP concentration and represent results of some physiological relevance. At pH = 7.4 and for a whole range of ATP concentrations, the concentration study suggested that the size and stoichiometry of the ATP–Al aggregates formed in solution were not affected by the total ATP concentration.

5.3 Quantitative Analysis of ATP–Aluminum Complexes

5.3.1 Introduction

In this section we report a quantitative analysis of the interaction between ATP and aluminum by use of phosphorus-31 NMR at three different fields and for three different ATP concentrations. NMR parameters like chemical shifts, coupling constants and linewidths for the free ATP and ATP–Aluminum complexes will be reported and analyzed. Finally, the formation of complexes in solution will be discussed by means of titration curves using ^{31}P nucleus as a probe for quantitative complexation.

5.3.2 Chemical Shifts and Coupling Constants

At pH = 7.4, the phosphorus-31 chemical shifts of the three phosphates of ATP were - 6.5, - 11.2 and - 21.5 ppm (see Table 5.1) for the γ, α and β phosphates respectively, in agreement with reported values in the literature [145].

When varying the Al/ATP ratio from 0 to 1.0, the ^{31}P chemical shifts of the free α, β and γ phosphate resonances of ATP (at pH = 7.4, 81 MHz and for a total ATP concentration of 100 mM) were not, within experimental errors, dependent

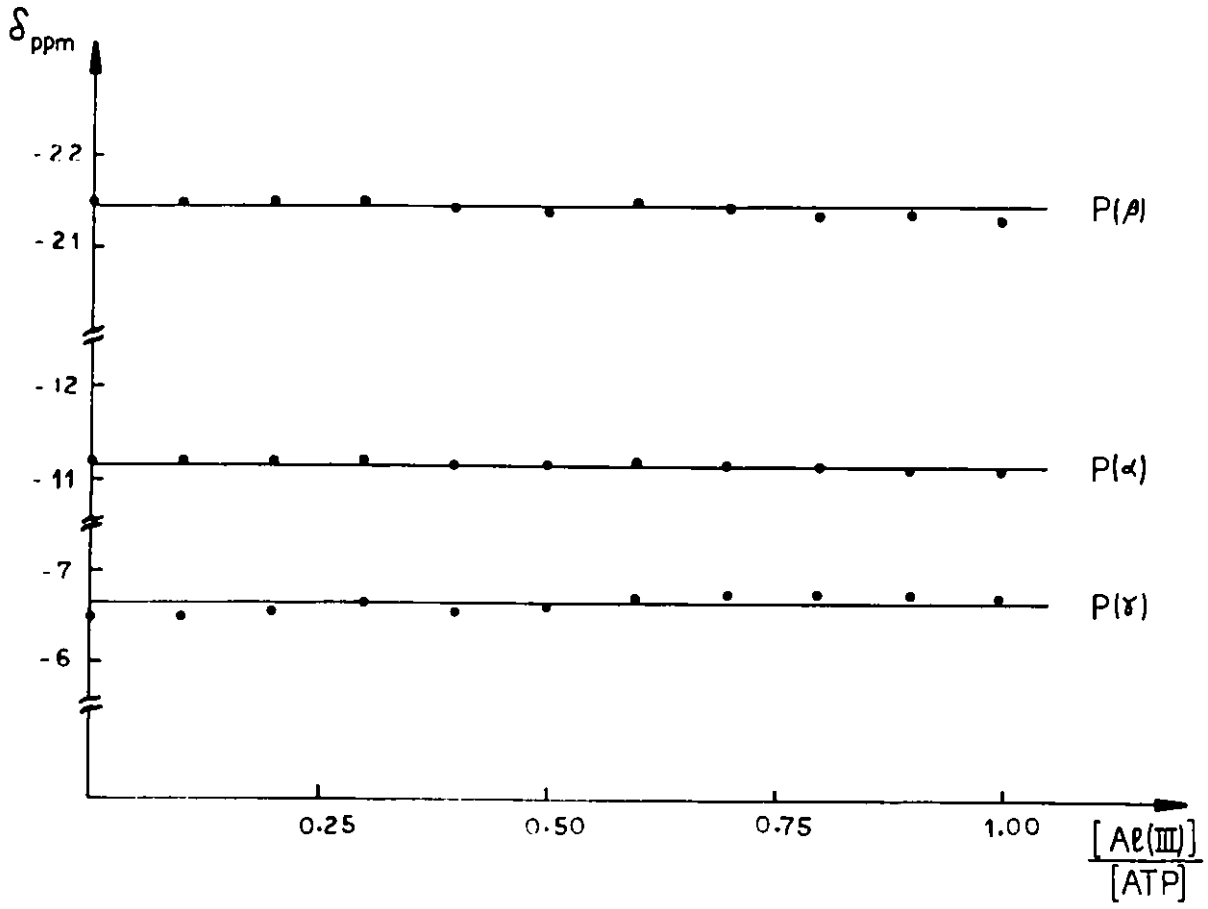

Figure 5.6: Plot of the ^{31}P chemical shifts versus the Al/ATP ratio for the three free resonances of ATP at 81 MHz. Each straight line represents the average chemical shift value reported in Table 5.1. For experimental conditions see Table 5.1.

upon the aluminum concentration (see Figure 5.6). No complex in fast equilibrium with the free ATP resonances was detected. The complexed species α', β' and γ' behaved similarly (see Figure 5.7) suggesting that they were not engaged in further fast equilibria. From the chemical shift point of view, the free (α, β, γ) and complexed (α', β', γ') resonances of ATP were in slow exchange on the NMR time scale and no fast chemical exchange was detected. For the chemical species in equilibrium, an upper limit for the exchange rate can be calculated from the frequency difference of the α and α' resonances. At 32 MHz, free and complexed resonances of ATP

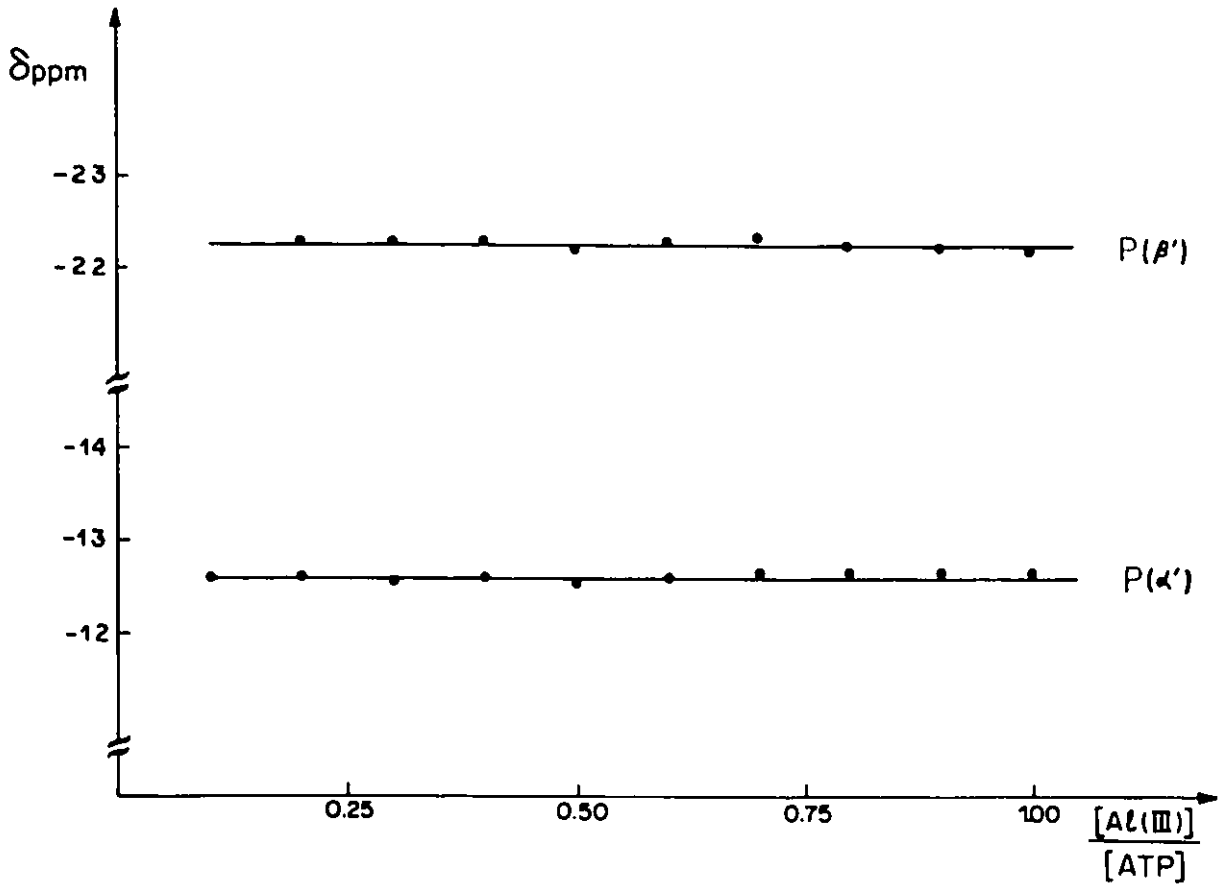

Figure 5.7: Plot of the ^{31}P chemical shifts versus the Al/ATP ratio for the complexed α' and β' resonances of ATP at 81 MHz. Each straight line represents the average chemical shift value reported in Table 5.1. For experimental conditions see Table 5.1.

exchange at a rate slower than 300 s^{-1}. In fact, from quantitative dynamic studies on the ATP-Al system (see Section 8.4), more precise conclusions will be reached concerning the kind of chemical exchange present in this system.

The coupling constants for the three phosphates of ATP are summarized in Table 5.1, for the various Al/ATP ratios. For Al/ATP = 0, the coupling constants for the three phosphates were identical and $^2J(P-P)$ = 19.4 Hz in full agreement with values reported in the literature [148,41]. As the aluminum content was increased in solution, the coupling constants of the free γ, α and β phosphates of ATP did not vary within experimental errors, and were the following values: $^2J(P_\gamma)$ = 19.1 ± 0.6 Hz, $^2J(P_\alpha)$ = 19.0 ± 0.7 Hz and $^2J(P_\beta)$ = 19.8 ± 0.6 Hz. These values were also similar to the phosphorus-phosphorus coupling constants observed for ATP when Al/ATP = 0, and provided confirmation that these ATP resonances (see Section 5.2) did not participate in aluminum complexation.

At 32 MHz, the phosphorus-phosphorus coupling constant for the α' resonance was readily observed on the spectra (see Figure 5.1). The values are listed in Table 5.1 and the average value of $^2J(P_{\alpha'})$ = 15.4 ± 0.3 Hz was calculated. The use of proton decoupling allowed the determination of the coupling constant for the γ' resonance which was $^2J(P_{\gamma'})$ = 21 ± 1 Hz (see spectrum A of Figure 5.2). Finally, at 32 MHz, for a total ATP concentration of 25 mM and an Al/ATP ratio of 0.80 and 1.0 (see Figure 5.1) the coupling constant value was determined for the β' phosphate resonance as $^2J(P_{\beta'})$ = 17 ± 1 Hz which represents the average between the γ' and α' coupling constants.

The complexed (α', β', γ') phosphate resonances and free (α, β, γ) phosphate resonances of ATP exhibited different phosphorus-phosphorus coupling constant values and confirmed (see Section 5.2) that the former set of resonances were representative

$\frac{Al(III)}{[ATP]}$	δ_{ppm}					J(P–P) $_{Hz}$			
	P_γ	P_α	P_β	$P_{\alpha'}$	$P_{\beta'}$	P_γ	P_α	P_β	$P^*_{\alpha'}$
0.00	-6.50	-11.19	-21.51	-12.64		19.4	19.4	19.4	
0.10	-6.48	-11.19	-21.49	-12.64		18.6	19.4	19.5	
0.20	-6.55	-11.18	-21.49	-12.62	-22.23	18.6	18.6	19.4	15.5
0.30	-6.67	-11.18	-21.50	-12.56	-22.28	19.4	19.4	21.1	15.1
0.40	-6.55	-11.15	-21.44	-12.59	-22.26	18.6	18.4	19.4	15.8
0.50	-6.63	-11.15	-21.42	-12.58	-22.16	19.0	17.8	20.3	15.1
0.60	-6.70	-11.18	-21.51	-12.63	-22.27	19.4	17.8		15.5
0.70	-6.77	-11.14	-21.47	-12.68	-22.31	18.6	19.0		15.8
0.80	-6.77	-11.15	-21.36	-12.68	-22.24	18.6	19.0		15.1
0.90	-6.74	-11.12	-21.36	-12.68	-22.23	20.5	19.0		
1.0	-6.71	-11.13	-21.27	-12.67	-22.17	18.6	19.0		15.1
$\hat{X}$	-6.67	-11.16	-21.44	-12.63	-22.24	19.1	19.0	19.8	15.4
σ	0.10	0.02	0.08	0.04	0.05	0.6	0.7	0.6	0.3

Table 5.1: Summary of phosphorus-31 NMR chemical shifts and coupling constants for the free (α, β, γ) and complexed (α', β') phosphate resonances of ATP when the Al/ATP ratio was varied from 0 to 1.0. $\hat{X}$ represents the average value associated with one standard deviation σ. The widely accepted 85% H_3PO_4 reference, with an internal coaxial tube filled with D_2O, was used throughout these studies. Experimental conditions were: [ATP] = 100 mM, pH = 7.4, 20 °C, 81 MHz and 20% D_2O. (*) The reported α' coupling constants were observed under similar experimental conditions but only at 32 MHz.

of phosphates involved in aluminum complexation. The decrease (for $^2J(P_{\alpha'})$ and $^2J(P_{\beta'})$) or increase (for $^2J(P_{\gamma'})$) in coupling constant values was previously observed for a large number of diamagnetic metal–ATP complexes and typically results from metallic complexation on the phosphates of ATP [148,41].

5.3.3 Titration Curves

Phosphorus-31 NMR was used as a probe for quantitative measurements of ATP–Al complexes present in solution. All spectra were recorded under proton decoupling to allow better resolution of the α and α' phosphate resonances. The influence of Nuclear Overhauser Enhancement (NOE) on the quantitative results was checked at 32 MHz. For an Al/ATP ratio of 0.5 and a total ATP concentration of 100 mM, quantitative measurements agreed within 5%, a lower value than the experimental errors estimated to be about 10%.

Calculation of the percentage of complexed ATP species was done by integration of the whole spectrum. The integral of the γ resonance was carefully measured and assigned to be proportional to the percentage of free γ ATP phosphate in solution. The rest of the spectrum was composed as follows. The integral of the α resonance region represented the sum of the α and γ' phosphates while the integral of the α' resonance was only composed of the α' phosphate. Finally, the integral of the β region was assigned as the sum of the β and β' phosphates. For any Al/ATP conditions we have the following set of equations:

$$\begin{cases} I_a &= \gamma \\ I_b &= \alpha + \gamma' \\ I_c &= \alpha' \\ I_d &= \beta + \beta' \end{cases} \tag{5.1}$$

For any Al/ATP ratio it was always observed that:

$$\begin{cases} I_d - I_a = I_b - I_a = I_c \\ \beta' + (\beta - \gamma) = \gamma' + (\alpha - \gamma) = \alpha' + (0) \end{cases}$$

or

$$\begin{cases} I_a + I_c = I_d = I_b \\ \gamma + \alpha' = \beta + \beta' = \alpha + \gamma' \end{cases}$$

These two sets of equations strongly suggest that the integrals for the free and complexed phosphates are related as follows:

$$\begin{cases} \alpha = \beta = \gamma \\ \alpha' = \beta' = \gamma' \end{cases} \tag{5.2}$$

As the γ resonance was well resolved throughout the study, its integral was utilized for quantitative determination of complexed ATP in solution using equation (5.1) and (5.2).

Figure 5.8 represents titration curves at 32 MHz (O) and 81 MHz ($\triangle$) for a total ATP concentration of 25 mM at pH = 7.4. Two distinct regions appear on the graph plotted. For $0 \leq$ Al/ATP ≤ 0.7 a steady linear increase of the complexed ATP was observed. The straight line represents a linear regression analysis of the data points and yields a slope of 1.04 with an intercept of 7%. The correlation factor was $\sigma = 0.978$ (for 8 data points). Above Al/ATP $= 0.7 \pm 0.1$, further increase of the aluminum concentration in solution did not change the percentage of total complexed ATP, which saturated at an average value of 76% $\pm$ 5%. Total ATP complexation was achieved for an Al/ATP ratio of 0.7 ± 0.1 given by the possible intercept region of the two straight lines (see Figure 5.8).

The same kind of titration curve is shown in Figure 5.9 at 32 MHz but for three different total ATP concentrations of 25 (O), 50 ($\times$) and 100 mM ($\triangle$) at pH = 7.4. From both studies (Figure 5.8 and 5.9) an identical qualitative complexation be-

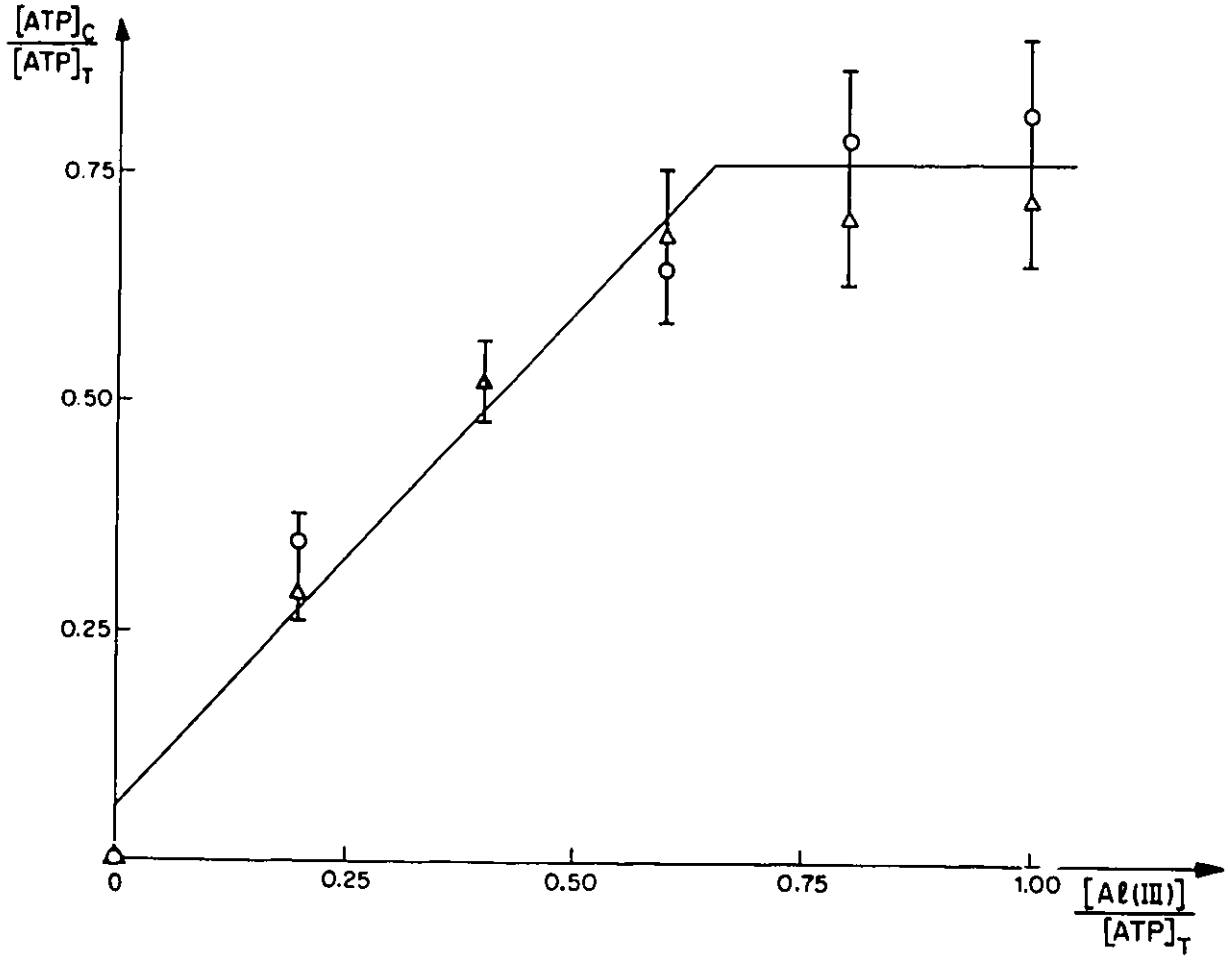

Figure 5.8: Variation of the percentage of complexed ATP versus the percentage of aluminum present in solution for a total ATP concentration of $[ATP]_T = 25$ mM, pH = 7.4, 20% D_2O, (O) at 32 MHz, (Δ) at 81 MHz.

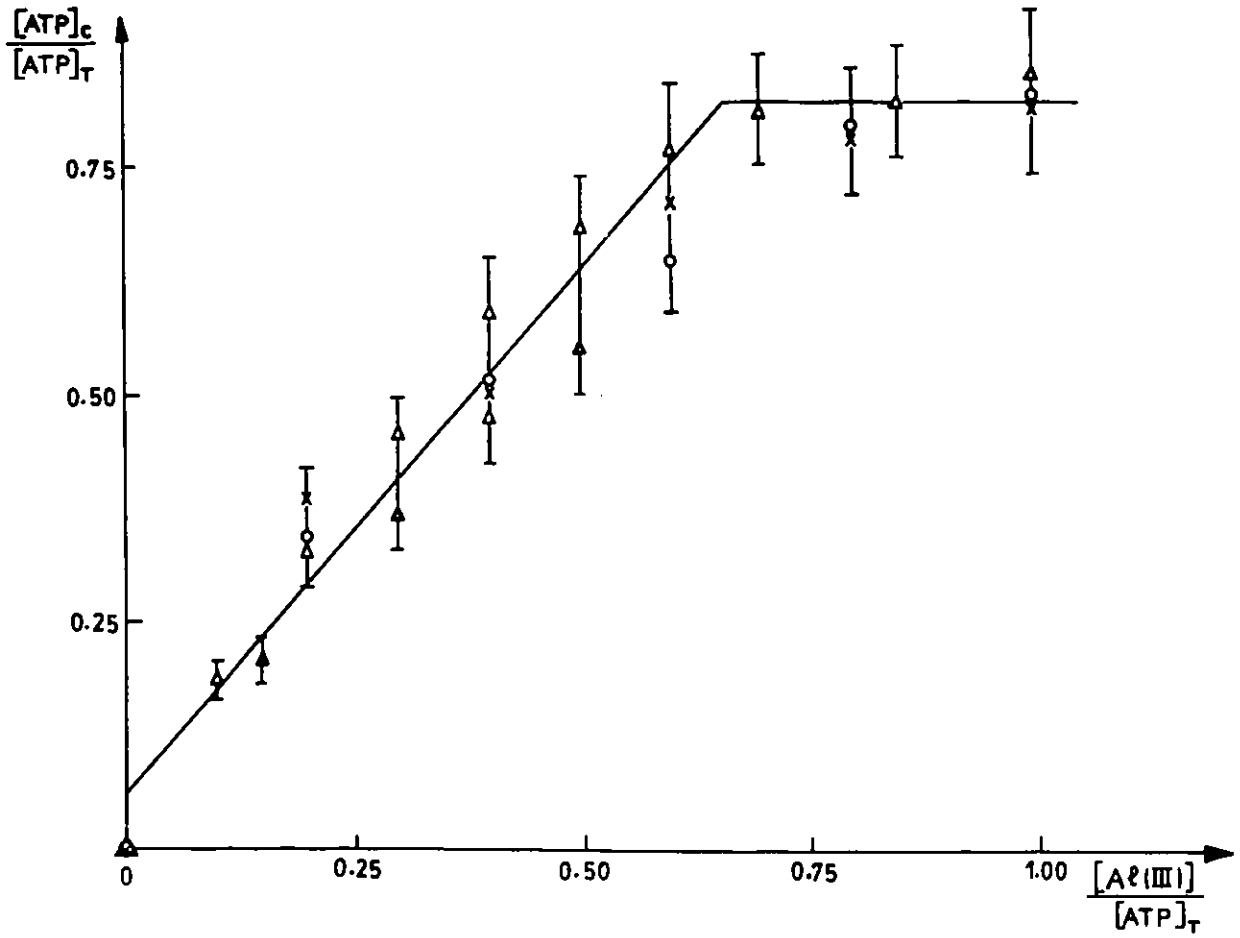

Figure 5.9: Variation of the percentage of complexed ATP versus the percentage of aluminum present in solution for different total ATP concentration of 25 mM (○), 50 mM (×) and 100 mM (△) at pH = 7.4, 20% D_2O and 32 MHz.

havior was observed. Furthermore, regardless of the total ATP concentration the same overall quantitative complexation phenomenon was taking place and confirmed our qualitative results based on phosphorus-31 NMR spectra (see Figure 5.4). The straight line resulted from a linear regression analysis for which $0 \leq \text{Al/ATP} \leq 0.70$ and gave a slope of 1.12 with a correlation factor of $\sigma = 0.973$ (for 20 points). The intercept of 6% , close to the ideal value of 0%, represented the experimental errors associated with integral measurements in the NMR spectrum as well as solution preparations.

In both studies, quantitative measurements of the total concentration of aluminum complexed in solution resulted in a straight line and allowed the estimation of a binding constant greater than 10^5 M^{-1} [149]. As a result, determination of ATP–Al complexed in solution was then measured quantitatively. Both studies also showed that, at pH = 7.4, there was only a single ATP–Al complex formed in solution, regardless of the total ATP concentration and Al/ATP ratio.

From the latter study (see Figure 5.9), total ATP complexation was estimated more accurately. It was achieved for an Al/ATP ratio of 0.70 ± 0.05 which represented the stoichiometry of the ATP–Al complex present in solution. For $\text{Al/ATP} \geq 0.70$ the remaining uncomplexed phosphate resonances of ATP, clearly observed in the NMR spectra (see Figure 5.1 and 5.3), were estimated to be $20 \pm 5\%$. These resonances were attributed to the phosphates taking part in the ATP–Al aggregate but without being directly involved in aluminum complexation .

As mentioned earlier (see Section 5.2 and Figure 5.4), the complexation phenomenon appeared to be independent of the total ATP concentration in solution. This interesting behavior was examined more precisely in Figure 5.10 in which the percentage of complexed ATP is shown for three different total ATP concentration

and for various percentages of aluminum. In this figure, the plot of the percentage of complexed ATP for a total ATP concentration of 100 mM (open data points) or 50 mM (filled data points) versus the percentage of complexed ATP for a total ATP concentration of 25 mM, at 81 MHz, for various percentage of aluminum. The linear regression gave a slope of 1.00 with a correlation factor of 0.990 (for 10 data points). This study quantitatively revealed that formation of the ATP–Al complex in solution was independent of the total ATP concentration in solution.

From this quantitative analysis, further insight into the type of complexation that is taking place into the ATP–Al aggregate can be gained. The new set of resonances appearing in the NMR spectra could be attributed to complexed γ', α' and β' ATP phosphates (see Section 5.2). By integration of the whole phosphorus-31 NMR spectrum and using equation (5.1) and (5.2), the percentage of each complexed phosphorus resonance (α', β' and γ') in the ATP–Al aggregate could be determined and are presented in Figure 5.11. Each data point represents an average value over six measurements for which the total ATP concentration was 100, 50 and 25 mM at 32 MHz and 81 MHz. Each horizontal line represents an average value of each complexed phosphate over the whole range of Al/ATP ratios. The percentage of complexed γ', α' and β' phosphate in the ATP–Al aggregate was 35 $\pm$ 7%, 34 $\pm$ 7% and 31 $\pm$ 3% respectively. These results indicated that, in the ATP–Al complex there was no preferred complexation of aluminum to any of the three phosphates. Within experimental error, each phosphate was equally complexed as each of the three resonances represented 33% of the total complexed ATP in solution.

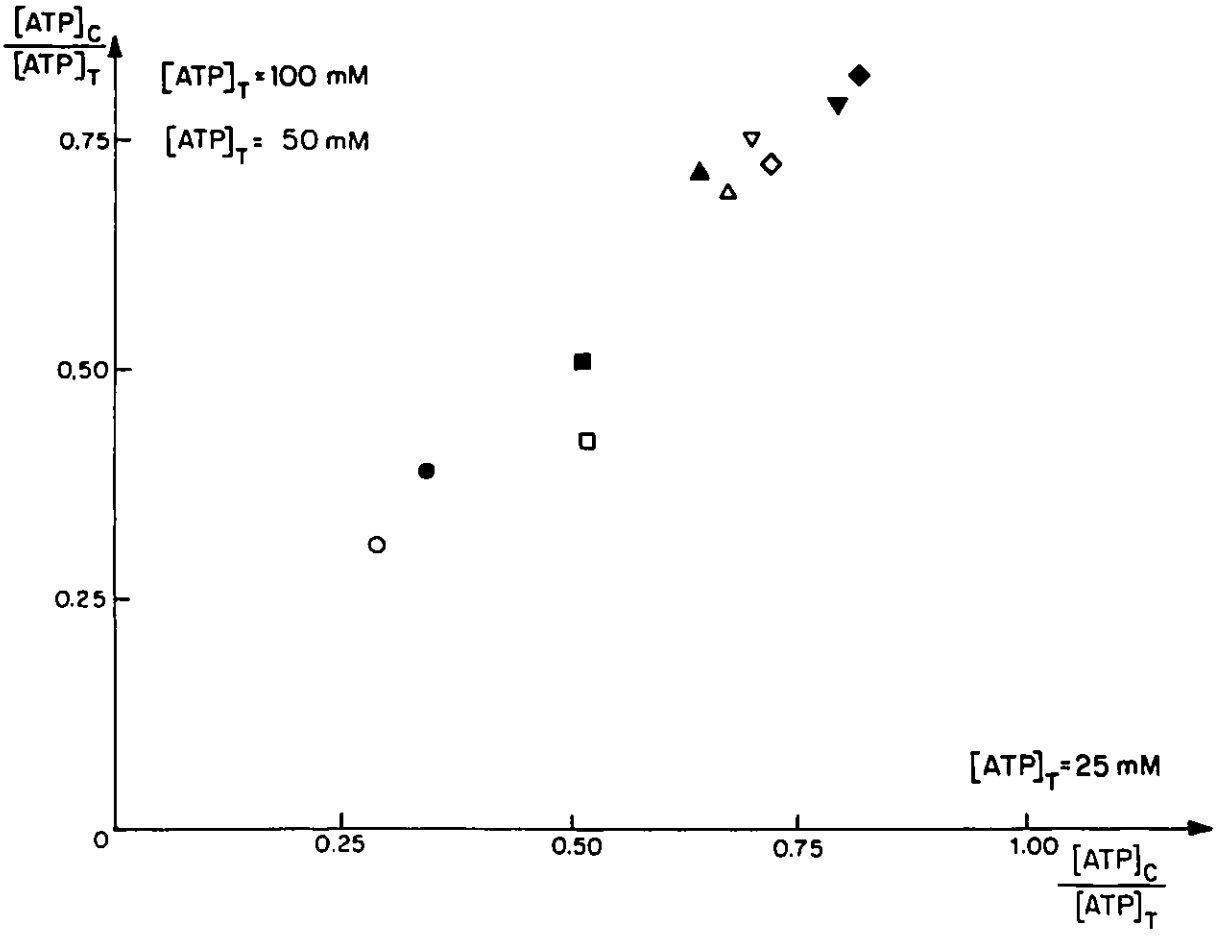

Figure 5.10: Percentage of complexed ATP for a total ATP concentration of 100 mM (open points) or 50 mM (filled points) versus the percentage of complexed ATP for a total ATP concentration of 25 mM, and for various percentages of aluminum: (○ , ●) 0.20; (□ , ■) 0.40; (△ , ▲) 0.60; (▽ , ▼) 0.80; (◇ , ◆) 1.0 at pH = 7.4, 20% D_2O and 81 MHz.

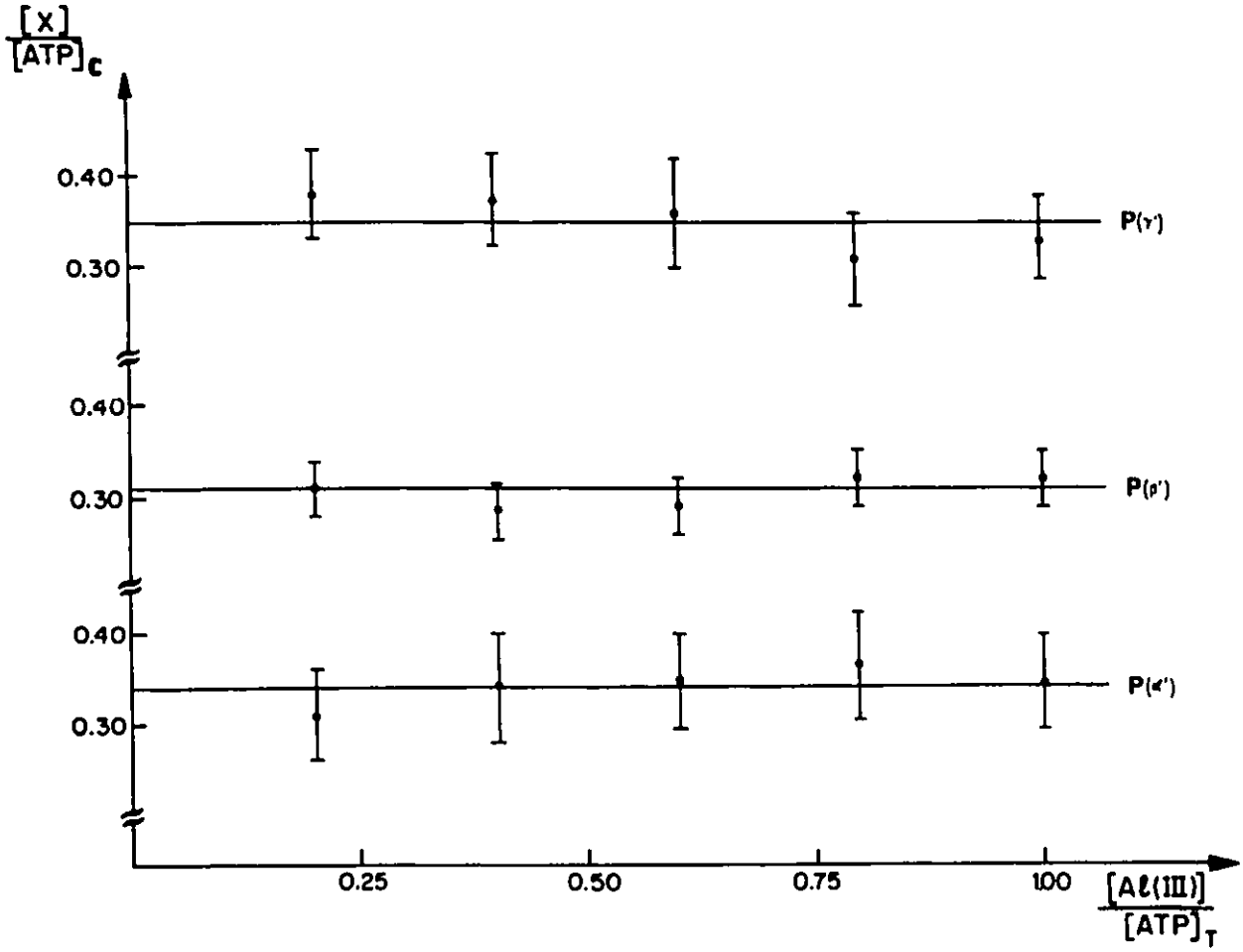

Figure 5.11: Percentage of each complexed phosphorus moieties, relative to the total complexed ATP, as a function of aluminum percentage. Each data point represents the average of six measurements made for a total ATP concentration of 100 mM, 50 mM and 25 mM at 32 and 81 MHz, pH = 7.4 and 20% D_2O.

5.3.4 Linewidths

Linewidth variations of the uncomplexed well resolved γ phosphate were followed at 32 and 121 MHz for various Al/ATP ratios. Although measurements of the β and α phosphate linewidths were not representative of their true linewidths, as they overlapped with their respective complexed resonances, they followed a similar qualitative linewidth variation. Without aluminum present in solution, the γ phosphate linewidth was 1.2 $\pm$ 0.1 Hz at 121 MHz and 2.1 $\pm$ 0.1 Hz at 32 MHz, which represented the natural phosphorus linewidth in solution. This linewidth gradually increased with aluminum content in solution to reach a constant value of 4.2 $\pm$ 0.6 Hz at 121 MHz and 4.4 $\pm$ 0.8 Hz at 32 MHz for any Al/ATP ratio greater than 0.70. These variations corresponded to a true linewidth increase of 3.0 Hz at 121 MHz and 2.3 Hz at 32 MHz.

Alteration of the solution viscosity could not be responsible for such linewidth variations. At 25° C, for an equimolar ATP–Al solution (ATP = 100 mM) the viscosity of the solution was measured (η = 1.028 cp), and represented an increase of only 15% compared to the viscosity of an aqueous ATP solution (η = 0.888). The linewidth increase rather originates from the uncomplexed ATP phosphates present in the ATP–Al aggregate.

The much longer correlation time τ_c = 2.8 ns (see later) of the phosphorus atoms involved in the ATP–Al complex results in a more efficient overall spin-spin relaxation rate. Heteronuclear phosphorus-proton and homonuclear phosphorus-phosphorus dipolar relaxation as well as CSA represent some possible relaxation mechanisms which could contribute to broaden the linewidth of these uncomplexed phosphates (see Section 4.3). The homonuclear phosphorus-phosphorus dipolar relaxation con-

tribution to the linewidth was expected to be negligible. Using standard structural parameters for a phosphate group (see footnote of page 54 and equation (4.17)), and a correlation time of 2.8 ns, one calculates a linewidth contribution to the γ phosphate less than 0.01 Hz at 121 MHz and 0.02 Hz at 32 MHz.

In the ATP–Al complex, the uncomplexed γ phosphates experienced a contribution from the CSA spin-spin relaxation mechanism due to an average CSA value of 147 ppm (see Table 4.7). The resulting calculated linewidth broadening of the γ resonance was 1.1 Hz at 121 MHz and 0.1 Hz at 32 MHz, compared to their respective broader true linewidths of 3.0 Hz and 2.3 Hz. The excess linewidths of 1.9 Hz at 121 MHz and 2.2 Hz at 32 MHz was due to heteronuclear phosphorus-proton dipolar interactions which arose from the phosphorus solvation sphere (see Section 4.3).

The linewidths of the two resolvable complexed phosphates α' and β' are listed in Table 5.2 and 5.3 at three different fields and for three different total ATP concentrations. For a given magnetic field and for identical total ATP concentrations (100, 50 or 25 mM) each complexed α' (Figure 5.12) and β' (Figure 5.13) resonance exhibited a constant linewidth throughout the entire Al/ATP ratio variation. Furthermore, changing the total ATP concentration did not affect their respective linewidths so that at 32, 81 and 121 MHz the α' phosphate linewidth averaged to 29 $\pm$ 2 Hz, 48 $\pm$ 4 Hz and 63 $\pm$ 4 Hz respectively. The case of the β' phosphate resonance was similar and the average linewidths were 55 $\pm$ 4 Hz, 88 $\pm$ 7 Hz and 128 $\pm$ 12 Hz at 32, 81 and 121 MHz respectively.

These calculated values do not represent the true linewidths of each resonance as they had to be corrected for the natural linewidth (2 Hz at 32 and 81 MHz and 1 Hz at 121 MHz) as well as for the phosphorus-phosphorus coupling constant $^2J(P_{\alpha'}) =$ 15 Hz and $^2J(P_{\beta'}) = 17$ Hz (see Section 5.3.2). The true linewidth values at 32, 81

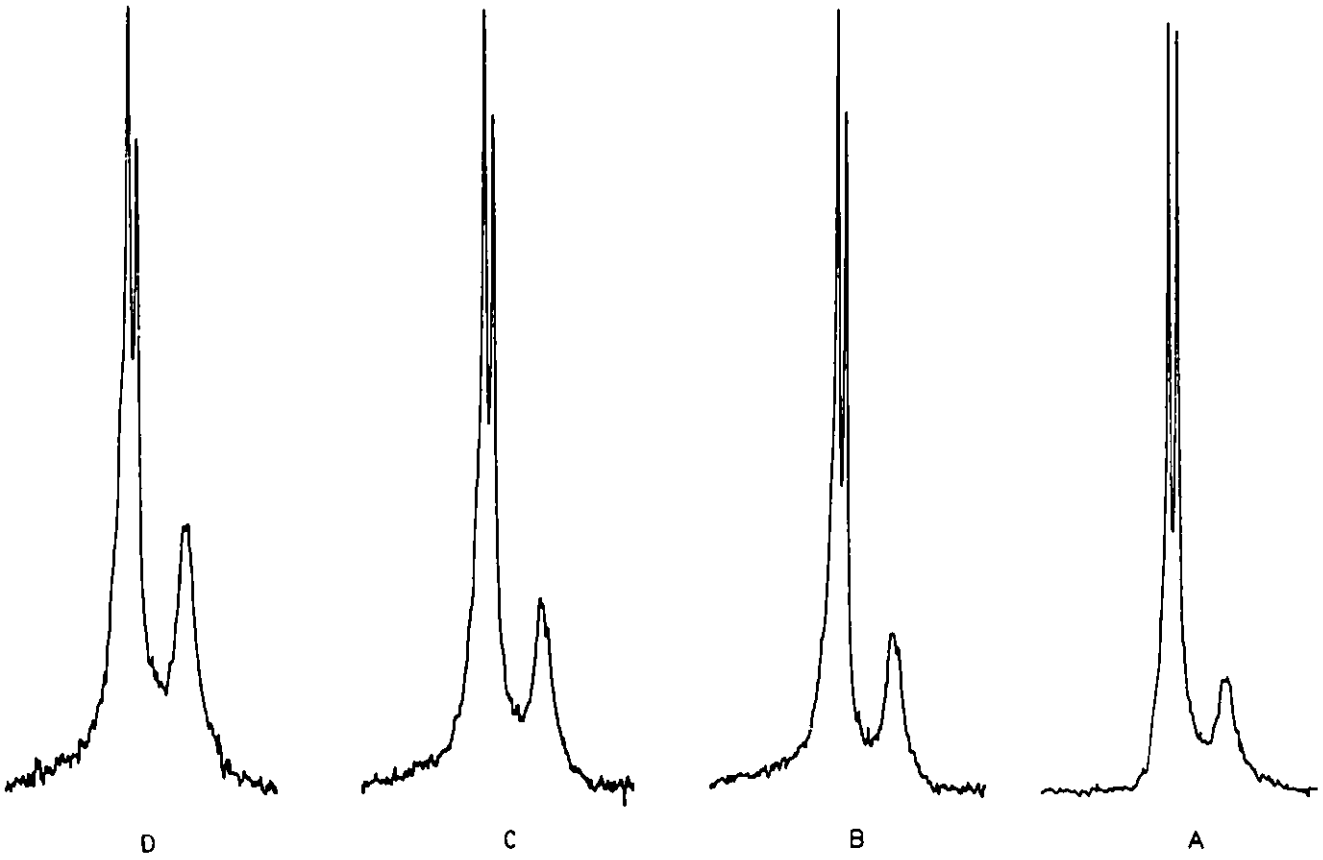

Figure 5.12: Display of the spectral region between – 7 and – 15 ppm for a set of spectra recorded under full proton decoupling and showing the α, γ' and α' resonances of ATP. The Al/ATP ratios were: A) 0.20; B) 0.30; C) 0.40 and D) 0.50 for a total ATP concentration of 100 mM at 81 MHz, pH = 7.4 and 20% D_2O.

$[ATP]_T$	$\frac{Al(III)}{[ATP]_T}$	0.20	0.30	0.40	0.50	0.60	0.70	0.80	0.90	1.0
100 mM	$\nu_{1/2}(\alpha')$	27	27	28	28	29	30		30	33
50 mM	in Hz at	27		28		29		30		31
25 mM	32 MHz	29		27		28		33		31
100 mM	$\nu_{1/2}(\alpha')$	50	45	50	55	42	48	54	54	54
50 mM	in Hz at	42		39		42		43		45
25 mM	81 MHz	51		51		54				
100 mM	$\nu_{1/2}(\alpha')$ in Hz at 121 MHz	60	62	60	60	62	69		72	62

Table 5.2: Summary of the α' resonance linewidth value at half height, under full proton decoupling, when the Al/ATP ratio was varied from 0.20 to 1.0, for three different total ATP concentration (100, 50 and 25 mM) and for three magnetic fields (121, 81 and 32 MHz) at pH = 7.4 in a 20% D_2O solution. All linewidths reported are not corrected for the natural phosphorus linewidth or the phosphorus-phosphorus coupling constant.

and 121 MHz were then 10 ± 2 Hz, 29 ± 4 Hz and 46 ± 4 Hz respectively for the α' resonance and 16 ± 4 Hz, 48 ± 7 Hz and 89 ± 12 Hz respectively for the β' resonance.

At 121 MHz the overlap between the complexed (α' and β') and uncomplexed (α and β) resonances was not negligible and may well have resulted in erroneous linewidth determinations. In order to test the validity of our linewidth data, the Carr-Purcell-Meiboom-Gill (CPMG) pulse sequence [149,150,151] was used at 121 MHz to obtain a measurement of the α' and β' true linewidth value. Figure 5.14 displays the α, γ' and α' region of a phosphorus-31 ATP spectrum for which the total ATP concentration was 100 mM, Al/ATP = 0.3, pH = 7.4 and for various time delays (τ)

$[ATP]_T$	$\frac{Al(III)}{[ATP]_T}$	0.20	0.30	0.40	0.50	0.60	0.70	0.80	0.90	1.0
100 mM	$\nu_{1/2}(\beta')$		54	54	57	50	50	57		54
50 mM	in Hz at	60		60		57		57		60
25 mM	32 MHz	54		57		57		57		50
100 mM	$\nu_{1/2}(\beta')$	90	95	95	95	84	90	96	96	96
50 mM	in Hz at	96		84		72		84		78
25 mM	81 MHz	100		80		80		80		80
100 mM	$\nu_{1/2}(\beta')$ in Hz at 121 MHz	133	120	143	142	124	110		130	120

Table 5.3: Summary of the β' resonance linewidth value at half height, under full proton decoupling, when the Al/ATP ratio was varied from 0.20 to 1.0, for three different total ATP concentration (100, 50 and 25 mM) and for three magnetic fields (121, 81 and 32 MHz) at pH = 7.4 in a 20% D_2O solution. All linewidths reported are not corrected for the natural phosphorus linewidth or the phosphorus-phosphorus coupling constant.

during which spin-spin relaxation affects the transverse magnetization:

$$M_{xy}(\tau) = M_z(0)\exp(-\tau/T_2) \tag{5.3}$$

In equation (5.3) $M_{xy}(t)$ represents the observed transverse magnetization after a delay τ, $M_z(0)$ the equilibrium longitudinal magnetization and T_2 the true spin-spin relaxation time. A two parameter non-linear regression analysis on equation (5.3) gave a spin-spin relaxation time of 7.2 ± 1.0 ms which translates into a true linewidth value for the α' resonance of 44 ± 5 Hz, in excellent agreement with an average linewidth value of 46 ± 4 Hz. The same experiment, performed on the β' resonance, gave a true linewidth value of 109 ± 10 Hz (T_2 = 2.9 ± 0.3 ms) in comparison with a

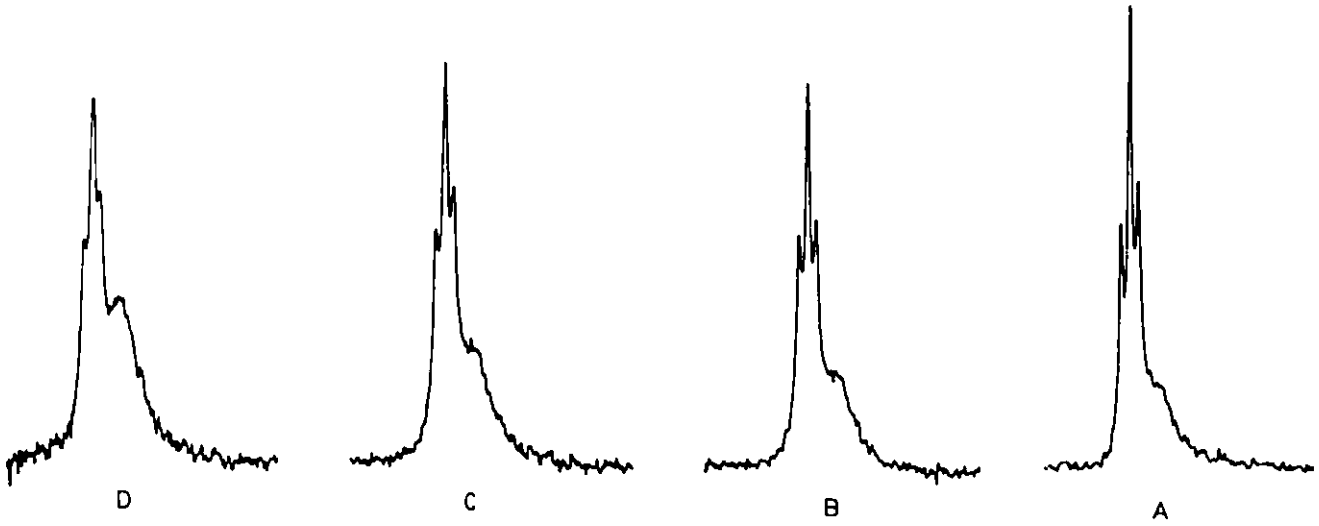

Figure 5.13: Display of the spectral region between – 19 and – 27 ppm for a set of spectra recorded under full proton decoupling and showing the β and β' resonances of ATP. The Al/ATP ratios were: A) 0.20; B) 0.30; C) 0.40 and D) 0.50 for a total ATP concentration of 100 mM at 81 MHz, pH = 7.4 and 20% D_2O.

average linewidth value of 89 $\pm$ 12 Hz. True linewidth values obtained by the CPMG method for both α' and β' resonances were thus in good agreement with linewidth values extracted from NMR spectra at 121 MHz. This result provided confidence in the α' and β' linewidth values obtained from NMR spectra at 32 and 81 MHz since they presented a similar degree of overlapping with their respective uncomplexed α and β resonances (compare Figure 5.3 with Figure 5.1 and Figure 5.3 with Figure 5.12 and 5.13).

For a given magnetic field strength, each α' and β' phosphate resonance was characterized by a constant well defined linewidth over a whole range of total ATP concentration and for any Al/ATP ratio value. A strong linewidth field dependency was observed for both complexed resonances. For example, at 121 MHz, the α' resonance was about five times broader (46 Hz) than at 32 MHz (10 Hz) for similar conditions.

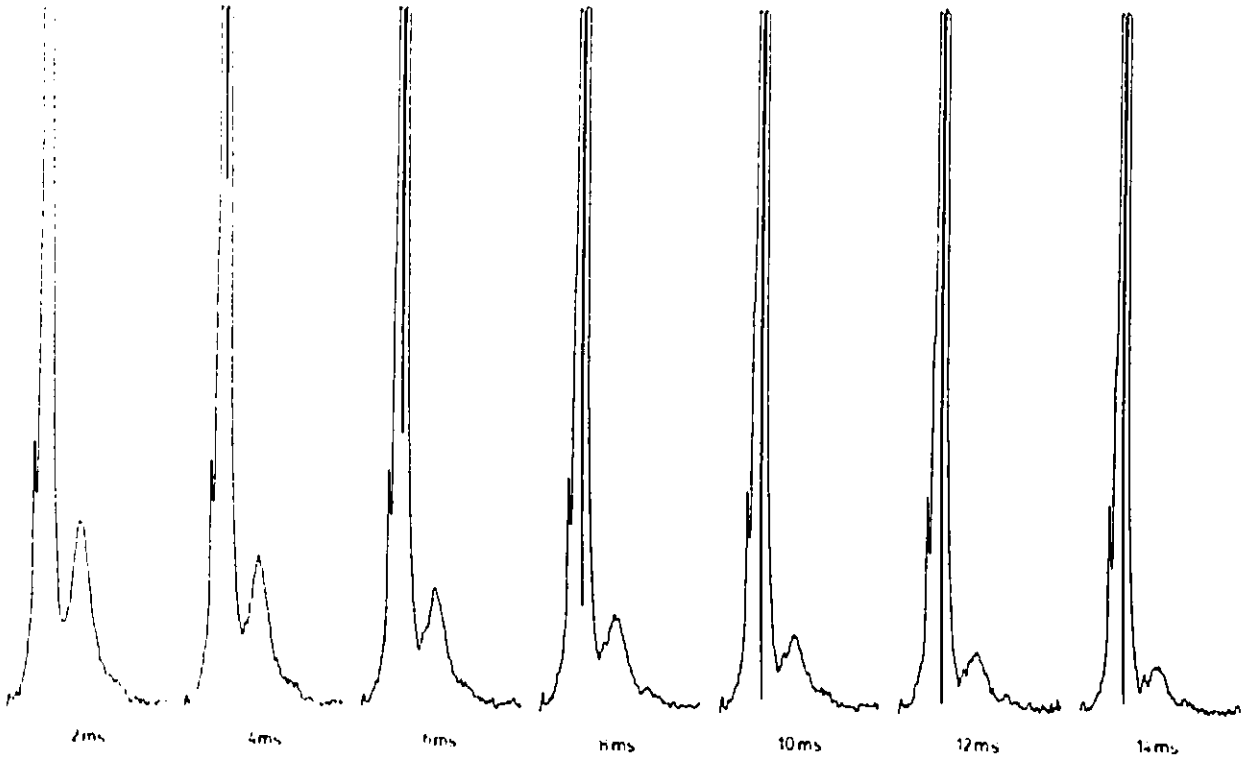

Figure 5.14: Display of a phosphorus-31 spin-spin relaxation time experiment on the α, γ' and α' region of an ATP spectrum at 121 MHz using the CPMG pulse sequence. The time delay τ during which spin-spin relaxation takes place is shown for each spectrum. The total ATP concentration was 100 mM, Al/ATP = 0.3, pH = 7.4 and 20% D_2O.

This experimental linewidth field dependency observed for each complexed resonance was analyzed and will be discussed in the next section.

Analysis of quantitative measurements like chemical shifts, coupling constants, titration curves and linewidths can be used to suggest a chemical structure of the triphosphate chains of the ATP–Al aggregate. The two complexes presented in Figure 5.15 are based on ^{31}P NMR studies. Unfortunately, using ^{31}P NMR results only, it was not possible to rule out one of the proposed models. They will now be discussed as they summarize and account for the observed qualitative and quantitative ^{31}P NMR data available from this study. Each aggregate is composed of four ATP molecules whose triphosphate chains are coordinated by three aluminum cations giving rise to a stoichiometry of 0.75. In these species, the three ATP phosphates (γ', β' and α') are equally complexed by aluminum in the ratio ($3\gamma' : 3\beta' : 3\alpha'$) while 25% of ATP phosphates, in the ratio ($\gamma : \beta : \alpha$) are not complexed by aluminum and account for the residual uncomplexed resonances observed in the ^{31}P spectra.

Formation of a dimer $(ATP_4Al_3)_2$ could not account for the observed quantitative results for the following reasons. This aggregate in which each phosphate is equally complexed by aluminum needs not six, but seven aluminum cations. The resulting complex stoichiometry of 0.90 with only 10% uncomplexed phosphates is in opposition with the titration curve results (see Figure 5.8 and 5.9). Furthermore, a ^{31}P spin-lattice relaxation study has confirmed the quantitatively observed 4:3 ATP:Al complex stoichiometry (see Chapter 8).

In these proposed species (see Figure 5.15) each complexed phosphate (γ', β', α') would exhibit its own true linewidth. Upon formation of the ATP_4Al_3 species in solution, free ATP phosphate resonances (when Al/ATP = 0) are gradually replaced by uncomplexed phosphate resonances of the aggregate. As their chemical environ-

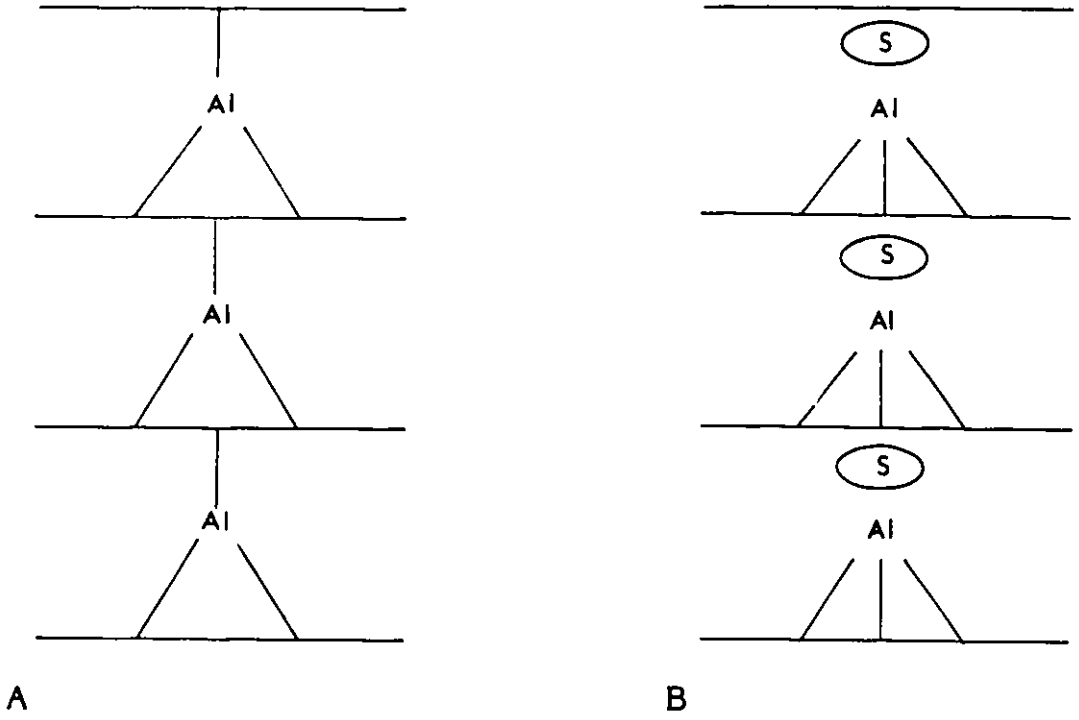

Figure 5.15: Schematic representation of two proposed models for the ATP_4Al_3 aggregate focusing on the triphosphate side chains. In structure A, the aluminum cations are complexed by two triphosphate ATP side chains while in structure B, they are only complexed by one triphosphate chain but separated from the next one by water solvent molecules (S).

ments do not differ significantly, the same ^{31}P chemical shifts were observed for both phosphates. In contrast, it was expected that their respective linewidths would differ due to an increase in the phosphorus correlation time.

Estimation of the aggregate correlation time was done using the Stoke-Debye-Einstein equation [35],

$$\tau_c = \frac{4\pi}{3}\frac{a^3\eta}{kT} \tag{5.4}$$

in which η and T represent the viscosity and temperature of the solution (η = 1.024 cp at 25 °C for an equimolar ATP–Al mixture), k the Boltzmann constant and a the radius of a sphere equivalent to the ATP–Al aggregate. Using the usual structural parameters for phosphate bond lengths (P=O = 1.5 Å; P–O = 1.6 Å; Al–O = 1.2 Å) [110], the ATP–Al complex can be idealized to a sphere whose radius is 10 Å. Using equation (5.4) a correlation time of 1 ns was calculated and is in agreement with earlier qualitative discussions.

5.3.5 Dynamics of ATP–Aluminum Interactions

As discussed earlier (see Section 5.2) the spin-spin CSA relaxation mechanism could be a plausible source of relaxation, and could be the reason for the linewidth field dependencies, as it depends upon the square of the magnetic field strength (see Section 2.3.2). Figure 5.16 depicts the true linewidth variation as a function of the square of the resonance frequency. Both straight lines result from a linear regression analysis and suggest that the CSA could be responsible for such linewidth variations.

It was possible to reproduce the observed true linewidth values of the α' and β' phosphates for the three experimental resonance pulsations (ω_0) using the following

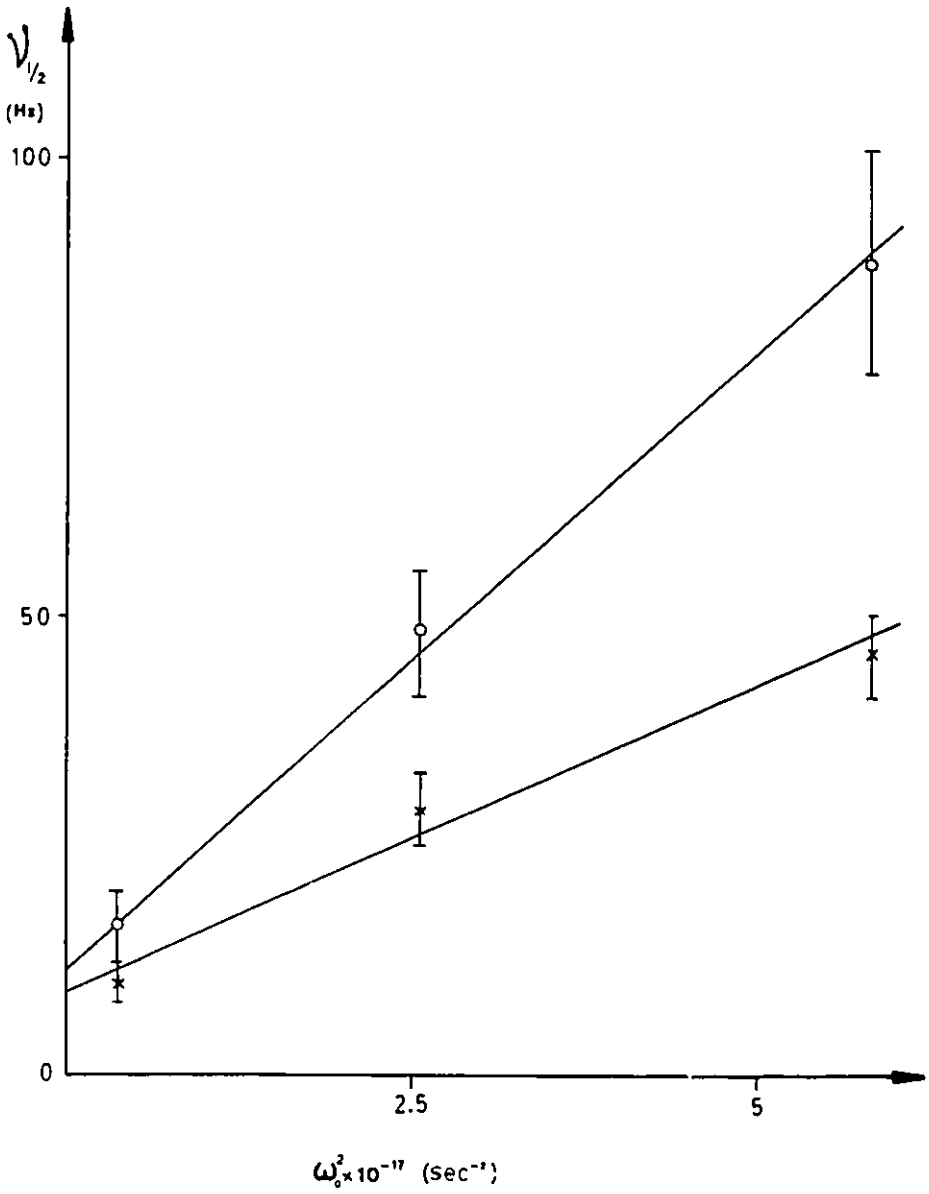

Figure 5.16: Variation of the true linewidth values of the α' (×) and β' (o) resonances as a function of the square of the experimental pulsation frequency.

equation (see equation (2.29)):

$$\mathcal{V}_{1/2}(\omega_0) = \frac{1}{90\pi}\omega_0^2(\Delta\sigma)^2\left(1+\frac{\eta^2}{3}\right)[4j(0)+3j(\omega_0)] \tag{5.5}$$

In equation (5.5) $\mathcal{V}_{1/2}(\omega_0)$ is the phosphate true linewidth at ω_0 and $\Delta\sigma\left(1+\frac{\eta^2}{3}\right)^{1/2}$ is the CSA value of the ATP phosphates which have been previously measured and discussed (see Table 4.7). Finally, $j(0)$ and $j(\omega_0)$ represent the spectral density function (see Section 2.2). From equation (5.5) the slope of each straight line in Figure 5.16 is equal to:

$$\text{"}Slope\text{"} = \frac{1}{90\pi}(\Delta\sigma)^2\left(1+\frac{\eta^2}{3}\right)[4j(0)+3j(\omega_0)] \tag{5.6}$$

Using this equation, the rotational correlation time was calculated. In order to satisfy equation (5.6) and henceforth reproduce the experimental linewidths of the α' and β' phosphates a correlation time of 36 ns and 105 ns respectively was required. The correlation time calculated for the α' phosphate can be compared to the correlation time of an ATP molecule bound to a G-actin protein (τ_c = 40 ns) whose molecular weight is 42300 [103]. The calculated correlation times clearly do not reflect the nature and dynamics of ATP aluminum interactions. Assuming that the CSA mechanism was the source of linewidth broadening, the conclusion that CSA did not successfully account for the α' and β' linewidths was supported by other factors. In the ATP-Al aggregate the three ATP phosphates were shown to be equally complexed by aluminum (33% each see Figure 5.11). Under these conditions, calculation of the α' and β' phosphate correlation times should have given similar values. This was in contradiction with the calculated β' correlation time three times higher (105 ns) than that of the α' phosphate (36 ns).

Linear regression analyses on both resonances yielded an intercept of 9 Hz for the α' phosphate and 11 Hz for the β' phosphate. These extrapolated values, at zero

magnetic field strength, represent the true linewidth of each complexed phosphate for which the CSA contribution has been cancelled. Such linewidth values were reported for the uncomplexed γ phosphate to be 2.2 Hz, much narrower than the extrapolated data for the α' (9 Hz) and β' (11 Hz) phosphates.

Linewidth field dependencies for both phosphates could alternatively be rationalized by a scalar relaxation of the second kind [35] between a phosphorus and aluminum nuclei, expressed as:

$$\frac{1}{T_{2,SC}} = \pi \mathcal{V}_{1/2} = \frac{4\pi^2 J^2}{3} S(S+1) \left[T_{1,S} + \frac{T_{2,S}}{1 + (\omega_P - \omega_{Al})^2 T_{2,S}^2} \right] \tag{5.7}$$

in which J is the phosphorus-aluminum coupling constant, S the nuclear spin of aluminum ($S = 5/2$), $T_{1,S}$ and $T_{2,S}$ the respective spin lattice and spin–spin relaxation times of ^{27}Al and $(\omega_P - \omega_{Al})$ the resonance pulsation difference between ^{31}P and ^{27}Al nuclei. The second term in parenthesis could be safely neglected, since in order to contribute significantly to scalar relaxation, the condition $(\omega_P - \omega_{Al})^2 T_2^2 \approx 1$ is required. This translated into an aluminum linewidth greater than 10 MHz while experiments showed linewidths in the order of the kilohertz. After these considerations, equation (5.7) reduces to:

$$\mathcal{V}_{1/2} = \frac{35}{3} \pi J^2 T_{1,S} \tag{5.8}$$

Equation (5.8) means that the observed ^{31}P linewidth variations resulted from a spin-lattice relaxation time of ^{27}Al which was field dependent. It suggested a correlation time of the ATP–Al aggregate in the nanosecond range. It also indicates that as the magnetic field was increased from 32 MHz (21 MHz for ^{27}Al) to 121 MHz (78 MHz for ^{27}Al), the extreme narrowing condition ($\omega_0 \tau_c \ll 1$) was not fulfilled any more for the ^{27}Al nucleus, giving rise to an ^{27}Al field dependent spin-lattice relaxation time (see Section 9.4). Spin-lattice and spin-spin quadrupolar relaxation of spin

5/2 nuclei, extended in the non-extreme narrowing limits and for different magnetic fields are dealt with in Chapter 9. The main result is that, for a spin 5/2 in the non-extreme narrowing region, both transverse and longitudinal magnetization decays are governed by a sum of three exponentials. Each one of the three components of the total magnetization possesses a characteristic relaxation rate which varies differently with the product $\omega_0\tau_c$. The situation is further complicated by the fact that the relative weight of each one of the three components is not constant but also varies with the product $\omega_0\tau_c$. In the case of the spin-lattice relaxation time, simplifications arise as two of the three components of the longitudinal magnetization have negligible weights. For example, with a correlation time of four nanoseconds, the relative weights of each component at 78 MHz are 95%, 4% and 1%. As a result, the longitudinal magnetization decay can be safely assumed to be governed by a single exponential decay.

The ratio of equation (5.8) at two different magnetic fields can be expressed as:

$$\frac{\mathcal{V}_{1/2}(X)}{\mathcal{V}_{1/2}(32\text{MHz})} = \frac{T_{1,S}(Y)}{T_{1,S}(21\text{MHz})} \tag{5.9}$$

where Y represents the equivalent resonance frequency of ^{27}Al when the resonance frequency of ^{31}P is X. In equation (5.9), the experimental ^{31}P linewidth ratio at two different magnetic fields is equal to a ratio of two ^{27}Al spin-lattice relaxation times. For two different given magnetic fields, this ratio varies only upon the correlation time τ_c. Figure 5.17 represents an example of such variation for the ^{27}Al spin-lattice relaxation time ratio at two different magnetic fields (78 MHz and 21 MHz) as a function of the correlation time τ_c. Resolution of equation (5.9) provided a unique solution for determining the correlation time. Two examples of correlation time determinations are indicated on Figure 5.17 for the α' and β' resonances of ATP.

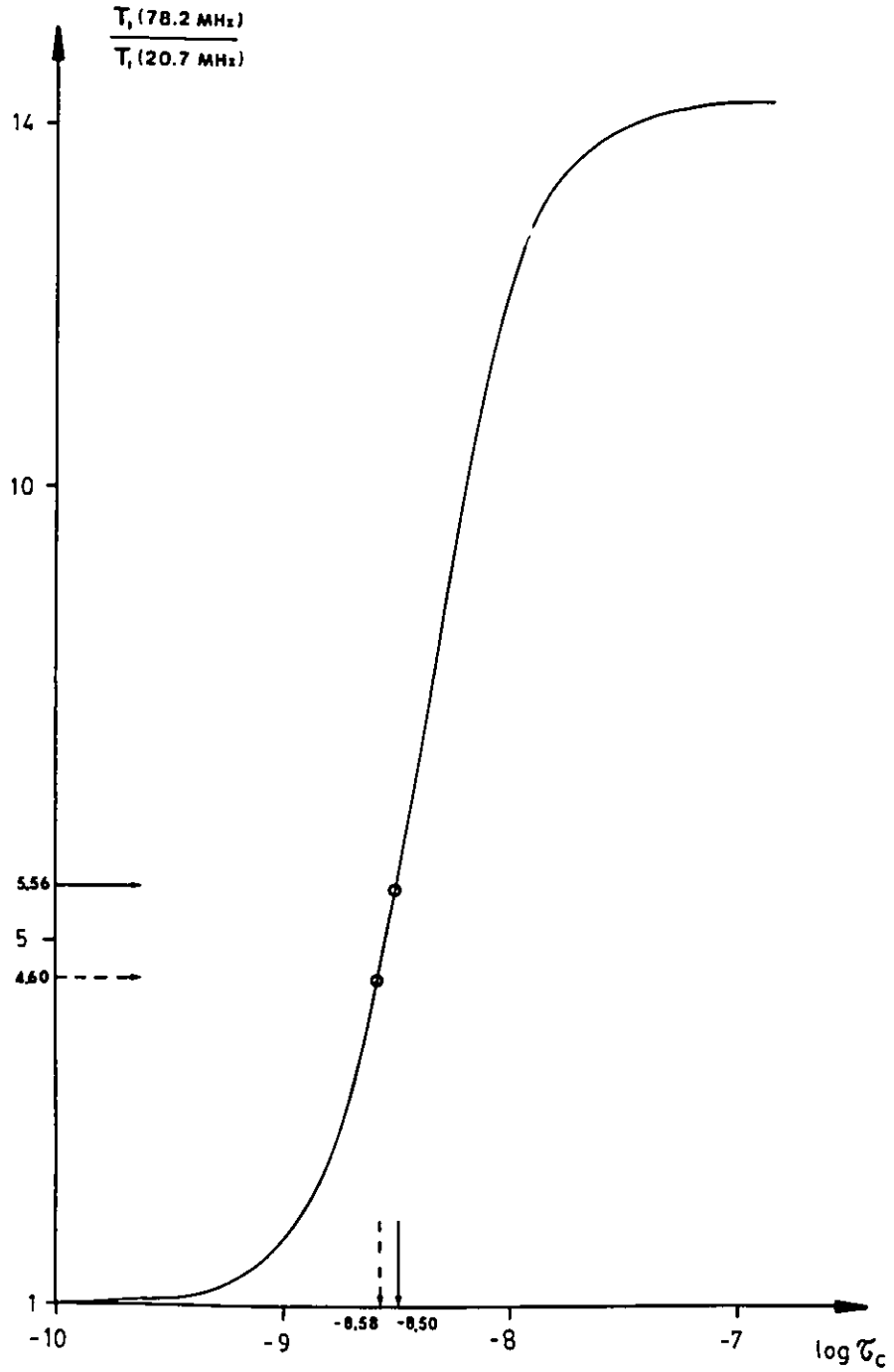

Figure 5.17: Theoretical variation of the aluminum-27 spin-lattice relaxation time ratio at two different magnetic fields (78.2 and 20.7 MHz) as a function of the correlation time τ_c. See text for the significance of the two arrows.

When the β' phosphorus-31 linewidth ratio is 5.56 (full arrows, X = 121 MHz, Y = 78 MHz), equation (5.9) was satisfied for a correlation time of 3.2 ns. Under the same conditions, the α' ^{31}P linewidth ratio was 4.60 (dotted arrows) and gave a correlation time of 2.6 ns. By varying the magnetic field (X = 81 MHz, Y = 52 MHz) and (X = 121 MHz, Y = 78 MHz), for both the α' and β' phosphates equation (5.9) yielded an average correlation time value of 2.8 $\pm$ 0.8 ns (for 6 data points).

Under these conditions (τ_c = 2.8 ns), the contribution of the spin–spin chemical shift anisotropy relaxation mechanism to the overall linewidth of each α' and β' phosphate resonance could be calculated. For the β' and α' resonances at 32, 81 and 121 MHz, a negligible linewidth contribution was calculated, as it accounted, in the worst case, for only 5% of the total linewidth. Then, for both the α' and β' phosphates, the observed true linewidths only resulted from a scalar relaxation of the second kind between ^{27}Al and ^{31}P nuclei.

In order to obtain the phosphorus-aluminum coupling constant ^2J introduced in equation (5.8), the value of the spin-lattice relaxation time of aluminum, complexed by ATP, was needed. It was calculated using ^{27}Al NMR results (see Section 9.5) which yielded a quadrupolar coupling constant of 2.6 MHz. Using this value and a correlation time of 2.8 ns, the spin-lattice relaxation times at 21, 52 and 78 MHz were 0.08 ms, 0.21 ms and 0.40 ms respectively. Using equation (5.8) an average phosphorus–aluminum coupling constant ^2J(P–Al) of 60 $\pm$ 4 Hz for the α' phosphate and 77 $\pm$ 4 Hz for the β' phosphate were calculated.

5.4 Conclusion

At pH = 7.4 ATP and aluminum formed a complex species in slow chemical exchange on the NMR time scale, giving rise to the appearance of a new set of three

resonances on the phosphorus-31 NMR spectrum. A detailed spectral study of an ATP–Aluminum spectrum permitted peak attribution for each new resonance and revealed that all three phosphates (α, β and γ) of ATP were involved in aluminum complexation, henceforth called (α', β' and γ') respectively. This result is in contrast with a previous study [20] which reported the β and γ (but not the α) phosphates of ATP as participating in aluminum complexation.

Phosphorus-31 chemical shifts of free and complexed resonances of ATP were not dependent upon aluminum concentration. A complex in fast equilibrium with free ATP was not detected, and the observed complexed species were apparently not engaged in further equilibria. Using phosphorus-31 NMR chemical shifts, it was not possible to distinguish between the free phosphate resonances of ATP and the uncomplexed phosphate resonances of the aggregate as they both had the same chemical shift.

Complexation of aluminum on each phosphate of ATP resulted in a change of their coupling constant values, which was in agreement with the general trend that coupling constants vary upon metallic complexation. In contrast, the coupling constant values for the uncomplexed phosphate of ATP were identical to the free ATP phosphates.

Measurement of the total concentration of complexed ATP was quantitative and showed the existence of a unique 4:3 ATP:Al complex present in solution over the entire range of Al/ATP ratios studied. The percentage of complexed ATP was independent of the total ATP concentration and, in this species, the three complexed resonances (α', β' and γ') were equally complexed by aluminum. The qualitative observations and quantitative measurements lead to a proposed chemical structure for the triphosphate chains of the ATP_4–Al_3 aggregate (see Figure 5.15). For stoichiometric reasons, this complex exists only as a monomeric species in solution.

For a given magnetic field strength, the complex was characterized by constant well defined α' and β' phosphorus-31 linewidth values through the complete range of ATP concentrations as well as Al/ATP ratios. The α' and β' spin-spin relaxation rates were not due to the CSA mechanism but resulted from a scalar relaxation of the second kind, due to scalar coupling between the aluminum-27 quadrupolar nucleus and the phosphorus-31 nucleus. The observed field dependence of both α' and β' phosphorus-31 spin-spin relaxation rates was indicative of an aluminum-27 spin-lattice relaxation time (T_1) which was field dependent and permitted the determination of the complex correlation time of 2.8 ns. Under these conditions, contribution of the CSA mechanism to the observed linewidths was estimated to be negligible.

Two bond phosphorus-aluminum coupling constants were calculated giving 60 Hz as the value for the coupling between the α' phosphorus and aluminum, and 77 Hz for the coupling between the β' phosphorus and aluminum.

Chapter 6

PROTON AND CARBON-13 NMR STUDIES PROBING THE GEOMETRY AND THE DYNAMICS OF ATP_4AL_3 AGGREGATES

6.1 Introduction

The advent of Fourier transformed NMR spectroscopy combined with the ease of observation of ^1H nuclei have led to numerous studies in many areas of chemistry. In a similar fashion, ^{13}C NMR spectroscopic studies [152,153] have blossomed in the past decade as a result of the availability of high field spectrometers and the existence of sophisticated pulse sequences [154] which have significantly broadened the field of application for low gamma nuclei. With such a wide choice of magnetically active nuclei [114], NMR spectroscopy has proven to be a powerful technique for determining molecular conformation [155] and solution dynamics [156,157,158]. As ^{31}P NMR was used to study the interactions and dynamics of aluminum with the triphosphate chain moiety, ^1H and ^{13}C nuclei were chosen to probe the molecular geometry and dynamics of the adenosine part of ATP.

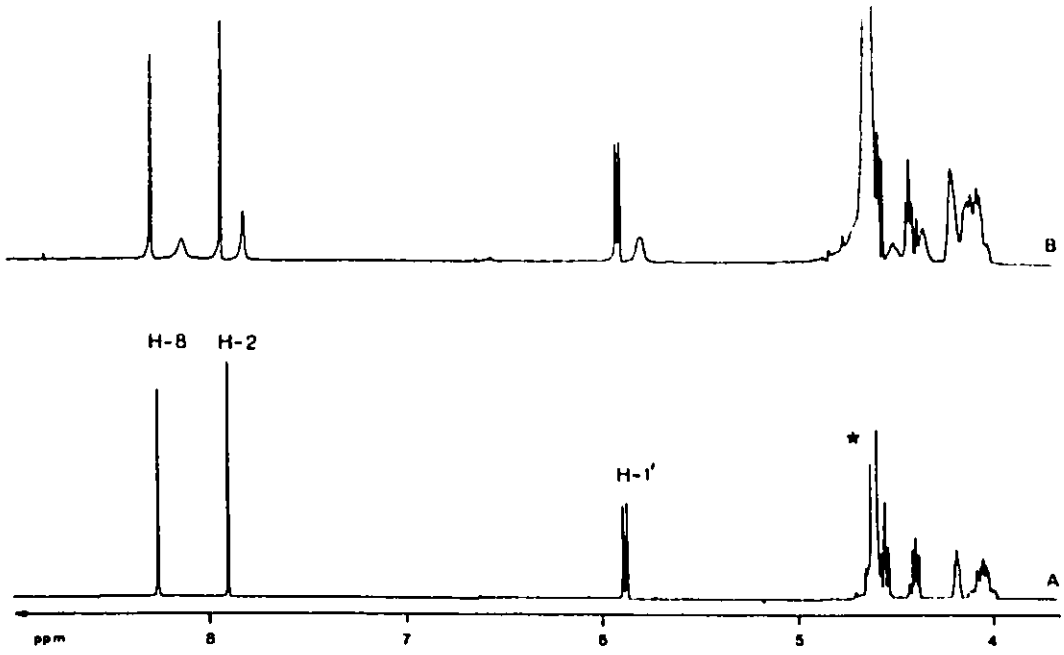

Figure 6.1: A series of ^{1}H NMR spectra of ATP–Al aqueous solutions at 300 MHz. The Al/ATP ratios were: A) 0 and B) 0.20. The instrumental conditons were as follows: spectral width of 4000 Hz, acquisition time of 1.5 sec, pulse delay of 15 sec, no line broadening. For experimental conditions see Table 6.1. (*) This resonance is due to the remaining protons of the water solvent.

In this chapter, a concentration study and spin-lattice relaxation time measurements are reported for the ATP–Al system using ^{1}H (300 MHz) and ^{13}C (75 MHz) NMR spectroscopies. The ATP concentration was 100 mM at pH = 7.4 and the Al/ATP ratio was varied from 0 to 0.75 for the ^{1}H series, and from 0 to 1.5 for the ^{13}C series.

6.2 Chemical Shifts Analysis

Spectrum A of Figure 6.1 displays the entire proton spectrum of ATP (100 mM, pH = 7.4) in D_2O solution. Two distinct regions were observed. They corresponded [159,160], on the left part of the spectrum, to the proton resonances of the adenine

base (H–8 and H–2) and the proton sugar ring (H–1′). The right part of the spectrum was composed of the sugar (H–2′, H–3′, H–4′, H–5′) and the solvent (HOD) proton resonances (see Figure 1.1 for the proton numbering of ATP). The adenine proton chemical shift values are summarized in Table 6.1 along with those of the H–1′ proton sugar ring. Spectrum B of Figure 6.1 shows a proton spectrum of an ATP solution to which aluminum was added (Al/ATP = 0.20). Upon addition of aluminum, ATP and aluminum formed complexes in slow exchange on the NMR time scale giving rise to the appearance of a new resonance for each proton of the base and sugar ring of ATP. The chemical shift values of the new proton resonances of the base and the H–1′ proton sugar ring were shifted upfield from their respective free resonance and attributed to ATP molecules involved in the ATP_4Al_3 aggregate.

The carbon-13 spectrum recorded under similar conditions exhibited some features comparable with the proton spectrum. Spectrum A of Figure 6.2 displays the entire ^{13}C spectrum of ATP in 20% D_2O solution. The left part of the spectrum is composed [161] of ^{13}C adenine resonances (C–5, C–8, C–4, C–2, C–6) while the right part of the spectrum shows the sugar ring resonances (C–3′, C–2′, C–4′, C–1′) and the C–5′ resonance of the methylene group (see Figure 1.1 for the carbon numbering of ATP). All ^{13}C chemical shift values are summarized in Table 6.2. Upon addition of aluminum to an ATP solution (see spectrum B of Figure 6.2, Al/ATP = 0.20) ATP and aluminum formed complexes in slow exchange on the NMR time scale. With results similar to the proton spectrum, a new resonance for each carbon of the adenine base and sugar ring of ATP appeared. The only exception was for the C–1′ ribose carbon which was observed as a single resonance. With the exception of the C–4′c resonance (c stands for complexed) shifted upfield from its free resonance, all the other ribose carbons were shifted downfield. In the case of the adenine car-

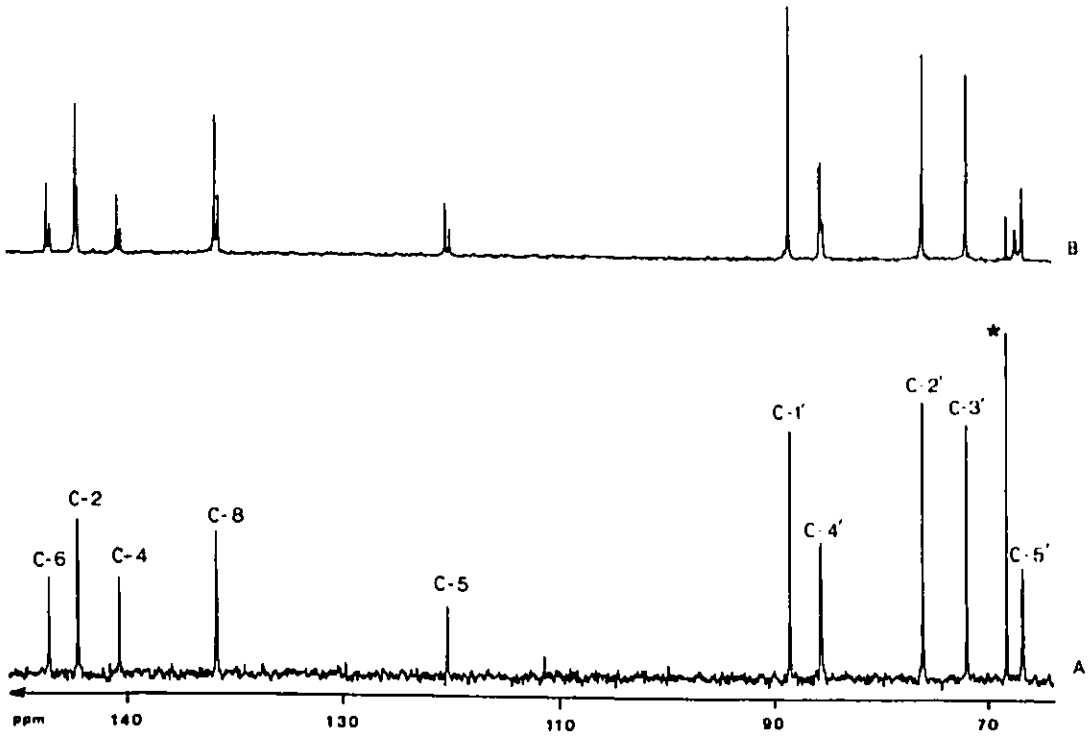

Figure 6.2: A series of proton decoupled ^{13}C NMR spectra of ATP--Al aqueous solutions at 75 MHz. The Al/ATP ratios were: A) 0 and B) 0.20. The instrumental conditions were as follows: spectral width of 9000 Hz, acquisition time of 3 sec, pulse delay of 15 sec, typically 5000 transients and 1 Hz line broadening. For experimental conditions see Table 6.2. (*) Corresponds to the resonance of dioxane used as an internal reference.

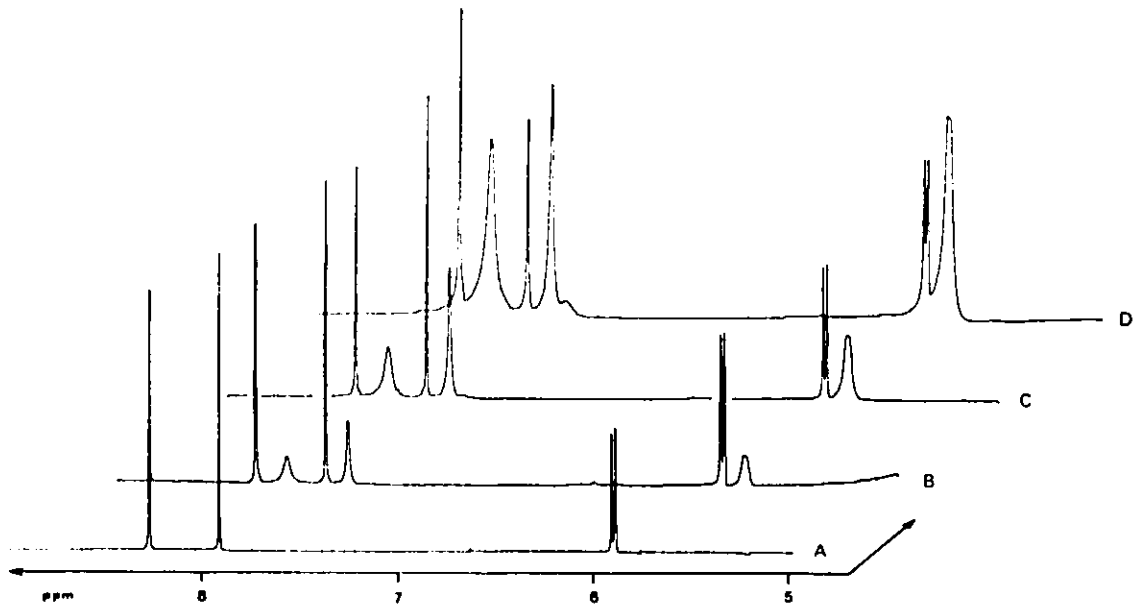

Figure 6.3: ^{1}H NMR spectral region display of the adenine and H–1′ proton resonances of ATP–Al solutions at 300 MHz. The Al/ATP ratios were: A) 0; B) 0.20; C) 0.37 and D) 0.75. The instrumental conditions were as follows: spectral width of 4000 Hz, acquisition time of 3.7 sec, pulse delay of 15 sec and no line broadening. For experimental conditions see Table 6.1.

bon resonances, like the proton resonances, they were all shifted upfield from their respective free resonances.

Figure 6.3 displays a set of proton NMR spectra for which the Al/ATP ratio varied from 0 to 0.75. The region shown focuses on the protons of the base (H–8 and H–2) and the H–1′ proton of the sugar ring as they were clearly resolved from their respective complexed resonances. As the Al/ATP ratio varied from 0 to 0.75, the proton chemical shifts of each complexed resonance were not dependent upon the aluminum concentration (see Table 6.1) and one could not detect any complex in fast equilibrium with the complexed ATP resonances (H–8c, H–2c and H–1′c) which are in slow chemical exchange with their respective free resonances (H–8, H–2 and

$\frac{Al(III)}{[ATP]}$	δ_{ppm}		δ_{ppm}		δ_{ppm}	
	H–8	H–8c	H–2	H–2c	H–1′	H–1′c
0.00	8.277 0.002		7.913 0.002		5.889 0.002	
0.37†	8.280 0.002	8.123 0.003	7.920 0.002	7.818 0.002	5.893 0.002	5.773 0.003
0.75‡	8.290 0.002	8.124 0.004	7.935 0.003	7.818 0.003	5.903 0.003	5.780 0.003
$\Delta\delta_{ppm}$ σ	0.013 0.004	≈ 0	0.022 0.005	≈ 0	0.014 0.005	≈ 0

Table 6.1: ^{1}H chemical shift values of the adenine and H–1′ resonances as a function of the Al/ATP ratio at 300 MHz. Experimental conditions were: [ATP] = 100 mM, pH = 7.4, T = 21 °C, 20% D_2O in 5 mm tube. Reported chemical shifts represent the average of at least two (†) or four (‡) measurements on different samples. Error given as 2σ.

H–1′). The free ATP resonances did not behave the same way. As the Al/ATP ratio varied from 0 to 0.75, they exhibited a constant downfield chemical shift variation (see Table 6.1), which can be observed in Figure 6.1. This suggested that the free ATP resonances were engaged in further fast equilibria. When the Al/ATP ratio was varied from 0 to 0.75, the observed chemical shift variations ($\Delta\delta$) were 5 ± 1 Hz for H–8, 7 ± 2 Hz for H–2, and 4 ± 2 for H–1′ (see Table 6.1).

For a ratio of Al/ATP = 0.75, apparently free (henceforth called "free"), ATP resonances were still observed in the proton spectrum (see spectrum D of Figure 6.3). For each set of resonances, proton integration gave a ratio of 3 (complexed) : 1

("free") proton. Analogous to the phosphorus-31 studies, the residual "free" resonances were attributed to one surface ATP molecule of the ATP_4Al_3 aggregate. The three other complexed ATP molecules of the aggregate resonated as one peak and were all shifted upfield from the proton resonance of the surface ATP molecule. From a chemical shift point of view, the chemical system under study could be described as a three site chemical exchange:

$$(ATP)_{solution} \overset{k_1}{\rightleftharpoons} (ATP)^{surface}_{aggregate} \overset{k_2}{\rightleftharpoons} (ATP)^{inside}_{aggregate}$$

$$fast \qquad\qquad slow$$

in which the free ATP molecule in solution is in rapid exchange with a surface ATP molecule of the aggregate, which is undergoing a slow exchange with the ATP molecules of the aggregate. Proton concentration studies provided an estimation of a lower limit for the rate constant as $k_1 \gg 40\ s^{-1}$ and a higher limit for the rate constant as $k_2 \ll 200\ s^{-1}$. Confirmation of this three site chemical exchange scheme, as well as the estimation of both rate constant values k_1 and k_2, was provided by phosphorus-31 spin-lattice relaxation time measurements (see Chapter 8).

Figure 6.4 displays a set of carbon-13 NMR spectra for which the Al/ATP ratio was varied from 0 to 1.5. The region shown focuses on the carbon atoms of the adenine base (C-3, C-8, C-4, C-2 and C-6). As the Al/ATP ratio was increased from 0 to 1.5, the chemical shift of each complexed resonance, reported in Table 6.2, was not dependent upon the aluminum concentration. The ^{31}P, ^{1}H and ^{13}C NMR results converge toward the same conclusion: one could not detect any complex in fast equilibrium, on the NMR time scale, with the complexed ATP resonances which are in slow chemical exchange with their respective "free" resonances. The free carbon-13 ATP resonances behaved in a similar fashion to the phosphorus-31 free resonances.

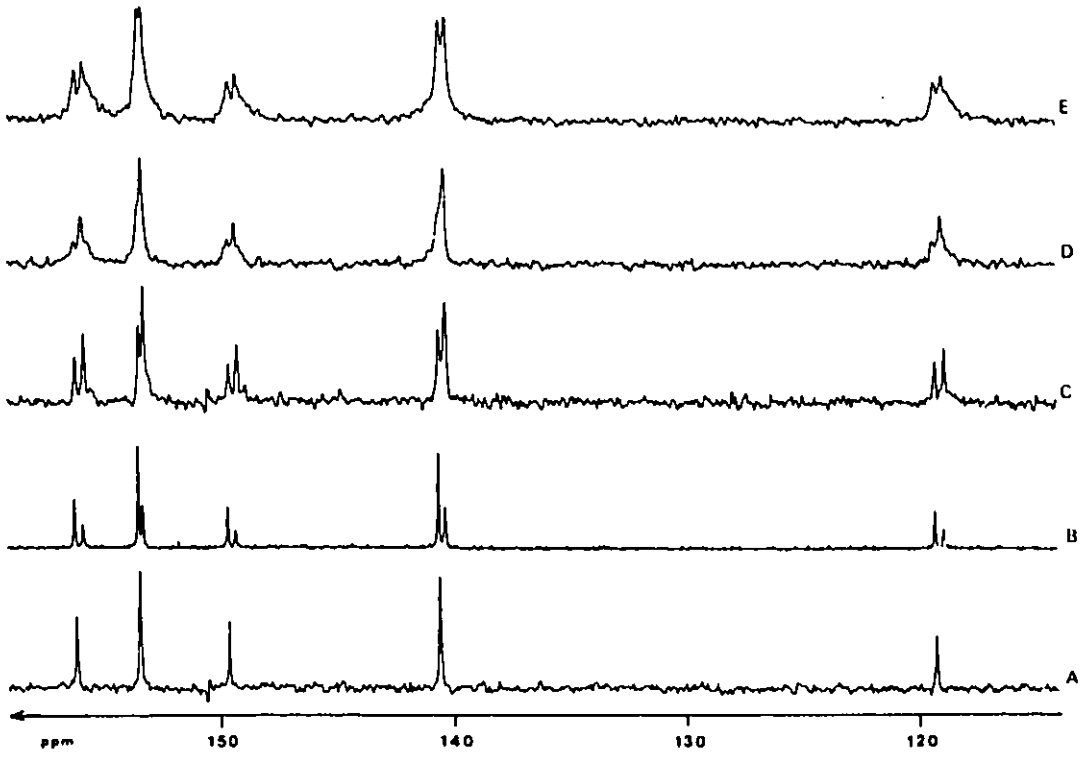

Figure 6.4: ^{13}C NMR spectral region display of the adenine resonances of ATP-Al solutions at 75 MHz. The Al/ATP ratios were: A) 0; B) 0.20; C) 0.40; D) 1.0 and E) 1.5. The instrumental conditions were as follows: spectral width of 4000 Hz, acquisition time of 3.7 sec, pulse delay of 15 sec, 5000 to 10000 transients, 3 Hz line broadening and full proton decoupling. For experimental conditions see Table 6.2.

$\frac{Al(III)}{[ATP]}$	δ_{ppm}		δ_{ppm}		δ_{ppm}		δ_{ppm}		δ_{ppm}	
	CH_2	CH_{2c}	C–3′	C–3′c	C–2′	C–2′c	C–4′	C–4′c	C–1′	
0.00	65.91		71.07		75.17		84.71		87.56†	
0.20	65.91	66.55	71.05	71.14	75.15	75.23	84.68	84.44	87.60†	
0.40	65.91	66.53	71.09	71.14	75.16	75.25	‡	‡	87.59†	
1.0	65.92	66.55	‡	71.12	75.18	‡	‡	84.45	87.65†	
1.5	‡	66.51	‡	‡	75.15	‡	‡	84.47	87.67†	
$\hat{\delta}_{ppm}$	65.91	66.54	71.06	71.13	75.15	75.24	84.69	84.45	87.61	
σ	0.01	0.02	0.02	0.01	0.01	0.01	0.02	0.02	0.04	

$\frac{Al(III)}{[ATP]}$	C–5	C–5c	C–8	C–8c	C–4	C–4c	C–2	C–2c	C–6	C–6c
0.00	119.20		140.58		149.59		153.40		156.14	
0.20	119.24	118.87	140.61	140.32	149.64	149.29	153.45	153.27	156.18	155.84
0.40	119.20	118.79	140.57	140.28	149.58	149.21	153.40	153.21	156.15	155.77
1.0	119.24	118.94	‡	140.36	149.61	149.32	153.46	153.33	156.14	155.86
1.5	119.21	118.90	140.61	140.33	149.63	149.32	153.48	153.34	156.20	155.87
$\hat{\delta}_{ppm}$	119.22	118.88	140.59	140.32	149.61	149.29	153.44	153.29	156.16	155.84
σ	0.02	0.06	0.02	0.03	0.02	0.04	0.03	0.05	0.02	0.04

Table 6.2: ATP ^{13}C chemical shift values as a function of the Al/ATP ratio at 75 MHz. Experimental conditions were: [ATP] = 100 mM, pH = 7.4, T = 21 °C, 20% D_2O in 10 mm tube. (‡) The chemical shift value could not be measured accurately because the resonance was not detected or resulted in a too severe overlap. (†) Only one resonance observed. One $\hat{\sigma} = 0.03$ for 19 carbons.

No chemical shift variations were observed as the Al/ATP ratio was varied from 0 to 1.5 (see Table 6.2). Both ^{31}P and ^{13}C NMR spectroscopies were unable to detect that the free ATP resonances were engaged in a further fast equilibrium, as shown by ^{1}H NMR, because the chemical shift difference between the two sites was probably too small to be observed. For Al/ATP $\geq$ 0.75 and like the ^{1}H and ^{31}P NMR spectra, "free" ATP resonances were still observed in the ^{13}C spectra, corresponding to the resonances of the surface ATP molecule of the aggregate. For Al/ATP = 1.0 and 1.5 (see Figure 6.4) a new, broad resonance appeared, located at the base of each carbon resonance of the adenine base. This suggested that, once the ATP_4Al_3 aggregate was formed, a further increase in the aluminum concentration led to the fixation of aluminum nuclei on the adenine base of ATP. Aluminum complexation to the adenine base of ATP was confirmed and discussed in more detail using ^{27}Al NMR studies (see Section 9.5).

^{1}H, ^{13}C and ^{31}P NMR have been extensively used to study molecular conformation [155] and aggregation of bases, nucleosides, and nucleotides by means of relaxation techniques [162,163,164,166,167], NOE measurements [164], and chemical shift analysis [164,165,94,166,167]. A closer examination of the observed proton and carbon chemical shifts gave further insight into the geometric arrangements of the adenine bases in the aggregate. As mentioned earlier, the chemical shifts of the complexed proton and carbon adenine resonances were all shifted upfield. Upfield chemical shifts for the proton or carbon atoms of the base is characteristic of molecular aggregation in which the stacking of the bases prevails [165]. The ring current magnetic anisotropy effects have been shown to represent the main factor responsible for the observed ^{1}H and ^{13}C upfield chemical shifts in purine [165].

Contrary to these results, the adenine proton resonances of the surface ATP

molecule of the aggregate were shifted downfield from their respective free resonances in solution (see Table 6.1). Thus, for the surface ATP molecule of the aggregate, the observed downfield shift suggests that this adenine base is oriented in a totally different way from the three other inner bases of the aggregate, so as not to experience a stacking effect.

In a purine dimer, the bases were shown to be stacked one on top of the other [165]. The resulting experimental dimerization and trimerization shifts were 1.05 and 1.53 ppm for the C–8 carbon nucleus and 0.46 and 1.00 ppm for the H–8 proton nucleus respectively [165]. In the present study, the observed upfield carbon and proton chemical shifts of the bases were much smaller, as they amounted to a maximum value of 0.27 ppm in the case of the C–8 carbon and 0.15 ppm for the H–8 proton. These experimental results suggest a different stacking geometry for the three inner bases of the aggregate.

The formation of the ATP_4Al_3 aggregate begins probably by the assembly of three ATP–Al monomers, in which the aluminum cation is complexed by the ATP triphosphate chain. The stacking of three monomeric units results in the formation of an aluminum-triphosphate chain sandwich-like complex. The hexacoordinated complexed aluminum cation certainly necessitates a special arrangement of the triphosphate chains which differs from one chain to another. Thus, at the site of complexation, the different arrangements of the triphosphate chains dictate a different spatial location for each adenosine base.

Inspection of molecular models of ATP gives a preferential overall orientation for the three bases of the aggregate. A molecular symmetry axis running through the stacking of the three triphosphate chains complexing two aluminum cations can be defined (see Figure 6.5). Then, looking down the axis, each adenosine base is partially

stacked and skewed by an angle of about 120° from the other bases (see Figure 6.6). The base stacking geometry of the aggregate is supported by the observed upfield proton chemical shifts of the bases. As the base stacking is less intense in the aggregate, the upfield shifts were smaller in magnitude than those observed for a purine or an ATP dimer [165,94].

The surface ATP molecule of the aggregate behaves as a distinct ATP molecule as confirmed by ^{1}H, ^{13}C and ^{31}P NMR results. For Al/ATP $\geq$ 0.75 all three nuclei showed the appearance of "free" ATP resonances in their respective NMR spectra. From ^{31}P NMR it can be concluded that the triphosphate chain of the surface ATP molecule is only loosely bound to the aluminum cation, probably through water molecules creating an outer sphere complex. ^{1}H and ^{13}C NMR spectra revealed that the base is definitely not stacked or skewed 120° from the previous base. Both nuclei rather suggest that the base of the surface ATP molecule stays away from any other base so as to experience little or no stacking effect. Inspection of a molecular model suggests that the surface ATP molecule sits on the top of the aggregate with its sugar and base moieties pointing away from other bases (see Figure 6.7).

6.3 Spin-Lattice Relaxation Analysis

Examination of the ^{1}H and ^{13}C chemical shifts of the free and complexed resonances of ATP enabled the deduction of an overall structure for the adenine bases of the aggregate. However, no information concerning their relative mobility in relation to the triphosphate chain was known.

The sensitivity of relaxation time measurements upon a change in molecular dynamics have already been used to study the aggregation phenomenon of ATP [162,163,106]. The percentage of ATP dimer in solution increases with the ATP con-

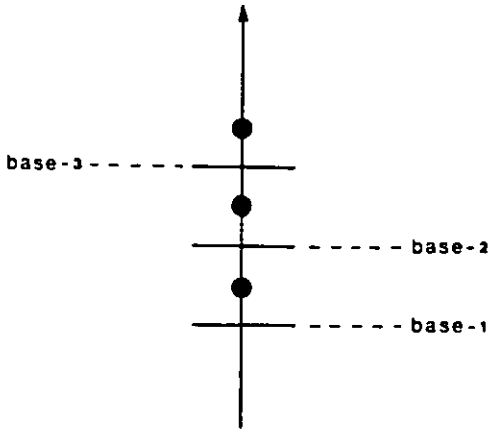

Figure 6.5: Schematic representation of the three aggregated ATP molecules with the molecular axis running through the triphosphate side chains.

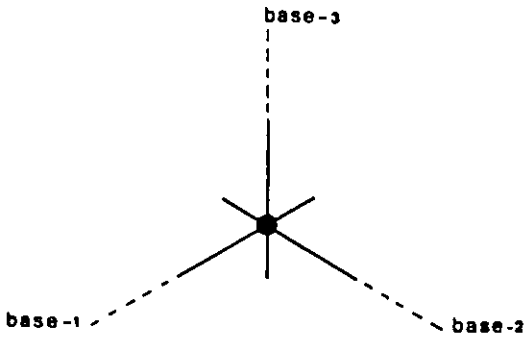

Figure 6.6: Schematic representation of the three aggregated ATP molecules looking down the molecular axis difined in Figure 6.5.

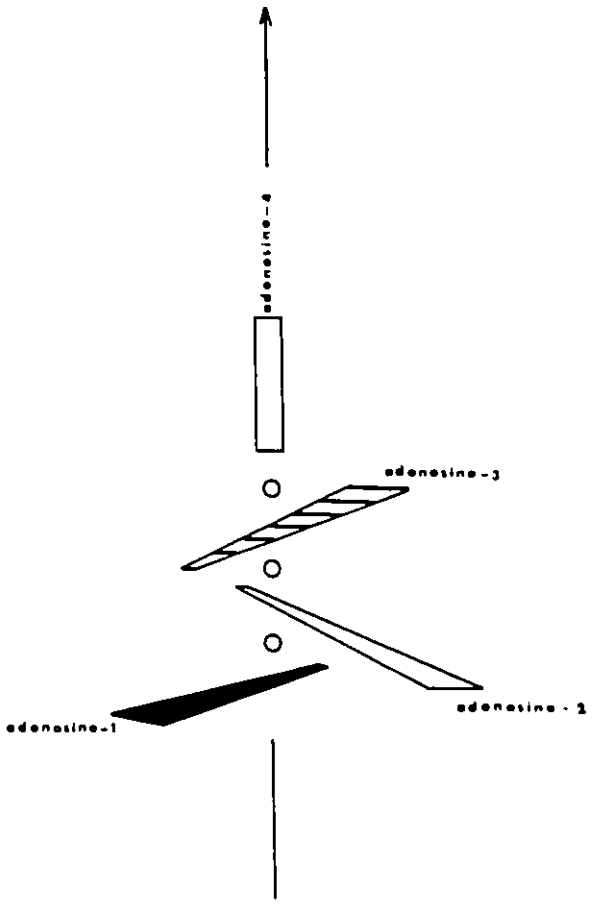

Figure 6.7: Three dimensional schematic representation of the ATP_4Al_3 molecular aggregate. (o) represent an aluminum cation.

centration [94] and resulted in a decrease of the overall spin-lattice relaxation time. In a dimer or trimer species, the adenine bases are stacked upon each other [165,131] and this reduction of mobility in solution, and the concomitant increase in the proton correlation time, had the effect of decreasing the T_1 values. Proton and carbon spin-lattice measurements were performed on the ATP–Al system and gave a better insight into the molecular dynamics of the adenine bases of the aggregate.

Figure 6.8 displays an example of a ^{1}H inversion recovery experiment for an Al/ATP ratio of 0.37 showing the free and complexed H–8, H–2 and H–1′ protons of ATP. Qualitatively, the relaxation behavior of the free and complexed proton resonances was similar. Table 6.3 sums up the results obtained for Al/ATP = 0, 0.37 and 0.75. Each free proton (H–2, H–8 and H–1′) was characterized by a unique relaxation rate. For the same type of proton, the relaxation rate values of a free ATP proton (Al/ATP = 0), a surface ATP proton and a complexed ATP proton (Al/ATP = 0.75) were all identical. For example, R(free) = 0.47 ± 0.03 sec^{-1}, R(surface) = 0.46 ± 0.02 sec^{-1} and R(complexed) = 0.50 ± 0.02 sec^{-1} for the H–1′ proton (see Table 6.3).

Although the three relaxation rates were identical for the same type of proton, it should be pointed out that they characterize three different chemical sites. Table 6.3 also shows that all the relaxation rate values were independent of the relative population of the three different chemically exchanging sites introduced earlier (see page 115). The relaxation rate values were not affected by the exchange and, the proton spin-lattice relaxation times of the surface and complexed ATP molecules of the aggregate were equal to the T_1 of a free ATP molecule in solution. This suggests that the mobility of the sugar and base moieties of the aggregate is similar to a free ATP molecule in solution. These findings support the ATP_4Al_3 structure discussed previously (using chemical shift studies) in which the internal adenosine molecules

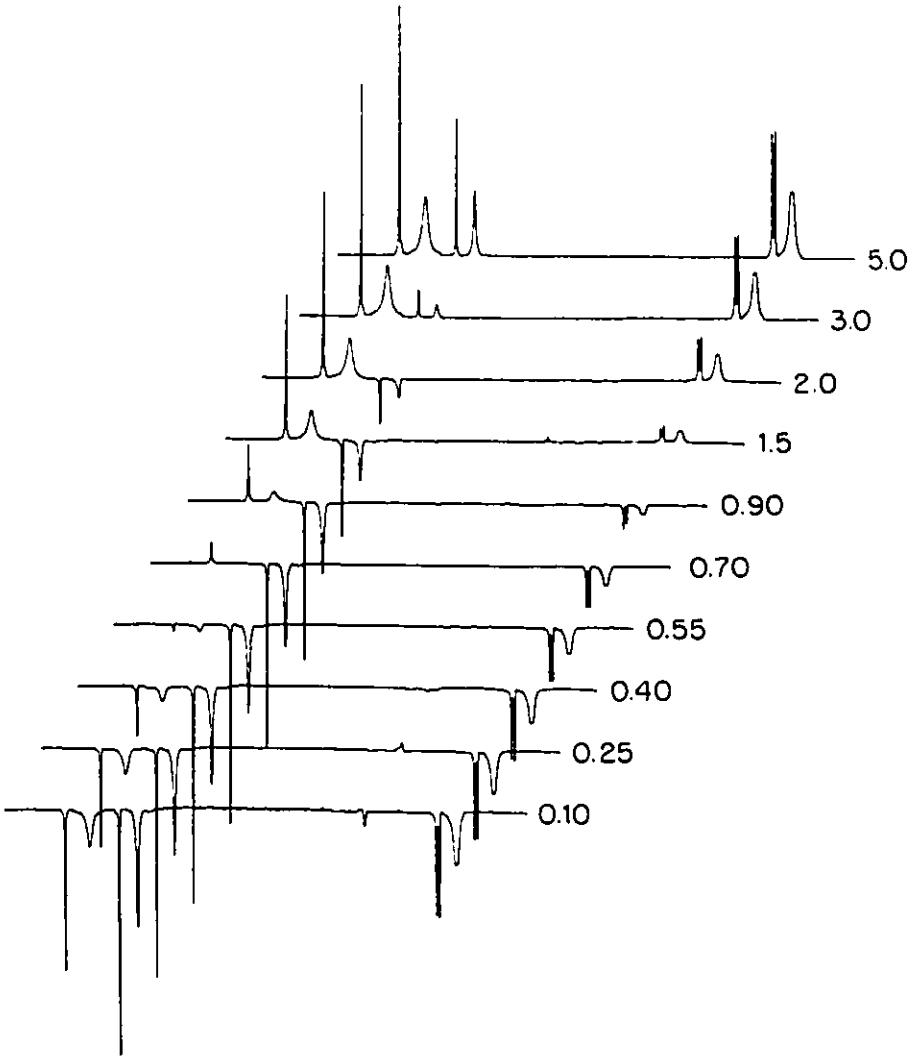

Figure 6.8: Spectral region display of a ^{1}H inversion recovery experiment of the adenine and H–1′ proton resonances of an Al/ATP = 0.37 solution at 300 MHz. For experimental conditions see Table 6.3. Instrumental conditions were: sweep width of 4000 Hz, acquisition time of 2 sec, pulse delay of 20 sec, and 32 transients. Recovery times in seconds are shown near each spectrum.

$\frac{Al(III)}{[ATP]}$	R_1 (sec^{-1})		R_1 (sec^{-1})		R_1 (sec^{-1})	
	H-8	H-8c	H-2	H-2c	H-1′	H-1′c
0.00	0.67		0.21		0.47	
	0.03		0.03		0.03	
0.37†	0.70	0.76	0.23	0.22	0.48	0.49
	0.04	0.08	0.02	0.02	0.01	0.03
0.75‡	0.70	0.76	0.23	0.23	0.46	0.50
	0.01	0.02	0.02	0.02	0.02	0.02
$\hat{R}_1$ (sec^{-1})	0.70	0.76	0.23	0.22	0.47	0.49
2σ	0.04	0.04	0.03	0.02	0.02	0.03

Table 6.3: ^{1}H relaxation rate values of the adenine and H-1′ sugar resonances of ATP as a function of the Al/ATP ratio at 300 MHz. Experimental conditions were: [ATP] = 100 mM, pH = 7.4, T = 21 °C, 20% D_2O in 5 mm tube. Reported relaxation rates represent the average of at least two (†) or four (‡) measurements on different samples.

were skewed 120° from one another, allowing them motional freedom.

Qualitative information about the mobility of the adenosine molecules of the aggregate, using ^{1}H relaxation measurements, was confirmed by the analysis of ^{13}C spin-lattice relaxation data which gave the correlation time of the adenosine molecules involved in the aggregate.

Figure 6.9 and Figure 6.10 display an inversion recovery and NOE experiment respectively for the resolved, free and complexed C-2, C-8 and C-5′ carbon resonances of ATP, for an Al/ATP ratio of 0.40. As observed in the case of ^{1}H, for each type of carbon, the relaxation of the free resonances appears similar to their respective

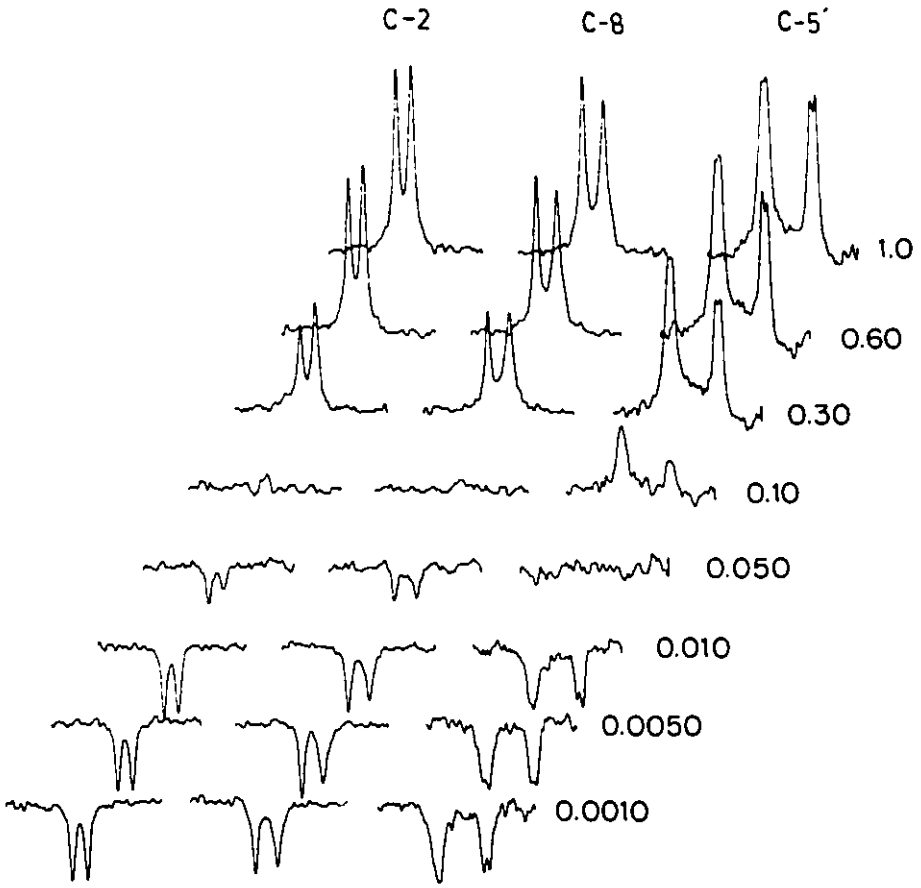

Figure 6.9: Spectral region display of a ^{13}C inversion recovery experiment of the free and complexed C-2, C-8 and C-5′ ATP carbon resonances of an Al/ATP = 0.40 solution at 75 MHz. For experimental conditions see Table 6.4. Instrumental conditions were: sweep width of 2500 Hz, acquisition time of 1.5 sec, full proton decoupling and 2500 transients. Recovery times in seconds are shown near each spectrum.

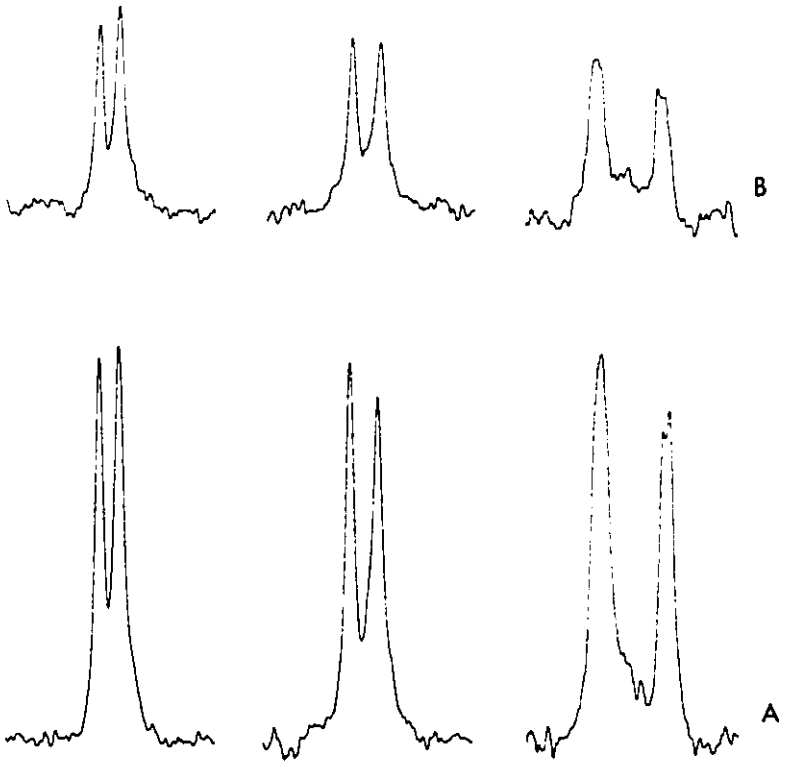

Figure 6.10: Spectral region display of the proton decoupled ^{13}C Nuclear Overhauser Effects of the free and complexed C–2, C–8 and C–5′ ATP carbon resonances of an Al/ATP = 0.40 solution at 75 MHz. For experimental conditions see Table 6.4. Instrumental conditions were: sweep width of 4000 Hz, acquisition time of 1.5 sec, pulse delay of 2 sec and 2500 transients. For spectrum (A) full proton decoupling, (B) proton decoupling during the acquisition only.

Al(III)/[ATP]		C–2	C–2c	C–8	C–8c	C–5′	C–5′c
	$T_{1,obs}$ (sec)	0.42		0.40		0.24	
	σ	0.03		0.03		0.02	
0.00	η_{obs}	1.20		1.45		1.73	
	σ	0.05		0.06		0.08	
	τ_c (ps)	67 ± 8		86 ± 10		85 ± 11	
	$T_{1,obs}$ (sec)	0.33	0.23	0.29	0.20	0.164	0.124
	σ	0.03	0.01	0.02	0.03	0.006	0.004
0.40	η_{obs}	1.12	0.96	1.12	0.90	1.44	1.35
	σ	0.07	0.06	0.07	0.05	0.08	0.10
	τ_c (ps)	74 ± 11	92 ± 10	84 ± 11	100 ± 20	105 ± 10	75 ± 10

Table 6.4: ^{13}C spin-lattice relaxation times, Nuclear Overhauser Effects and correlation time values of the C–2, C–8 and C–5′ resonances of ATP–Al solutions at 75 MHz. See text for the calculation of each correlation time. Experimental conditions were: [ATP] = 100 mM, pH = 7.4, T = 21 °C, 20% D_2O in 10 mm tube.

complexed resonances. Table 6.4 summarizes the spin-lattice relaxation times and NOE factors obtained for Al/ATP = 0 and 0.40. From this table, a general trend was observed for each type of carbon resonance. The T_1 value of the free ATP carbon nuclei was longer than the T_1 value of the "free" carbon nuclei (representing a mixture of free ATP carbon nuclei and surface ATP carbon nuclei of the aggregate), which was longer than the T_1 value of the carbon nuclei at the inside of the aggregate:

$$T_1(free) > T_1(\text{“}free\text{”}) > T_1(inside)$$

Following the three site chemical exchange model introduced earlier, the free ATP

carbon nuclei are in fast exchange (on the T_1 NMR time scale) with the surface ATP carbon nuclei of the aggregate. Therefore the observed T_1 value of the "free" carbon resonances represent their average values. The second chemical exchange involves the surface ATP carbon nuclei of the aggregate which are in slow chemical exchange (on the T_1 NMR time scale) with the ATP carbon nuclei located at the inside of the aggregate. The exchange contribution to the observed carbon T_1 values at the inside of the aggregate can be expressed as (see Section 2.3.4.b):

$$\frac{1}{T_{1,obs}} = \frac{1}{T_{1,inside}} + k_2 x_B \tag{6.1}$$

in which $x_B = 0.25$ represents the molar fraction of the surface ATP molecules. The rate constant $k_2 = 0.8 \pm 0.2\ s^{-1}$ was determined by two-dimensional exchange NMR (see Chapter 7). Then, using the relaxation data from Table 6.4 it can be shown that chemical exchange does not contribute by more than 2 to 4% of the observed relaxation rates. As a result, the effects of chemical exchange can be safely ignored in the following discussions.

Analysis of NOE and relaxation data of the carbon resonances arising from the inside ATP molecules of the aggregate (C–2c, C–8c and C–5′c) require that internal motion of the base and of the CH_2 group, coupled with the isotropic rotational reorientation of the aggregate, must be considered. The case of anisotropic rotational reorientation has been treated theoretically [140] and general expressions for the NOE and carbon-proton dipolar relaxation were available. For a CH_2 rotating group, with one degree of internal motion, attached to a molecule undergoing isotropic reorientation, with τ_R and τ_G being the correlation times for over-all reorientation and internal motion respectively, the NOE factor (η_{max}) and the dipolar carbon-

proton spin-lattice relaxation time (T_1^{DD}) are given by:

$$\frac{1}{T_1^{DD}} = \frac{A}{T_{1R}} + \frac{B}{T_{1B}} + \frac{C}{T_{1C}} \tag{6.2}$$

$$\eta_{max} = \frac{\gamma_H}{\gamma_C} \frac{A\phi_R + B\phi_B + C\phi_C}{A\chi_R + B\chi_B + C\chi_C} \tag{6.3}$$

with

$$\frac{1}{T_{1j}} = N\left(\frac{1}{10}\frac{\hbar^2\gamma_H^2\gamma_C^2}{r^6}\right)\chi_j$$

$$\chi_j = \frac{\tau_j}{1+(\omega_H-\omega_C)^2\tau_j^2} + \frac{3\tau_j}{1+\omega_C^2\tau_j^2} + \frac{6\tau_j}{1+(\omega_H+\omega_C)^2\tau_j^2}$$

$$\phi_j = \frac{6\tau_j}{1+(\omega_H+\omega_C)^2\tau_j^2} - \frac{\tau_j}{1+(\omega_H-\omega_C)^2\tau_j^2}$$

$$\tau_B^{-1} = \tau_R^{-1} + (6\tau_G)^{-1} \qquad \tau_C^{-1} = \tau_R^{-1} + 2(3\tau_G)^{-1}$$

$$A = \frac{1}{4}(3\cos^2\theta - 1)^2 \qquad B = \frac{3}{4}\sin^2 2\theta \qquad C = \frac{3}{4}\sin^4\theta$$

in which N represents the number of protons contributing to relaxation and θ the angle between the C–H vector and the axis of internal reorientation.

Figure 6.11 and 6.12 show the variations of the T_1^{DD} and η_{max} values with the internal correlation time τ_G for an isotropic reorientational correlation time of 2.8 ns. For $\tau_G \geq \tau_R$, that is for internal motion slower than the isotropic reorientation, the dipolar carbon relaxation time is not sensitive to internal motion. In this case, the T_1^{DD} value corresponds to the isotropic reorientation model. However, for internal motion faster than the isotropic reorientation, $\tau_G \leq \tau_R$, the T_1^{DD} increases gradually as it becomes sensitive to internal motion (see Figure 6.11). For internal motion in the range of $10^{-12} \leq \tau_G \leq 10^{-8}$ the bell shaped NOE factor evolves between $0.35 \leq \eta_{max} \leq 0.25$ and reaches a maximum value of 1.38 for an internal motion of

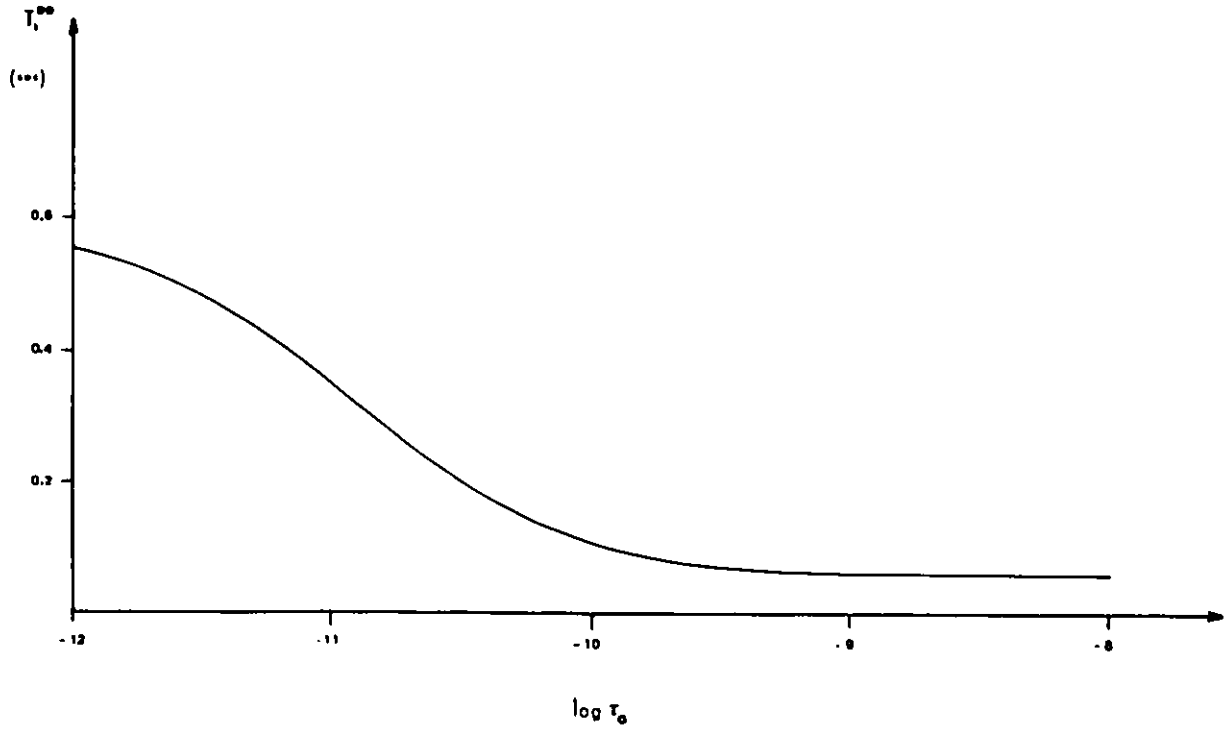

Figure 6.11: Plot of the dipolar ^{13}C spin-lattice relaxation time (T_1^{DD}) of a tetrahedral CH_2 group versus the logarithm of the internal rotational correlation time τ_G. The group is undergoing internal rotation while attached to a molecule with an isotropic rotational reorientation of $\tau_R = 2.8$ ns. Equation (6.2) was used for the simulation.

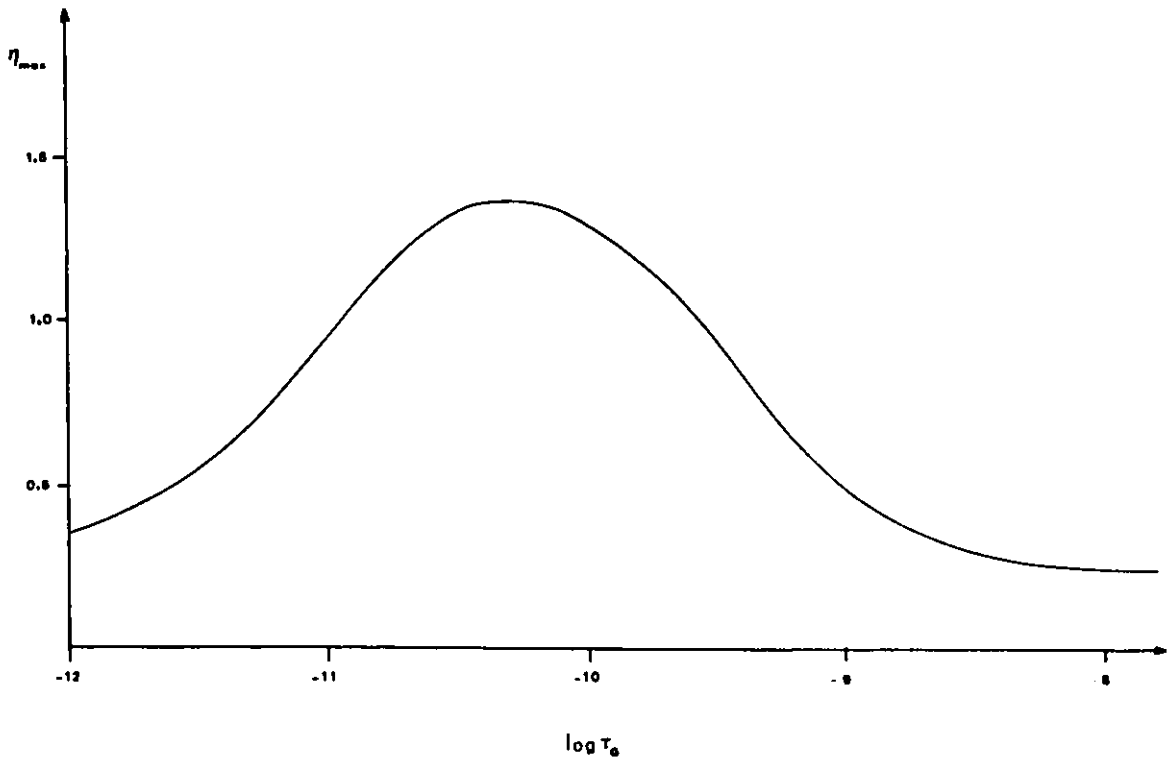

Figure 6.12: Plot of the ^{13}C–$\{^1H\}$ Nuclear Overhauser Effect (η_{max}) for pure dipolar C–H relaxation versus the logarithm of the internal rotational correlation time τ_{c_j}. The group is undergoing internal rotation while attached to a molecule with an isotropic rotational reorientation of τ_R = 2.8 ns. Equation (6.3) was used for the simulation.

50 ps. However, for an isotropic reorientation model (no internal motion, $\tau_G > 10^{-8}$), the maximum theoretical NOE value is 0.25 (see Figure 6.12).

The CH_2 group, located at the inside of the aggregate had an experimental NOE value of 1.35, which indicated that the CH_2 group undergoes internal rotation around the PO-CH_2 bond. The observed NOE and T_1 values are related to equations (6.2) and (6.3) by the following equation:

$$T_{1,obs} = T_1^{DD} \frac{\eta_{obs}}{\eta_{max}} \tag{6.4}$$

Using equations (6.2)(6.3) and (6.4), as well as the relaxation and NOE data of Table 6.4, a unique solution was found for an internal rotational correlation time of 75 $\pm$ 10 ps.

For the C-2c and C-8c carbons of the inside adenine bases of the aggregate, rotation about the PO-CH_2, CH_2-(C-4′) and the glycosidic (C-1′)-(N-9) bonds represent three degrees of internal rotational motion and equations (6.2) and (6.3) do not properly describe the dynamics of the bases. However, for an over-all reorientation much slower than the segmental internal motions, which prevails in this study since τ_R(aggregate) $\approx$ 40 $\tau_G(CH_2)$, theoretical considerations and experimental results on polystyrene solutions showed that the carbon-13 T_1 values were independent of τ_R [168]. The solution dynamics may be analyzed using a simple isotropic model and, for the C-2c and C-8c carbon nuclei, the carbon correlation time was calculated using:

$$\frac{1}{T_1^{DD}} = N \left(\frac{\hbar^2 \gamma_H^2 \gamma_C^2}{r^6} \right) \tau_c \tag{6.5}$$

with

$$T_{1,obs} = T_1^{DD} \frac{\eta_{obs}}{1.988} \tag{6.6}$$

The "free" carbon resonances (C-2 and C-8) represented a mixture of free and surface ATP resonances, as were their relaxation data. For Al/ATP = 0.40, the "free" NMR signal was composed of 80% free ATP and 20% arising from the surface ATP molecules of the aggregate. The previous discussions, concerning the degrees of motion, also apply to the surface ATP molecules and, as a result, relaxation and NOE data were analyzed using an isotropic model (see equation (6.5) and (6.6)).

Finally, the T_1 of the "free" CH_2 carbon resonance is predominantly (80%) governed by the T_1 of the free ATP molecules. As a result, the correlation time was calculated by assuming an isotropic reorientational model (see equation (6.5) and (6.6)). Table 6.4 summarizes the results for each carbon atom and shows that the "free", complexed and free ATP carbon atoms have similar correlation time values. The averaged correlation time of 89 $\pm$ 10 ps for the ATP carbon atoms located at the inside of the aggregate was similar to the correlation time of a free ATP molecule in solution (72 ps). These results show that in the aggregate, the adenosine bases undergo fast rotational motion. This result supports the aggregate structure proposed earlier, based on ^1H and ^{13}C chemical shifts. The internal bases, skewed by about 120° from each other, do not experience steric hindrance factors (which would lead to an increase in the rotational correlation time) as they are free for rotational motion in the aggregate. However, the observed ^1H and ^{13}C chemical shifts, given by the trace of the anisotropic chemical shift tensor, were sensitive to the overall stacking geometry of the adenosine molecules.

6.4 Conclusion

In a concentration study, the examination of ^1H chemical shifts of the "free" and complexed resonances of ATP lead to the conclusion that the chemical system could

be described as a three site chemical exchange. The free ATP molecule in solution is in rapid exchange with a surface ATP molecule of the aggregate, the latter being in slow exchange with an aggregated ATP molecule. Both ^{1}H and ^{13}C chemical shifts suggested that each aggregated adenine base was partially stacked and skewed from the other bases. Contrary to this, the surface ATP molecule has a distinct spacial arrangement from the inner bases of the aggregate. The overall geometry of the complex is a helix-like arrangement of bases with the surface ATP molecule sitting on the top of the aggregate, its adenine base pointing away from the other three inner bases. The overall complex geometry allows for motional freedom of the bases (see Figure 6.7). Indeed, ^{1}H and ^{13}C relaxation experiments were in agreement with the proposed overall structure of the aggregate as they revealed that the adenosine molecules were undergoing fast internal motion coupled with the slow overall reorientation of the whole aggregate.

Chapter 7

INVESTIGATION OF CHEMICAL EXCHANGE PROCESSES USING TWO-DIMENSIONAL NMR SPECTROSCOPY

7.1 General Concepts in Two-Dimensional NMR Spectroscopy

The concepts involved in a two-dimensional NMR (2D NMR) spectroscopy experiment were first described in 1971 [169], but it was not until 1976 that the first 2D spectra were published [170]. As an introduction to 2D NMR experiments [173,180,181,182], the basic fundamental concepts differing between one-dimensional and two-dimensional NMR will be presented.

In one-dimensional NMR spectroscopy [154] the basic pulse sequence is described in Figure 7.1. In this simple experiment the spin system is prepared during a time PD, perturbed by a radio frequency pulse, allowing the transverse magnetization to be recorded during the detection period t_2.

In a two-dimensional experiment [170] there is an additional independent time

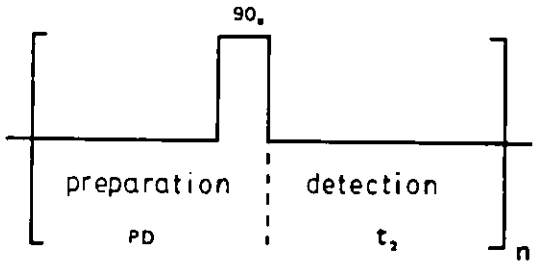

Figure 7.1: Basic one-dimensional pulse sequence scheme widely used in "routine" NMR spectroscopy. It involves only two successive time periods: the preparation and the detection period during which the transverse magnetization is recorded.

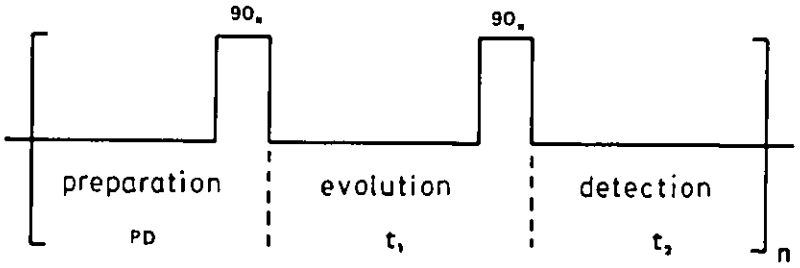

Figure 7.2: Basic two-dimensional pluse sequence scheme for the homonuclear chemical shift correlation (COSY) experiment. See text for a detailed description of the pulse sequence.

variable t_1 in the basic pulse sequence presented in Figure 7.2. A two-dimensional experiment consists of acquiring a series of n Free Induction Decays (FIDs), each FID differing from the previous one by a constant incremental value t_1, called the evolution period. Two-dimensional spectroscopy is based on the main principle that nuclear spins observed during the detection period t_2, have a memory of what happened during the evolution period t_1. In a 2D experiment, the only length of time which varies from one FID to another is the evolution time period t_1. It creates a nuclear spin history as it affects the phase and the amplitude of the magnetization detected

during the time t_2.

The classical description of a two-dimensional experiment [173] given below gives more insight into what is happening physically to a set of isolated non-coupled spin systems. The basic 2D pulse sequence used in the following treatment is given in Figure 7.2 and was the first 2D homonuclear chemical shift correlation experiment proposed by Jeener [169,170]. The preparation period consists of a time long enough, compared with the spin-lattice relaxation time T_1, for the macroscopic magnetization to be at its equilibrium value M_0. After the preparation period, the first non-selective 90°_x pulse applied to the spin system in equilibrium creates a transverse magnetization M_{xy}. During the evolution period t_1, the transverse magnetization is labelled with its own characteristic angular frequency Ω_1 in the rotating frame of reference. This period is ended by a second non selective 90°_x pulse, called the mixing pulse because it allows the transfer of information (like spin-spin coupling, NOE or chemical exchange) between related spins. Finally, transverse magnetization components are recorded as a function of the time variable t_2. If the phase of the transverse magnetization is monitored during the detection period t_2, as a function of the evolution time t_1, the time domain signal $S(t_1, t_2)$ using quadrature phase detection will be given by:

$$S(t_1, t_2) = M_0 \exp(i\Omega_1 t_1) \exp(-t_1/T_2) \exp(i\Omega_2 t_2) \exp(-t_2/T_2) \qquad (7.1)$$

The two terms $\exp(i\Omega_1 t_1)$ and $\exp(i\Omega_2 t_2)$ express the phase dependence of the signal on the two domains t_1 and t_2 while relaxation during evolution and detection is expressed by the relaxation rate $1/T_2$.

After the first complex Fourier transformation with respect to t_2, the signal, for a given value of t_1, has the following form:

$$S(t_1, \omega_2) \;=\; M_0 \exp(i\Omega_1 t_1) \exp(-t_1/T_2) \tilde{F}(\omega_2) \qquad (7.2)$$

with

$$\tilde{F}(\omega_2) = \frac{T_2}{1+T_2^2(\Omega_2-\omega_2)^2} + i\frac{T_2^2(\Omega_2-\omega_2)}{1+T_2^2(\Omega_2-\omega_2)^2} \tag{7.3}$$

the complex function $\tilde{F}(\omega_2)$ is more often conveniently written as:

$$\tilde{F}(\omega_2) = Re(\omega_2) + iIm(\omega_2) \tag{7.4}$$

in which $Re(\omega_2)$ and $Im(\omega_2)$ are the real and imaginary parts of the complex function $\tilde{F}(\omega_2)$ and represent the absorption and dispersion parts of the signal respectively. Equation (7.2) represents a set of spectra for different values of t_1, each spectrum experiencing the phase modulation expressed by $\Omega_1 t_1$. It is usual to use the real (absorption) part of the signal and Figure 7.3 shows an example of a phase modulation for different values of t_1 after the first Fourier transformation. The modulation along the t_1 axis is centered at $\omega_2 = \Omega_2$ along the F_2 axis and equation 7.2 becomes:

$$S(t_1, \Omega_2) = M_0 T_2 \cos(\Omega_1 t_1) \exp(-t_1/T_2)$$

After the second complex Fourier transformation with respect to the evolution period t_1, the 2D frequency domain signal is:

$$S(\omega_1, \omega_2) = M_0 \tilde{F}(\omega_1) \times \tilde{F}(\omega_2) \tag{7.5}$$

with

$$\tilde{F}(\omega_1) = Re(\omega_1) + iIm(\omega_1) \tag{7.6}$$

$Re(\omega_1)$ and $Im(\omega_1)$ are formulated in a similar way as $Re(\omega_2)$ and $Im(\omega_2)$ (see equation (7.3) and (7.4)). After multiplication:

$$\begin{aligned} S(\omega_1, \omega_2) = {} & M_0[\{Re(\omega_1)Re(\omega_2) - Im(\omega_1)Im(\omega_2)\} \\ & + i\{Re(\omega_1)Im(\omega_2) + iIm(\omega_1)Re(\omega_2)\}] \end{aligned} \tag{7.7}$$

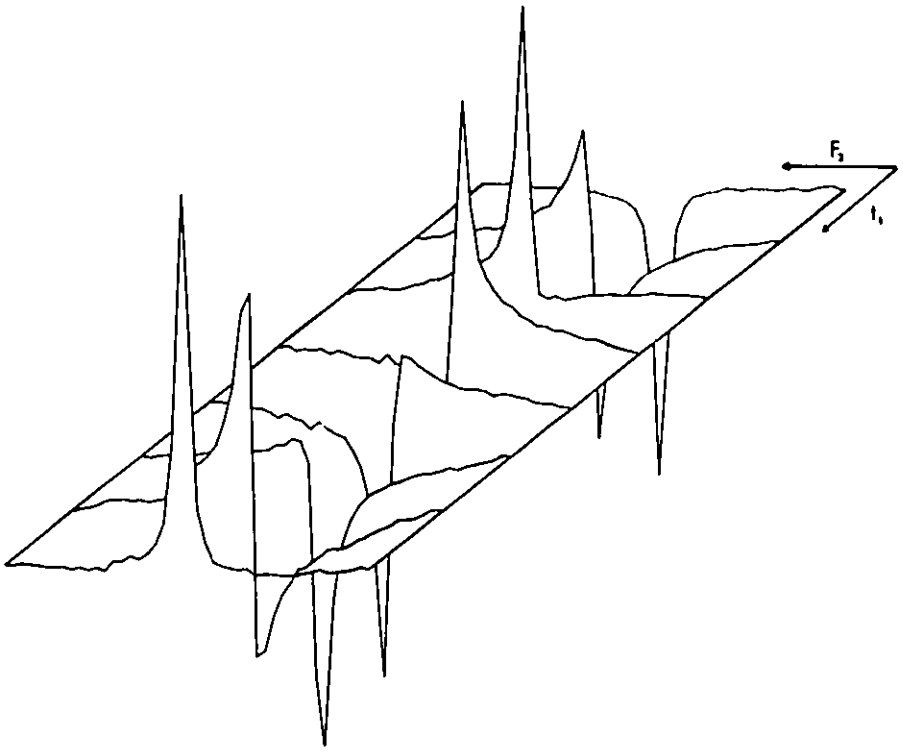

Figure 7.3: Display of a two-dimensional NMR spectrum after the first Fourier transformation (with respect to t_2, the detection period) showing the phase modulation of the signals during the evolution period t_1. The second Fourier transformation with respect to t_1 yields the frequency F_1. The H–2 resonance of ATP was used in this example. For experimental and instrumental conditions see Figure 7.9 and 7.10 respectively.

Equation (7.7) can also be formulated as:

$$S(\omega_1,\omega_2) = M_0[Re(\omega_1,\omega_2) + iIm(\omega_1,\omega_2)]$$

where both $Re(\omega_1,\omega_2)$ and $Im(\omega_1,\omega_2)$ contain a mixture of absorption and dispersion of the signal. The signal of interest is given by the real part $Re(\omega_1,\omega_2)$ of the signal $S(\omega_1,\omega_2)$. From equation (7.7), the real part of the signal consists of the superposition of a two-dimensional absorption $Re(\omega_1)Re(\omega_2)$ and a two-dimensional dispersion $Im(\omega_1)Im(\omega_2)$ giving rise to a complicated so called phase twisted 2D lineshape [170,174], as seen in Figure 7.4. It is very difficult to modify these phase twisted 2D lineshapes into a pure two-dimensional absorption spectrum by a simple phase correction routine. However, the phase sensitive mode can be used to display and phase a cross-section of a 2D spectrum into an absorption mode. When the entire 2D spectrum needs to be displayed, the absolute value representation is used [170,173], as seen in Figure 7.5, and defined as:

$$|S(\omega_1,\omega_2)| = \sqrt{Re^2(\omega_1,\omega_2) + Im^2(\omega_1,\omega_2)}$$

It overcomes the problem of phasing a 2D spectrum, but, because of the dispersion contribution to the absolute intensity, lineshape distortions occur. Lineshapes are globally broader than a pure Lorentzian in the absorption mode (see spectrum A of Figure 7.6), especially at the base of the line (see spectrum B of Figure 7.6), giving rise to a pronounced star shape in the contour plot (see spectrum A of Figure 7.7). As a result, in crowded 2D spectra, poor resolution may be expected which, in the worst case leads to false correlation peaks.

For a qualitative analysis of a 2D spectrum, the resonance wings can be removed by digital filtering. Among the digital filters available [172], the Lorentzian to Gaussian [175,176] and the pseudo-echo [176] transformations are commonly used for data

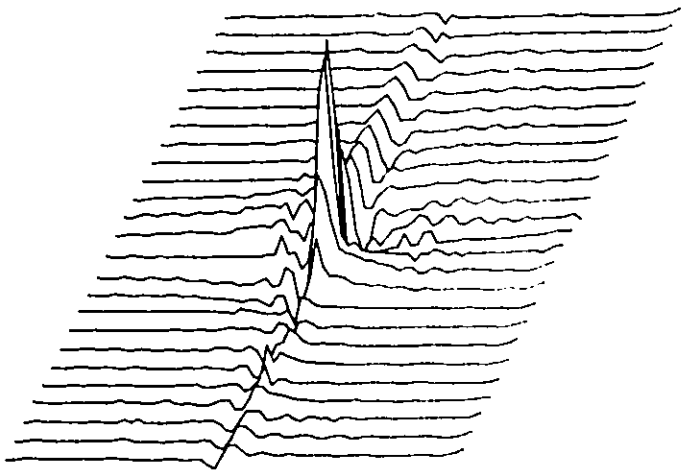

Figure 7.4: Display of a two-dimensional spectrum processed in the phase sensitive mode and showing an example of a phase twisted 2D lineshape. The 2D spectrum was obtained by performing a second Fourier transformation of the spectrum displayed in Figure 7.3.

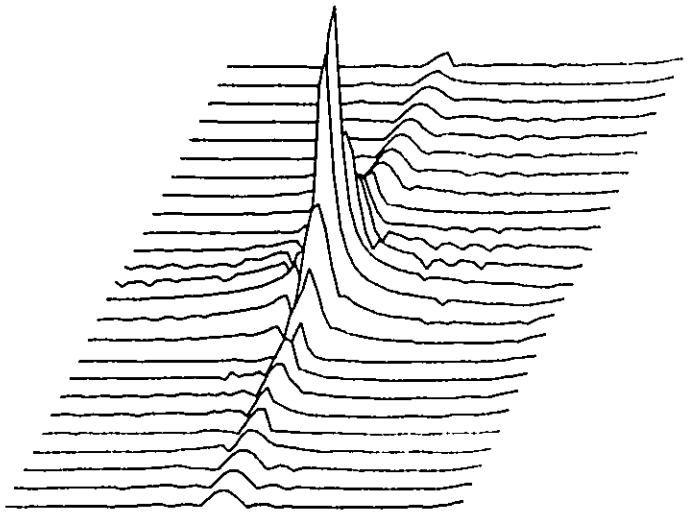

Figure 7.5: Display of a two-dimensional spectrum processed in the absolute value mode. The problem of phasing the 2D spectrum is no longer necessary in this mode of representation. The 2D spectrum was obtained by performing a second Fourier transformation of the spectrum displayed in Figure 7.3.

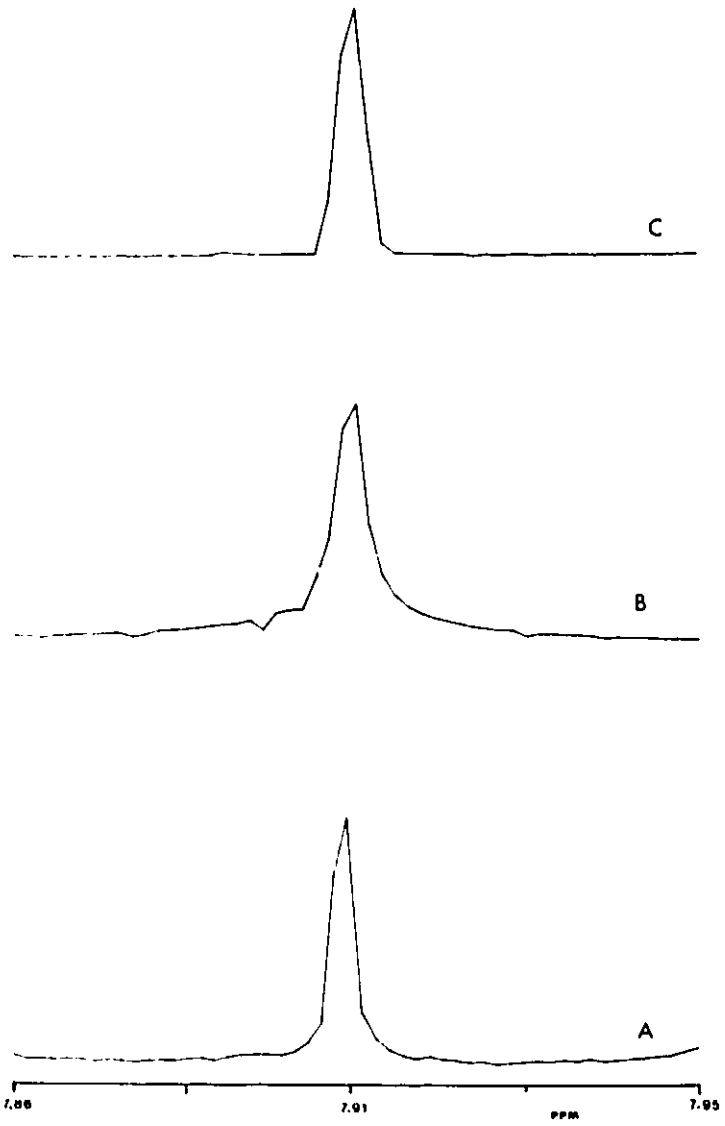

Figure 7.6: Lineshape comparison between A) a one-dimensional pure Lorentzian lineshape in the absorption mode; B) a cross-section of a 2D spectrum in the absolute value representation and C) the removal of the dispersion contribution present in spectrum (B) by using a pseudo-echo filtering function in both dimensions before Fourier tranformation. Experimental and instrumental conditions as in Figure 7.9 and 7.10.

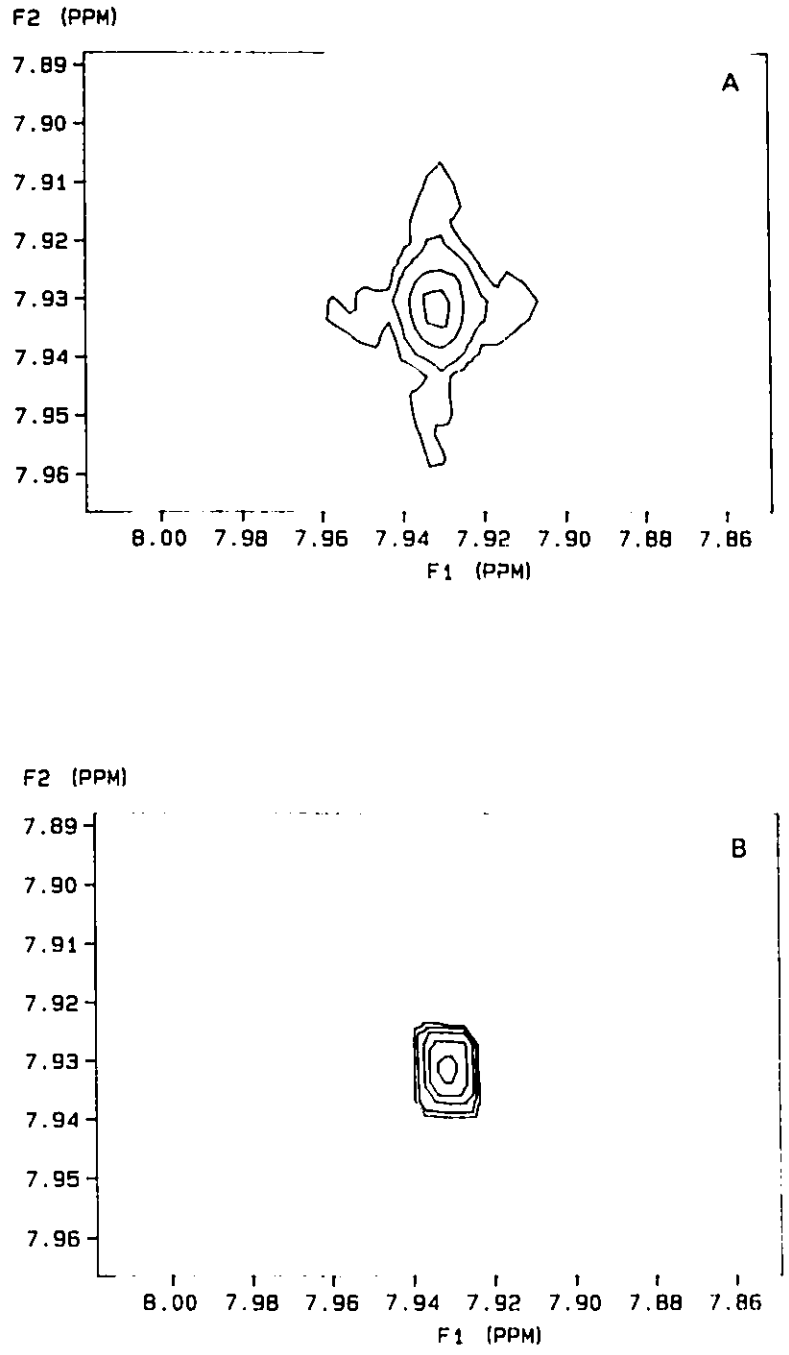

Figure 7.7: Contour plot comparison between A) a two-dimensional spectrum displayed in the absolute value representation and B) the same spectrum after using a pseudo-echo filtering function in both dimensions. Experimental and instrumental conditions as in Figure 7.9 and 7.10.

treatment of 2D spectra. These filters reduce the dispersive components of an absolute value representation and produce a 2D spectrum with a less pronounced star shape in the contour plot (see spectrum B of Figure 7.7), and reduce strong tailing in a cross-section (see spectrum C of Figure 7.6). However, if quantitative rate constant measurements are intended, the use of filtering functions should be avoided since they distort peak intensities. From this discussion it follows that in order to obtain reliable rate constant values, the two chemically exchanging sites should have well resolved resonances in the one-dimensional spectrum and the NOESY spectrum should have a good signal-to-noise ratio.

7.2 Two-Dimensional NMR Exchange Spectroscopy (NOESY)

NMR techniques are particularly well suited for the investigation of molecular dynamics like molecular relaxation or chemical exchange processes. Depending upon the relative magnitude of the governing rate processes, different methods can be used to extract relaxation or chemical exchange rate constants.

Lineshape analyses [158] are often used to study two-site chemical exchange processes whose rate lies in the order of $10\text{–}10^4$ s^{-1}. Multiple resonance techniques [178] give information about dynamics by utilizing the NOE effects [208], as well as tracing chemical exchange pathways by saturation transfer experiments [199,200,201]. Finally, relaxation experiments generally give more insight into the different types of relaxation processes operating in the lattice and, under certain conditions, exchange rates may even be measured [202]. Up to the late 70's, investigation of chemical exchange and magnetization transfer in liquids could only be studied by one-dimensional NMR spectroscopy. In 1979, 2D NMR spectroscopy was applied to magnetization

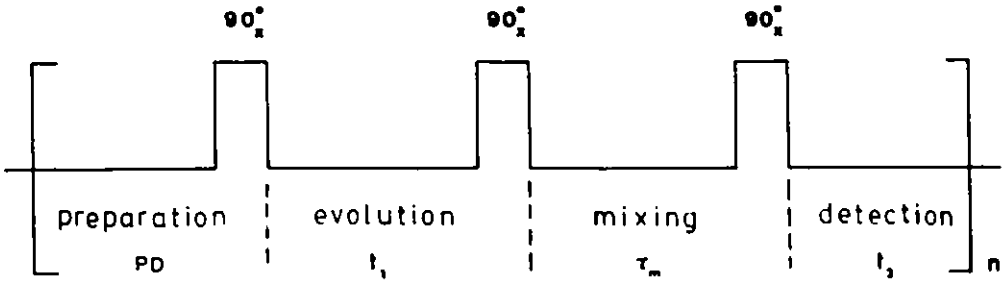

Figure 7.8: Basic pulse sequence for a two-dimensional exchange NMR spectroscopy (NOESY) experiment. See text for a detailed description of the pulse sequence.

transfer processes [179], resulting in the appearance of a new general technique called 2D NMR exchange spectroscopy (NOESY).

Figure 7.8 presents the basic (NOESY) pulse sequence which only differs from the classic 2D pulse sequence (see Figure 7.2) by a fourth, constant time period τ_m, called the mixing period. It is during this period that the exchange processes take place. The signal $S(t_1, \tau_m, t_2)$ is recorded during the evolution time t_2, the double Fourier transformation of which gives the 2D spectrum $S(\omega_1, \omega_2)$. In the case of a two site (A and B) chemical exchange process, the appearance of diagonal peaks, at frequencies (ω_A, ω_A) and (ω_B, ω_B) in the 2D spectrum, indicates that the magnetization components processing at ω_A and ω_B , during the evolution period, did not undergo chemical exchange during the mixing period. As a result, they still nutate with their own frequency ω_A and ω_B during the detection period. On the other hand, the appearance of a cross-peak at frequencies (ω_A, ω_B) in the 2D spectrum indicates that transfer of magnetization components precessing at ω_A, to a site precessing at ω_B, has occurred during the mixing period. The same reasoning applies for the cross-peak centered at (ω_B, ω_A).

The signal observed during the detection period is the sum of four magnetization

components [179]:

$$M_{xy}^{AA}(t_1,\tau_m,t_2) = a_{AA}(\tau_m)\cos(\omega_A t_1)\cos(\omega_A t_2)\exp(-t_1/R_{AA})\exp(-t_2/R_{AA})$$

$$M_{xy}^{BB}(t_1,\tau_m,t_2) = a_{BB}(\tau_m)\cos(\omega_B t_1)\cos(\omega_B t_2)\exp(-t_1/R_{BB})\exp(-t_2/R_{BB})$$

$$M_{xy}^{AB}(t_1,\tau_m,t_2) = a_{AB}(\tau_m)\cos(\omega_A t_1)\cos(\omega_B t_2)\exp(-t_1/R_{AA})\exp(-t_2/R_{BB})$$

$$M_{xy}^{BA}(t_1,\tau_m,t_2) = a_{BA}(\tau_m)\cos(\omega_B t_1)\cos(\omega_A t_2)\exp(-t_1/R_{BB})\exp(-t_2/R_{AA})$$

with:

$$a_{AA}(\tau_m) = x_A e^{-\sigma\tau_m}\left[\cosh(D\tau_m) - \frac{\delta}{D}\sinh(D\tau_m)\right] \tag{7.8}$$

$$a_{BB}(\tau_m) = x_B e^{-\sigma\tau_m}\left[\cosh(D\tau_m) + \frac{\delta}{D}\sinh(D\tau_m)\right] \tag{7.9}$$

$$a_{AB}(\tau_m) = a_{BA}(\tau_m) = -\,x_A x_B \frac{k_2}{D} e^{-\sigma\tau_m}\sinh(D\tau_m) \tag{7.10}$$

and:

$$\sigma = \tfrac{1}{2}(R_{AA}+R_{BB}) \quad R_{AA} = R_{1A} + x_B k_2 \tag{7.11}$$

$$\delta = \tfrac{1}{2}(R_{AA}-R_{BB}) \quad R_{BB} = R_{1B} + x_A k_2 \tag{7.12}$$

$$D = \sqrt{(\delta^2 + x_A x_B k_2^2)}$$

$a_{AA}(\tau_m)$, $a_{BB}(\tau_m)$ and $a_{AB}(\tau_m)$, $a_{BA}(\tau_m)$ are called the mixing coefficients and they determine the intensities of the two diagonal and the two cross-peaks in the 2D spectrum respectively. In equations (7.11) and (7.12) x_A, R_{1A} and x_B, R_{1B} are the nuclei populations and the intrinsic relaxation rates in the site A and B respectively. k_2 represents the first-order rate constant of the exchange process (k_2 is normalized for the population differences of each site). From equations (7.8)(7.9) and (7.10) the

intensities of the diagonal peaks and cross-peaks are a function of the mixing time τ_m. By recording several 2D spectra with different mixing times, one obtains an intensity variation of the diagonal and cross-peaks as a function of τ_m. x_A and x_B can be obtained from a one-dimensional spectrum while both relaxation rates R_{AA} and R_{BB} can be determined by a spin-lattice relaxation experiment. Then, the only unknown of equations (7.8)(7.9) and (7.10) is the rate constant k_2, which can be determined by a non-linear regression analysis of the diagonal and cross-peak intensities as a function of the mixing time.

This new two-dimensional technique represents an extension of the one-dimensional Forsen-Hoffman saturation transfer method [199,200,201] which, under conditions of multi-site exchange or crowded spectra, presents some difficulties of irradiation. Also, standard NMR spectrometers are not equipped to deliver multiple or even a single selective irradiation for nuclei other than protons. Two-dimensional exchange spectroscopy (NOESY) overcomes all of these problems at once and it has been successfully applied to numerous chemical [183,184,185,186,187] and biochemical [188,189,190,191] problems and, in certain cases, has led to the determination of the rate constant [184,186,187,189,191]. Moreover, with the advent of 2D NMR it is now possible to obtain and elucidate, in a single experiment, the chart of the exchange pathways for multi-site chemical exchange processes.

It should also be mentioned that NOESY is a powerful method for the elucidation of the overall spatial structures and conformations of biological macromolecules in solutions [192,193,194,195,196,197,198,203,204]. In these experiments magnetization transfer occurs via cross-relaxation rates which are quantitatively measured and yield distances between cross-relaxing nuclei in the macromolecule.

In the case of chemical exchange processes, rate constant measurements by 2D

NMR were, in several examples [186,191,205], in good agreement with rate constants obtained by other one-dimensional NMR methods, like saturation transfer or relaxation experiments.

In this chapter, the kinetics of chemical exchange processes taking place in the ATP_4 Al_3 aggregate was investigated by ^1H 2D NMR. It led to the determination of the pseudo first-order rate constant k_2 which characterized the exchange taking place between a surface and the complexed ATP molecules in the aggregate.

7.3 Materials and Methods

Two-dimensional NOESY spectra were obtained by using the pulse sequence described in Figure 7.8. To obtain an adequate signal-to-noise ratio, 16 transients were accumulated for each of the 128 FIDs, using a pulse delay of 1 second. Quadrature phase detection was combined with the frequency carrier set in the middle of the spectrum. The remaining solvent water resonance was suppressed by a selective, continuous soft (100 mW) irradiation [192,193,206] at the water resonance frequency using the homo-decoupler mode of a Waltz–16 decoupler [77]. Eight NOESY spectra were recorded with different mixing times. The acquisition time was 1 second, over a spectral width of 500 Hz, which covered the H–8 and H–2 adenine proton chemical shift region. The number of data points taken in the double Fourier transformation were 1024 in both dimensions. No filtering function was used in the double Fourier transformation and the spectral resolution achieved was 1 Hz in both dimensions. After the double Fourier transformation, the two-dimensional spectra were submitted to a data symmetrization technique [207] which has been shown to improve the signal-to-noise ratio and cancel peak artifacts of a 2D spectrum. All spectra were displayed using the absolute value mode representation. Integrated peak volumes of

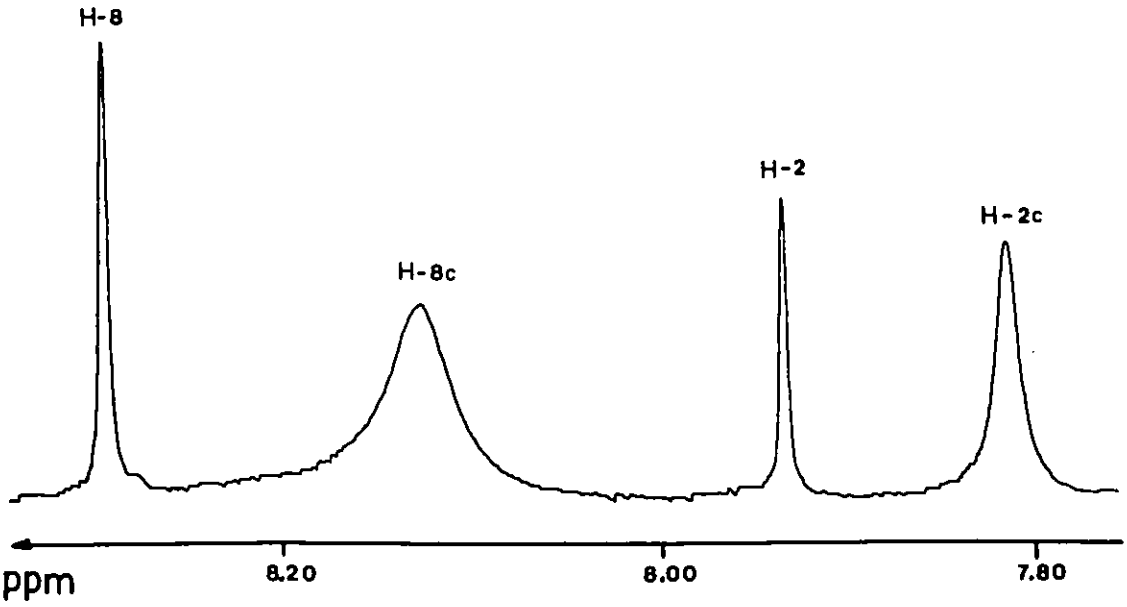

Figure 7.9: One-dimensional ^{1}H NMR spectral region of the H–8 and H–2 adenine resonances of an ATP–Al solution in D_2O at 300 MHz. Experimental conditions were: [ATP] = 100 mM, pH = 7.4 and 22 °C. The Al/ATP ratio was 0.75. Instrumental conditions were: spectral width of 500 Hz, acquisition time of 1 sec, pulse delay of 1 sec, 16 transients and no line broadening.

the diagonal and cross-peaks were computed in order to take into account linewidth differences between the two diagonal peaks (see Figure 7.9). The reported integrated cross-peak volumes represent the average value of the two cross-peaks.

7.4 Results

Figure 7.9 displays the H–8 and H–2 spectral region of a one-dimensional proton spectrum of ATP in D_2O (pH = 7.4, ATP = 100 mM) and for an Al/ATP ratio of 0.75. For each kind of proton, under these conditions, the resonances shifted upfield were attributed to a complexed ATP molecule of an ATP_4-Al_3 aggregate (δ(H–8c) = 8.124 ppm and δ(H–2c) = 7.818 ppm), while the remaining two reso-

nances (δ(H-8) = 8.290 ppm and δ(H–2) = 7.935 ppm) were attributed to a surface ATP molecule of the aggregate (see Figure 7.9 and Section 6.2). The 2D NOESY spectra were all recorded in this spectral region because both resonances of the aggregate were well resolved for both types of protons. The H–2 proton resonances were chosen to follow the intensity variations of the diagonal and cross-peaks of the NOESY spectra because of the narrower linewidth of the complexed ATP resonance ($\mathcal{V}_{1/2}$(H-2c) = 3.6 Hz while $\mathcal{V}_{1/2}$(H–8c) = 11 Hz), leading to a better resolution of the diagonal and cross-peaks in the 2D spectrum.

Figure 7.10 displays, in a contour plot representation, a series of 2D NOESY spectra of the H–2 proton resonances for three different mixing times (0.3, 0.5 and 1.0 sec). With a mixing time of 0.3 sec, cross-peaks were already present. This indicates that, during the mixing time, transfer of magnetization from a surface ATP molecule to a complexed ATP molecule has occurred by chemical exchange. As the mixing time increased, cross-peak intensities clearly also increased while the intensities of the diagonal peaks decreased. The intensity variations were more pronounced for the surface ATP resonance since its linewidth was narrower ($\mathcal{V}_{1/2}$ = 1.5 Hz) than that of the complexed ATP resonance ($\mathcal{V}_{1/2}$ = 3.6 Hz).

Figure 7.11 displays, in a whitewashed stacked plot representation, the NOESY spectra obtained for τ_m = 0.3, 0.5 and 1.0 sec which can be compared to the respective contour plot representation in Figure 7.10. The 2D stacked plot spectra give an example of the resolution and signal-to-noise ratio obtained in the NOESY spectra. It also allows for comparisons of the relative peak intensity variations of the diagonal and cross-peaks.

These relative peak volume variations are summarized in Figure 7.12 for eight different mixing time values. The intrinsic relaxation times of equation (7.11) and

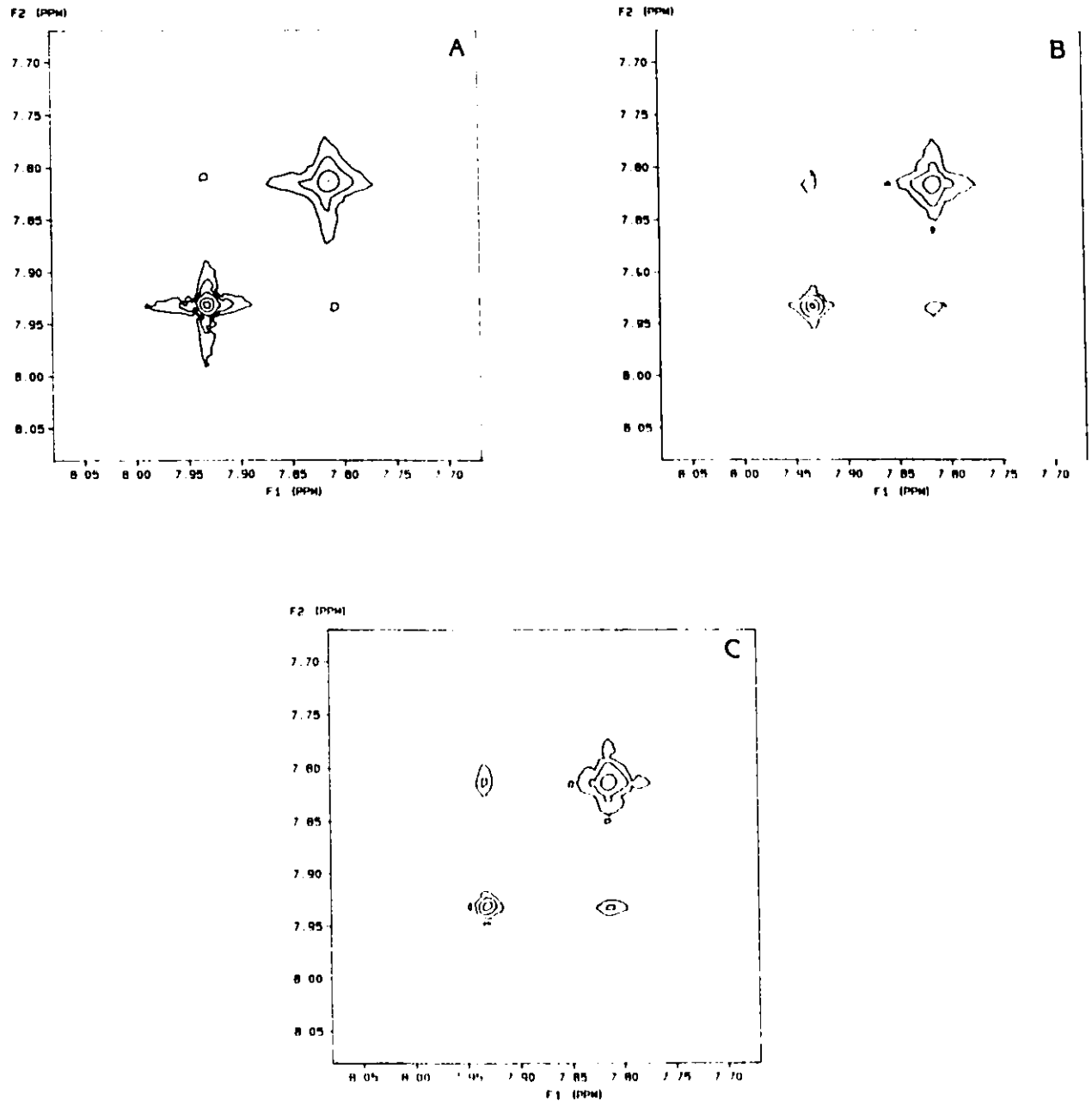

Figure 7.10: A series of ^{1}H 2D exchange NMR spectra of the "free" and complexed H–2 adenine resonances of an ATP–Al solution in D_2O at 300 MHz. The spectra are shown in a contour plot using an absolute value representation. Experimental conditions were as in Figure 7.9. Instrumental conditions were: spectral width of 500 Hz, acquisition time of 1 sec and a pulse delay of 1 sec. The mixing times were: A) 0.30; B) 0.5℃ and C) 1.0 sec. The residual HOD resonance was continously decoupled with a low proton decoupling power (100 mW). 16 FIDs were coadded for each of the 128 t_1 values. A 1024 × 1024 data matrix was Fourier transformed in both dimensions, without using any filtering function.

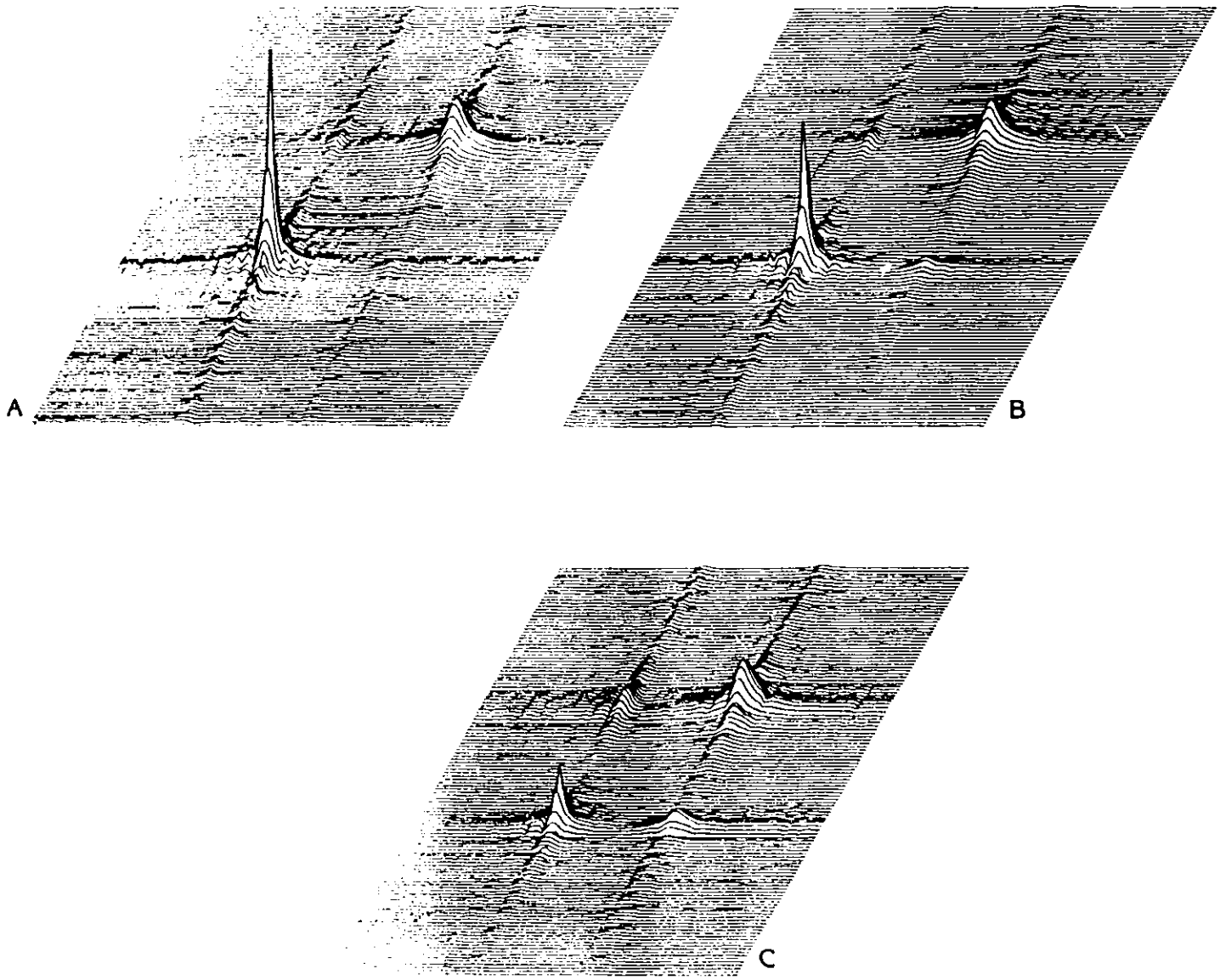

Figure 7.11: A series of of ^{1}H 2D exchange NMR spectra of the "free" and complexed H-2 adenine resonances of an ATP-Al solution in D_2O at 300 MHz. The spectra are shown in a whitewashed stacked plot using an absolute value representation. The different mixing times in seconds were: A) 0.30; B) 0.50 and C) 1.0. For experimental and instrumental conditions see Figure 7.9 and 7.10 respectively.

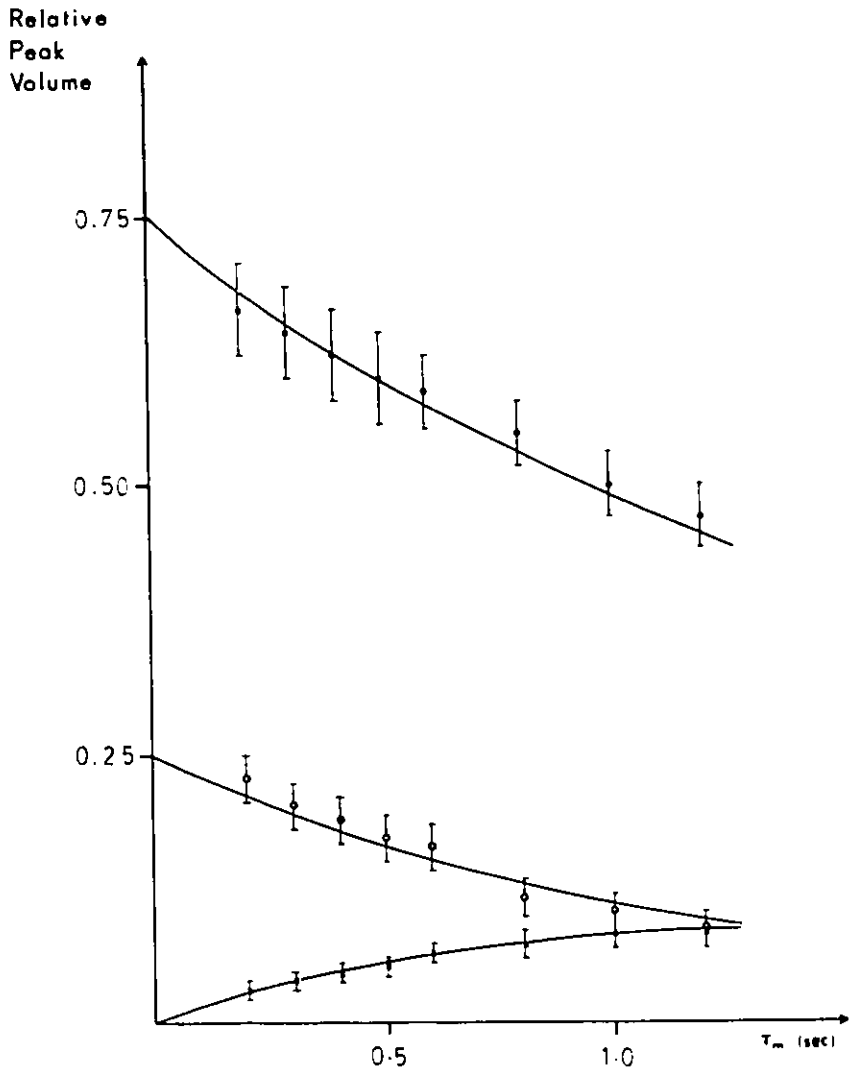

Figure 7.12: Variation of the relative peak volume for the diagonal and cross-peaks of the H–2 resonances of ATP in the NOESY spectra as a function of the mixing time τ_m. Experimental data points are shown for: (•) the complexed (H–2c) resonance; (o) the surface (H–2) resonance and (×) the average for the two cross-peaks. The full lines represent the result of a non-linear regression analysis using equations (7.8)(7.9) and (7.10).

(7.12) in site A (surface ATP molecule) and B (complexed ATP molecule) were previously determined by ^{1}H inversion recovery experiments (see Section 6.3), and were both 0.27 sec^{-1}. The molar fractions x_A and x_B were fixed to 0.25 and 0.75 respectively. Using these parameters and 24 data points given by the NOESY spectra, a non-linear regression analysis performed on both the diagonal and cross-peaks gave $k_2 = 0.8 \pm 0.2$ s^{-1}. The three full lines in Figure 7.12 represent the theoretical peak volume variations of the diagonal and cross peaks, using equation (7.8)(7.9) and (7.10), and for a rate constant of 0.8 s^{-1}.

7.5 Discussion

2D NMR exchange could only provide the value of the pseudo first-order rate constant and, since no concentration studies were available, it was not possible to decide on the mechanism of the chemical exchange process taking place in solution. However, an intramolecular chemical exchange mechanism is a plausible working hypothesis. It is in agreement with the three-site chemical exchange existing for the ATP–Al system (see Section 6.2 and 8.4). Figure 7.13 summarizes the overall suggested mechanism. Each square represents an ATP molecule of the aggregate. A small letter (a,b,c or d) denotes a surface ATP molecule while a capital letter (A,B,C or D) represents a complexed ATP molecule. The vertical straight line emphasizes that in the aggregate, there are three complexed ATP molecules for one surface ATP molecule. Figure 7.14 shows in more detail what happens for the steps (1) and (2) of Figure 7.13. In the first step (1), an intramolecular exchange takes place between a surface (d) and complexed (A) ATP molecule. This chemical exchange, slow enough on the NMR time scale, was detected by 2D NMR. In the second step (2), a surface ATP molecule (a) dissociates from the aggregate, giving rise to a free ATP molecule in solution (L). This chemical

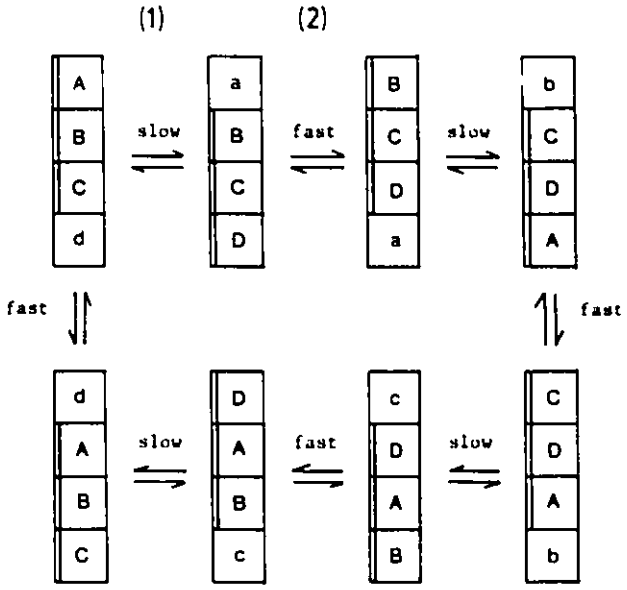

Figure 7.13: Suggested overall intramolecular chemical exchange mechanism occuring in the ATP_4Al_3 aggregate. Each square represent an ATP molecule of the aggregate, a small letter denoting a surface ATP molecule while a capital letter is representative of a complexed ATP molecule. Figure 7.14 shows in more detail what happens for the steps (1) and (2).

exchange has been shown to exist by proton chemical shift measurements (see Section 6.2) and phosphorus-31 spin-lattice relaxation experiments (see Section 8.4). Finally, the free ATP molecule (L) returns at the other side of the aggregate as a surface ATP molecule (a). This overall chemical exchange is fast on the NMR frequency time scale, and corresponds to a jump of a surface ATP molecule to the other end of the aggregate via a free ATP molecule in solution. Successive repetition of these fast and slow exchanges, presented in Figure 7.14, generates the overall chemical exchange pathway existing in the aggregate and shown in Figure 7.13. Finally, Figure 7.15 summarizes schematically the overall intramolecular chemical exchange of a surface ATP molecule presented in Figure 7.13, each step characterized by a rate constant of 0.8 s^{-1}.

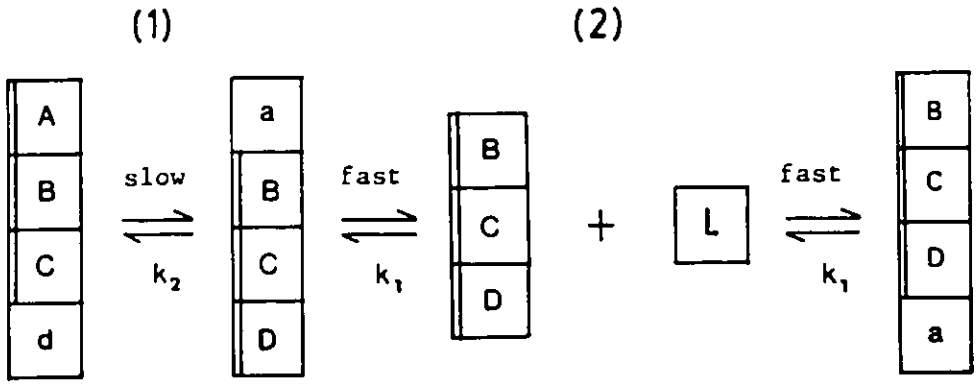

Figure 7.14: A detailed scheme showing the two successive slow and fast chemical exchange steps which characterize the dynamics of the ATP–Al system. (L) represents a free ATP molecule in solution. For other symbols see text of Figure 7.13.

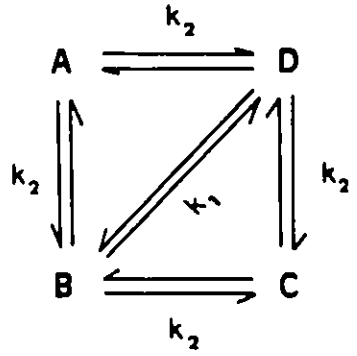

Figure 7.15: Schematic overall chemical exchange pathway occuring in the aggregate. (A,D) (D,C) (C,B) and (B,C) are in slow exchange ($k_2 = 0.8\ s^{-1}$) while (D,B) are in fast exchange.

7.6 Conclusion

The intramolecular chemical exchange model discussed previously could be tested by a concentration study experiment. Although 2D NMR exchange spectroscopy is an attractive tool for studying chemical exchange processes, it is still a time consuming technique. To remedy this problem, a concentration study of the rate constant could be done by performing one-dimensional proton saturation transfer experiments [199,200,201]. This technique has been shown to be a powerful tool to measure the slow chemical exchange rates of enzyme catalysed reactions in a variety of *in vivo* [190,209,210] and *in vitro* [211,212,213] biochemical living systems. The application of the saturation transfer method has also been discussed for multi-site exchange [214], and applied to three-site exchange systems of protein-ligand complexes [215,216]. Finally, it should be pointed out that experimental difficulties may arise and prevent the completion of the magnetization transfer experiment. In this case, other NMR techniques have been developed for the determination of slow chemical exchange rates, and magnetization transfer in the rotating frame [217], as well as the Carr-Purcell-Meiboom-Gill (CPMG) [218] pulse sequence may provide an alternative for kinetic experiments.

Chapter 8

PHOSPHORUS-31 RELAXATION PROCESSES IN ATP_4Al_3 AGGREGATES

8.1 Introduction

Phosphorus-31 relaxation studies have been shown to provide important information on the conformation and dynamics of nucleic acid, oligonucleotides and phosphoproteins [219,220]. In order to gain sensitivity and resolution, phosphorus-31 NMR studies are often performed at high magnetic field strengths ($\nu_0 > 40$ MHz). The advantages gained by the use of high field spectrometers are somewhat diminished by the phosphorus-31 relaxation mechanisms. In most cases, the sum of two contributions [223] must be considered: the dipole-dipole phosphorus-proton interaction and the chemical shift anisotropy interaction. Fortunately, the latter interaction is field dependent and only becomes preponderant at high field. As a result, in order to unravel the phosphorus-31 relaxation parameters, relaxation studies generally require measurements at different magnetic field strengths.

Phosphorus-31 dipole-dipole and CSA relaxation theories [55] (see Section 2.3.1 and 2.3.2) have been applied to simple cases of isotropic molecular reorientation

[90,113] (see Chapter 4). However, molecular reorientation of a residue imbedded into a macromolecule is often anisotropic. In this case, the correct description of molecular dynamics requires a double correlation time relaxation model [221,140,222], which allows for one mode of internal motion coupled with the isotropic tumbling of the whole molecule. Such motional models have been applied to the phosphodiester linkages of DNA [224,132,137,100,136], RNA and oligonucleotides [225,133], showing the sensitivity of NOE and spin-lattice relaxation measurements upon internal motions in the subnanosecond time scale (0.2 - 0.4 ns).

In a concentration study, NOE and phosphoras-31 spin-lattice relaxation measurements were performed on the ATP–Al system. It provided important information about the different types of chemical exchange taking place in solution at pH = 7.4. The combination of NOE and T_1 measurements at two different fields permitted each relaxation mechanism contributing to the overall experimental relaxation rates to be resolved. As well, ^{31}P NMR relaxation experiments gave information about the internal dynamics of the aggregate which could then be compared to the results obtained by ^{13}C spin-lattice relaxation measurements (see Section 6.3).

8.2 Materials and Methods

In a concentration study, the total ATP concentration was kept constant at 100 mM while the Al/ATP ratio was varied from 0 to 1.25. ^{31}P spin-lattice relaxation measurements were performed at 121 MHz for the various Al/ATP ratios. T_1 measurements were also done at 32 MHz for $0.75 \leq$ Al/ATP ≤ 1.25. Finally, NOE spectra were recorded for Al/ATP = 0.75, at both fields. All samples were prepared in 20% D_2O solution, pH = 7.4 and recorded at 22 °C. The experimental sample preparation, NOE and T_1 measurements were dealt with in Section 3.6, 3.4 and 3.3 respectively.

8.3 Results

The T_1 variations of the free phosphorus nuclei can be qualitatively observed in Figure 8.1 and 8.2 which display two sets of partially relaxed ^{31}P spectra at 121 MHz, for Al/ATP = 0.33 and 0.90 respectively. Figure 8.3 and 8.4 correspond to an enlarged spectral region of Figure 8.1 and 8.2 respectively, showing the α' and β' complexed phosphates. For both resonances, the constancy of the T_1 values can be clearly seen by comparing Figure 8.3 and 8.4. Figure 8.5 displays a ^{31}P inversion recovery experiment at 32 MHz for Al/ATP = 0.90, which can be compared to the same experiment performed at 121 MHz and presented in Figure 8.2. Table 8.1 summarizes the spin-lattice relaxation time results at two different magnetic fields, for the free α, β and γ and complexed α' and β' phosphates of ATP. At 121 MHz, all the T_1 values of the free phosphorus nuclei decreased as the Al/ATP ratio increased up to 0.75, after which a plateau T_1 value was reached. Table 8.1 reports the averaged values ($\widehat{T}_1$(obs)) for Al/ATP $\geq$ 0.75. For example, the T_1 value of the free γ phosphate steadily decreases from 3.95 sec (Al/ATP = 0) to an averaged T_1 value of 1.31 sec (Al/ATP $\geq$ 0.75). The complexed α' and β' phosphates showed no T_1 variation as a function of the Al/ATP ratio. For a given magnetic field they all had the same T_1 value of about 1 sec at 121 MHz and 2 sec at 32 MHz (see Table 8.1). Finally, the T_1 value of the free and complexed phosphorus nuclei was always smaller at 121 MHz than at 32 MHz. For example, the β' phosphate had a T_1 (121 MHz) of 1.02 sec while the T_1 (32 MHz) was 2.05 sec (see Table 8.1). This observed field dependency is the result of a more efficient CSA relaxation mechanism at higher field strength.

All of the T_1 values reported in Table 8.1 correspond to samples which were treated for the removal of paramagnetic impurities (see Section 3.6). Many reports have

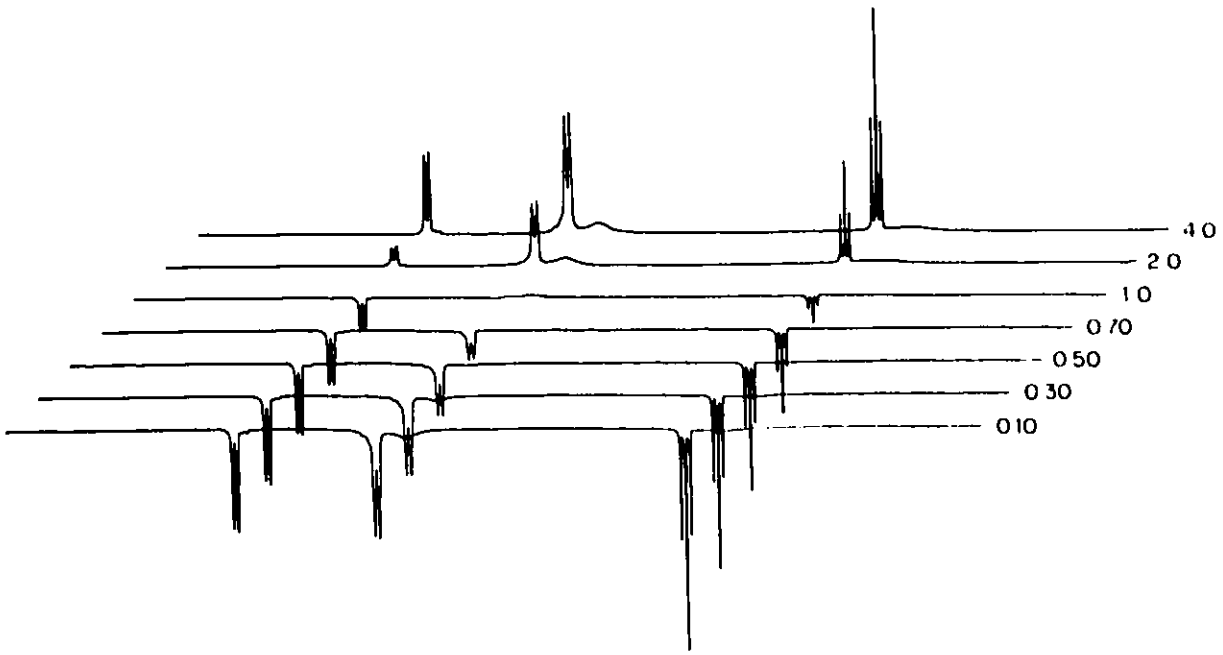

Figure 8.1: Display of a ^{31}P inversion recovery experiment at 121 MHz of an ATP-Al solution for which the Al/ATP ratio was 0.33. This figure predominantly shows the magnetization recovery of the free (α, β, γ) phosphate resonances of ATP. For experimental conditions see Table 8.1. Instrumental conditions were: sweep width of 4000 Hz, aquisition time of 3.8 sec, pulse delay of 8 sec, no proton decoupling, 400 transients and 1 Hz line broadening. Recovery times in seconds are shown near each spectrum.

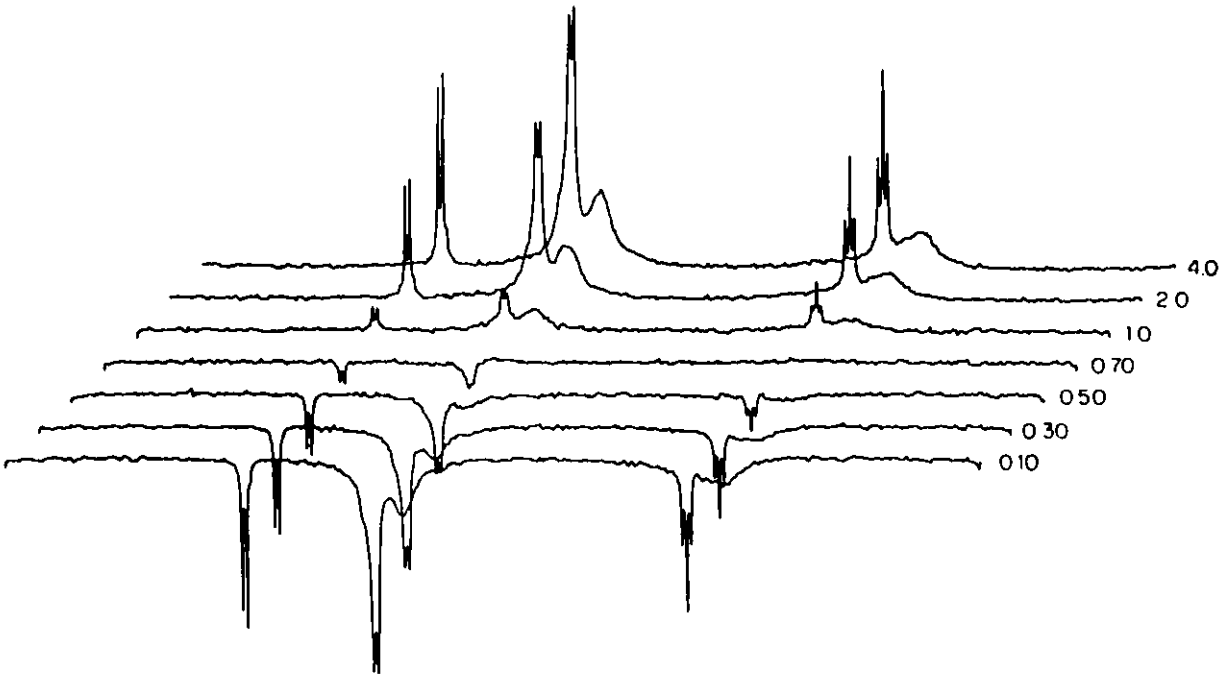

Figure 8.2: Display of a ^{31}P inversion recovery experiment at 121 MHz of an ATP–Al solution for which the Al/ATP ratio was 0.90. This figure predominantly shows the magnetization recovery of the free (α, β, γ) phosphate resonances of ATP. For experimental and instrumental conditions see Table 8.1 and Figure 8.1 respectively. Recovery times in seconds are shown near each spectrum.

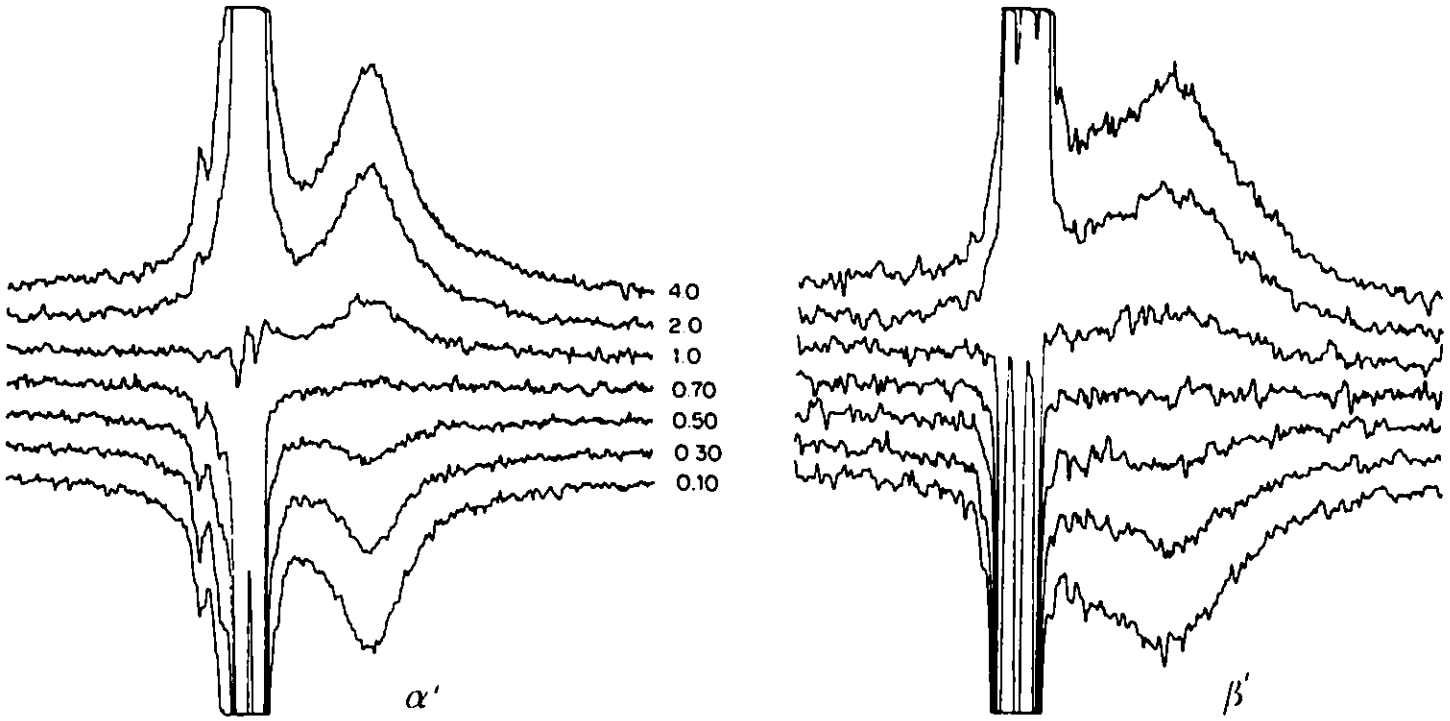

Figure 8.3: Display of a ^{31}P inversion recovery experiment at 121 MHz of an ATP-Al solution for which the Al/ATP ratio was 0.33. This figure predominantly shows the magnetization recovery of the complexed α' and β' phosphate resonances of ATP. For experimental and instrumental conditions see Table 8.1 and Figure 8.1 respectively. Recovery times in seconds are shown near each spectrum.

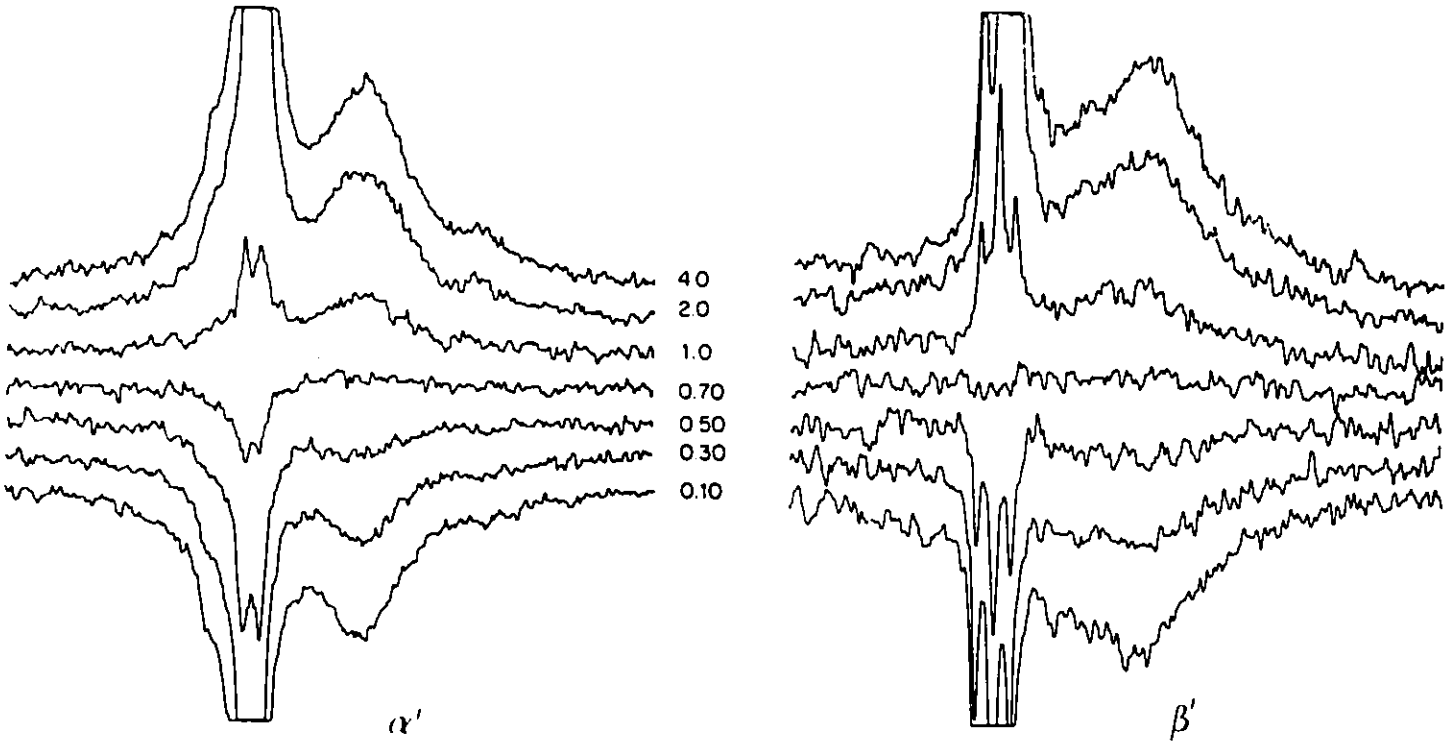

Figure 8.4: Display of a ^{31}P inversion recovery experiment at 121 MHz of an ATP–Al solution for which the Al/ATP ratio was 0.90. This figure predominantly shows the magnetization recovery of the complexed α' and β' phosphate resonances of ATP. For experimental and instrumental conditions see Table 8.1 and Figure 8.1 respectively. Recovery times in seconds are shown near each spectrum.

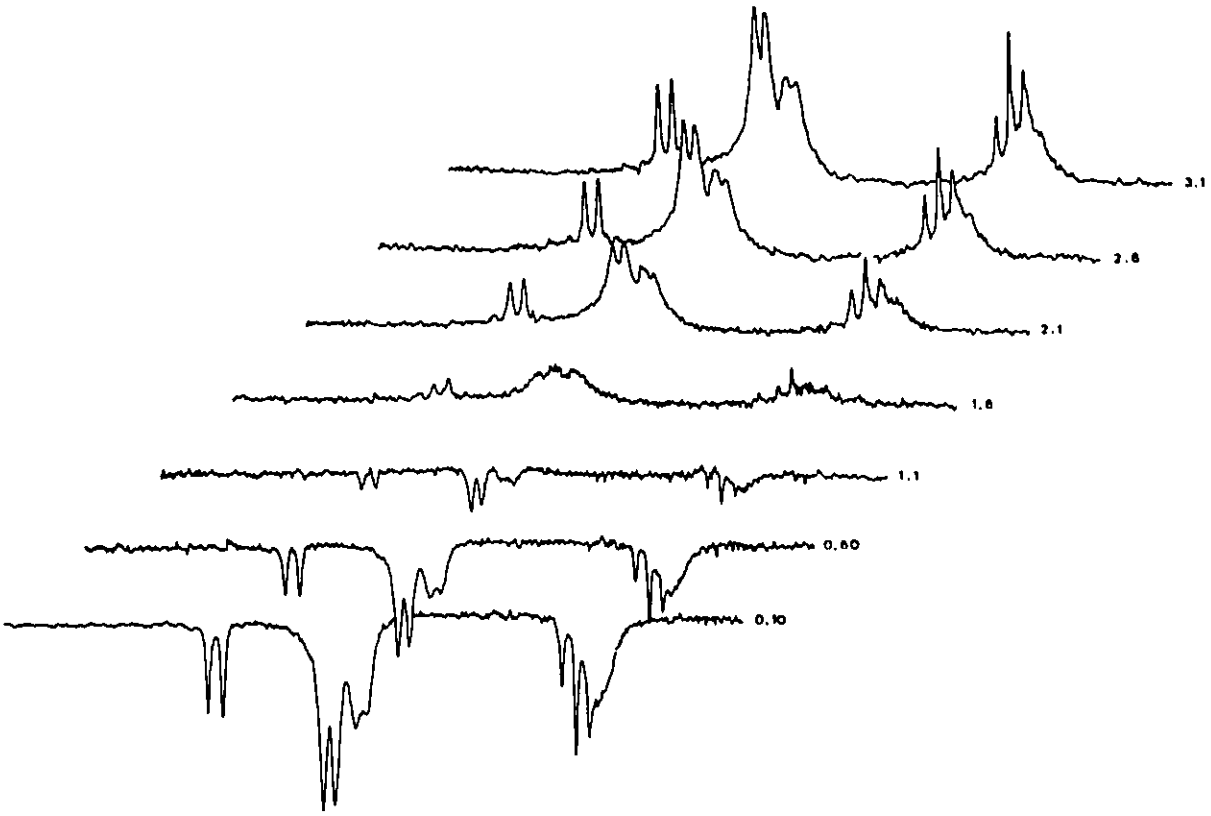

Figure 8.5: Display of a ^{31}P inversion recovery experiment at 32 MHz of an ATP–Al solution for which the Al/ATP ratio was 0.90. This figure shows the magnetization recovery of the free and complexed phosphate resonances of ATP. For experimental conditions see Table 8.1. Instrumental conditions were: sweep width of 1000 Hz, aquisition time of 4.1 sec, pulse delay of 8 sec, no proton decoupling, 500 transients and 1 Hz line broadening. Recovery times in seconds are shown near each spectrum.

$\frac{Al(III)}{[ATP]}$	$T_1(P_\gamma)$ (sec)		$T_1(P_\alpha)$ (sec)		$T_1(P_\beta)$ (sec)		$T_1(P_{\alpha'})$ (sec)		$T_1(P_{\beta'})$ (sec)	
	ν_1	ν_2	ν_1	ν_2	ν_1	ν_2	ν_1	ν_2	ν_1	ν_2
0.00	3.95	7.34	1.92	5.55	2.69	7.80				
0.33	2.69		1.60		1.96		1.02		1.08	
0.40	2.42		1.54		1.73		1.00		1.00	
0.50	2.19		1.44		1.64		1.02		1.02	
0.60	1.82		1.30		1.30		1.00		0.99	
0.75	1.34	1.93	1.11	2.08	1.08	2.01	0.97	2.07	0.99	2.15
0.90	1.29	1.95	1.21	2.00	1.09	2.01	1.09	2.07	1.09	1.98
1.00	1.34	1.93	1.15	1.95	1.08	1.98	0.99	1.94	0.98	2.10
1.25	1.25	1.86	1.06	2.02	0.95	2.03	1.07	1.80	1.01	1.97
$\hat{T}_1(obs)^\dagger$ (sec)	1.31	1.92	1.13	2.01	1.05	2.01	1.03	1.97	1.02	2.05
σ	0.04	0.03	0.06	0.05	0.06	0.02	0.05	0.11	0.04	0.08

Table 8.1: Variation of the spin-lattice relaxation time at 32 and 121 MHz of the free (α, β and γ) and complexed (α' and β') phosphorus resonances of ATP when the Al/ATP ratio was varied from 0 to 1.25. The T_1 measurement errors were typically 5%–10%. Experimental conditions were: $\nu_1 = 121$ MHz, $\nu_2 = 32$ MHz, [ATP] = 100 mM, pH = 7.4, 20% D_2O and at 21 °C. All solutions were carefully treated for the removal of paramagnetic ions (see Section 3.6). (†) $\hat{T}_1(obs)$ represents the average T_1 value for Al/ATP = 0.75. The error is given as one σ.

$\frac{Al(III)}{[ATP]}$	$T_1(P_\gamma)$ (sec)		$T_1(P_\alpha)$ (sec)		$T_1(P_\beta)$ (sec)		$T_1(P_{\alpha'})$ (sec)		$T_1(P_{\beta'})$ (sec)	
	ν_1	ν_2	ν_1	ν_2	ν_1	ν_2	ν_1	ν_2	ν_1	ν_2
0.00	1.1	1.0	1.4	1.8	1.0	1.0				
0.33	0.5	0.5	1.0	1.0	0.5	0.5	1.0	1.0	0.9	0.9
0.50	0.5	0.5	1.0	1.0	0.5	0.5	1.0	1.0	0.8	0.9
1.00	0.5	0.5	0.8	0.7	0.5	0.5	0.9	0.8	0.7	0.7

Table 8.2: ^{31}P–T_1 variation of the free and complexed ATP resonances as a function of the Al/ATP ratio at $\nu_1 = 121$ MHz and $\nu_2 = 32$ MHz for non purified samples. For further experimental conditions see Table 8.1.

already shown the tremendous dependency of phosphorus-31 spin-lattice relaxation times upon paramagnetic contamination [87,90] (see also Chapter 4). For example, ^{31}P spin-lattice relaxation times were recorded under the same conditions of Table 8.1, but for solution samples which were not treated for paramagnetic impurities. The results are presented in Table 8.2 at two different magnetic fields, for the free and complexed phosphates of ATP. In this study, the free α, β and γ phosphates did not show the T_1–Al/ATP ratio dependency observed in the case of purified samples (compare Table 8.1 and 8.2). As well, for each phosphate group, the field dependency was lost. These results stress that non-purified solution samples will undoubtably lead to erroneous T_1 measurements.

The NOE values are presented in Table 8.3 for Al/ATP = 0.75 and at two magnetic fields. At 121 MHz, the NOE values were too small (< 0.10) to be quantitatively measured with accuracy. However, at 32 MHz, higher NOE values permitted quantitative measurements (see Figure 8.6).

	P_γ		P_β		$P_{\alpha'}$		$P_{\beta'}$	
	ν_1	ν_2	ν_1	ν_2	ν_1	ν_2	ν_1	ν_2
$\hat{R}$(obs)† (sec^{-1})	0.76	0.52	0.95	0.50	0.97	0.51	0.98	0.49
σ	0.02	0.01	0.05	0.01	0.04	0.03	0.04	0.02
η_{obs}	≈ 0	0.21	≈ 0	‡	≈ 0	0.64	≈ 0	‡
σ		0.02				0.04		
R(P–H_2O) (sec^{-1})	0.09	0.09	0.06	0.06	0.03	0.03	0.03	0.03
σ	0.01	0.01	0.01	0.01	<0.01	<0.01	<0.01	<0.01
R(P–CH_2+H–3′) (sec^{-1})					0.15	0.30		
σ					0.01	0.02		
R(P–P) (sec^{-1})	0.01	0.05	0.02	0.11	0.01	0.05	0.02	0.11
R(CSA) (sec^{-1})	0.66	0.38	0.87	0.33	0.78	0.13	0.93	0.35
±	0.09	0.05	0.19	0.06	0.16	0.03	0.14	0.06

Table 8.3: Decomposition of the ^{31}P overall relaxation rates of the free (γ and β) and complexed (α' and β') resonances of the ATP_4Al_3 aggregate into the different operating sources of relaxation. Experimental conditions were: ν_1 = 121 MHz, ν_2 = 32 MHz, [ATP] = 100 mM, pH = 7.4, 20% D_2O and at 21 °C. (†) Each $\hat{R}_1$(obs) is taken from Table 8.1. (‡) NOE values could not be measured accurately due to overlapping resonances.

For example, the NOE value of the surface γ phosphate was measured as 0.21 $\pm$ 0.02 while the complexed α phosphate NOE value was 0.64 $\pm$ 0.04. It was not possible to detect the NOE values of the α and γ' phosphate nuclei separately since they had the same resonance frequency (the overall NOE observed was 0.40 $\pm$ 0.03). As well, the severe overlap of the β and β' resonances prevented an estimation of their respective NOE value (the overall NOE observed was 0.29 $\pm$ 0.02).

8.4 Discussion

The variations of the free and complexed ^{31}P spin-lattice relaxation times are displayed in Figure 8.7 at 121 MHz as a function of the Al/ATP ratio. As the Al/ATP ratio was varied from 0 to 0.75 the α, β and γ phosphates exhibited a similar T_1 variation which started from the T_1 values of the free ATP phosphates in solution (Al/ATP = 0) and linearly decreased until an Al/ATP ratio of 0.75 was reached. Above this latter value, no T_1 variation was observed for the α, β and γ phosphate resonances. Phosphorus-31 spin-lattice relaxation times confirmed, with acute sensitivity, the complex stoichiometry obtained by ^{31}P concentration studies (see Section 5.3.3). For 0 < Al/ATP < 0.75 there is quantitative formation of an ATP_4Al_3 complex in solution and, on the T_1 NMR time scale, there is a rapid exchange between a free ATP molecule in solution and a surface ATP molecule of the aggregate. The observed relaxation times represent an averaged T_1 value between a free and a surface phosphate nucleus. The T_1 value of a surface phosphorus-31 nucleus is given for Al/ATP $\geq$ 0.75 (see Table 8.1).

On the other hand, regardless of the value of the Al/ATP ratio, the two α' and β' complexed phosphates did not exhibit any variation in T_1 values and, on the T_1

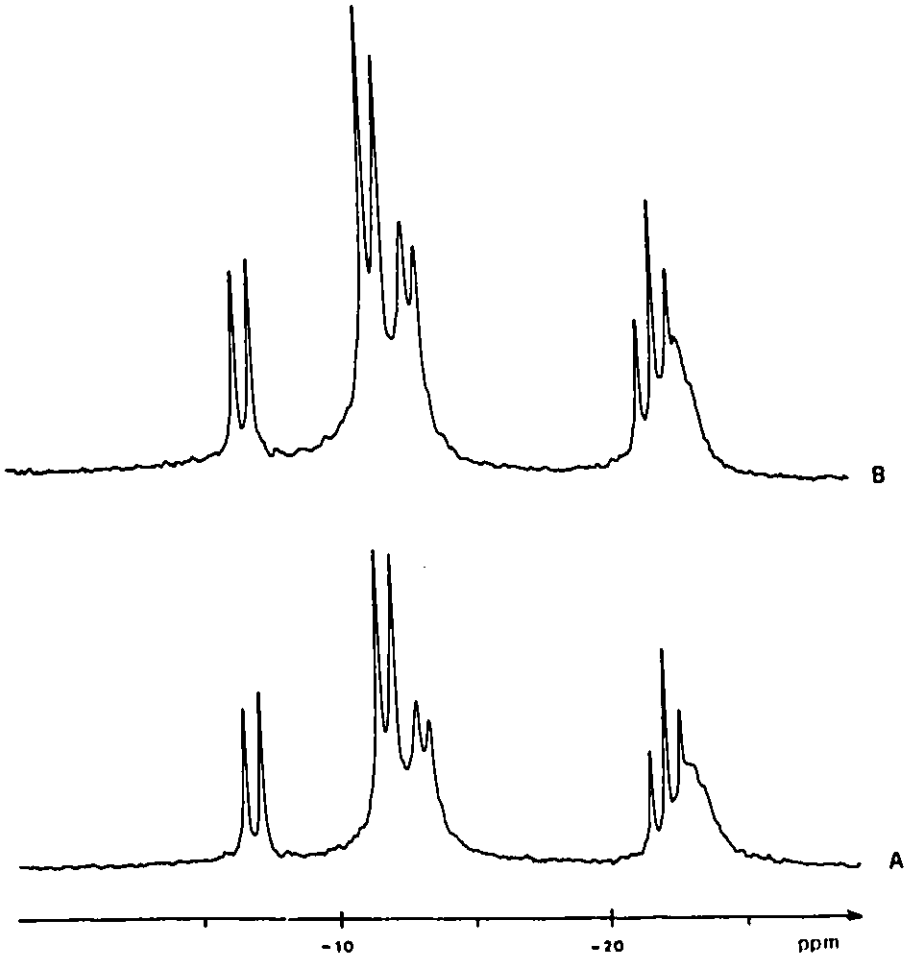

Figure 8.6: Proton decoupled ^{31}P Nuclear Overhauser Effects at 32 MHz of an ATP–Al solution for which the Al/ATP ratio was 0.90. For experimental conditions see Table 8.3. Instrumental conditions were: sweep width of 1000 Hz, acquisition time of 4 sec, pulse delay of 20 sec, 400 transients and 0.5 Hz line broadening. For spectrum (A) proton decoupling during the aquisition only, (B) full proton decoupling.

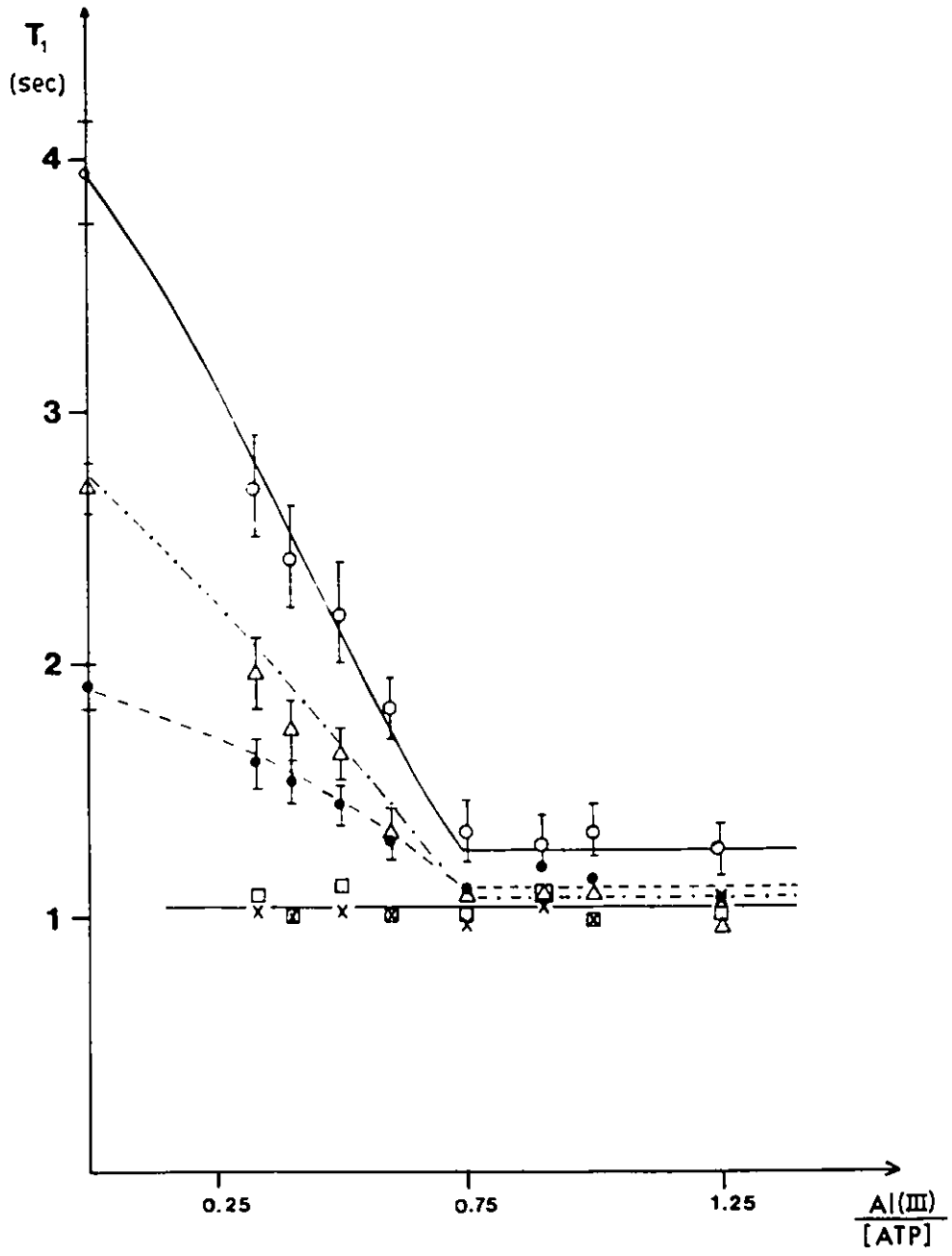

Figure 8.7: Variation of the spin-lattice relaxation times of the free α (•), β (Δ), γ (o) and complexed α' ($\times$) and β' ($\square$) phosphorus resonances of ATP versus the Al/ATP ratio at 121 MHz. For experimental conditions see Table 8.1.

NMR time scale, the resonances were in slow exchange with their respective "free" resonances. ^{31}P relaxation studies showed that the ATP–Al system could be described by a three-site chemical exchange, which was previously observed by ^{1}H chemical shift studies (see Section 6.2). In the first step, a free ATP molecule is in rapid exchange (k_1) with a surface ATP molecule of the aggregate which, in a second step, undergoes a slow exchange (k_2) with a complexed ATP molecule of the aggregate:

$$(\mathrm{ATP})^{free}_{solution} \xrightleftharpoons{k_1} (\mathrm{ATP})^{surface}_{aggregate} \xrightleftharpoons{k_2} (\mathrm{ATP})^{complexed}_{aggregate}$$

However, the free ATP molecules are not directly involved in chemical exchange with the complexed ATP molecule of the aggregate. In order to obtain meaningful information from the T_1 values of the complexed and surface ATP phosphate nuclei, the intrinsic relaxation times were required, that is the relaxation times free of any exchange contribution. For a three-site chemical exchange system of the form:

$$A \xrightleftharpoons{k_{AB}} B \xrightleftharpoons{k_{BC}} C$$

the equation of motion [226] of the longitudinal magnetization vector in each site i, may be written as:

$$\frac{d\,M_{zi}(t)}{dt} = P\,M_{zi}(t) \tag{8.1}$$

where P represents a 3 x 3 exchange matrix [226] given by:

$$P = \begin{pmatrix} -\frac{1}{T_{1A}} - k_{AB} & k_{BA} & 0 \\ k_{AB} & -\frac{1}{T_{1B}} - k_{BA} - k_{BC} & k_{CB} \\ 0 & k_{BC} & -\frac{1}{T_{1C}} - k_{CB} \end{pmatrix} \tag{8.2}$$

The solutions of the differential equation (8.1) are given by the eigenvalues of P and the corresponding eigenvectors [227]. The eigenvalues λ_i are found by solving the characteristic equation of P:

$$\det(\lambda I - P) = 0$$

where I represents the identity matrix. For a three-site chemical exchange, the eigenvectors are of the form [228]:

$$M_{zi}(t) = M_{zi}(0) + C_{1i}e^{-\lambda_1 t} + C_{2i}e^{-\lambda_2 t} + C_{3i}e^{-\lambda_3 t} \tag{8.3}$$

Since the resonance frequencies of the site A (the free ATP molecules in solution) and the site B (a surface ATP molecule of the aggregate) were identical in the ^{31}P NMR spectra, the magnetization detected during the acquisition was:

$$M_{zA}(t)+M_{zB}(t) = M_{zA}(0)+M_{zB}(0)+(C_{1A}+C_{1B})e^{-\lambda_1 t}+(C_{2A}+C_{2B})e^{-\lambda_2 t}+(C_{3A}+C_{3B})e^{-\lambda_3 t}$$

which, in an abbreviated notation, may be written as:

$$M_{zAB}(t) = M_{zAB}(0) + C_{1AB}e^{-\lambda_1 t} + C_{2AB}e^{-\lambda_2 t} + C_{3AB}e^{-\lambda_3 t} \tag{8.4}$$

while for the site C (the complexed ATP molecules of the aggregate):

$$M_{zC}(t) = M_{zC}(0) + C_{1C}e^{-\lambda_1 t} + C_{2C}e^{-\lambda_2 t} + C_{3C}e^{-\lambda_3 t} \tag{8.5}$$

Although the theoretical evolution of the longitudinal magnetizations in both sites is governed by three exponentially decaying functions, it is possible to derive [229] a theoretical apparent relaxation time $T_{1,app}$ for the recovery of $M_{zAB}(t)$ and $M_{zC}(t)$:

$$M_{zAB}(t) = M_{zAB}(0) + (C_{1AB} + C_{2AB} + C_{3AB})e^{-t/T_{1,app,AB}} \tag{8.6}$$

$$M_{zC}(t) = M_{zC}(0) + (C_{1C} + C_{2C} + C_{3C})e^{-t/T_{1,app,C}} \tag{8.7}$$

Since all the experimental ^{31}P T_1 values were derived by a non-linear regression analysis of a single exponential decay function (see Section 3.5), at this stage of the discussion the obtained T_1 values could only represent experimental apparent relaxation times. However, it was possible to assume that the obtained experimental apparent

relaxation times of the surface and complexed ATP molecules of the aggregate represented the true relaxation time of each site. For the three-site chemical exchange system under investigation, the rate constant $k_2 = 0.8\ s^{-1}$ was determined by 2D NMR (see Section 7.4), while ^1H NMR studies gave a lower limit for $k_1 \gg 40\ s^{-1}$ (see Section 6.2). Thus, the exchange matrix P is fully determined for any value of the Al/ATP ratio and resolution of equation (8.6) and (8.7) yielded two theoretical apparent relaxation times for the magnetization recovery of sites AB and C.

If the theoretical apparent relaxation times, obtained by the proposed full treatment, are identical to the experimental ones over the whole range of Al/ATP ratios, the assumption made earlier was true: the experimental apparent relaxation times are the true relaxation times of each site A, B and C.

Figure 8.7 displays the variation of the experimental apparent relaxation time data as a function of the Al/ATP ratio at 121 MHz. The full lines represent the theoretical apparent relaxation times obtained by solving equation (8.1) for each Al/ATP ratio. For each T_1 simulation, the true relaxation times of the sites A, B and C were taken from Table 8.1. For example, for the β phosphate, $T_{1A} = 2.69$ sec, $T_{1B} = 1.05$ sec and $T_{1C} = 1.02$ sec while the rate constants k_1 and k_2 were $1000\ s^{-1}$ and $0.8\ s^{-1}$ respectively. Figure 8.7 shows the very good agreement between the theoretical and experimental apparent relaxation times. Thus, the experimental relaxation time values were without exchange contributions and represented the true relaxation times of each site. Figure 8.8 shows what happens to the theoretical apparent relaxation times when the rate constant k_2 was chosen as ten times greater (- × -) or one hundred times smaller (- · -) than the experimental rate constant ((—), $k_2 = 0.8\ s^{-1}$). When the rate constant k_2 is $8\ ms^{-1}$, there is virtually no chemical exchange taking place between the sites B and C. The theoretical curves still fit the experimental

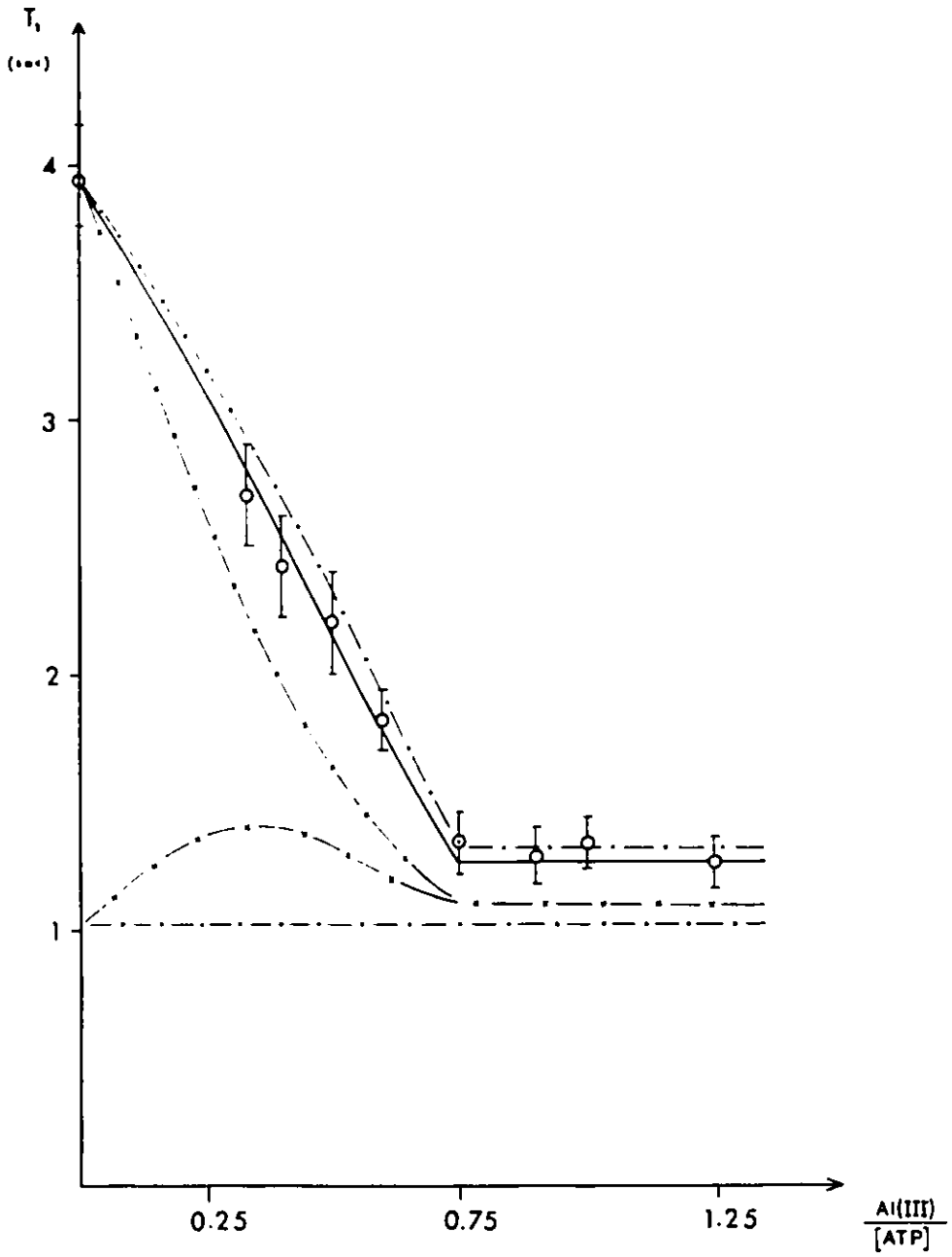

Figure 8.8: Variation of the theoritical apparent relaxation time of the free and complexed γ phosphates versus the Al/ATP ratio as a function of the exchange rate constant k_2 at 121 MHz. The open circles represent the experimental data points while the straight lines were the result of the full theoretical treatment (see equation 8.1). Conditions were as follows: the rate constant k_2 was chosen as 0.008 s^{-1} (- · -), 0.8 s^{-1} (---) and 8 s^{-1} (- × -), $k_1 = 1000\ s^{-1}$, $T_{1A} = 3.95$ sec, $T_{1B} = 1.31$ sec and $T_{1C} = 1.02$ sec in all cases.

data points, within the experimental errors. The chemical exchanges are very fast (between A and B) or very slow (between B and C) on the T_1 NMR time scale and the magnetization recovery of each site is mono-exponential. The apparent relaxation times in sites B and C are not perturbed by the exchange processes and represent the true relaxation times. However, if the exchange rate increases to 8 s^{-1}, the magnetization recovery becomes multi-exponential and the apparent relaxation times do not fit the experimental values (see Figure 8.8). Also, the apparent relaxation times in sites B and C are no longer equal to the true relaxation times of each site. The site B is mostly influenced by the chemical exchange which introduces a contribution of 16% to the true relaxation rate.

The T_1 analyses could be done using the T_1 values presented in Table 8.1 since the previous discussion has shown that they were not influenced by chemical exchange and represented the true phosphorus-31 spin-lattice relaxation times of each site. As the dynamics of the free phosphorus nuclei of ATP was already treated in detail in a separate chapter (see Chapter 4), the following section focuses on the T_1 and NOE analyses of the surface and complexed ATP molecules of the aggregate.

From a previous analysis of the ^{31}P spin-lattice relaxation times of ATP in solution (see Section 4.3), at least two relaxation mechanisms were expected to contribute to the overall relaxation rates: the heteronuclear phosphorus-proton dipole-dipole interaction and the chemical shift anisotropy (CSA) interaction. Finally, the homonuclear phosphorus-phosphorus dipolar interaction had to be examined due to the longer reorientational correlation time of the aggregate. The overall relaxation rate could be written as:

$$R(\text{obs}) = R(\text{P-H}) + R(\text{CSA}) + R(\text{P-P}) \qquad (8.8)$$

The detection of NOE effects at 32 MHz for all phosphate resonances confirmed that

phosphorus-proton dipolar relaxation was contributing to the observed relaxation rates. Table 8.3 summarizes the different phosphorus-proton interactions and NOE values for the surface (γ and β) and complexed (α' and β') ATP phosphates of the aggregate.

For an ATP molecule in solution, the origin of the NOE values was interpreted by a solvation model of the triphosphate chain moiety. It was shown that the first solvation sphere of the γ phosphate was composed of three water molecules while that of the β and α phosphates consisted of two water molecules. ^{1}H, ^{13}C and ^{31}P NMR spectroscopies have shown that the surface ATP molecule of the aggregate had many properties (chemical shift, spin-lattice relaxation time, CSA value, NOE effect) similar to a free ATP molecule in solution. As a result, the solvation model developed for a free ATP molecule was applied to a surface ATP molecule. Using the NOE value of Table 8.3 and equation (4.8) and (4.15), a correlation time characteristic of the P H_2O vector fluctuations of 88 $\pm$ 10 ps was calculated for a γ phosphate surrounded by three water molecules. This result is in accord with the previous value of 65 $\pm$ 16 ps for a free ATP molecule in solution (see Section 4.3) Finally, since the reorientation of the aggregate is thirty times slower in solution, this correlation represents an average residence time of the water molecules in the first phosphate solvation sphere. Based on this solvation model, the phosphorus-proton dipolar relaxation rate of the surface β, complexed β' and α' phosphates were calculated using equation (4.15) and are reported in Table 8.3. For the β' and α' complexed phosphates the existence of a P O Al bond reduced the number of water molecules present in the solvation sphere to one.

The more intense NOE value ($\eta_{obs} = 0.64$) of the α' phosphate reflected the participation of other phosphorus- proton dipolar interactions. For this nucleus,

three dipolar interactions were considered: the presence of one water molecule, ($\eta(H_2O) = 0.07$), and the CH_2 group and H-3′ proton ($\eta(CH_2 + H\text{-}3') = 0.57$) which have been shown to promote phosphorus relaxation (see Section 4.3). The appropriate description of the solution dynamics of the α′ phosphate required the use of an anisotropic reorientation model already introduced and described for ^{13}C relaxation analysis of the CH_2 group (see Section 6.3).

Figure 8.9 and 8.10 show the variation of the α′ phosphorus-proton dipolar relaxation rate and NOE factor respectively in the presence of internal rotation τ_G, and for an overall aggregate reorientational correlation time of 2.8 ns. These theoretical simulations were done by using equations (6.2) and (6.3), in which the phosphorus nuclei replaced the carbon nuclei, and by considering three protons located at an average distance of 2.8 Å [132,137] from the α phosphorus nucleus. The angle of internal rotation about the rotation axis was taken as 40° [100]. If an isotropic reorientation model was assumed ($\tau_G > 10^{-8}$ sec) the theoretical maximum NOE factor could have been only 0.39 much smaller than the experimental NOE value of 0.57. As well, the phosphorus-proton dipolar relaxation rate would have been 0.70 sec^{-1}, 40% higher than the observed overall relaxation rate. As a result, analysis of the dynamics of the α′ phosphate could not be described by a single correlation time reorientation model. The higher experimental NOE value showed that the internal rotation of the CH_2 group was much faster than the reorientation of the aggregate (see Figure 8.10). Using the anisotropic model introduced in Section 6.3, the correlation time for internal rotation of the P-H dipolar interactions was 90 ± 10 ps. This result is in good agreement with the analysis of ^{13}C spin-lattice relaxation time measurements which gave a correlation time of 75 ± 10 ps for the internal rotation of the CH_2 group.

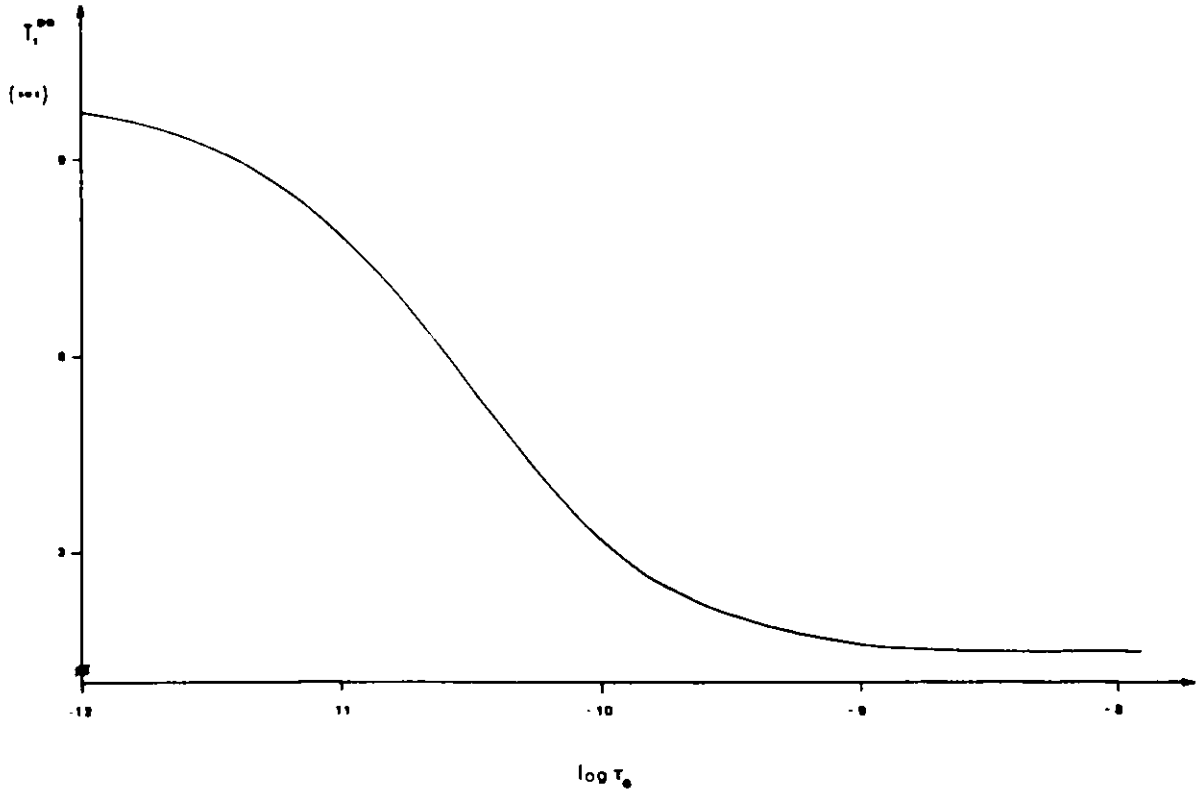

Figure 8.9: Plot of the dipolar ^{31}P spin-lattice relaxation time (T_1^{DD}) of an α phosphate group versus the logarithm of the internal rotational correlation time τ_G. The group is undergoing internal rotation while attached to a molecule with an isotropic rotational reorientation of $\tau_R = 2.8$ ns. The ^{31}P nucleus is relaxing by pure dipolar interactions with the CH_2 and H-3′ protons. Equation (6.2) was used for the simulation.

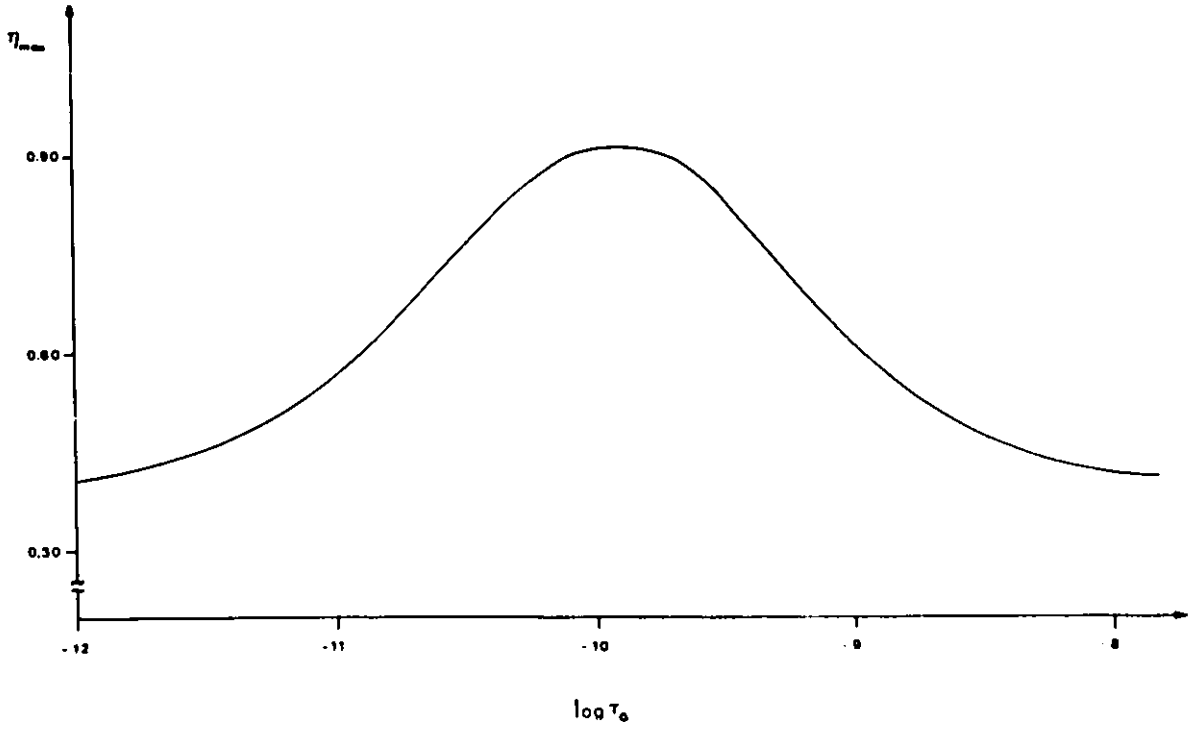

Figure 8.10: Plot of the ^{31}P-{^{1}H} Nuclear Overhauser Effect (η_{max}) for pure dipolar P–H relaxation versus the logarithm of the internal rotational correlation time τ_{C_i}. The group is undergoing internal rotation while attached to a molecule with an isotropic rotational reorientation of τ_R = 2.8 ns. Equation (6.3) was used for the simulation.

For a phosphorus nucleus of a triphosphate chain moiety slowly reorientating in solution, the homonuclear phosphorus-phosphorus dipolar interaction may not be negligible. This relaxation rate is given by (see Section 2.3.1):

$$R(\text{P–P}) = \frac{3}{2} n \hbar^2 \gamma_P^4 r^{-6} \tau_c$$

Using a phosphorus-phosphorus internuclear distance of $r = 2.95$ Å [96,116], and a correlation time of 2.8 ns, this homonuclear dipolar interaction accounted for a relaxation rate of 0.05 s^{-1} and 0.01 s^{-1} per phosphorus nucleus at 32 and 121 MHz respectively (see Table 8.3). Finally, the last relaxation mechanism to be considered was the CSA mechanism, well known to induce phosphorus-31 spin-lattice relaxation. From equation (8.8) the CSA relaxation rate values, reported in Table 8.3, were readily accessible:

$$R(\text{CSA}) = R(\text{obs}) - R(\text{P–P}) - R(\text{P–H}) \tag{8.9}$$

with:

$$R(\text{CSA}) = \frac{2}{15} \omega_0^2 (\Delta\sigma)^2 \left(1 + \frac{\eta^2}{3}\right) \tau_c \tag{8.10}$$

At 32 MHz, the CSA relaxation rates were all smaller than at 121 MHz, showing the field dependency expressed in equation (8.10). Using this equation and a phosphorus correlation time of 2.8 ns, the CSA values ($\Delta\sigma \left(1 + \frac{\eta^2}{3}\right)^{1/2}$) of the surface ($\gamma$ and β) and complexed (β' and α') phosphates could be calculated. Table 8.4 summarizes the CSA results obtained for the aggregate and for a free ATP molecule in solution (see Table 4.7). Two general trends were apparent from the data. Firstly, the phosphate CSA values of a surface ATP molecule were, within experimental error, similar to the CSA values of a free ATP molecule in solution. For example, for the γ phosphate, CSA(free) = 140 - 150 ppm which is comparable to CSA(surface) =

$\Delta\sigma(1+\frac{\eta^2}{3})^{\frac{1}{2}}$ (ppm)	P_γ	P_β	P_α
Surface ATP	130–180	150–180	
Complexed ATP		150–170	110–140
Free ATP	140–150	210–220	250-260

Table 8.4: ^{31}P chemical shift anisotropy values in the ATP_4Al_3 aggregate compared to the chemical shift anisotropy values in a free ATP molecule in solution (see Table 4.7). For experimental conditions see Table 8.1.

130 – 180 ppm. This confirmed that in the aggregate, the triphosphate chain moiety of the surface ATP molecule is not directly complexed to an aluminum cation, but is probably linked to the cation via the phosphorus water solvation sphere. As a result, the chemical environment of each phosphate group was not perturbed enough to create a noticeable change in the CSA values, or in their ^{31}P chemical shift values. As a consequence, the free and surface phosphorus nuclei appeared at the same resonance frequency in the NMR spectra. The second general trend concerns the CSA values of the complexed phosphate groups which were slightly smaller than in a free ATP molecule. The α phosphate showed the most pronounced difference with CSA(complexed) = 110 – 140 ppm while CSA(free) = 250 - 260 ppm.

8.5 Conclusion

In a concentration study, phosphorus–31 spin-lattice relaxation studies confirmed with accute sensitivity, the aggregate stochiometry obtained by ^{31}P quantitative measurements (see Section 5.3.3). As well, the experiments showed that ATP–Al interactions can be described as a three-site chemical exchange, previously observed by ^1H

chemical shift studies. Simulations of the recovery of the longitudinal magnetization in the presence of chemical exchange showed that the experimental ^{31}P spin-lattice relaxation time values were not affected by chemical exchange. Phosphorus-proton and phosphorus-phosphorus dipolar interactions, as well as chemical shift anisotropy represent the different dynamic contributions for the observed relaxation rates of the three phosphate groups of ATP. Finally, analysis of the molecular dynamics of the α phosphate showed that the reorientation of the P–CH_2 and P–H–3′ dipolar interactions were anisotropic. The internal dynamics of the aggregate determined by ^{31}P NMR relaxation experiments was in accord with ^{13}C results (see Section 6.3).

Chapter 9

ALUMINUM-27 NMR PROBING ATP-ALUMINUM INTERACTIONS IN QUEOUS SOLUTION

9.1 Introduction

Despite the fact that aluminum-27 is a quadrupolar nucleus with a nuclear spin of 5/2, it possesses some favorable physical properties that make it a very attractive nucleus for the NMR spectroscopist. With a natural abundance of 100%, a relative receptivity of 0.206 compared to protons, a relatively small quadrupole moment of 0.149 Barn and a chemical shift range which spans over 260 ppm [230], one is indeed tempted to use this nucleus as a probe for determination and characterization of different sites of complexation or different species present in solution.

The actual picture is darkened however, by its quadrupolar relaxation mechanism which, under loss of octahedral or tetrahedral molecular symmetry, occasionally produces broad lines of up to several kilohertz in width. In extreme cases, the signal may even disappear into the baseline noise. Although severe quadrupolar line broadening represents a serious spectroscopic disadvantage, it is partially compensated by

the additional information gained about the environment and molecular symmetry present around the nuclei. For example, an aluminum nucleus surrounded by substituents in a perfect cubic symmetry arrangement will yield very sharp lines [231]. This is the case of the widely used aqueous aluminum reference $Al(H_2O)_6^{3+}$ which exhibits a typical linewidth of 4 Hz [232]. Deviations from cubic symmetry around the aluminum atom by either Al–X bond distortions or ligand (X) replacements in the aluminum coordination sphere, to give multidentate complexes, results in an increase of the electric field gradient (*efg*) and a concomitant linewidth broadening.

Aluminum-27 chemical shifts are, with a few exceptions, dependent upon the molecular symmetry about the nucleus. This chemical shift-coordination number relationship represents some interesting potential, particularly in chemical symmetry investigations. For example, using ^{27}Al NMR, a clear distinction can be made between octahedral (– 40 to + 20 ppm) and tetrahedral (+ 60 to + 110 ppm) species [230].

Using ^{27}Al linewidths and chemical shifts, a pair of powerful NMR parameters, the spectroscopist is able to characterize the ligand molecular symmetry and chemical environment of the nucleus. The use of this quadrupolar nucleus as a probe to investigate the nature of ATP–Al interactions was a logical and appropriate choice. This chapter will discuss the nature of complexes formed between aluminum and ATP by means of ^{27}Al NMR at two different fields (21 and 78 MHz). A concentration study, in which the ATP/Al ratio was varied from 0.60 to 3.0, revealed the presence of different aluminum species in solution at pH = 7.4. By using a spectral deconvolution technique, each species has been successfully assigned and quantitatively measured.

Theoretical treatment of a spin 5/2 spin-lattice and spin-spin relaxation in the non-extreme narrowing conditions, including the effects of Dynamic Frequency Shifts (DFS) are examined in detail and will allow determination of the Quadrupole Cou-

pling Constant (QCC) of the aluminum implicated in the ATP_4Al_3 aggregate.

9.2 Experimental Approach to ^{27}Al NMR

In multinuclear magnetic resonance spectroscopy, chemical shifts have to be measured accurately in order to allow full use and comparison of reported values in the literature. The spectroscopist also needs a common sample reference for which the concentration, the kind of salt used, solvent, temperature and pH of the solution are clearly specified [114].

In the case of aluminum, many authors have used the widely accepted $Al(H_2O)_6^{3+}$ reference without reporting the concentration, pH or the salt utilized for their referencing. This crucial problem of referencing has already been mentioned [230] and is believed to be responsible for some chemical shift discrepancies amounting up to 5 ppm! In order to remedy this problem, a solution of 0.2 M aluminum perchlorate and 0.1 M perchloric acid was recently proposed [230] as a common standard reference for ^{27}Al NMR. To date, this reference has not received much attention from spectroscopic laboratories, possibly because of the handling precautions necessary for the preparation of this solution. Instead, all ^{27}Al chemical shifts could be referenced to an hexa-aquated aluminum cation at infinite dilution to prevent any anions effects [232]. In the case of ^{27}Al NMR, this criteria is met for a solution of 50 mM anhydrous $AlCl_3$ in 100% D_2O, T = 22 °C, at pH = 2.0 and has been used as a reference to express all chemical shift values reported in this study. Under these conditions, the ^{27}Al linewidth is sharp (4 Hz). Dilution of this solution to 1 mM $AlCl_3$, 100% D_2O and pH = 2.0 did not change the aluminum chemical shift, nor its linewidth value. The chemical shift difference between a 1 M and 50 mM aqueous $AlCl_3$ solution under the same conditions of pH and D_2O content was measured as 0.508 ppm.

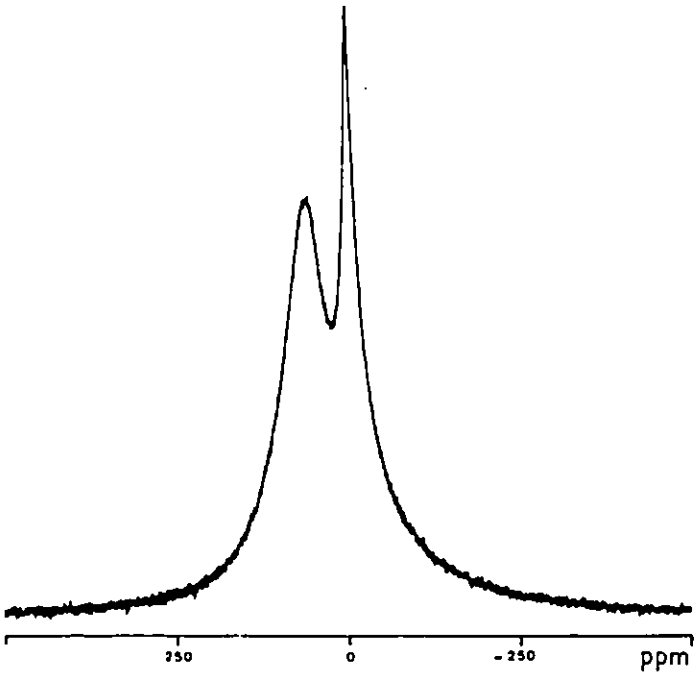

Figure 9.1: ^{27}Al spectrum of an ATP–Al aqueous solution at 78 MHz for which the ATP/Al ratio was 0.60. Instrumental conditions were: spectral width of 100 KHz, aquisition time of 0.02 sec, 100,000 transients, α delay of 0 and 20 Hz line broadening. For experimental conditions see Table 9.1.

At 78 MHz, ^{27}Al NMR performed on the ATP–Al system typically results in an extremely broad spectrum, which spans over 100 ppm and is composed of at least two resonances (Figure 9.1). As a result, a spectral window of 100 KHz is necessary to prevent folding of the Lorentzian wings. In the liquid state, such situations are rarely encountered. For the spectroscopist whose desire is to gain quantitative information about different species in solution, such experimental situations raise some questions about the experimental capabilities of the NMR instrument. For example, it was pertinent to know if the spectral power of irradiation was uniformly distributed over the spectral window of interest, preventing distorted quantitative results. Such information can be obtained by successively shifting the frequency carrier over the entire sweep width and recording the reference sample spectrum each time. Figure 9.2

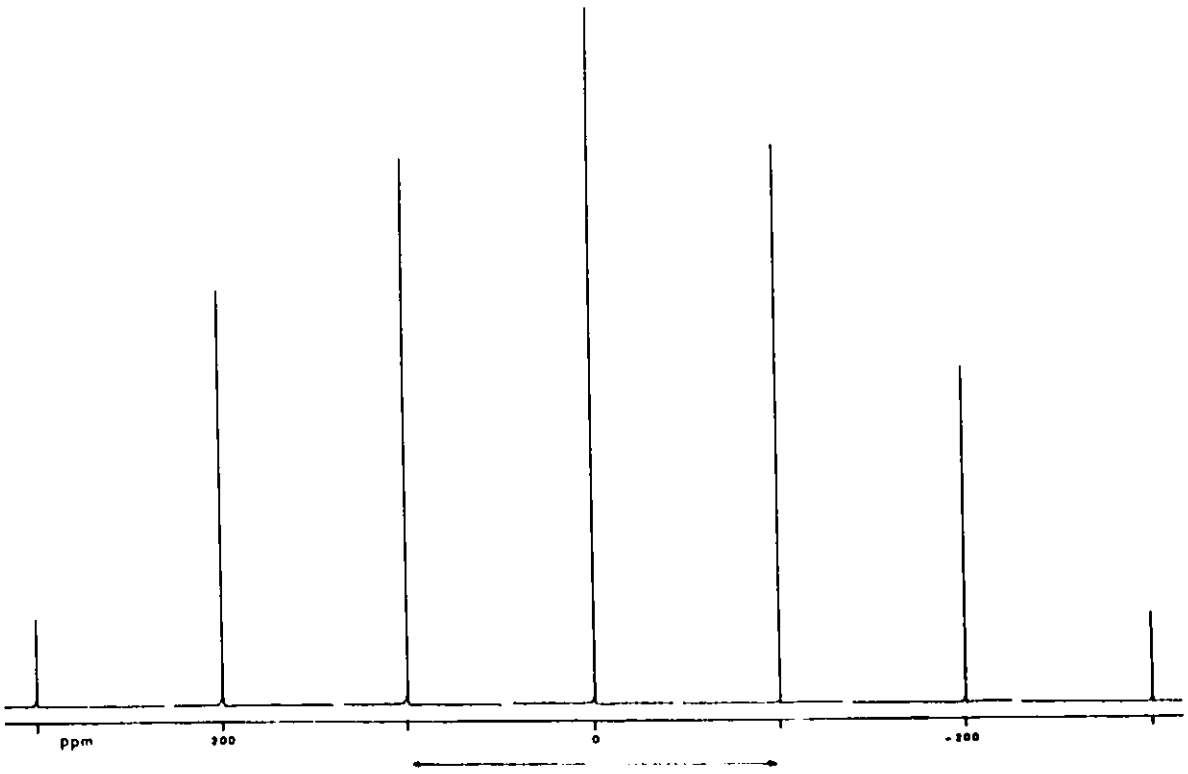

Figure 9.2: ^{27}Al spectral power distribution at 78 MHz using the reference sample solution. For each spectrum, the transmitter frequency was successively shifted by 10 KHz.

shows that the spectral power distribution available at 78 MHz is far from being uniform over the entire sweep width of 600 ppm. In fact, it can be seen that, at both ends of the spectrum, the pulse power available is almost inexistent. Fortunately, there exists a spectral window of 200 ppm located in the middle of the spectrum and indicated by two arrows, in which the pulse power distribution is constant to $\pm$ 5%. The same experiment was performed at 21 MHz to insure proper instrumental performance and is presented in Figure 9.3. The two arrows delimit a spectral region of 160 ppm in which the pulse power distribution is constant to $\pm$ 6%. At both fields, a constant pulse power distribution was then insured over a spectral window

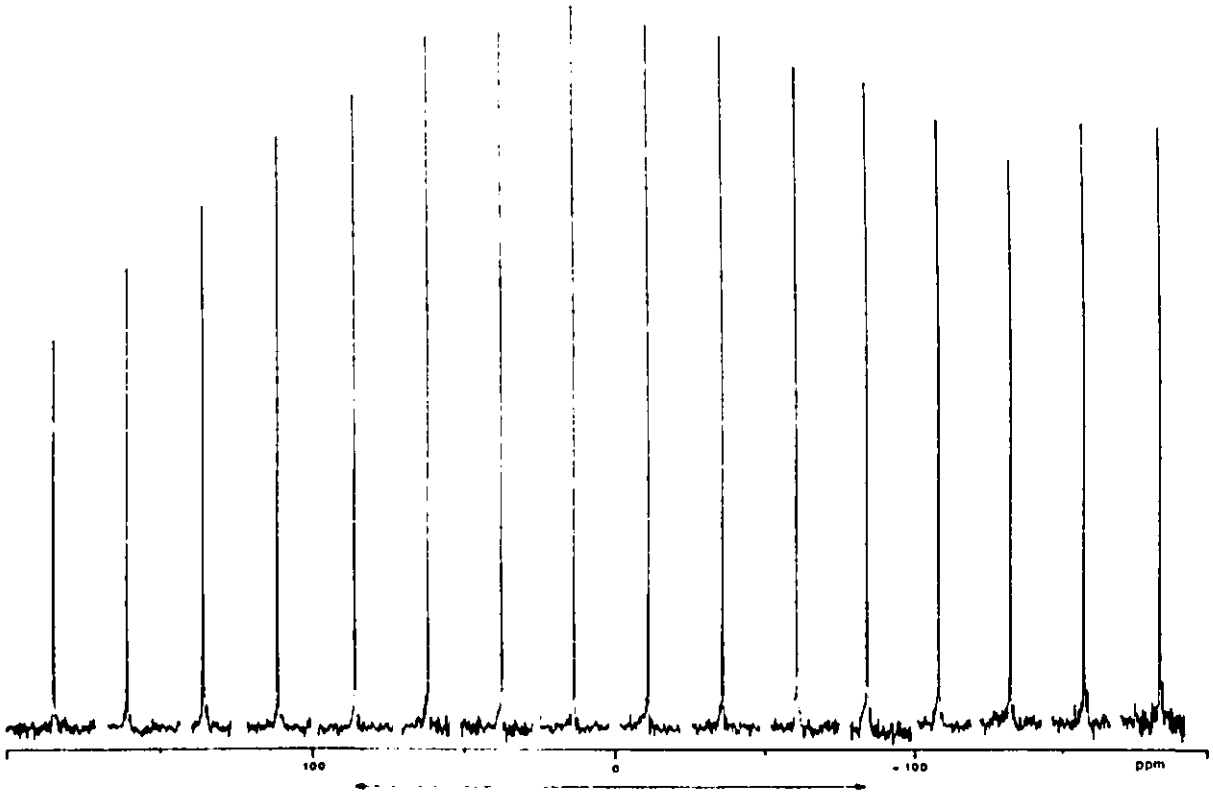

Figure 9.3: ^{27}Al spectral power distribution at 21 MHz using the reference sample solution. For each spectrum, the transmitter frequency was successively shifted by 1 KHz.

of 160 ppm, much greater than the required experimental chemical shift range of 100 ppm. As a consequence, the true relative peak intensities were observed and quantitative measurements were expected to be significant.

After a 90° excitation pulse, it is usually common to wait for a short period of time before the digital recording of the magnetization [114]. The length of this delay varies depending upon the nuclei under study and the spectrometer capabilities. Without any delay and for low γ nuclei (for example ^{39}K, ^{43}Ca, and ^{67}Zn) the 90° pulse is usually followed by a more or less intense response of the probe, called acoustic ringing [239]. This introduces a strong baseline waviness in the NMR spectrum and represents some severe limitations to the analysis of very broad spectra. In order to cancel such undesirable effects, a delay of about 20 to 100 μs is generally introduced before data acquisition. Specific pulse sequences have been suggested to get rid of the acoustic ringing, and have been successfully applied to ^{67}Zn for example [240]. In the case of ^{27}Al NMR such annoying effects have never been previously reported in the literature, and it was important to verify that acoustic ringing was not present to perturb the baseline of the experimental spectra.

Figure 9.1 shows a typical ATP–Al spectrum recorded with a 90° pulse, without using any delay before the sampling of the magnetization began. No phasing problems were encountered and the spectrum displayed a clean baseline precluding the existence of any acoustic ringing or baseline distortions. These results represented an attractive instrumental capability of the spectrometer when dealing with broad absorption lines. The magnetization could be sampled immediately after the 90° pulse, cancelling any relaxation effects taking place during the spectrometer dead time (the delay between the 90° pulse and the data acquisition), or simply preventing the loss of information of very broad lines. Working without the necessity of

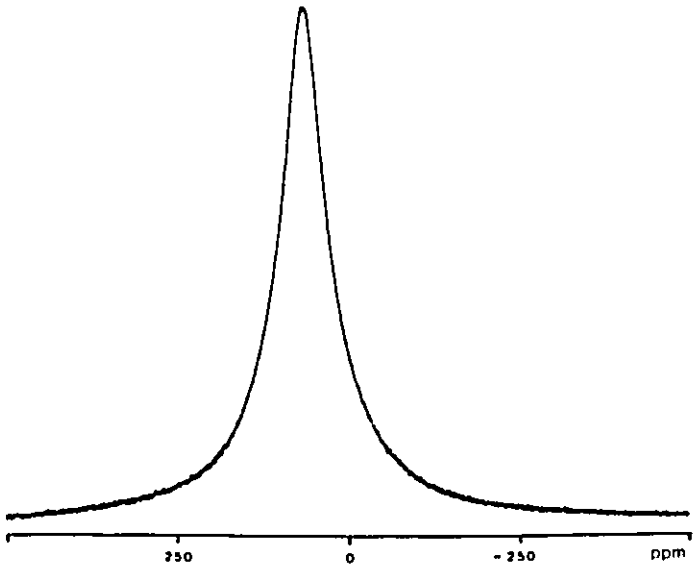

Figure 9.4: ^{27}Al spectrum of the probe resonance at 78 MHz. No solution sample was introduced into the NMR probe head. Instrumental conditions were as in Figure 9.1.

using a spectrometer dead time also represented some advantages for quantitative measurements, as no correction for peak intensities, due to relaxation effects, was required for resonances with different T_2 relaxation. It was surprising to sample the FID under such conditions without recording any interfering signal. An easy way of verifying that there was no baseline distortion or undulation introduced in the spectrum of Figure 9.1 was to record a blank sample.

The result of this experiment was quite spectacular and is shown in Figure 9.4. Although no baseline distortion was observed over the entire spectral window, a very broad resonance appeared in the spectrum, centered at 61.9 $\pm$ 0.3 ppm with a linewidth of 6.8 $\pm$ 0.1 KHz. This resonance can be assigned to aluminum-silicates or aluminates present in the probe that have chemical shifts which fall in the range of 55 to 80 ppm, depending upon the degree of aluminum branching or silicon present in the aluminum second coordination sphere [262,263]. Detection of the aluminum probe

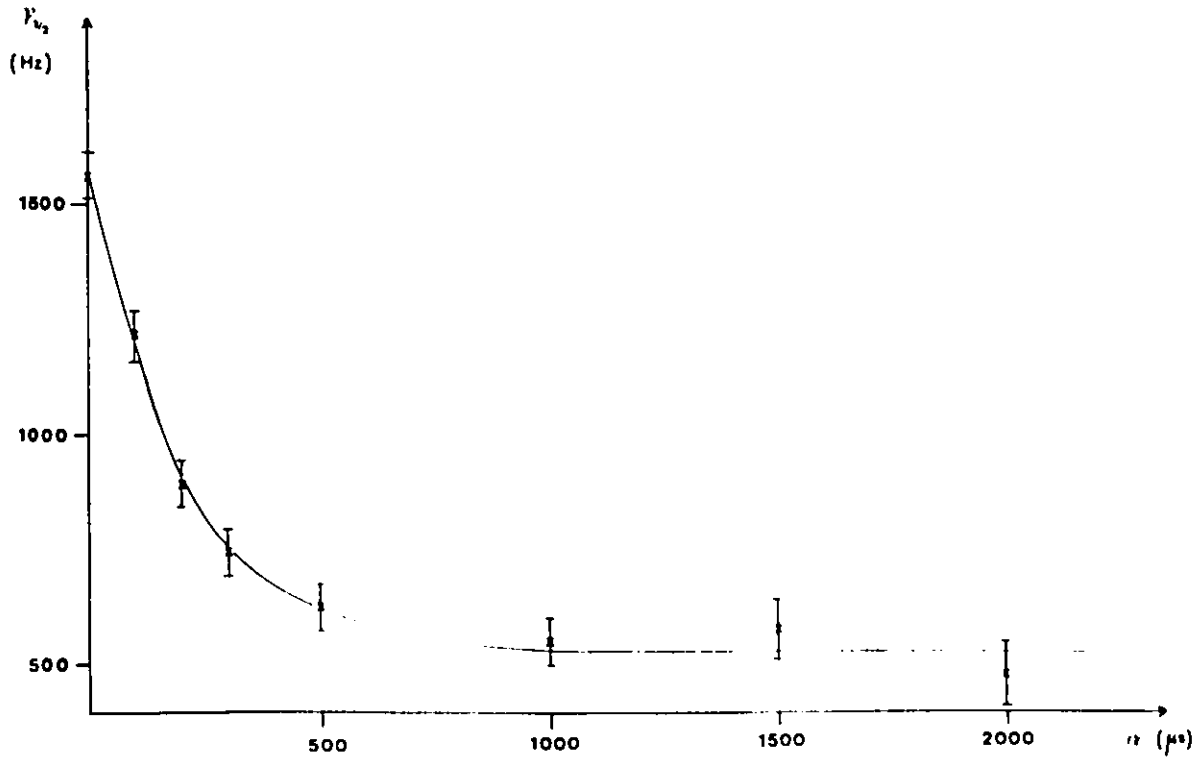

Figure 9.5: Linewidth variation of the central peak as a function of the spectrometer dead time (α delay) at 78 MHz. The ATP/Al ratio was 1.0. Instrumental conditions were as in Figure 9.1. For experimental conditions see Table 9.1.

head signal has already been mentioned in the literature [236,237] and constitutes a serious problem in certain cases. This resonance can also be clearly seen in Figure 9.1 and significantly contributed to give misleading ATP-Al spectrum. In order to attenuate or eventually cancel this resonance, the spectrometer dead time was steadily increased from 0 to 2000 μs.

The effect of this time delay variation on the overall appearance of the ATP Al spectrum was quantified by measuring the apparent linewidth of the central peak of interest versus the spectrometer dead time, called α. Figure 9.5 summarizes this experiment. For $\alpha = 0$ the apparent linewidth of the central peak, which overlaps

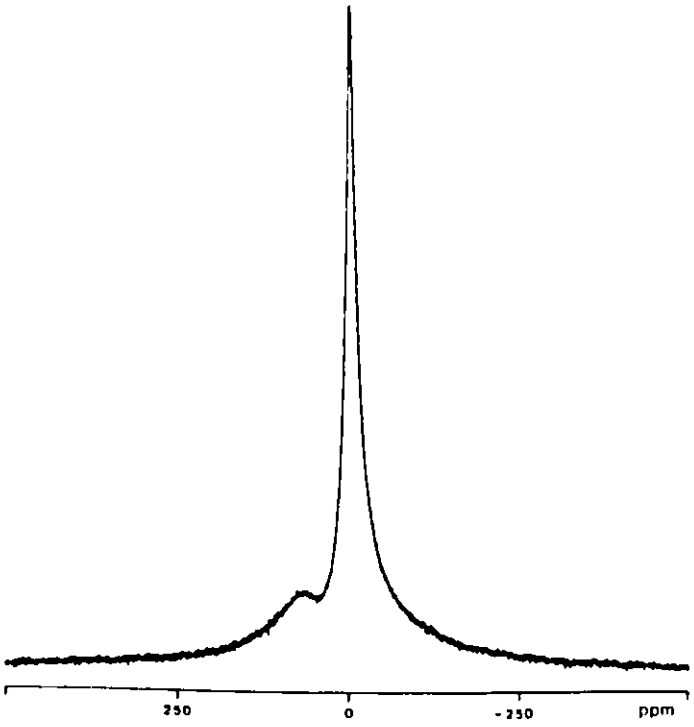

Figure 9.6: General appearance of an ^{27}Al spectrum at 78 MHz for a spectrometer dead time (the α delay) of 0. The ATP/Al ratio was 1.0. Instrumental conditions were as in Figure 9.1. For experimental conditions see Table 9.1.

quite extensively with the probe resonance, was 1560 ± 50 Hz (see Figure 9.6). As the α delay was increased, a sharp decrease in linewidth was observed, which finally reached a constant value of 530 ± 50 Hz for α values greater than 1000 μs (see spectrum B of Figure 9.7). It is interesting to note that, even though the probe resonance was not detected for α values greater than 100 μs, (see spectrum A of Figure 9.7), a further increase of the α delay resulted in still further decrease of the remaining resonance linewidth. This indicates that the broad resonance of interest, centered at 0 ppm (see spectrum A of Figure 9.7) was composed of at least two Lorentzians.

Aluminum-27 NMR on this system raises a conflicting choice: the spectroscopist

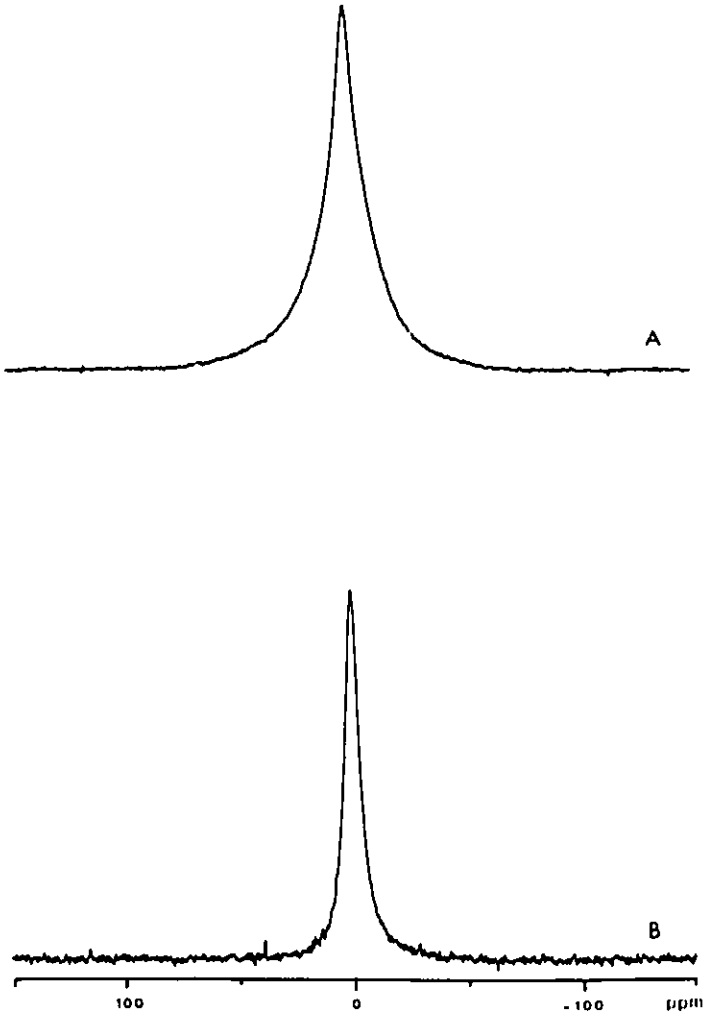

Figure 9.7: General appearance of an ^{27}Al spectrum as a function of the spectrometer dead time (the α delay) at 78 MHz. The ATP/Al ratio was 1.0. For A) $\alpha = 100$ μs and B) $\alpha = 1000$ μs. Note the spectral width differences between these two spectra and the spectrum of Figure 9.6. For experimental and instrumental conditions see Table 9.1 and Figure 9.1 respectively.

is faced with the embarrassing situation of detecting a probe resonance but recording quantitative spectra (when $\alpha = 0$) or, cancelling this parasitic resonance (when $\alpha > 100$ μs) but, at the same time, risking the loss of information about other very broad resonances present in the spectrum. Since obtaining information about ^{27}Al spectra will necessitate deconvolution of overlapping resonances, the quantitative method ($\alpha = 0$) was chosen to study the ^{27}Al NMR spectra of ATP–Al interactions in solution. This method was particularly appropriate for our experiments, as the removal of the probe resonance would also have cancelled two other resonances of importance (see later), as they had similar spin-spin relaxation times.

In the case of the FT–80 Varian spectrometer, the setting of the spectrometer dead time also greatly influenced the appearance of the NMR spectra. Although the probe resonance was never detected, the choice of a too short dead time ($\alpha < 100$ μs) resulted in wide baseline undulations, superimposed on a broad NMR signal. In fact, even for a relatively long delay ($\alpha = 600\mu$s) successive NMR spectra of the same solution gave, most of the time, irreproducible line shapes (See spectrum A and B of Figure 9.8). Spectrum A exemplifies a typical example of a line shape with "contamination" in comparison to spectrum B which displays a clean resonance. The experiment shows that reproducible linewidth values are obtained when $\alpha \geq 1500$ μs (see spectrum C of Figure 9.4.3). At 21 MHz, this long dead time was used for the recording of ^{27}Al NMR spectra of ATP–Al solutions (see Table 9.2).

9.3 Spectral Deconvolution Procedure

As the Aluminum-27 spectra were composed of broad overlapping resonances, they have been submitted to data processing in order to extract information like the chemical shift and linewidth of each resonance. Deconvolution processes have already been

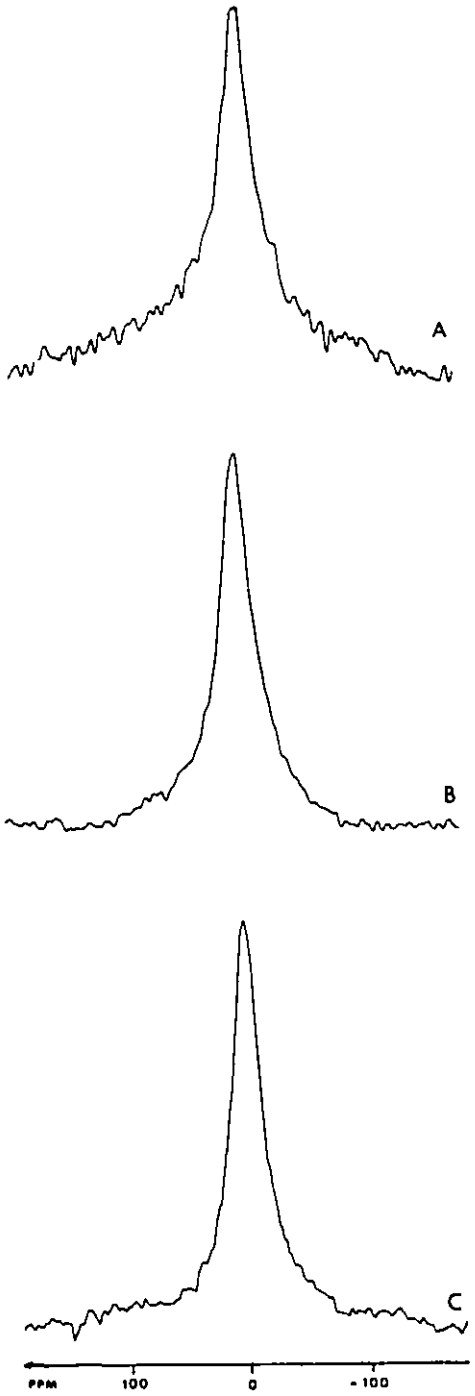

Figure 9.8: General appearance of an ^{27}Al spectrum as a function of the spectrometer dead time (the α delay) at 21 MHz. The ATP/Al ratio was 0.60. For A) and B) α = 600 μs and C) α = 1500 μs. Instrumental conditions were: spectral width of 8 KHz, acquisition time of 0.01 sec, typically 300,000 transients and 10 Hz line broadening. For experimental conditions see Table 9.1.

successfully applied to ^{27}Al spectra of aluminum halides [238,239,240] and represented the data processing choice of this study. The method of deconvoluting a spectrum is based on how many Lorentzian lines are *sufficient* and *necessary* to reproduce the experimental spectrum. For a spectrum composed of n lines, a program routinely finds the chemical shift and linewidth of each resonance so as to simulate a spectrum identical to the observed experimental one. The spectral deconvolution program, written in Fortran was based on a routine which optimized the input parameters in order to minimize the difference between the simulated and experimental spectrum. Using a plotter routine, the resulting optimized parameters were used to generate each resonance. The overall simulated spectrum was then compared to the experimental spectral data points, taken as the input for the deconvolution procedure. The initial experimental approach to determine the number of resonances used to simulate the experimental spectra will now be discussed.

At the beginning, two lines were utilized for the deconvolution procedure. The result, shown in Figure 9.9, indicates clearly that the experimental spectrum cannot be deconvoluted in a satisfactory manner with only two resonances. The introduction of a third Lorentzian was necessary and Figure 9.10 displays the deconvolution result. We obtained three broad resonances centered at + 83 ppm (the probe resonance), 1.3 and - 14.9 ppm with characteristic linewidths of 1.3 and 5.5 KHz respectively.

Although the overall deconvolution appears to be satisfactory with three lines, the experimental slowly relaxing resonance ($\mathcal{V}_{1/2}$ = 590 Hz, see Table 9.2) observed when the spectrometer dead time is increased to 1000 μs was not obtained. The effect of setting the delay to 1000 μs killed any fast relaxing component of the spectrum except the slowly relaxing resonance still detectable. This experimental resonance had to be introduced into the deconvolution procedure which then called for four

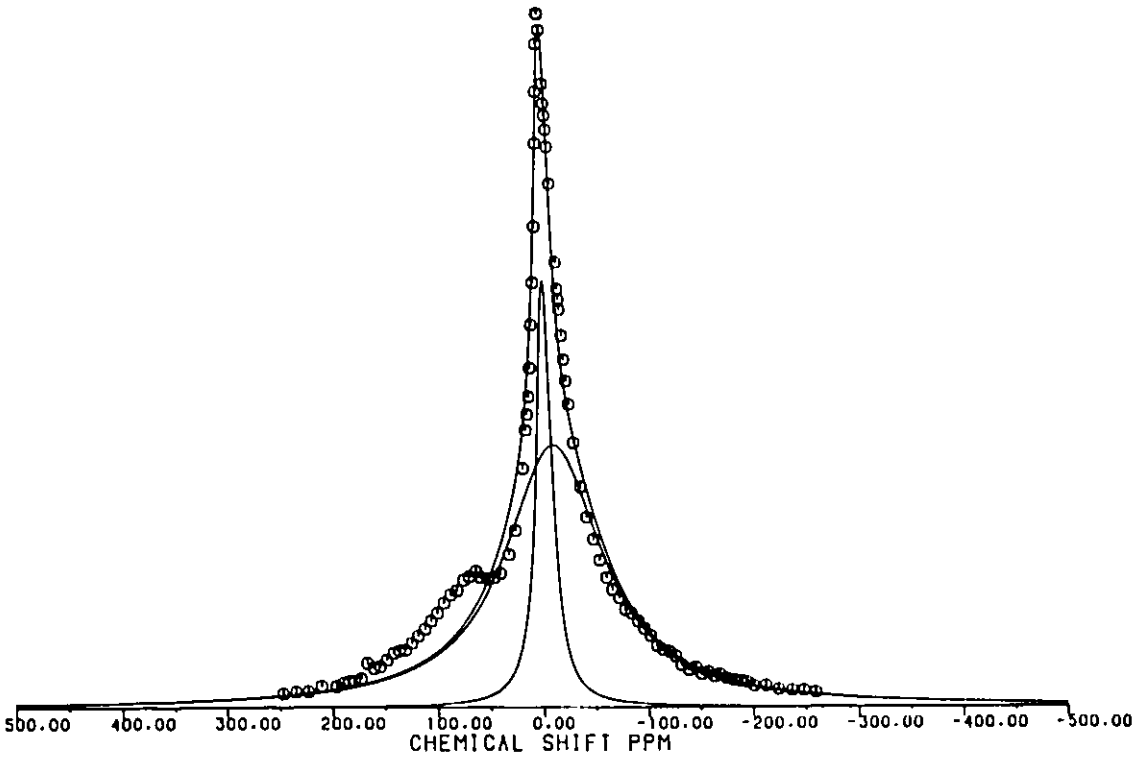

Figure 9.9: Deconvolution of an ^{27}Al NMR spectrum at 78 MHz assuming that it is composed of only two Lorentzian lineshapes. The ATP/Al ratio was 0.80. The circles represent the experimental data points taken as the input for the deconvolution procedure (see Section 9.3).

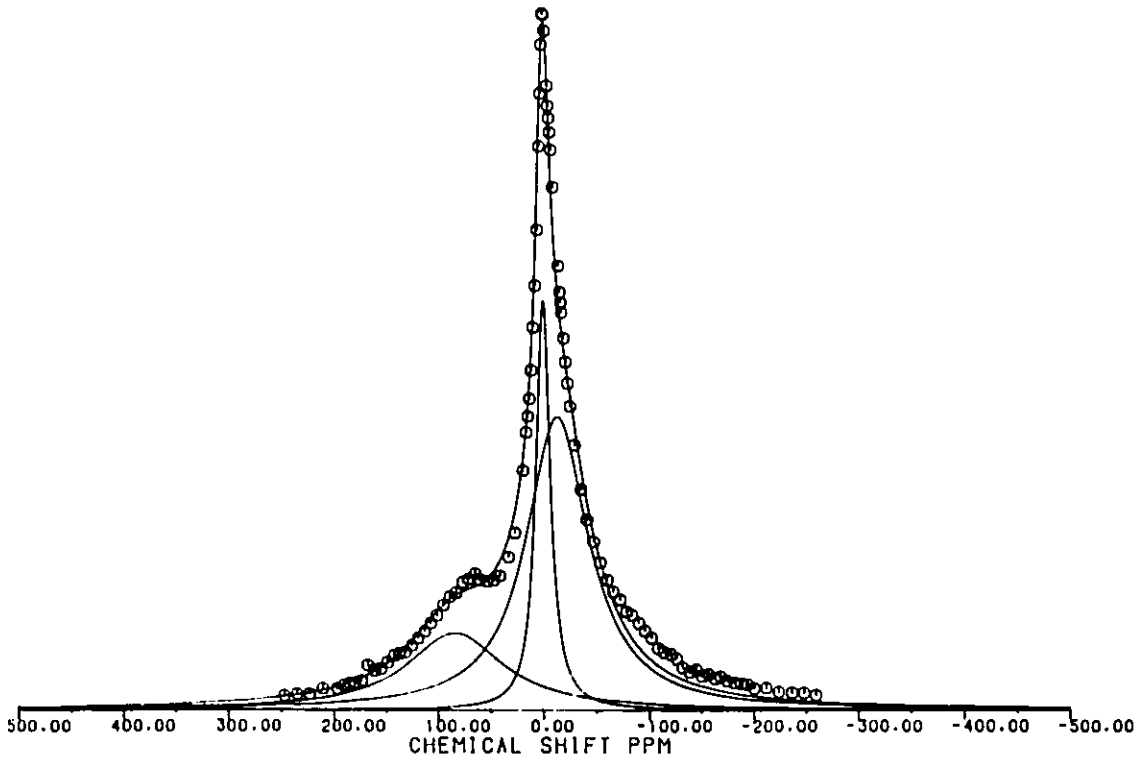

Figure 9.10: Deconvolution of an ^{27}Al NMR spectrum at 78 MHz assuming that it is composed of three Lorentzian lineshapes. The ATP/Al ratio was 0.80. The circles represent the experimental data points taken as the input for the deconvolution procedure (see Section 9.3).

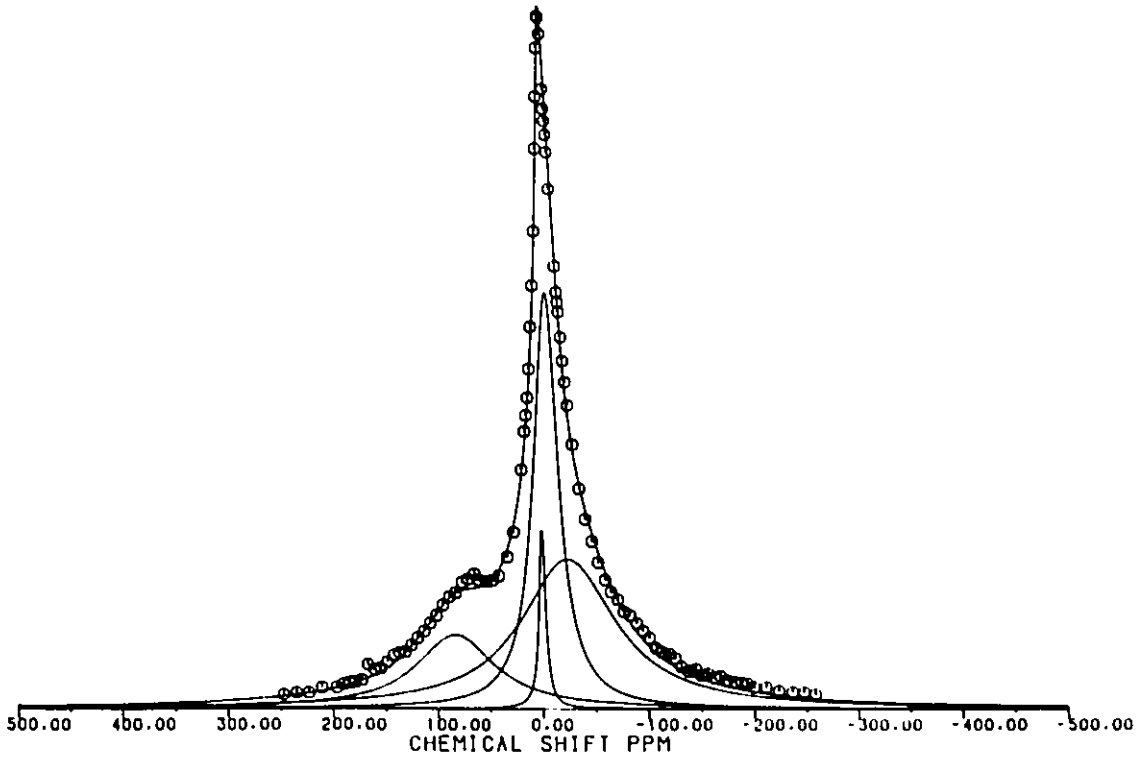

Figure 9.11: Deconvolution of an ^{27}Al NMR spectrum at 78 MHz assuming that it is composed of four Lorentzian lineshapes. The ATP/Al ratio was 0.80. The circles represent the experimental data points taken as the input for the deconvolution procedure (see Section 9.3). The linewidth of the fourth Lorentzian lineshape, given by the experiment when $\alpha \geq 1000$ μs (see Table 9.2), was kept constant during the deconvolution procedure.

Lorentzians (see Figure 9.11) to account for our experimental data. The linewidth of the most narrow experimental resonance (see Table 9.2) was kept constant in the deconvolution procedure, while its chemical shift value was entered as a variable. As a result, ^{27}Al spectral deconvolutions were carried out using four Lorentzian resonances which required the optimization of eleven parameters (intensity, chemical shift and linewidth for each resonance). Spectral deconvolutions using five resonances were tried, but did not give satisfactory results except for ATP/Al = 1.40 (see Table 9.1).

The fifth resonance was either shifted to extreme chemical shift values or resulted in negative intensity or linewidth values.

9.4 Nuclear Spin Relaxation of a Spin 5/2 in Non-Extreme Narrowing Conditions

9.4.1 Evolution of the Transverse and Longitudinal Magnetization

From phosphorus-31 NMR studies (see Section 5.3.5), it was possible to determine the correlation time, $\tau_c = 2.8$ ns, of the ATP_4Al_3 aggregate in solution. Thus, working at an aluminum-27 resonance frequency of 78.2 MHz implied a product $\omega_0\tau_c$ of 1.38 and the extreme narrowing conditions were not satisfied anymore. Under these conditions, not only the expression of the quadrupolar spin-lattice and spin-spin relaxation times (see Section 2.4.2) were no longer valid, but the entire concept of nuclear spin relaxation had to be revised. In the region of $\omega_0\tau_c \geq 1$, the evolution of the longitudinal and transverse magnetizations are no longer represented by a mono-exponential decay characterized by a unique relaxation rate. For a spin 5/2, the transition probabilities between the three different eigenstates $|+1/2> \rightarrow |-1/2>$ (1), $|\pm 3/2> \rightarrow |\pm 1/2>$ (2) and $|\pm 5/2> \rightarrow |\pm 3/2>$ (3) are not equivalent and, as a consequence, both macroscopic longitudinal and transverse magnetizations evolve as a weighted sum of three exponentials [51,241]:

$$M_z(t) = M_z^0 \left[1 - \left(\sum_{i=1}^{3} C_{1i} \exp(-t/T_{1i})\right)\right] \tag{9.1}$$

$$M_{xy}(t) = M_{xy}^0 \left[\sum_{i=1}^{3} C_{2i} \exp(-t/T_{2i})\right] \tag{9.2}$$

Each of the three components possesses its own relaxation time (T_{2i}, T_{1i}) and pre-exponential factor (C_{2i}, C_{1i}). An interesting case for nuclear spins $I = 5/2$ is in the

regime of nearly extreme narrowing limits characterized by an $\omega_0\tau_c$ product inferior or equal to 1. In this region, both magnetization decays can be approximated to a mono-exponential decay and analytical expressions for longitudinal and transverse relaxation times have been obtained [241,245]:

$$\frac{1}{T_{11}} = \frac{3\pi^2}{625}\chi^2\left[2j(\omega_0) + 8j(2\omega_0)\right] \tag{9.3}$$

$$\frac{1}{T_{21}} = \frac{3\pi^2}{625}\chi^2\left[3j(0) + 5j(\omega_0) + 2j(2\omega_0)\right] \tag{9.4}$$

the pre-exponential factors of equation (9.1) and (9.2) are $C_{11} = C_{21} = 1$ respectively (see also Figure 9.13 and 9.15). Such equations should be used with care as they correctly describe nuclear relaxation behaviors in the region of $\omega_0\tau_c$ not greater than 1.0 [245]. Above this limit, equations (9.3) and (9.4) are no longer valid and relaxation becomes multi-exponential as the pre-exponential factors $C_{a,i>1}$ of equation (9.1) and (9.2) (the intensity of each component) are not negligible (see Figure 9.13 and 9.15).

9.4.2 Transition Probabilities

For a spin $I = 5/2$ (^{25}Mg, ^{27}Al, ^{67}Zn), or 7/2 (^{43}Ca, ^{59}Co, ^{133}Cs, ^{139}La) the relaxation behavior is complicated by the pre-exponential factors C_{1i} and C_{2i} which are dependent upon the spectrometer resonance frequency ω_0 and the correlation time τ_c. This means that the relative weight (the intensity) of each component varies upon the product $\omega_0\tau_c$. There are therefore no analytical expressions available for the longitudinal and transverse relaxation times although they can be solved numerically for each set of $(\omega_0\,,\tau_c)$ values [242,243,244]. It was then necessary to find the eigenvalues and eigenvectors of the longitudinal or transverse relaxation matrix [243,251,253]. The real part of the eigenvalues give the values of the three relaxation rates (T_{2i} and T_{1i}) while the eigenvectors will yield the weight (C_{2i} and C_{1i}) of each component of

the total magnetization.

Figure 9.12 represents the variation of the three longitudinal relaxation times versus the product $\omega_0\tau_c$. The behavior of each relaxation rate is similar as they all steadily increase up to approximately $\omega_0\tau_c = 1$, after which they all decrease gradually. Note that, even in the extreme narrowing conditions, the three relaxation rate components of the total magnetization are not equal.

Figure 9.13 displays the relative percentages associated to the three components of the longitudinal magnetization. From the graph, there is only one component which possesses a significant weight. Then in practice, regardless of the $\omega_0\tau_c$ product, the longitudinal magnetization decay can be approximated to a mono-exponential corresponding to the $|+1/2> \rightarrow |-1/2>$ nuclear spin transition.

Figure 9.14 represents the variation of the three transverse relaxation times versus the product $\omega_0\tau_c$. Each relaxation rate gradually increases up to $\omega_0\tau_c = 1$. Above this region, the most slowly relaxing component decreases while the other two continue to steadily increase.

Figure 9.15 shows the variation of the relative percentages of each component versus $\omega_0\tau_c$. Below $\omega_0\tau_c = 1$, the transverse magnetization is basically composed of only one component as the percentages of the other two are negligible. This case was treated earlier for the regime of nearly extreme narrowing limits with the analytical equations proposed for the longitudinal and transverse relaxation times (see equation (9.3) and (9.4)). Above $\omega_0\tau_c = 1$, the weight of each component becomes significant and multi-exponential relaxation behavior is expected for the transverse magnetization.

In practice, multi-exponential relaxation behavior will translate into the observation of non-Lorentzian line shapes due to the superposition of several lines of differ-

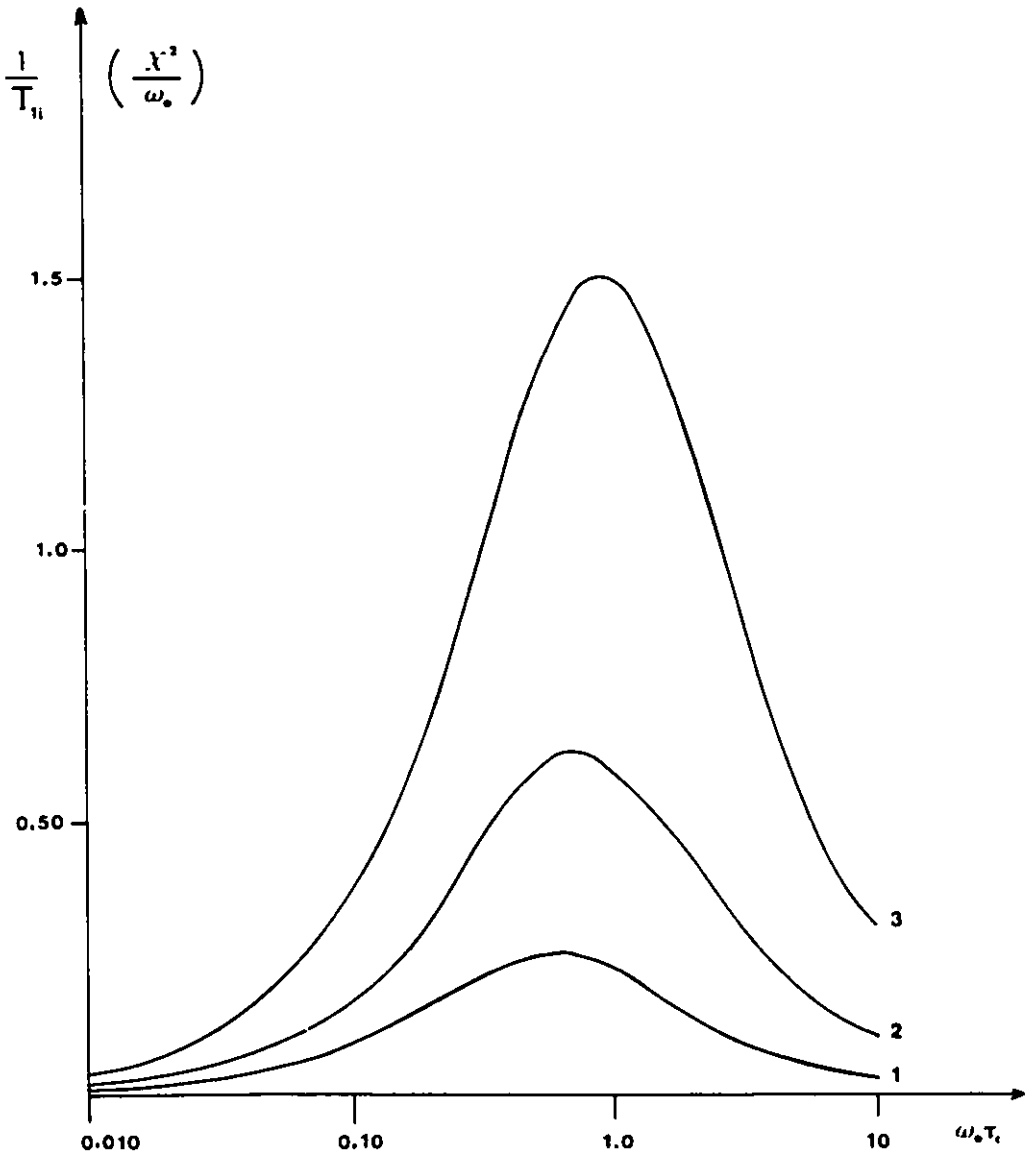

Figure 9.12: Variation of the three longitudinal relaxation rates T_{1i} of a spin 5/2 as a function of $\omega_0\tau_c$ (see equation (9.1)).

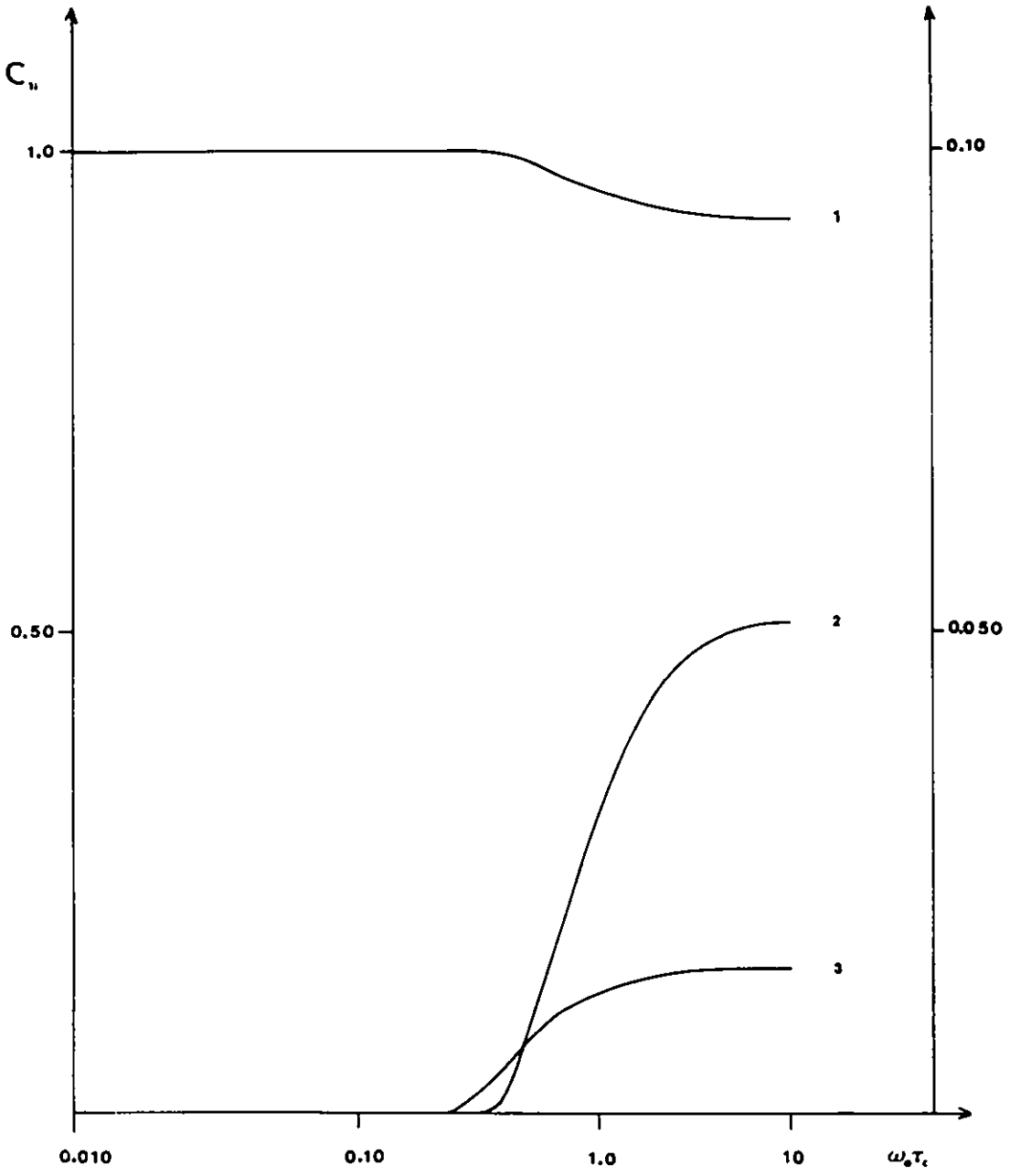

Figure 9.13: Variation of the three normalized pre-exponential factors C_{1i} of a spin 5/2 as a function of $\omega_0\tau_c$ (see equation (9.1)). Note that the coefficients C_{12} and C_{13} are plotted on the expanded scale given to the right.

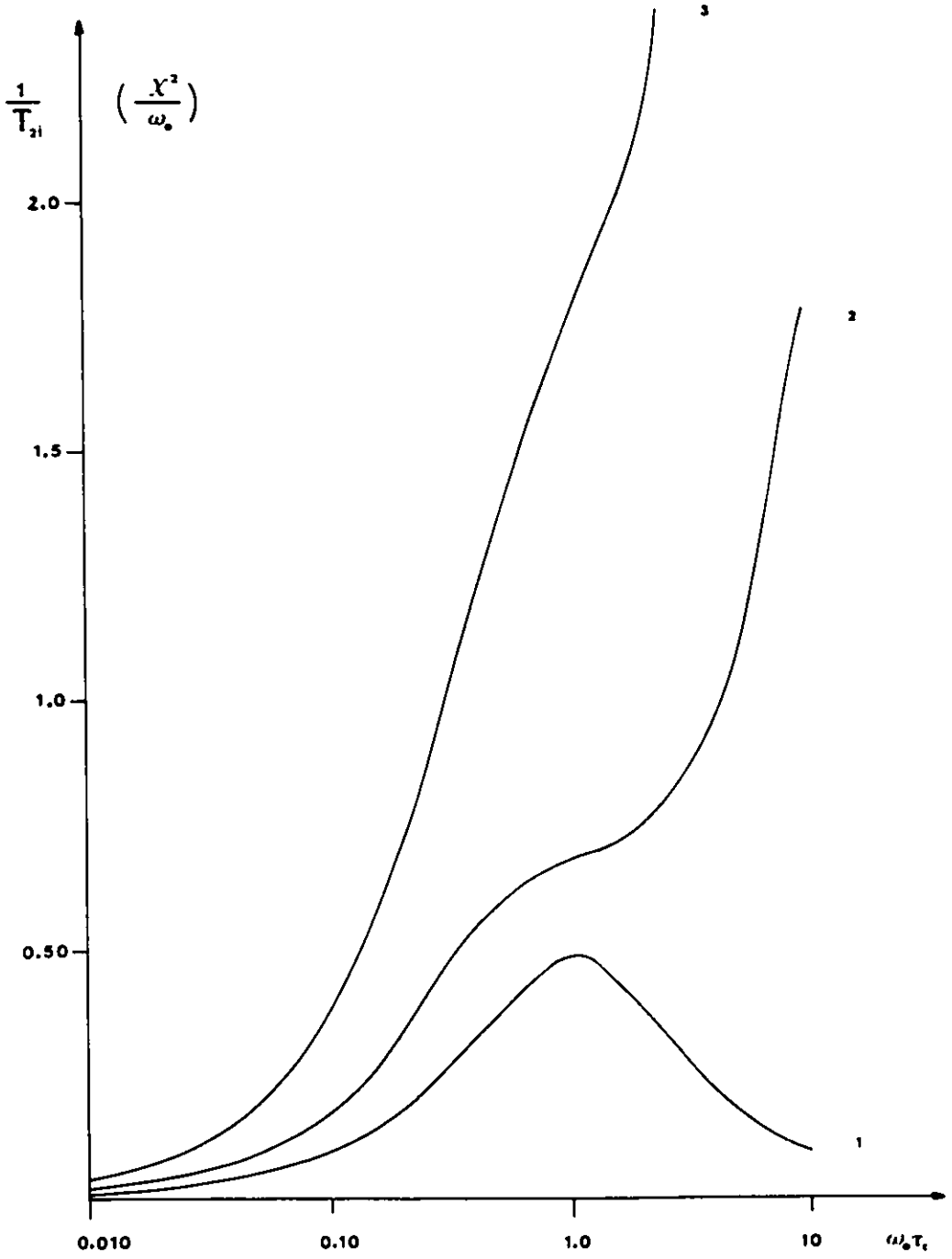

Figure 9.14: Variation of the three transverse relaxation rates T_{2i} of a spin 5/2 as a function of $\omega_0\tau_c$ (see equation (9.2)).

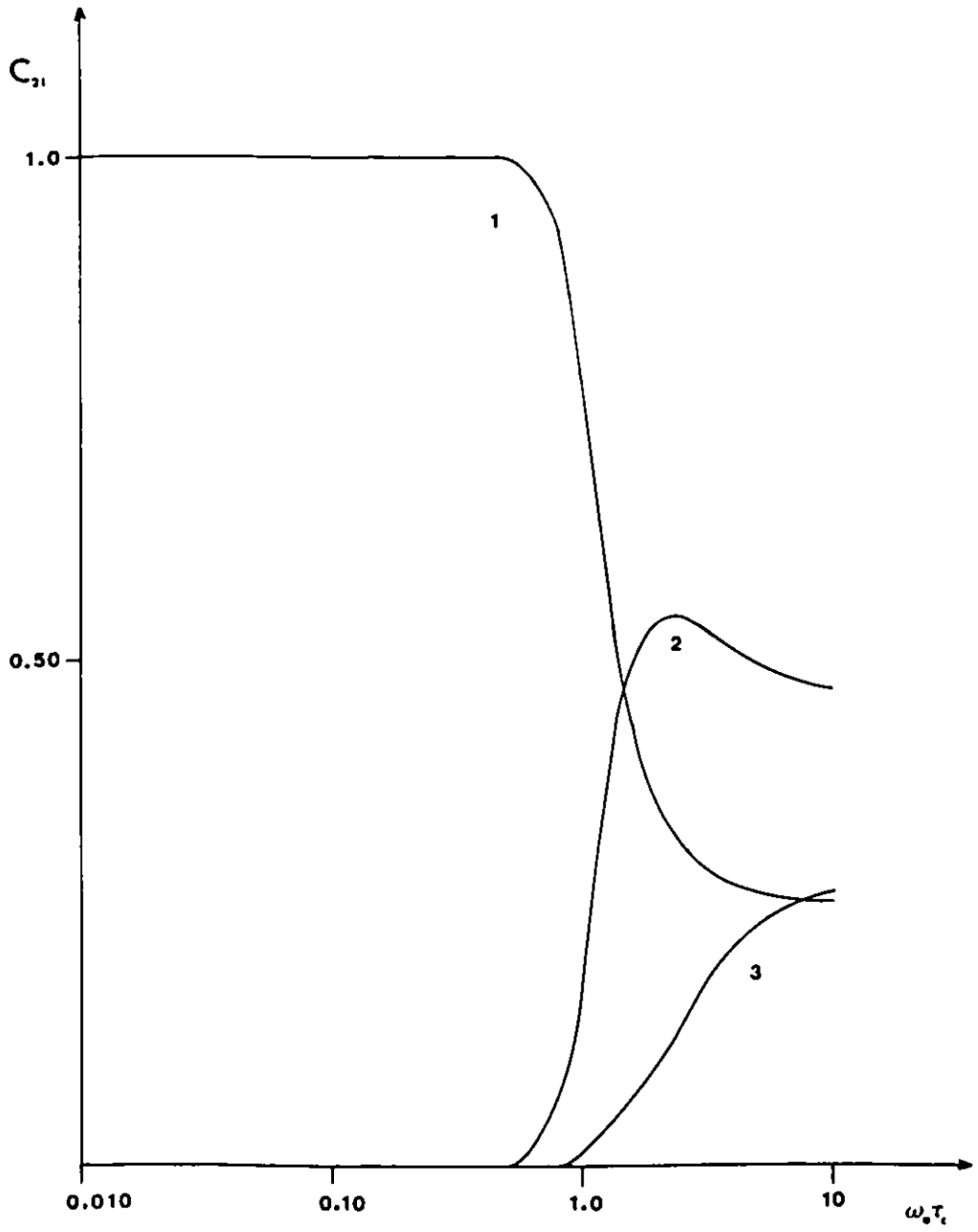

Figure 9.15: Variation of the three normalized pre-exponential factors C_{2i} of a spin 5/2 as a function of $\omega_0\tau_c$ (see equation (9.2)).

ent widths and intensities. However, the appearance of non-Lorentzian line shapes in ^{27}Al NMR are rarely observed. Favorable conditions for the detection of multi-exponential relaxation behavior should include a low QCC for the aluminum cation under investigation as well as an $\omega_0\tau_c$ product in the range of $1.2 \leq \omega_0\tau_c \leq 3.0$. Under these conditions, two of the three components will have a significant weight (see Figure 9.15). and the linewidth of the second component, much broader than the first one (see Figure 9.14), will be detectable due to the low QCC of the aluminum nucleus.

Finally, Figure 9.16 shows a comparison of the variations of the spin-spin relaxation times of the slowest relaxing component ($i = 1$, see Figure 9.14) at two different fields (21 and 78 MHz) versus the correlation time. For any τ_c value, the linewidth of the resonance associated to the $|+1/2> \rightarrow |-1/2>$ nuclear spin transition is always broader at 21 MHz. As a result, NMR spectroscopy of 5/2 quadrupolar nuclei in non-extreme narrowing conditions performed at high field represents an advantage as the resonance linewidths are always narrower.

9.4.3 Second Order Dynamic Frequency Shifts

The appropriate description of the relaxation behavior for nuclei $I \geq 3/2$ in the non-extreme narrowing region is further complicated by a quadrupolar relaxation matrix [247,248] containing imaginary spectral density functions which are frequency dependent and defined as [252]:

$$q(m\omega) = \frac{m\omega\tau_c^2}{1 + (m\omega\tau_c)^2} \tag{9.5}$$

so that quadrupolar interaction not only gives rise to relaxation but also generates a specific second-order Dynamic Frequency Shift (DFS) [247,248,249] for each component of the transverse magnetization. For a spin 5/2 nucleus, under non-extreme

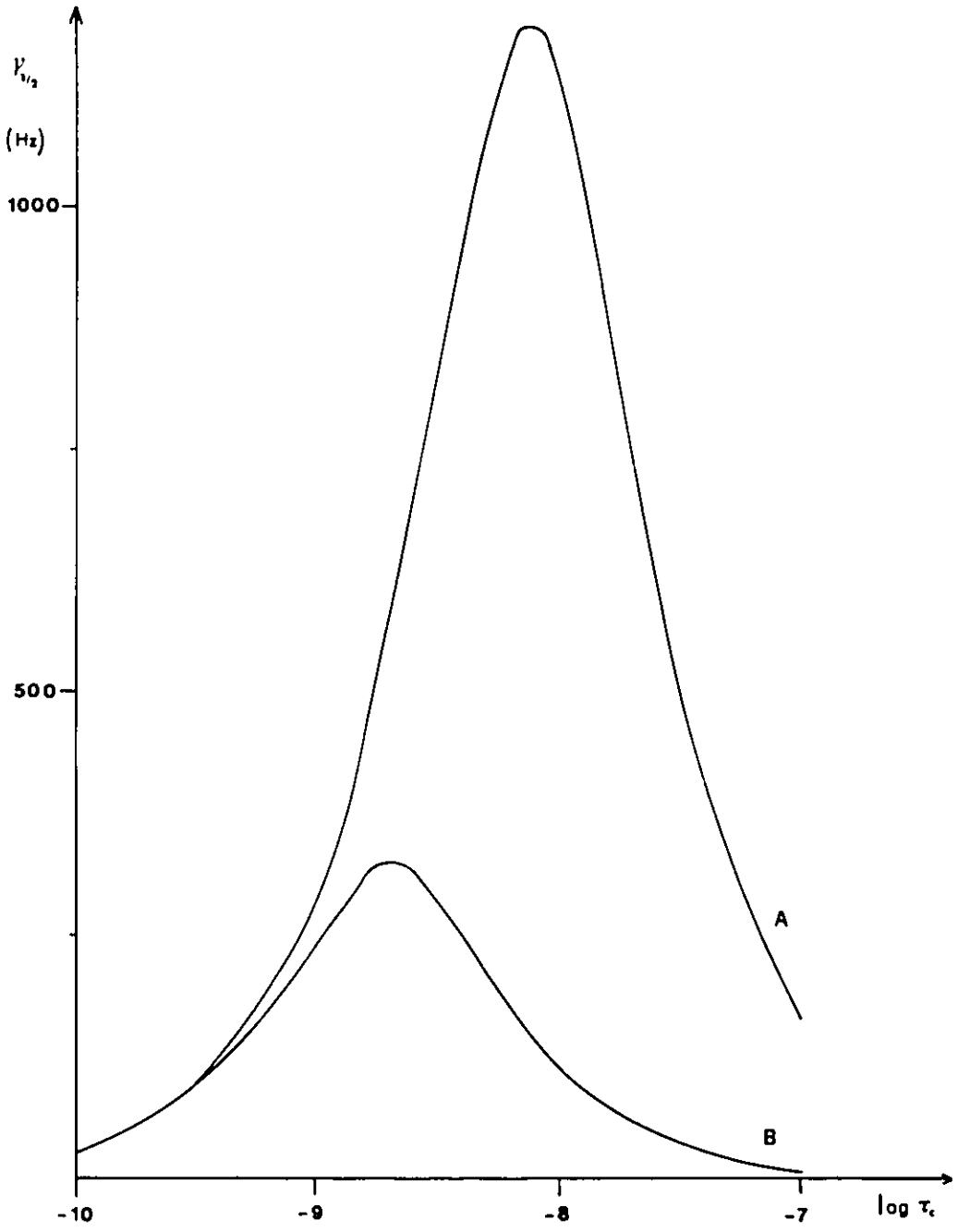

Figure 9.16: Variation of the linewidth of the most narrow component ($i = 1$, see Figure 9.14) of a spin 5/2 nucleus at two magnetic field strengths: A) 21 and B) 78 MHz as a function of the correlation time τ_c. The QCC was 1 MHz in both cases.

narrowing conditions, the three transverse relaxation components will not only experience different relaxation rates, but will also differ in their respective chemical shifts.

In the near extreme narrowing limits, when $\omega_0\tau_c \leq 1$, the spectrum is composed of a single Lorentzian corresponding to the m = +1/2 → m = −1/2 transition and whose spin–spin relaxation is given by equation (9.4). In this case the second-order dynamic frequency shift ω_{DS} of this resonance is given by [247,250,245]:

$$\omega_{DS} = \frac{6\pi^2}{625}\chi^2\left[q(\omega_0) + 2j(2\omega_0)\right] \tag{9.6}$$

and the signal is shifted downfield (see Figure 9.17). On the other hand, in the slow motion limit ($\omega_0\tau_c \geq 10$) the dynamic frequency shift of this transition reaches a limit proportional to χ^2/ω_0 [247,250,245]:

$$\Delta\omega_{DS} = -\frac{6\pi^2}{125}\chi^2\left[q(\omega_0) - j(2\omega_0)\right] = -\frac{3\pi^2}{125}\frac{\chi^2}{\omega_0} \tag{9.7}$$

and the absorption is shifted upfield (see Figure 9.17). In the intermediate region $1 \leq \omega_0\tau_c \leq 10$ there is no analytical equation available for the dynamic frequency shift and a full treatment of the relaxation matrix is required to obtain correct dynamic frequency shift values [248]. These three typical regions are summarized on Figure 9.17 which gives the dynamic frequency shift for the three components of the transverse magnetization versus the product $\omega_0\tau_c$. Note that for the two other components (i = 2 and 3), regardless of the $\omega_0\tau_c$ region, they are always shifted downfield.

9.5 Results and Discussion

^{27}Al NMR on the ATP–Al system was performed at 21 and 78 MHz, at pH = 7.4 ± 0.1, in 20% D_2O solution and for a total aluminum concentration of 50 mM. In a con-

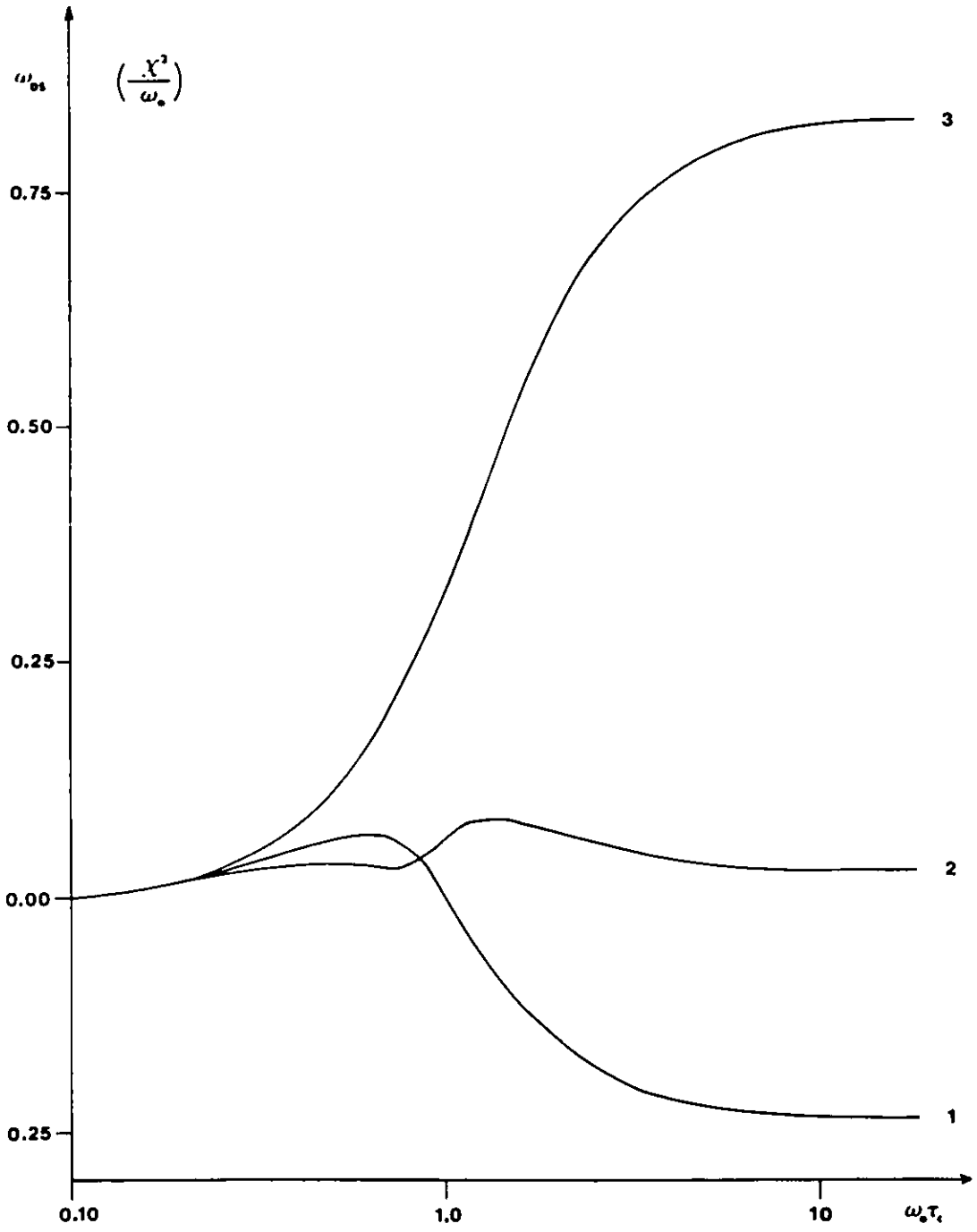

Figure 9.17: Variation of the dynamic frequency shift ω_{DS} for the three components of the transverse magnetization (see equation (9.2)) as a function of $\omega_0\tau_c$ and for a spin 5/2 nucleus.

centration study, the ATP/Al ratio was varied from 0.60 to 3.0. At 78 MHz, each spectrum was then submitted to a deconvolution procedure which gave the chemical shift, linewidth and population of each resonance (see Section 9.3). In contrast, at 21 MHz, for any ATP/Al ratio, each recorded spectrum yielded only one Lorentzian line, probably due to the long α delay (1500 μs) necessary to record meaningful spectra. At 78 MHz, for each solution, two spectra were recorded. One spectrum for which the α delay was set to 0, was used for deconvolution, while the second, recorded using a long α delay of 1000 μs, yielded the only slowly relaxing component left in the spectrum, which was also observed at 21 MHz (see Table 9.2).

Table 9.1 summarizes all the results obtained from ten spectral deconvolutions at 78 MHz when the ATP/Al ratio was varied from 0.60 to 3.0. Average chemical shift and linewidth values are also reported with their respective associated errors. This table shows that, for any ATP/Al ratio (except 1.4), each NMR spectrum was composed of three Lorentzian lines. Due to the theory of nuclear spin relaxation of a 5/2 quadrupolar nucleus in the non-extreme narrowing limits, which predicts three components for the transverse magnetization, the three experimental resonances may possibly account for only one aluminum species in solution.

Each of the three components was characterized by a different linewidth value whose ratio 1.0 (660 Hz) : 3.0 (2.0 KHz) : 10.9 (7.2 KHz) gave a solution for the ^{27}Al correlation time of 6 $\pm$ 1 ns (see Figure 9.14). Thus, for $\omega_0\tau_c$ = 2.95, the relative population of each line should be 29%, 53% and 18% (see Figure 9.15) respectively and constant throughout the variation of the ATP/Al ratio. The two latter points are in disagreement with the calculated population of each line which varies from ATP/Al = 0.60 to 1.6 (see Figure 9.20). Above ATP/Al = 1.6 even though the weight of the three resonances present in the NMR spectra are constant values

$\frac{[ATP]}{Al(III)}$	δ (ppm)	$\mathcal{V}_{1/2}$ (KHz)	P %	δ (ppm)	$\mathcal{V}_{1/2}$ (KHz)	P %	δ (ppm)	$\mathcal{V}_{1/2}$ (KHz)	P %	δ (ppm)	$\mathcal{V}_{1/2}$ (Hz)	P %
0.60	-23	7.7	65				-4.1	1.8	29	0.7	560	6
0.80	-25	8.5	55				-5.0	2.2	40	-0.5	590	5
1.0	-28	7.3	36				-5.0	2.1	55	0.5	550	9
1.2	-25	7.5	28				-3.5	2.0	63	0.6	660	9
1.4	-25	7.0	14	-38	7.0	13	-4.0	2.2	65	1.0	670	8
1.6				-40	7.1	31	-4.9	2.0	61	0.0	680	8
1.8				-36	6.3	35	-7.3	1.8	54	-1.5	700	11
2.0				-36	6.9	37	-7.6	1.8	54	-1.5	700	9
2.5				-39	6.8	38	-9.0	2.0	55	-1.0	780	7
3.0				-41	7.1	40	-8.8	2.1	51	-0.5	750	8
$\hat{X}$	-25	7.6		-38	6.9		-6	2.0		0	660	
σ	-2	0.6		3	0.5		2	0.2		1	80	

Table 9.1: Summary of the chemical shift (δ), linewidth ($\mathcal{V}_{1/2}$) and the normalized population of each resonance (P) resulting from a deconvolution procedure using four Lorentzian lineshapes (see Section 9.3). The ATP/Al ratio was varied from 0.60 to 3.0. Experimental conditions were: Al = 50 mM, pH = 7.4, 20% D_2O and T = 21 °C.

(8%, 57% and 35%), the population of two lines (8% and 35%) do not agree with calculated theoretical values (29% and 18%). Examination of the chemical shifts of the peaks further confirms that the three observed ^{27}Al resonances do not belong to the same aluminum species. As discussed earlier (see Section 9.4.3), a 5/2 quadrupolar nucleus outside the extreme narrowing conditions will experience a dynamic frequency shift. If the $|+1/2> \rightarrow |-1/2>$ narrow component appears at 0 ppm (see Table 9.1), then the two other resonances should be shifted downfield (see Figure 9.17), in contradiction with the observed resonances shifted in opposite directions at - 6 and - 38 ppm. Finally, the correlation time of 6 ns found earlier, does not agree with the phosphorus-31 NMR results which gave $\tau_c = 2.8 \pm 0.8$ ns. In the case of a correlation time of 2.2 ± 0.9 ns found by ^{27}Al NMR experiments (see at the end of this discussion), the relative population associated with the three nuclear spin transitions are 71% ($|+1/2> \rightarrow |-1/2>$), 27% ($|\pm 1/2> \rightarrow |\pm 3/2>$) and 2% ($|\pm 3/2> \rightarrow |\pm 5/2>$) (see Figure 9.15) while the linewidth of each resonance is in the ratio of 1 : 1.4 : 3.7 respectively (see Figure 9.14). Under these conditions, with a resonance having a linewidth of 2.2 KHz, an intensity of 120 (ATP/Al = 0.80), then the $|\pm 1/2> \rightarrow |\pm 3/2>$ and $|\pm 3/2> \rightarrow |\pm 5/2>$ nuclear transitions will be characterized by a resonance linewidth of 3.1 KHz and 8.1 KHz with an intensity of about 30 and 1 respectively. Due to the deconvolution method used in this study to distinguish different aluminum resonances, even under the most favorable conditions (intense line with a relatively "narrow" linewidth), the only ^{27}Al nuclear spin transition detectable for each aluminum species is the $|+1/2> \rightarrow |-1/2>$ transition. The two other resonances ($|\pm 1/2> \rightarrow |\pm 3/2>$ and $|\pm 3/2> \rightarrow |\pm 5/2>$) are lost in the baseline of the spectrum because of their much lower associated intensity and wider linewidth.

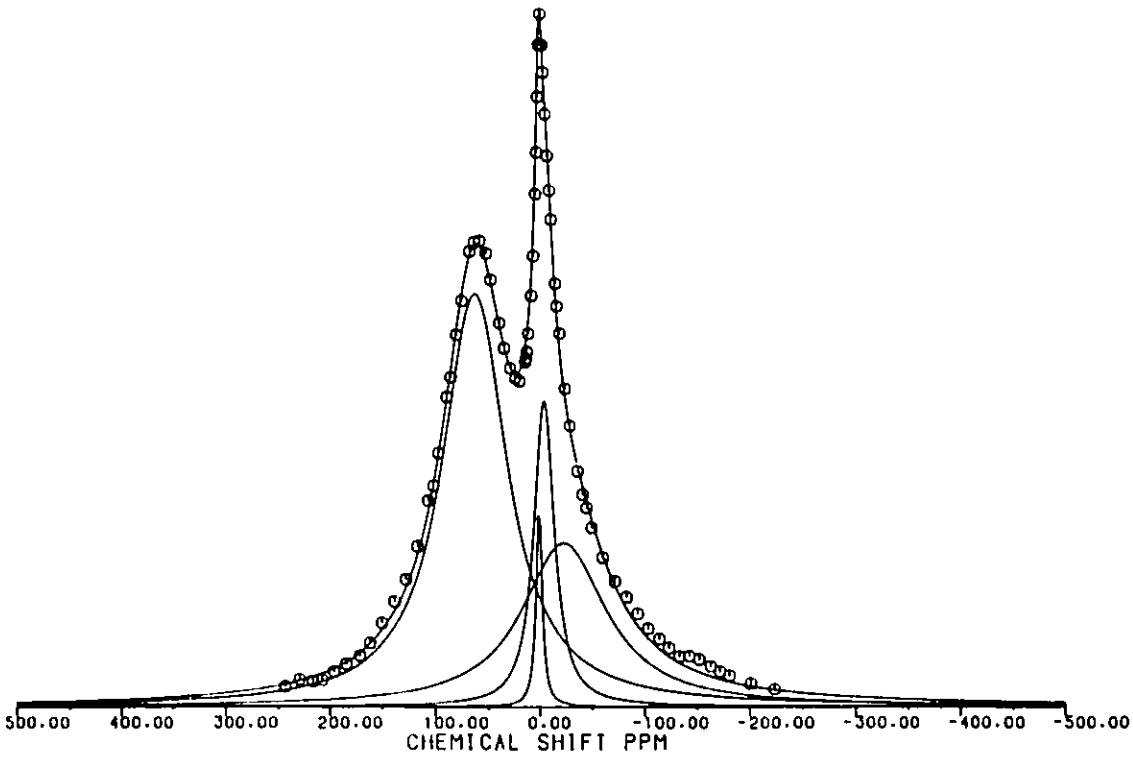

Figure 9.18: Deconvolution of an ^{27}Al NMR spectrum using four Lorentzian lineshapes (see Section 9.3). The ATP/Al ratio was 0.60.

This study shows that for any given ATP/Al ratio, at least three different aluminum species are present in an aqueous solution of ATP–Al complexes. Furthermore, there are two ATP/Al distinct regions. For ATP/Al < 1.4, three resonances appear in each spectrum, characterized by chemical shifts of 0 ± 1 ppm, -6 ± 2 ppm and -25 ± 2 ppm and linewidths of 660 ± 80 Hz, 2.0 ± 0.2 KHz and 7.6 ± 0.6 KHz respectively (see Table 9.1 and Figure 9.18). For ATP/Al > 1.4, the more shielded resonance at -25 ppm disappears, and was replaced by a resonance centered at -38 ± 3 ppm with a linewidth of 6.9 ± 0.5 KHz. The two other resonances at 0 and -6 ppm remain unchanged (see Table 9.1 and Figure 9.19).

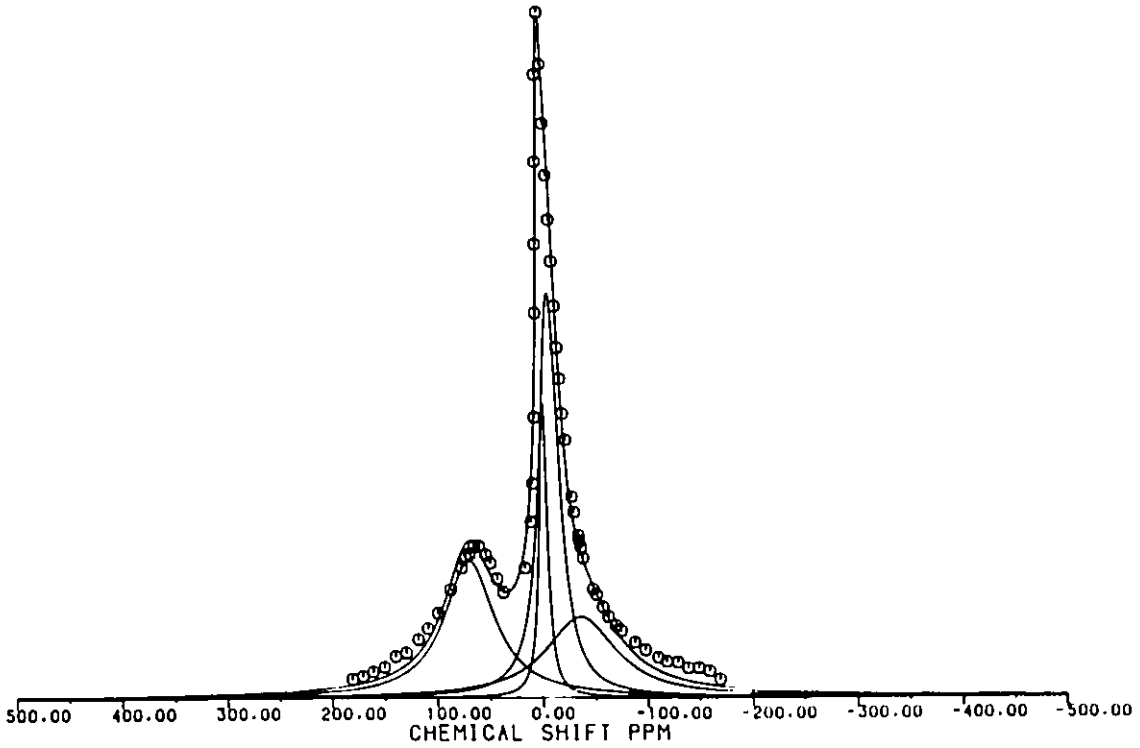

Figure 9.19: Deconvolution of an ^{27}Al NMR spectrum using four Lorentzian lineshapes (see Section 9.3). The ATP/Al ratio was 1.8.

$\frac{[ATP]}{Al(III)}$	δ (ppm)	$\nu_{1/2}$ (Hz)	δ (ppm)	$\nu_{1/2}$ (Hz)
	78 MHz α = 1000 μs		21 MHz α = 1500 μs	
0.60	1.3	560		
0.80	0.7	590	1.9	560
1.0	0.7	550	1.1	560
1.2	0.9	660	1.0	590
1.4	1.1	670	0.2	690
1.6	0.7	680	-0.2	640
1.8	1.1	700	2.2	610
2.0	0.8	700	2.3	700
2.5	0.8	780		
3.0	0.2	750		
$\hat{X}$	0.8	660	1.2	620
σ	0.3	70	0.9	50

Table 9.2: Parameter summary of the most narrow ^{27}Al resonance detected when the α delay was increased to 1000 μs (78 MHz) or 1500 μs (21 MHz), and as a function of the ATP/Al ratio. For experimental conditions see Table 9.1.

Table 9.2 gives the chemical shifts and linewidth values of the relatively narrow resonance observed at 21 MHz, centered at 1.2 ± 0.9 ppm, which can be compared to the one observed at 78 MHz, centered at 0.8 ± 0.3 ppm and in very good agreement with the deconvolution results of 0 ± 1 ppm (compare Table 9.2 with Table 9.1). No field effect on the linewidth of this resonance was detected, with an average linewidth of 620 ± 50 Hz at 21 MHz compared to 660 ± 70 Hz at 78 MHz. This means that the aluminum species corresponding to this resonance is characterized by a short correlation time, probably resulting from a small aluminum species in solution. The

three other resonances described earlier, were not detected at 21 MHz and may be the direct consequence of the necessary long α delay used to record reliable spectra (see Section 9.2).

Figure 9.20 illustrates the relative percentage of each aluminum species present in solution at 78 MHz, pH = 7.4, for ATP/Al ratios from 0.60 to 3.0. The two distinct regions previously mentioned are clearly distinguished by the vertical dotted line centered at ATP/Al = 1.4. This frontier corresponds to the disappearance of a broad resonance (7.6 KHz) centered at – 25 ppm which was replaced by another similar broad resonance (6.9 KHz) shifted upfield at – 38 ppm. This ATP/Al ratio value of approximately 1.4, using ^{27}Al NMR, corresponds to an Al/ATP ratio of 0.71, very close to the ATP:Al aggregate stoichiometry of 4:3 determined by ^{31}P NMR (see Section 5.3.3 and 8.4). At this ratio value, the resonance centered at – 6 ppm, which constitutes 65% of the total aluminum concentration, corresponds to an aluminum species complexed by the triphosphate side chain of ATP. The region of the graph for ATP/Al ratios smaller than 1.4 corresponds to an aluminum concentration in solution in excess of ATP. As the ratio decreased, a very broad resonance appeared and the relative percentage of the aluminum species complexed by the triphosphate chain of ATP decreased. Characterization of the ^{27}Al species responsible for the appearance of this resonance will now be discussed.

Aqueous solutions containing aluminum salts have been the subject of extensive work [237,254,260] and several reviews [230,231,261]. ^{27}Al NMR has shown that hydrolysis of the hexa-aquated aluminum species results in the formation of an aluminum dimer bridged by two hydroxyl groups:

$$2Al(H_2O)_6^{3+} \rightleftharpoons [(H_2O)_4Al(\mu - OH)_2Al(H_2O)_4]^{4+} + 2H_3O^+$$

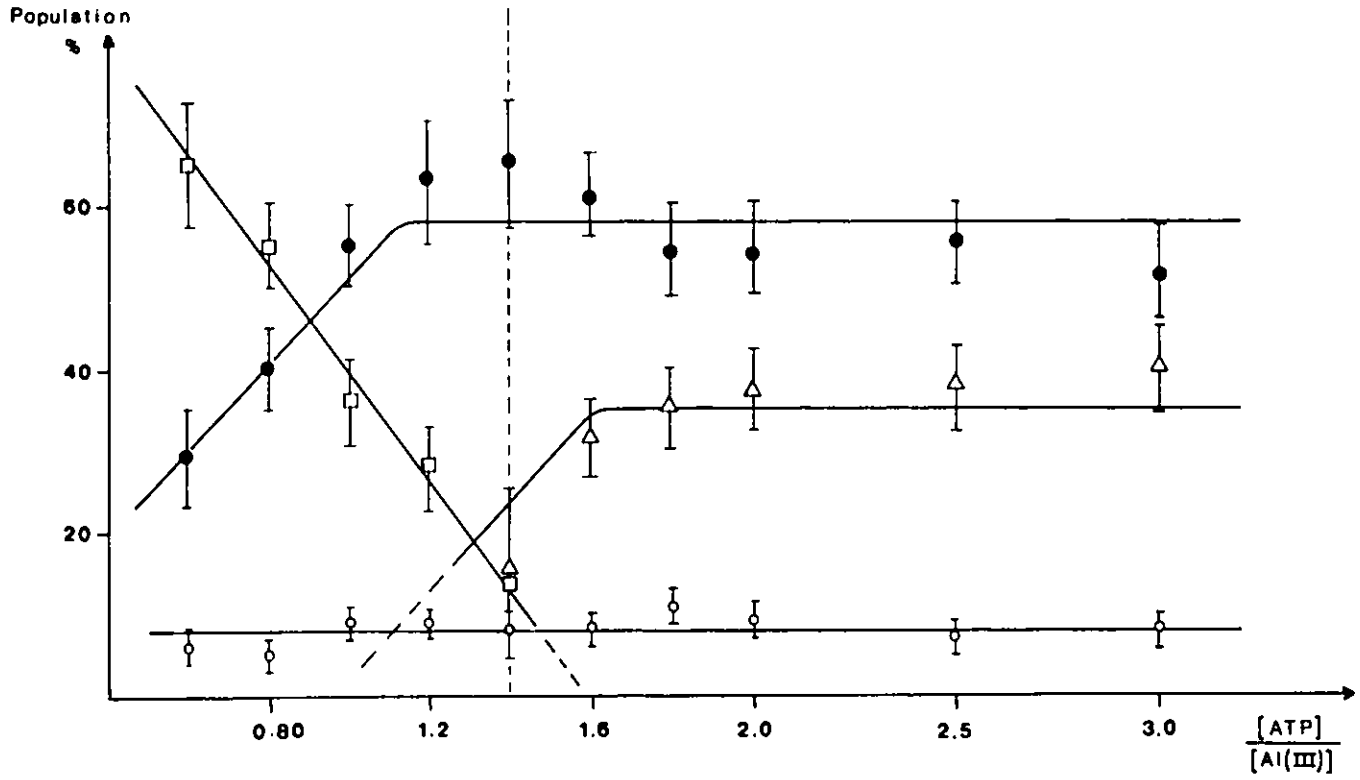

Figure 9.20: Variation of the relative population of each ^{27}Al resonance for $0.60 \leq \mathrm{ATP/Al} \leq 3.0$ at 78 MHz. See text for the significance of the vertical dotted line at ATP/Al = 1.4 as well as the attribution of the different species (•), (o), (△) and (□) present in solution. See Table 9.1 for experimental conditions. For each ATP/Al ratio, the experimental NMR spectrum was submitted to a deconvolution procedure assuming four Lorentzian lineshapes, except for ATP/Al = 1.4 which necessitated five Lorentzian lineshapes (see Section 9.3).

This species is characterized by a chemical shift value of 4 ppm (close to the $Al(H_2O)_6^{3+}$ reference) and a linewidth of approximately 500 Hz [237,254,255]. The pK_a of the dimerization process was reported to be 6.95 at 30 °C [264]. Under the working experimental conditions of this study (pH = 7.4, T = 24 °C) formation of this dimer might be expected. The narrowest resonance detected at both fields was characterized by a total average chemical shift value of 1 ± 0.7 ppm and a total average linewidth of 640 ± 70 Hz, confirming the presence of the aluminum dimer. Throughout the study, its concentration was independent of the ATP/Al ratio and represented 8% of the total aluminum population present in solution. Hydrolysis has been known to proceed beyond the dimerization stage, yielding a polymeric cation $[AlO_4\ Al_{12}(OH)_{24}(OH_2)_{12}]^{7+}$, called Al_{13} [255,259,260]. Both the dimer and polymeric species are water soluble and have been detected by ^{27}Al NMR [254,237]. The addition of a suitable counter anion, to these species, like the sulfate anion, gives rise to precipitates and have been the subject of crystal structure determinations [264,265,266]. The structure of the polymeric cation Al_{13} consisted of twelve aluminum atoms, surrounded by an octahedral arrangement of oxygen atoms, which are grouped around a central tetrahedral aluminum atom AlO_4. Due to the high symmetry of the tetrahedral aluminum atom, ^{27}Al NMR gives rise to a well defined sharp resonance of 50 Hz centered at 62.5 ppm [254]. In contrast, the resonance of the octahedral aluminum sites is broad (evaluated at 2000 Hz) and centered at 0 ppm [237].

None of these resonances described as characteristic of the polymeric cation Al_{13} have ever been observed in the ^{27}Al spectra of ATP–Al solutions for which the ATP/Al ratio varied from 0.60 to 1.4. In contrast, the aluminum resonance we observed was shifted upfield to – 25 ppm with a much broader linewidth of 7.5 KHz,

and has never been reported in the literature as being the product of an hydrolyzed aluminum species in solution. Although the aluminum dimer is present as a small percentage in solution, it does not undergo further hydrolysis to form the polymeric cation Al_{13}. This would indicate that the observed ^{27}Al resonance was due to another species.

Nucleotides involved in cation complexation are usually viewed as having three potential binding sites [119]: the phosphate site chain, the sugar moiety and the base each representing a site for fixation of a metallic cation.

For Al/ATP > 0.75, further complexation of the ATP_4Al_3 aggregate triphosphate side chains was not taking place in solution as quantitative phosphorus-31 analysis shows a complexation plateau (see Section 5.3.3). Formation of a 2:1 ATP–Al species using the triphosphate side chains for metallic complexation can be excluded on the basis that phosphorus-31 NMR does not detect the appearance of new ^{31}P resonances or chemical shift variations of the ^{31}P aggregate resonances (see Section 5.3.2).

Among the three potential binding sites of ATP, two of them, the purine base and the sugar ring have not yet been investigated. With three nitrogen atoms N 1, N 3 and N-7 the purine base possesses some interesting complexation sites for a metallic cation. In the ATP molecule, the N-3 site is sterically hindered by the ribose sugar and, as a result, this particular nitrogen atom has never been reported in the literature as a competitive chelation site compared to N-1 and N-7.

In order to detect if complexation was occurring on the nitrogen atom of the purine base of ATP, ^{13}C NMR spectra were recorded at 75 MHz. The study showed that, above Al/ATP = 0.75, each carbon atom of the base is further perturbed, giving rise to a new broad resonance at the base of each carbon resonance (see Figure 6.4). As a result, ^{13}C NMR suggests that, when Al/ATP > 0.75, complexation occurs on

the available nitrogen atoms N–1 and N–7 of the adenine base. This was confirmed by ^{27}Al in which a new broad resonance appeared in the region of ATP/Al < 1.4. ^{13}C NMR also revealed that aluminum complexation does not take place at a specific nitrogen binding site (N–1 or N–7) but, as all carbon atoms seem to be equally perturbed, N–1 and N–7 both represent a binding site for aluminum. In contrast, the carbons of the ribose sugar are only slightly broadened, as is the dioxane reference peak, probably resulting from an increase of the solution viscosity and/or an increase of the carbon's correlation time.

Complexation of hexa-aquated aluminum by nitrogen ligands, like acetonitrile, has been the subject of several spectroscopic investigations [238,239,240,267,268,271]. ^{27}Al NMR shows that progressive replacement of its hexa-aquated solvation sphere by nitrogen ligands leads to higher aluminum chemical shifts in the range of – 4 to – 33 ppm [268], depending upon the number of nitrogen ligands. In the present study, the observed chemical shift value of – 25 ppm agrees with the trend of chemical shift values reported for mixed water-nitrogen complexes of aluminum [239,268]. In the ATP–Al aggregate, it was possible to consider an aluminum species involved with the adenine base through complexation with one or two nitrogen atoms. In the latter case, the aluminum would be bridging two adenine bases. In the case of an aquated aluminum species complexed by one or two nitrogen ligands, reported chemical shift values [239,268] are about – 4 and – 9 ppm respectively, much less shielded than the observed resonance of – 25 ppm. The existence of base stacking in the ATP–Al aggregate, detected by both ^{13}C and ^{1}H NMR, could account for an increased shielding of this resonance. Similar shielding effects have been reported for the ^{27}Al resonance of the aluminum tribromide dimer in bromine [269] or benzene [270] solvents which resulted in a chemical shift difference of – 16 ppm. In fact, the

high upfield shift of this resonance results from the addition of two distinct effects: the adenosine base staking and a dynamic frequency shift of – 10 ppm (see later).

For ATP/Al < 1.4, examination of the relative population (see Figure 9.20) between the two aluminum species assigned to aluminum-phosphorus complexes (•) (see later) and aluminum-nitrogen complexes (□) will give the number of aluminum atoms complexing the four adenine bases present in the ATP–Al aggregate. When the ATP/Al reached the value of 0.60, the relative population ratio of the two resonances was 2 (Al–N) : 1 (Al–P). Since the Al–P resonance accounts for the detection of two aluminum nuclei (see later), the number of aluminum nuclei complexing the four adenine bases amounts to four, that is, one aluminum cation per base. Although each adenine base of ATP possesses two potential nitrogen site of chelation, N–1 and N–7, ^{13}C NMR results have shown that there is no preferential site of complexation. Combination of ^{27}Al quantitative analysis and ^{13}C results allows the following conclusion to be drawn. In the aggregate, the N–1 and N–7 nitrogen atoms are quantitatively, equally complexed (2 (Al–N–1) : 2 (Al–N–7)). In the overall complexation scheme, each of the four adenine bases is complexed by one aluminum atom which binds alternatively to an N–1 or N–7 nitrogen atom. Another complexation scheme involves the establishment of an aluminum bridge between two adenine bases. In this complex the aluminum cation would be bound via two nitrogen atoms and confer an additional rigidity to the overall aggregate structure.

Although replacement of a water molecule by a nitrogen ligand in the solution sphere of aluminum may distort the octahedral symmetry around the cation and result in a linewidth broadening this effect was expected to be weak since both nitrogen N–1 and N–7 of the adenine base are not sterically hindered. Studies of aluminum trichloride in water-acetonitrile solutions by ^{27}Al NMR [268] showed the

formation of a series of water (X) – nitrogen (Y) aluminum solvates (AlX_nY_{6-n}), each species exhibiting a characteristic chemical shift and linewidth value. The major contribution to the observed linewidth variations between the different solvates were attributed to the perturbation of the *efg* around the nucleus, rather than a distortion of the aluminum octahedral symmetry. Reported linewidth values for mixed water-nitrogen aluminum solvates are relatively narrow, about 300 Hz, compared to the very broad 7.6 KHz resonance observed in the present study, representing more than a 20 fold increase in linewidth.

If one assumes that a mixed water-nitrogen aluminum species generates a similar *efg* around the quadrupolar nucleus in both studies, then, it is not reasonable to conclude that the variation of *efg* is solely responsible of the observed aluminum linewidth of this ATP–Al complex. This implies that the ^{27}Al correlation time represents the parameter which influences the linewidth of the resonance of interest. ^{27}Al NMR then behaves as a dynamic molecular probe of the cation–base interactions located at the other end of the aggregate. Due to the large linewidth value of this resonance, it also suggests that the whole complex reorients as a rigid entity in solution. Assuming a re-orientational correlation time of 2.8 ± 0.8 ns, found by ^{31}P NMR, a quadrupole coupling constant of 5.1 ± 0.9 MHz was calculated.

At the ^{27}Al resonance frequency of 78 MHz, the product of $\omega_0\tau_c$ is 1.38, violating the extreme narrowing conditions. Due to the large QCC value associated with the long correlation time of this aluminum species, quadrupolar relaxation in the non-extreme narrowing limit shows that this resonance will experience a dynamic frequency shift (see Section 9.4.3). Knowing the values of $\omega_0\tau_c$ and χ^2/ω_0, the DFS is readily calculated from Figure 9.17. It accounts for an upfield shift of - 10 ± 3 ppm which contributes to the observed high upfield shift of this resonance (- 25 ppm).

The intrinsic chemical shift of this resonance was only – 15 ppm.

When the ATP/Al ratio was smaller than 0.60, precipitation occurred in solution. Below this limit, the triphosphate chains and the base of the ATP–Al aggregate were saturated in aluminum. No further complexation occurred and, at pH = 7.4, aluminum precipitated in solution possibly as aluminum hydroxide [259] or as a polymeric Al_{13} species.

The second region of Figure 9.20, corresponding to ATP/Al > 1.4, will now be discussed in detail.

This region, equivalent to an ATP/Al ratio < 0.75, has been extensively studied and characterized by phosphorus-31 NMR. These spectra support the formation of an ATP_4Al_3 aggregate in solution. ^{27}Al NMR detected two well characterized resonances, both shifted upfield from the reference, centered at – 6 ± 2 ppm (•) and – 38 ± 3 ppm (△) with a linewidth of 2.0 ± 0.2 KHz and 6.9 ± 0.5 KHz respectively (see Table 9.1 and Figure 9.20). While differences in chemical shift values for the two resonances show that there are two distinct aluminum complexation sites present in the ATP–Al aggregate, quantitative measurements can be used to determine their population ratio.

Throughout the variation of the ATP/Al ratio, their relative population stayed constant with a ratio of 2 (•) : 1 (△) (see Figure 9.20). The resonance at – 38 ppm, which accounts for one of the three complexed aluminum nuclei, can be thought to arise from an aluminum species located on the "outside" of the aggregate while the other resonance at – 6 pm is responsible for two "inside" aluminum cations tightly buried in the middle of the aggregate (see Figure 10.1). This assignment for the two aluminum complexation sites existing in the molecular aggregate was supported by analysis of their respective chemical shift and linewidth values.

^{27}Al NMR studies of aluminum–phosphate complexes in aqueous solution of various nucleotides [272] and phospholigands [273,274,275] all indicate that the phosphoryl P=0 group induces an upfield shift in the ^{27}Al spectra. The extent of the chemical shift is directly proportional to the number of phosphate groups present in the octahedral aqueous aluminum solvation sphere [275]. The shift ranges between – 3 and – 22 ppm, in agreement with the reported intrinsic chemical shift (δ_{int}) values of – 4 and – 29 ppm. The intrinsic chemical shift was obtained after correction for the DFS which resulted from a combination of the molecular size of the aggregate and QCC value (see later). The observed chemical shift values of the two complexation sites were in accord with both ^{27}Al resonances corresponding to a metallic cation complexed by three phosphate groups (see Figure 5.15). The detection of a coupling constant, by ^{31}P NMR between the quadrupolar nuclei and the phosphorus atom reinforces the existence of a chemical bond between the phosphate oxygen and the aluminum nuclei (see Section 5.3.5).

For the octahedral complexation site located in the "inside" of the molecular aggregate (δ_{int} = – 4 ppm, $\mathcal{V}_{1/2}$ = 2.0 KHz) the cation can be visualized as surrounded by three phosphate groups while the rest of the solvation sphere would be filled by three water molecules.

The second complexation site located in the "outside" of the aggregate (δ_{int} = 29 ppm, $\mathcal{V}_{1/2}$ = 6.9 KHz), is characterized by an aluminum resonance shifted by – 25 ppm from the former site. It is generally agreed that the electron donating properties of the ligands represent a major factor in the ^{27}Al chemical shift [276,275,268]. It suggests that the cation retaining its aquated solvation sphere composed of three water molecules, experiences the effects of the negatively charged triphosphate chain of the surface ATP molecule. The metallic cation ligand environment of this site was

supported by a very broad observed resonance linewidth (6.9 KHz). There are two distinct molecular properties which are responsible for the observed broad line. First, the slow molecular tumbling of the aggregate (τ_c = 2.8 ns), contributes to a ten fold linewidth increase, in comparison to the aluminum reference ($\mathcal{V}_{1/2}$ = 4 Hz, τ_c = 67 ps and χ = 0.4 MHz). Secondly, linewidth broadening is also enhanced by the QCC of 4.8 ± 0.8 MHz, characterizing the complexation site. In comparison to the QCC value of a hexa-aquated aluminum cation in solution (χ = 0.4 MHz), this study has shown that replacement of a water molecule by a nitrogen ligand in the aluminum coordination sphere increased the QCC values by a factor of thirteen (χ = 5.1 MHz), reflecting the decrease in the octahedral ligand field symmetry around the quadrupolar nucleus. Thus, the large QCC characterizing the aluminum cation joining the surface ATP molecule to the rest of the aggregate is likely to arise from a loss of octahedral ligand field symmetry around the aluminum cation [230].

In the case of the aluminum cation located in the "inside" of the aggregate, a QCC of χ = 2.6 ± 0.5 MHz could be calculated for this hexacoordinated complex. This value lies in the middle range of QCC reported in this study and as well probably results from the loss of octahedral ligand field symmetry.

Finally, for a series of octahedral mixed complexes (AlX_3Y_{6-n}), computed values of the *cfg* tensor as a function of the ligand symmetry around the cation showed that the resonances of the two trans-(mer) or cis-(fac) AlX_3Y_3 isomers were associated with very different linewidths [268]. In fact the resonance of the cis-isomer becomes as sharp as the octahedral AlX_6 species and results from a fortuitous cancellation of the *cfg* around the nucleus. In contrast, the trans-(mer) AlX_3Y_3 species is associated with a linewidth theoretically twenty seven times broader than its cis-isomer counterpart. Such linewidth dependency upon the ligand field symmetry acting on the aluminum

nucleus was successfully utilized to identify a series of cis-trans isomers of aluminum halides in acetonitrile and acetonitrile–water solutions [268].

In the present study, because there is a molecular size effect on the linewidth of the resonance, it prevents any conclusion based upon the linewidth value of this resonance. Rather, the reasoning should be done by using QCC values. These AlX_3Y_3 (X = water, Y = phosphate) complexation sites were characterized by an ^{27}Al QCC value of respectively 2.6 MHz ("inside") and 4.8 MHz ("outside") which, in comparison to the QCC value of an hexaaquated aluminum cation (χ = 0.4 MHz), led to the conclusion that ^{27}Al NMR was probably detecting in both cases a trans AlX_3Y_3 species in the ATP_4Al_3 aggregate.

Both resonances centered at – 6 and – 38 ppm are endowed by a DFS which results from ^{27}Al NMR performed in the non-extreme narrowing limits. Knowing the $\omega_0\tau_c$ product (1.38) and their respective QCC values of 2.6 ± 0.5 and 4.8 ± 0.8 MHz, a DFS of – 2 ± 1 and – 9 ± 3 ppm was calculated for each line respectively. Their intrinsic chemical shifts, when corrected for their DFS were then 4 and 29 ppm respectively.

In the above discussion, calculation of the QCC values assumed that no chemical exchange contributed to the linewidth and that each linewidth resulted from pure quadrupolar relaxation of the ^{27}Al nucleus with a correlation time of 2.8 ns. The support for each of these assumptions will now be discussed.

The results from the deconvolution of every NMR spectrum showed that, over a wide range of ATP/Al ratios, the chemical shifts and linewidth values of each resonance were constant within experimental error (see Table 9.1) and a rapid or intermediate chemical exchange situation was ruled out. As a result, all observed resonances are in slow chemical exchange on the NMR time scale. The contribution

of slow chemical exchange to the observed linewidth values will now be examined in detail.

For the aluminum dimer, the absence of a significant chemical exchange contribution to the linewidth of the ^{27}Al dimer resonance was shown by a constant linewidth value (640 $\pm$ 70 Hz) throughout the various ATP/Al ratios.

Because the ATP_4Al_3 aggregate possesses different complexation sites, two on the stacked phosphate residues and two on the adenine base, the possibility of intramolecular exchange will be considered.

In order to demonstrate that each linewidth value originates from a pure quadrupolar interaction, ^{27}Al spin-lattice and spin-spin relaxation time measurements were made on the ATP–Al system (see Figure 9.21). For an ATP/Al ratio of 1.4, population analysis showed that the central peak was mainly composed of two resonances, in the ratio of 9:1, which were attributed to the aluminum dimer (10%), and to an aluminum–phosphate complex located in the "inside" of the aggregate (90%). In this ^{27}Al relaxation studies, the intensity variation of the central peak behaves as a function of two exponential decays and for the longitudinal magnetization:

$$I_z(t) = I_z(0)[1 - 2\{0.90\ \exp(-t/T_1') + 0.10\ \exp(-t/T_1)\}] \qquad (9.8)$$

while for the tranverse magnetization:

$$I_{xy}(t) = 0.90\ I_{xy}(0)\exp(-t/T_2') + 0.10\ I_{xy}(0)\exp(-t/T_2) \qquad (9.9)$$

in which the pre-exponential factors account for the population differences of the two species. T_1 and T_2 represent the spin-lattice and spin-spin relaxation times respectively of the aluminum dimer. The setting of the spin-lattice relaxation time of the aluminum dimer was equal to its T_2 value in equation (9.8) ($T_1 = T_2 = 1/\pi\mathcal{V}_{1/2}$). A non-linear regression analysis of equation (9.8) and (9.9) yielded the spin-lattice

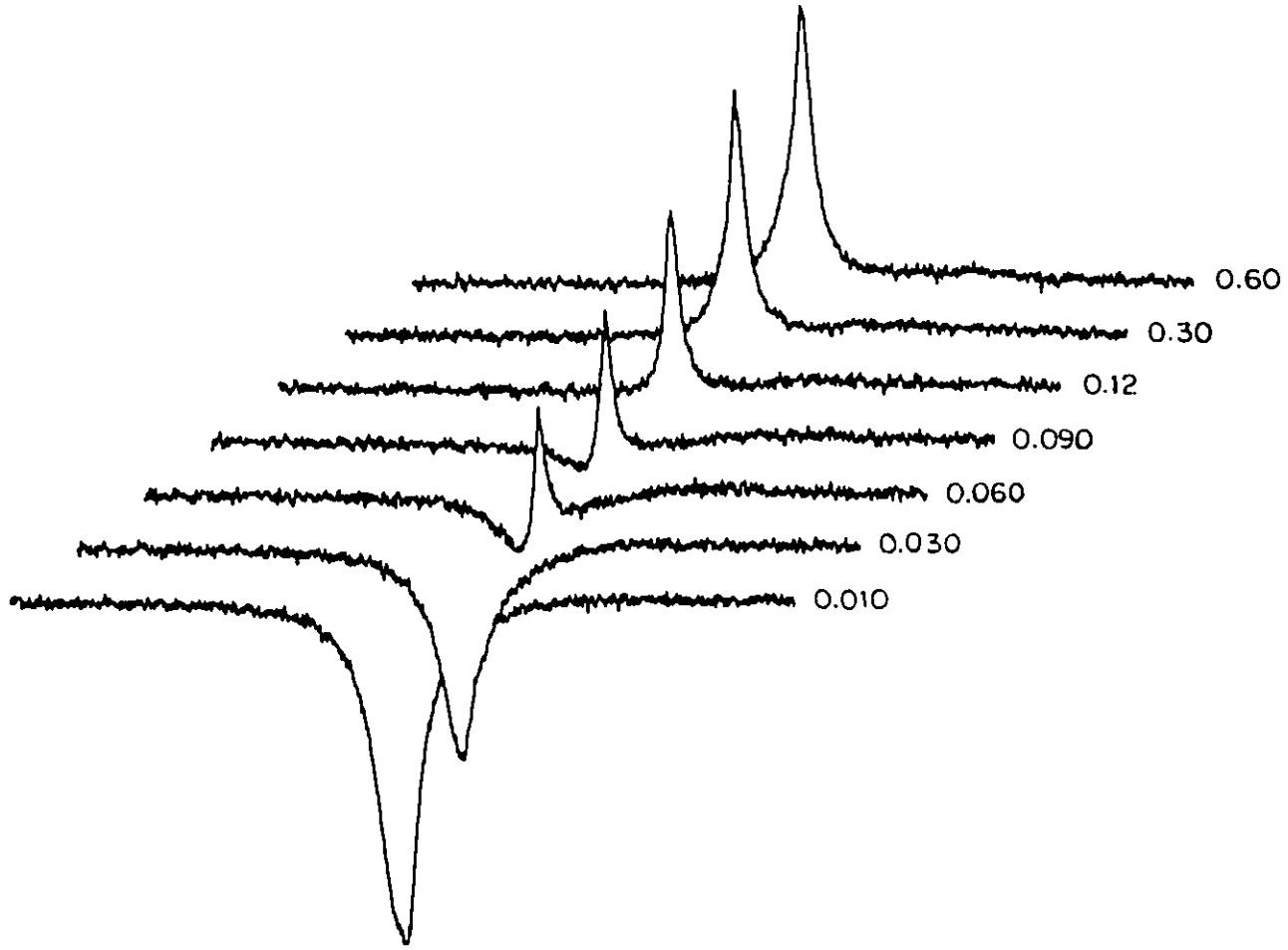

Figure 9.21: ^{27}Al inversion recovery experiment of an ATP-Al solution at 78 MHz. The ATP/Al ratio was 1.4. Instrumental conditions were: 100 KHz sweep width, acquisition time of 0.02 sec, α delay of 50 μs, 1000 transients for each spectrum and 20 Hz line broadening. Recovery times in milliseconds are shown near each spectrum. For experimental conditions see Table 9.1.

and spin-spin relaxation times of the phosphate complexed aluminum cation, with $T_1' = 0.32 \pm 0.06$ msec and $T_2' = 0.135 \pm 0.020$ msec.

The value of the spin-spin relaxation time translates into a resonance linewidth of 2.3 ± 0.3 KHz, in accordance with the linewidth value by spectral deconvolution (2.2 ± 0.2 KHz). This experimental result is in agreement with the absence, within experimental error, of any chemical exchange contribution to the linewidth of this complexation site located in the inside of the aggregate. Assuming pure quadrupolar relaxation, the ratio of the spin-lattice to spin-spin relaxation time T_1'/T_2' yields an ^{27}Al reorientational correlation time of 2.2 ± 0.9 ns, in good agreement with phosphorus-31 NMR results ($\tau_c = 2.8 \pm 0.8$ ns, see Section 5.3.5).

Finally, in the case of the adenine complexation site, the constant linewidth value of this resonance, within experimental error, also rules out any chemical exchange contribution. The ^{27}Al correlation time of this site was assumed to be identical to the two other sites of the aggregate and the validity of this assumption has already been discussed earlier.

9.6 Conclusion

Deconvolution of ^{27}Al NMR spectra of aluminum and ATP solutions showed the existence of four resonances in slow exchange on the NMR time scale. For each ATP/Al ratio value, each resonance was characterized by constant chemical shift and linewidth values. Theoretical treatment of nuclear spin relaxation of a spin 5/2 nucleus in the non-extreme narrowing condition, including the effect of dynamic frequency shift, leads to the conclusion that each observed resonance arises from the $|+1/2> \rightarrow |-1/2>$ nuclear spin transition. For each aluminum species, population analysis shows the presence of two distinct ATP/Al regions.

While in the region of ATP/Al > 1.4 phosphorus-31 NMR detects the overall complexation phenomena taking place on the triphosphate chains of the aggregate ^{27}Al NMR reveals the existence of two distinct complexation sites in the ratio of 2:1. For each resonance, the observed chemical shift values are typical of aluminum-phosphate complexes in solution. Quadrupole coupling constants of each site were estimated by using their respective linewidth and numerical solutions of nuclear spin relaxation occurring in the non-extreme narrowing limits.

Examination of chemical shifts and quadrupole coupling constant values suggest that two aluminum cations are buried in the "inside" of the aggregate and surrounded by a coordination sphere composed of three phosphate groups in the trans position, and three solvent water molecules. In the second binding site, located on the "outside" of the aggregate, the aluminum nucleus retains the same octahedral coordination sphere but is strongly influenced by the negatively charged triphosphate chain of the surface ATP molecule (see Figure 10.1).

When aluminum exceeds the ATP concentration in solution (ATP/Al < 1.4), ^{27}Al NMR detected the appearance of a new resonance which accounts for four aluminum nuclei. Its chemical shift value, falling in the range of aluminum-nitrogen complexes in solution, suggests that, once the ATP_4Al_3 aggregate is formed, further aluminum complexation occurs with the N-1 and N-7 nitrogen atoms of the adenine bases of the aggregate. This complexation scheme is in agreement with ^{13}C NMR results and the overall stoichiometry of the complex is ATP_4Al_7.

Finally, for various ATP/Al ratios and at both fields, ^{27}Al NMR reveals the presence of the aluminum dimer which only accounts for a small constant percentage (8%) of the total aluminum concentration.

For each aluminum species involved in the ATP-Al aggregate, the combination

of a long correlation time with large quadrupole coupling constant values resulted in a dynamic frequency shift for each resonance. Each resonance linewidth arises from pure quadrupolar relaxation and there is no chemical exchange contribution to the linewidth as confirmed by ^{27}Al relaxation time measurements.

The combination of spin-lattice and spin-spin relaxation experiments gave an ^{27}Al correlation time of 2.2 $\pm$ 0.9 ns, in agreement with ^{31}P NMR studies (see Figure 5.8). The results from ^{27}Al relaxation experiments also justify the quadrupole coupling constant and dynamic frequency shift values calculated in this study which assumed a correlation time of 2.8 ns.

Chapter 10

GENERAL CONCLUSION

Using multinuclear magnetic resonance techniques, it has been possible to gather information concerning the interactions occurring between ATP and Al in aqueous solutions at pH = 7.4. ^{1}H, ^{13}C, ^{31}P and ^{27}Al NMR results were combined in order to propose a detailed model for the ATP_4Al_3 aggregate believed to exist in aqueous solution. The overall structure is presented in Figure 10.1. Several features like the site of aluminum complexation, the stoichiometry, the geometric arrangement of the adenosine bases and the overall and internal dynamics of the complex have been discussed in detail in previous chapters. Each of these properties are summarized in Figure 10.1.

The proposed coordination sphere around the aluminum cation results from a mixture of ^{31}P and ^{27}Al NMR data. Proton-phosphorus NOE measurements suggested that each phosphate group of the aggregate was still solvated by one (α and β) or two (γ) water molecules. On the other hand,the chemical shift of the two different aluminum nuclei present in the aggregate were characteristic of a hexacoordinated cation. By combining these results it is not unreasonable to propose that the phosphate solvation sphere also belongs to the aluminum coordination sphere. This proposition is supported by the general chemistry of aqueous aluminum solu-

tions, which favors aqueous octahedral complexes. Finally, if the phosphate-water-aluminum assembly represents the basic motif of the aggregate, the sharing of water molecules between the phosphate ions and the aluminum cation gives an extra stability to the overall structure.

Although this study has enabled the proposition of a general structure, supported by a great deal of complementary results, there are still many fundamental questions to be answered. *In vitro* mixing of aluminum and ATP gave rise to a ATP_4Al_3 aggregate while many other binary mixtures of ATP and metallic cations showed the formation of monomers or dimers [41,148,283]. Studies of nucleotide aggregation induced by metallic cations generally result in an equilibrium of monomer, dimer, trimer species etc... dependent upon the nucleotide concentration [94]. In contrast to this, the complexation phenomenon between ATP and aluminum was independent over a wide range (1 to 100 mM) of total nucleotide concentration. Aggregate formation is accompanied by some striking particularities. For example, the existence of a surface ATP molecule confined in a pre-aggregated state represents an intriguing phenomenon. Intramolecular chemical exchange does occur, but the passage of this ATP molecule into an aggregated state is followed by the release of an aggregated ATP molecule at the other end of the aggregate.

Examination of molecular models show that the octahedral complexation of the aluminum cation, by a sandwich of triphosphate chains seems to dictate the spatial location of the adenosine molecules. As a result, the three inner bases of the aggregate tend to form a helix-like spatial arrangement. The surface ATP molecule which cannot adopt an aggregated conformation could result from steric hindrance factors with the aggregated bases. X-ray studies on the ATP–Al system could confirm the three dimensional structure proposed from NMR studies. For Al/ATP ratios greater

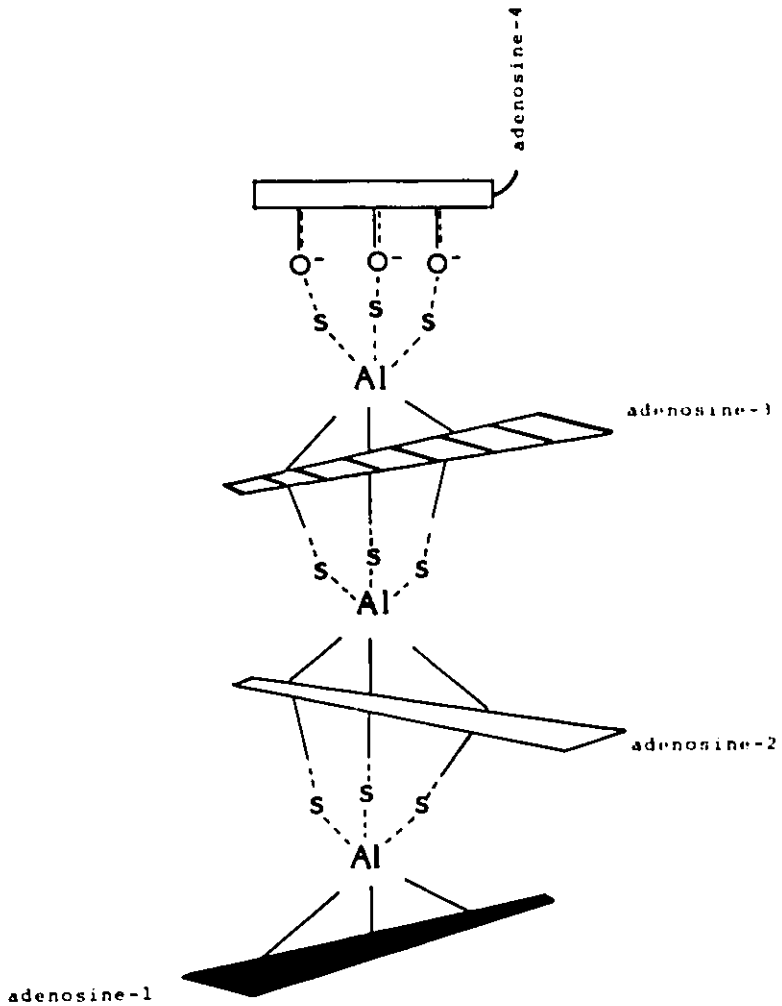

Figure 10.1: Final proposed model for the ATP_4Al_3 aggregate in solution. See text for details concerning the aluminum solvation sphere (S).

than 0.75, ^{13}C and ^{27}Al NMR results suggested that further complexation occurred on the adenine bases, the ATP_4Al_3 aggregate behaving as an aluminum sponge.

Information regarding the nature of complexation on the bases could be gained by ^{15}N NMR spectroscopy [277]. Also, it could provide more insight into the base geometry in the aggregate. Finally, since this work was performed to gain some insight into the nature of ATP–Aluminum complexes formed *in vitro*, the next step could be the study of ATP–Aluminum interactions in a biological system. ^{31}P NMR spectroscopy has proven to be a powerful tool in many areas of biological [278,280,281,282] and medicinal [279] chemistry.

Appendix A

Eigenfunctions, Eigenvalues and Matrix Elements [36,37]

For the states of a given quantum system, the wave functions $\Psi_1, \Psi_2, \ldots, \Psi_n, \ldots, \Psi_m$ are normalized and orthogonal that is:

$$\int_{-\infty}^{+\infty} \Psi_m^* \Psi_n d\tau = \delta_{mn} \tag{A.1}$$

δ_{mn} is called the Krőnecker delta and is always zero except for n = m when $\delta_{mn} = 1$. For the sake of simplicity the Dirac notation [40] is introduced. Equation A.1 then is written:

$$< m|n >= \delta_{mn} \tag{A.2}$$

in which Ψ_n and Ψ_m^* are designated by $|n >$ and $< m|$ respectively. If A represents an operator, the following integrals in the Dirac notation:

$$\int_{-\infty}^{+\infty} \Psi_m^* A \Psi_n d\tau =< m|A|n >= A_{mn} \tag{A.3}$$

are known as the matrix elements of A and give a matrix representation of the operator A, of the form:

$$A = \begin{pmatrix} A_{11} & A_{12} & \ldots & A_{1n} \\ A_{21} & A_{22} & \ldots & A_{2n} \\ \vdots & \vdots & \ddots & \vdots \\ A_{n1} & A_{n2} & \ldots & A_{nn} \end{pmatrix} \tag{A.4}$$

The matrix is Hermitian if $A_{mn} = A^*_{nm}$. A state which will satisfy the relation

$$A\Psi_n = a_n\Psi_n \tag{A.5}$$

is called an eigenstate and Ψ_n and a_n are the corresponding eigenfunction and eigenvalue of the operator A. All eigenfunction $\Psi_1, \Psi_2, \ldots, \Psi_n, \ldots, \Psi_m$ of the operator A which have different eigenvalues $a_1, a_2, \ldots, a_n, \ldots, a_m$ are orthogonal to each other and the matrix A using equation A.5 takes the form:

$$A = \begin{pmatrix} A_{11} & 0 & \ldots & 0 \\ 0 & A_{22} & \ldots & 0 \\ \vdots & \vdots & \ddots & \vdots \\ 0 & 0 & \ldots & A_{nn} \end{pmatrix} \tag{A.6}$$

Bibliography

[1] P. Galle; "La Recherche" 17, 764 (1986)

[2] A.I. Arieff; J. Cooper; D. Armstrong; V.C. Lararomtz; *Ann. Inter. Med.* 90, 741 (1979)

[3] .C. Alfrey; G.R. Le Gendre; W.D. Kaehny; *N. Engl. J. Med.* 294, 184 (1976)

[4] D.R. Crapper; S.S. Krishman; A.J. Dalton; *Science* 180, 511 (1973)

[5] D.P. Perl; A.R. Brody; *Science* 208, 297 (1980)

[6] P. Galle; C. Meyrignac; P. Heine; *C. R. Acad. Sci. (III)* 299, 535 (1984)

[7] D.R. Crapper McLachlan; *Neurobiol. Aging* 7, 525 (1986)

[8] V. De Boni; J.W. Scott; D.R. Crapper; *Histochemistry* 40, 31 (1974)

[9] G.L. Eichhorn; G.A. Elgavish; S.J. Karlic; *J. Am. Chem. Soc.* 105, 602 (1983)

[10] R.E. Viola; J.F. Morrison; W.W. Cleland; *Biochemistry* 19, 3131 (1980)

[11] L.P. Solheim; H.J. Fromm; *Biochemistry* 19, 6074 (1980)

[12] L.G. Marzilli; "Advances in Inorganic Biochemistry" G.L. Eichhorn and L.G. Marzilli (Eds.); Elsevier North-Holland; 3, 47 (1981)

[13] W.W. Cleland; A.S. Mildvan; "Advances in Inorganic Biochemistry" G.L. Eichhorn and L.G. Marzilli (Eds.); Elsevier North-Holland; 1, 163 (1979)

[14] L.G. Marzilli; *Prog. Inorg. Chem.* 23, 211 (1977)

[15] R.W. Gellert; R. Bau; "Metal Ions in Biological Systems" H. Sigel (Eds.); Marcel Dekker, New York, 8, 1 (1979)

[16] R.B. Martin; Y.H. Mariam; "Metal Ions in Biological Systems" H. Sigel (Eds.); Marcel Dekker, New York, 8, 57 (1979)

[17] G.L. Eichorn; L.G. Marzilli; "Advances in Inorganic Biochemistry" G.L. Eichhorn and L.G. Marzilli (Eds.); Elsevier North-Holland; 2, (1980)

[18] J.P. Laussac; J.P. Laurent; *C. R. Acad. Sc. Paris* 291, 157 (1980).

[19] J-P. Laussac; G. Commenges; *Nouv. J. Chim.* 7, 579 (1983).

[20] S.J. Karlik; G.A. Elgavish; G.L. Eichhorn; *J. Am. Chem. Soc* 105, 602 (1983).

[21] R.J Boegman; L.A Bates; *Can. J. Physiol. Pharmacol.* 62, 1010 (1984)

[22] F.C. Womack; S.P. Colowick; *Proc. Natl. Acad. Sci. USA* 76, 5080 (1979)

[23] G.V. Ohning; K.E. Neet; *Biochemistry* 22, 2987 (1983)

[24] R.L. Bertholf; M.R. Wills; J. Savory; *Biochem. Biophys. Res. Commun.* 125, 1020 (1984)

[25] M. Cochran; J. Coates; S. Neoh; *FEBS. Letters* 176, 129 (1984)

[26] M. Cochran; D. Patterson; S. Neoh; B. Stevens; R. Mazzachi; *Clin. Chem.* 31, 1314 (1985)

[27] A.A. Moshtaghie; A.W. Skillen; *Biochem. Soc. Trans.* 14, 916 (1986)

[28] S.J. Karlik; G.L. Eichhorn; P.N. Lewis; D.R. Crapper; *Biochemistry* 19, 5991 (1980)

[29] D. Dyrssen; C. Haraldsson; E. Nyberg; M. Wedborg; *J. Inorg. Biochem.* 29, 67 (1987)

[30] A.S. Tracey; T.L. Boivin; *J. Am. Chem. Soc.* 105, 4901 (1983)

[31] M. Deleers; *Res. Commun. Chem. Pathol. Pharmacol.* 49, 277 (1985)

[32] M. Deleers; J-P. Servais; E. Wulfert; *Biochim. Biophys. Acta.* 813, 195 (1985)

[33] J. Patocka; J. Bajgar; *Inorg. Chim. Acta.* 135, 161 (1987)

[34] J.C.K. Lai; F.F. Guest; T.K.C. Leung; L. Lim; A.N. Davison; *Biochem. Pharmacol.* 29, 141 (1980)

[35] A. Abragam; "Principles of Nuclear Magnetism" W.C. Marshall and D.H. Wilkinson (Ed), Oxford University Press (1982)

[36] P. Sohar; "Nuclear Magnetic Resonance Spectroscopy" CRC Press Vol.1 and Vol.2 (1983)

[37] A. Carrington; A.D. McLachlan; "Introduction to Magnetic Resonance" Harper and Row (1967)

[38] F. Bloch; *Phys. Rev.* 70, 460 (1946)

[39] H.J. Osten; C.J. Jameson; *Mol. Phys.* 57, 553 (1986)

[40] P.D. Buckley; K.W. Jolley; D.N. Pinder; *Prog. NMR Spectro.* 10, 1, (1975)

[41] J.L. Bock; *J. Inorg. Bioch.* 12, 119 (1980)

[42] E.L. Hahn; *Phys. Rev.* 80, 580 (1950).

[43] D. Shaw; "Fourier Transform N.M.R. Spectroscopy" Elsevier Scientific Publishing Company, Amsterdam (1976).

[44] H.M. McConnell; *J. Chem. Phys.* 28, 430 (1957).

[45] D.E. Woessner; *J. Chem. Phys.* 35, 41 (1960).

[46] J.S. Leigh, Jr.; *J. Magn. Reson.* 4, 308 (1971).

[47] J.S. Leigh, Jr.; A.C. McLaughlin; *J. Magn. Reson.* 9, 296 (1973).

[48] J.R. Zimmerman; W.E. Brittin; *J. Phys. Chem.* 61, 1328 (1957).

[49] D.E. Woessner; J.R. Zimmerman; *J. Phys. Chem.* 67, 1590 (1962).

[50] K.J. Packer; in "Progress in Nuclear Magnetic Resonance Spectroscopy" Alden press, Oxford, Vol. 3, Chap 3, p. 87.

[51] P.S. Hubbard; *J. Chem. Phys.* 53, 985 (1970).

[52] T.E. Bull; *J. Magn. Reson.* 8, 344 (1972)

[53] P. Laszlo; in "The Multinuclear Approach to NMR Spectroscopy" J.B. Lambert and F.G. Riddell (Eds.), D. Reidel Publishing Company, Dordrecht, Chap 12 (1982)

[54] A. Delville; C. Detellier; P. Laszlo; *J. Magn. Reson.* 34, 301 (1979)

[55] H. Monoi; H. Vedaira; *J. Magn. Reson.* 38, 119 (1980)

[56] A.G. Marshall; T.C.L. Wang; C.E. Cottrell; L.G. Werbelow; *J. Am. Chem. Soc.* 104, 7665 (1982)

[57] G.C. Levy; J.R. Lyerla; in "Topics in C-13 NMR Spectroscopy" (G.C. Levy, Ed) Vol.1 John Wiley and Sons, New York (1974).

[58] R.L. Vold; J.S. Waugh; M.P. Klein; D.E. Phelps; *J. Chem. Phys.* 48, 3831 (1968).

[59] H.Y. Carr; E.M. Purcell; *Phys. Rev.* 94, 630 (1954).

[60] R.K. Harris; R.H. Newman; *J. Magn. Reson.* 24, 449 (1976).

[61] D. Canet; G.C. Levy; I.R. Peat; *J. Magn. Reson.* 48, 199 (1975).

[62] R.K. Gupta; J.A. Ferretti; E.D. Becker; G.H. Weiss; *J. Magn. Reson.* 38, 447 (1980).

[63] J.L. Markley; W.J. Horsley; M.P. Klein; *J. Chem. Phys.* 55, 3604 (1971).

[64] G.G. McDonald; J.S. Leigh; *J. Magn. Reson.* 9, 358 (1973).

[65] E.L. Hahn; *Phys. Rev.* 80, 580 (1950).

[66] R. Freeman; H.D.W. Hill; *J. Chem. Phys.* 54, 3367 (1971).

[67] R.K. Gupta; *J. Magn. Reson.* 25, 231 (1977).

[68] R.K. Gupta; G.H. Weiss; J.A. Ferretti; E.D. Becker; *J. Magn. Reson.* 35, 301 (1979).

[69] G.C. Levy; I.R. Peat; *J. Magn. Reson.* 18, 500 (1975).

[70] R. Freeman; H.D.W. Hill; R. Kaptein; *J. Magn. Reson.* 7, 82 (1972).

[71] J.Sass; D. Ziessow; *J. Magn. Reson.* 25, 263 (1977).

[72] E.D. Becker; J.A. Ferretti; R.K. Gupta; G.H. Weiss; *J. Magn. Reson.* 37, 381 (1980).

[73] G.H. Weiss; R.K. Gupta; J.A. Ferretti; E.D. Becker; *J. Magn. Reson.* 37, 369 (1980).

[74] D.L. De Fontaine; D.K. Ross; B. Ternai; *J. Magn. Reson.* 18, 276 (1972).

[75] R. Crouch; S. Hurlbert; A. Ragouzeos; *J. Magn. Reson.* 49, 371 (1982).

[76] J. Kowalewski; G.C. Levy; L.F. Johnson; L. Palmer; *J. Magn. Reson.* 26, 533 (1977).

[77] A.J. Shaka; J. Keeler; R. Freeman; *J. Magn. Reson.* 53, 313 (1983).

[78] D. Canet; *J. Magn. Reson.* 23, 361 (1976).

[79] G.H. Weiss; J.A. Ferretti; *J. Magn. Reson.* 55, 397 (1983).

[80] G.H. Weiss; J.A. Ferretti; J.E. Kieffer; L. Jacobson; *J. Magn. Reson.* 53, 7 (1983).

[81] C.J. Turner; *Prog. NMR. Spectrosc.* 16, 311 (1984).

[82] H. Hanssom; H. Ruterjans; *J. Magn. Reson.* 39, 65 (1980).

[83] G.H. Weiss; J.A. Ferretti; *J. Magn. Reson.* 61, 499 (1985).

[84] H. Hanssom; W. Maurer; H. Ruterjans; *J. Magn. Reson.* 31, 231 (1978).

[85] W.E. Morgan; J.R. Van Wazer; *J. Am. Chem. Soc.* 97, 6347 (1975)

[86] H.S. Kielman; J.C. Leyte; *Ber. Bun. Ges.* 79, 1201 (1975)

[87] J. Granot; G.A. Elgavish; J.S. Cohen; *J. Magn. Reson.* 33, 569 (1979)

[88] P.L. Yeagle; W.C.Hutton; R.B. Martin; *J. Am. Chem. Soc.* 97, 7175 (1975)

[89] G.A. Elgavish; J. Granot; *J. Magn. Reson.* 36, 147 (1979)

[90] D.C. McCain; J.L. Markley; *J. Am. Chem. Soc.* 102, 5565 (1980)

[91] F.E. Evans; *Arch. Biochem. Biophys.* 193, 63 (1979)

[92] R.K. Nanda; A.Ribeiro; T.S. Jardetzky; O. Jardetzky; *J. Magn. Reson.* 39, 119 (1980)

[93] A.M. Avedikian; D. Besserre; M. Delepierre; *J. Chim. Phys.* 79, 81 (1982)

[94] K.H. Scheller; F. Hofstetter; P.R. Mitchell; B. Prijs; H. Sigel; *J. Am. Chem. Soc.* 103, 247 (1981)

[95] H. Sigel; *J. Inorg. Nucl. Chem.* 39, 1903 (1977)

[96] O. Kennard; N.W. Isaacs; W.D.S. Motherwell; J.C. Coppola; D.L. Wampler; A.C. Larson; D.G. Watson; *Proc. R. Soc. Lond.* A325, 401 (1971)

[97] O. Kennard; N.W. Isaacs; J.C.Coppola; A.J. Kirby; S. Warren; W.D.S. Motherwell; D.G.Watson; D.L. Wampler; D.H. Chenery; A.C. Larson; K.A.Keer; L. Riva Di Sanseverino; *Nature* 225, 333 (1970)

[98] D. Perahia; B. Puilman; A. Saran; *Biochem. Biophys. Res. Commun.* 47, 1284 (1972)

[99] P. Tanswell; J.M. Thornton; A.V. Korda, R.J.P. Williams; *Eur. J. Biochem.* 57, 135 (1975)

[100] P.H. Bolton; T.L. James; *J. Am. Chem. Soc.* 102, 25 (1980)

[101] H. Santos; A.V. Xavier; C.F.G.C. Geraldes; *Can. J. Chem.* 61, 1456 (1983)

[102] P.A. Hart; *Biophys. J.* 24, 833 (1978)

[103] M. Brauer; B.D. Sykes; *Biochem.* 20, 6767 (1981)

[104] P.A. Hart; *J. Am. Chem. Soc.* 98, 3735 (1976)

[105] T.A. Glassman; C. Cooper; L.W. Harrison; T.J. Swift; *Biochem.* 10, 843 (1971)

[106] Y.F. Lam; G. Kotowycz; *Can. J. Chem.* 55, 3620 (1977)

[107] B.E. Conway; in "Ionic Hydration in Chemistry and Biophysics" Elsevier Scientific, Amsterdam, Chap 9 and 27 (1981)

[108] O.Y. Samoilov; *Discuss. Faraday Soc.* 24, 141 (1957)

[109] C.Devrell; *Prog. NMR Spectrosc.* 4, 235 (1969)

[110] D.E.C. Corbridge; in "The Structural Chemistry of Phophorus" Elsevier Scientific Publishing Company, Amsterdam, Chap. 7 and 9 (1974)

[111] I. Solomon; *Phys. Rev.* 99, 559 (1955)

[112] I.D. Campbell; R. Freeman; *J. Magn. Reson.* 11, 143 (1973)

[113] J.M. Neumann; S.Tran-Dinh; *Biopolymers* 20, 89 (1981)

[114] C. Brevard; P. Granger; "Handbook of High Resolution Multinuclear NMR" Wiley-Interscience, New York, (1981)

[115] G. Govil; R.V. Hosur; "NMR Basic Principles and Progress" Springer-Verlay, Berlin, Vol. 20 (1982)

[116] A.C. Larson; *Acta. Cryst.* B34, 3601 (1978)

[117] E. Ayranci; B.E. Conway; *J. Chem. Soc. Faraday Trans.* (1) 79, 1357 (1983)

[118] M. Bisnaire; C. Detellier; D. Nadon; *J. Can. Chem.* 60, 3071 (1982)

[119] R.B. Martin; Y.H. Mariam; "Metal Ions in Biological Systems" H. Sigel (Ed), Marcel Dekker, New York, Chap. 2 (1979)

[120] A.Paris; P.Laszlo; "Magnetic Resonance in Colloid and Interface Science" H.A. Resing and C.G. Wade (Eds), A.C.S. Symposium Series, American Chemical Society, Washington, 34, 418 (1976)

[121] "CRC Handbook of Chemistry and Physics" 63rd ed., R.C. Weast (Ed), C.R.C. Press, Florida (1982)

[122] C. Deverell; *Prog. NMR Spectrosc.* 4, 235 (1969)

[123] M. Falk; K.A.Hartman, Jr.; and R.C. Lord; *J. Am. Chem. Soc.* 84, 3843 (1962)

[124] B. Lubas; T.Wilczok; *Biochem. Biophys. Acta* 120, 427 (1965).

[125] B. Lubas; T. Wilczok; *Bipolymers* 10, 1267 (1971).

[126] G.I. Rhyw; W.J. Ray, Jr.; and J.L. Markley; *Biochemistry* 23, 252 (1984).

[127] C.H. Wang; D.M. Grant; J.R. Lyerla; *J. Chem. Phys.* 55, 4674 (1971).

[128] P.S. Hubbard; *Phys. Rev.* 131, 1155 (1963)

[129] R.G. Kidd; "NMR of Newly Accessible Nuclei" P.Laszlo (Ed), Academic Press, New York, Vol. 1, 103 (1983)

[130] T. Glonek; *J. Am. Chem. Soc.* 98, 7090 (1976)

[131] M.P. Heyn; R. Bretz; *Biophys. Chem.* 3, 35 (1975)

[132] J.W. Keepers; T. James; *J. Am. Chem. Soc.* 104, 929 (1982)

[133] P. Davanloo; I.M. Armitage; D.M. Crothers; *Biopolymers* 18, 663 (1979)

[134] T.D. Alger; S.W. Collins; D.M. Grant; *J. Chem. Phys.* 54, 2820 (1971)

[135] D.B. Davies; *Prog. NMR Spectrosc.* 12, 135 (1978)

[136] D.C.McCain; R. Virudachalam; R.E. Santini; S.S.Abdel-Meguid; J.L.Markley; *Biochemistry* 21, 5390 (1982)

[137] P. Bendel; O. Laub; T.L. James; *J. Am. Chem. Soc.* 104, 6748 (1982)

[138] L.M. Rhodes; P.R. Schimmel; *Biochemistry* 10, 4426 (1971)

[139] O. Roder; H.D. Ludemann; E. Von Goldammer; *Eur. J. Biochem.* 53, 517 (1975)

[140] D.Doddrell; V. Glushko; A. Allerhand; *J. Chem. Phys.* 56, 3683 (1972)

[141] E.A.L. Luchen; D.F. Williams; *Mol. Phys.* 16, 17 (1969)

[142] J.B. Lambert; R.J. Nienhuis; J.W. Keepers; *Angew. Chem. Int. Ed.* 20, 487 (1981)

[143] J.L. Bock; D.E. Ash; *J. Inorg. Biochem* 13, 105 (1980).

[144] G.L. Eichhorn in "Inorganic Biochemistry" ; G.L. Eichhorn (Ed.), Elsevier, New York, Vol. 2, 1191 (1973).

[145] M. Cohn; T.R. Hughes; *J. Biol. Chem.* 237, 176 (1962).

[146] P. Chaudhuri; H. Sigel; *J. Am. Chem. Soc.* 99, 3142 (1977).

[147] D.G. Gorenstein; in "Phosphorus-31 NMR" , D.G. Gorenstein (Ed.); Academic Press, New York, Chap 1 (1984).

[148] Y.J. Shyy; T.C. Tsai; M.D. Tsai; *J. Am. Chem. Soc.* 107, 3478 (1985).

[149] S. Meiboom; D. Gill; *Rev. Sci. Instrum.* 29, 688 (1958).

[150] R.L. Vold; R.R. Vold; *Prog. NMR Spectrosc.* 12, 79 (1978).

[151] R. Freeman; H.D.W. Hill;
in "Dynamic Nuclear Magnetic Resonance Spectroscopy" , F.A. Cotton and L.M. Jackman (Eds); Academic Press, New York, p. 131 (1975).

[152] G.C. Levy (Ed.); "Topics in Carbon-13 NMR Spectroscopy" , Wiley-Interscience, New-York (1979)

[153] G.C. Levy; R.L. Lichter; G.L. Nelson;
"Carbon-13 Nuclear Magnetic Resonance Spectroscopy" , 2nd Edition, Wiley-Interscience, New-York (1980)

[154] R. Benn; H. Gunther; *Angew. Chem. Int. Ed. Engl.* 22, 350 (1983)

[155] G. Govil; R.V. Hosur; "NMR Basic Principles and Progress" , P. Diehl, E. Fluck, R. Kosfeld (Eds.), Springer-Verlag, Berlin, Vol. 20 (1982)

[156] P. Laszlo; *Prog. NMR Spectrosc.* 13, 257 (1979)

[157] M. Oki; "Methods in Stereochemical Analysis" , A.P. Marchand (Ed.) VCH Publishers, Florida, Vol. 4 (1985)

[158] J. Sandstrom; "Dynamics NMR Spectroscopy" , Academic Press, New-York (1982)

[159] C.D. Jardetzky; O. Jardetzky; *J. Am. Chem. Soc.* 82, 22 (1960)

[160] L. Gatlin; J.C. Davis; *J. Am. Chem. Soc.* 84, 4464 (1962)

[161] L.F. Johnson; W.C. Jankowski; "Carbon-13 NMR Spectra" , Wiley-Interscience, New-York (1972)

[162] R. Rymden; P. Stilbs; *Biophys. Chem.* 21, 145 (1985)

[163] I. Stokkeland; P. Stilbs; *Biophys. Chem.* 22, 65 (1985)

[164] C.L. Fisk; E.D. Becker; H.T. Miles; T.J. Pinnavaia; *J. Am. Chem. Soc.* 104, 3307 (1982)

[165] D.M. Cheng; L.S. Kan; P.O.P. Ts'O; C. Giessner-Prettre; B. Pullman; *J. Am. Chem. Soc.* 102, 525 (1980)

[166] S.B. Petersen; J.J. Led; E.R. Johnston; D.M. Grant; *J. Am. Chem. Soc.* 104, 5007 (1982)

[167] M. Borzo; C. Detellier; P. Laszlo; A. Paris; *J. Am. Chem. Soc.* 102, 1124 (1980)

[168] A. Allerhand; R.K. Hailstone; *J. Chem. Phys.* 56, 3718 (1972)

[169] J. Jeener; in an unpublished lecture to the Ampere International Summer School, Basko Polje, Yugoslavia (1971)

[170] W.P. Aue; E. Bartholdi; R.R. Ernst; *J. Chem. Phys.* 64, 2229 (1976)

[171] W.A. Anderson; R. Freeman; *J. Chem. Phys.* 37, 85 (1962)

[172] J.C. Lindon; A.C. Ferrige; *Prog. NMR Spectrosc.* 14, 27 (1980)

[173] A. Bax; in "Two-Dimensional Nuclear Magnetic Resonance in liquids" , Delft University Press, Dordrecht, Holland (1982)

[174] R. Freeman; *Proc. R. Soc. Lond.* A373, 149 (1980)

[175] J.C. Lindon; A.G. Ferrige; *J. Magn. Reson.* 36, 277 (1979)

[176] A.G. Ferrige; J.C. Lindon; *J. Magn. Reson.* 31, 337 (1978)

[177] A. Bax; R. Freeman; G.A. Morris; *J. Magn. Reson.* 43, 333 (1981)

[178] W. McFarlane; D.S. Rycroft; *Annu. Rep. NMR Spectrosc.* 16, 293 (1985)

[179] B.H. Meier; P. Bachmann; R.R. Ernst; *J. Chem. Phys.* 71, 4546 (1979)

[180] D.L. Turner; *Prog. NMR Spectrosc.* 17, 281 (1985)

[181] R.R. Ernst; G. Bodenhausen; A. Wokaun;
"Principles of Nuclear Magnetic Resonance in One and Two Dimensions" , R. Breslow; J.B. Goodenough, J. Halpern, J.S. Rowlinson (Eds.), Clarendon Press, Oxford (1987)

[182] D.L. Turner; *J. Magn. Reson.* 61, 28 (1985)

[183] Y. Huang; S. Macura; R.R. Ernst; *J. Am. Chem. Soc.* 103, 5327 (1981)

[184] G. Bodenhausen; R.R. Ernst; *J. Am. Chem. Soc.* 104, 1304 (1982)

[185] A.L. Schwartz; J.D. Cutnell; *J. Magn. Reson.* 53, 398 (1983)

[186] G.E. Hawkes; S. Aime; *J. Chem. Soc. Dalton Trans.* 225 (1985)

[187] C.M. Dobson; L.Y. Lian; C. Redfield; K.D. Topping; *J. Magn. Reson.* 69, 201 (1986)

[188] P.B. Garlick; C.J. Turner; *J. Magn. Reson.* 51, 536 (1983)

[189] R.S. Balaban; J.A. Ferretti; *Proc. Natl. Acad. Sci. USA* 80, 1241 (1983)

[190] J.R. Alger; R.G. Shulman; *Q. Rev. Biophys.* 17, 83 (1984)

[191] G.L. Mendz; G. Robinson; P.W. Kuchel; *J. Am. Chem. Soc.* 108, 169 (1986)

[192] A. Kumar; G. Wagner; R.R. Ernst; K. Wuthrich; *Biochem. Biophys. Res. Commun.* 96, 1156 (1980)

[193] A. Kumar; R.R. Ernst; K. Wuthrich; *Biochem. Biophys. Res. Commun.* 95, 1 (1980)

[194] C. Bosch; A. Kumar; R. Baumann; R.R. Ernst; K. Wuthrich; *J. Magn. Reson.* 42, 159 (1981)

[195] A. Kumar; G. Wagner; R.R. Ernst; K. Wuthrich; *J. Am. Chem. Soc.* 103, 3654 (1981)

[196] J. Feigon; J.M. Wright; W. Leupin; W.A. Denny; D.R. Kearns; *J. Am. Chem. Soc.* 104, 5540 (1982)

[197] S. Macura; K. Wuthrich; R.R. Ernst; *J. Magn. Reson.* 47, 351 (1982)

[198] R.M. Scheek; N. Russo; R. Boelens; R. Kaptein; *J. Am. Chem. Soc.* 105, 2914 (1983)

[199] S. Forsen; R.A. Hoffman; *Acta Chem. Scand.* 17, 1787 (1963)

[200] S. Forsen; R.A. Hoffman; *J. Chem. Phys.* 39, 2892 (1963)

[201] S. Forsen; R.A. Hoffman; *J. Chem. Phys.* 40, 1189 (1964)

[202] J.B. Lambert; R.J. Nienhuis; J.W. Keepers; *Angew. Chem. Int. Ed. Engl.* 20, 487 (1981)

[203] K.E. Kover; G. Batta; *J. Magn. Reson.* 69, 344 (1986)

[204] K.E. Kover; G. Batta; Z. Madi; *J. Magn. Reson.* 69, 538 (1986)

[205] P. Baine; *Magn. Reson. Chem.* 24, 304 (1986)

[206] G. Wider; R.V. Hosur; K. Wuthrich; *J. Magn. Reson.* 52, 130 (1983)

[207] R. Baumann; G. Wider; R.R. Ernst; K. Wuthrich; *J. Magn. Reson.* 44, 402 (1981)

[208] J.H. Noggle; R.E. Schirmer; "The Nuclear Overhauser Effect" , Academic Press, London (1971)

[209] J.R. Alger; J.A. Den Hollander; R.G. Shulman; *Biochemistry* 21, 2957 (1982)

[210] T.R. Brown; K. Vgurbil; R.G. Shulman; *Proc. Natl. Acad. Sci. USA* 74, 5551 (1977)

[211] D.G. Gadian; G.K. Radda; T.R. Brown; E.M. Chance; M.J. Dawson; D.R. Wilkie; *Biochem. J.* 194, 215 (1981)

[212] P.M. Matthews; J.L. Bland; D.G. Gadian; G.K. Radda; *Biochem. Biophys. Res. Commun.* 103, 1052 (1981)

[213] T.R. Brown; *Phil. Trans. R. Soc. Lond.* B289, 441 (1980)

[214] C.L. Perrin; E.R. Johnston; *J. Magn. Reson.* 33, 619 (1979)

[215] G.M. Clore; G.C.K. Roberts; A. Gronenborg; B. Birdsall; J. Feney; *J. Magn. Reson.* 45, 151 (1981)

[216] P.D. Ellis; P.P. Yang; A.R. Palmer; *J. Magn. Reson.* 52, 254 (1983)

[217] J. Hennig; H.H. Limbach; *J. Magn. Reson.* 49, 322 (1982)

[218] J. Frahm; *J. Magn. Reson.* 47, 209 (1982)

[219] P.A. Hart; in "Phosphorus 31 NMR: Principles and Applications" , D.G. Gorenstein (Ed.), Academic Press, London, Chapt. 11 (1984)

[220] J.L. James; in "Phosphorus-31 NMR: Principles and Applications" , D.G. Gorenstein (Ed.), Academic Press, London, Chapt. 12 (1984)

[221] D.E Woessner; *J. Chem. Phys.* 36, 1 (1962)

[222] W.E. Hull, B.D Sykes; *J. Mol. Biol.* 98, 121 (1975)

[223] B.D Sykes; *Can. J. Biochem.* 61, 155 (1983)

[224] L. Klevan; I.M. Armitage; D.M. Crothers; *Nuclei Acids Res.* 6, 1607 (1979)

[225] H. Shindo; *Biopolymers* 19, 509 (1980)

[226] J. Sandstrom; "Dynamic NMR Spectroscopy" , Academic Press, New-York (1982)

[227] H. Anton; "Elementary Linear Algebra" , John Wiley and Sons, New-York, Chapt. 6 and 7 (1984)

[228] K. Ichikawa; *J. Chem. Soc. Faraday Trans.* 82, 1913 (1986)

[229] J.B. Lambert; J.W. Keepers; *J. Magn. Reson.* 38, 233 (1980)

[230] J.J. Delpuech; in "NMR of Newly Accessible Nuclei" P. Laszlo (Ed), Academic Press, New-york, Vol. 2 Chapt. 6 (1983)

[231] J.W. Akitt; *Annu. Rep. NMR Spectrosc.* 5A, 465 (1972)

[232] J.W. Akitt; J.M. Elders; *J. Magn. Reson.* 63, 587 (1985)

[233] A. Brevard; in "Multinuclear Approach to NMR Spectroscopy" J.B. Lambert and F.G. Riddell (Eds), D. Reidel Publishing Company, Dordrecht (1982)

[234] A. Delville; C. Detellier; *Can. J. Chem.* 64, 1845 (1986)

[235] E. Fukushima; S.B.W. Roder; *J. Magn. Reson.* 33, 199 (1979)

[236] R. Benn; A. Rufinska; E. Janssen; H. Lehmkuhl; *Organometallics* 5, 825, (1986)

[237] J.W. Akitt; B.E. Mann; *J. Magn. Reson.* 44, 584 (1981)

[238] M. Dalibart; J. Derouault; P. Granger; *Inorg. Chem.* 20, 3975 (1981)

[239] M. Dalibart; J. Derouault; P. Granger; *Inorg. Chem.* 21, 1040 (1982)

[240] M. Dalibart; J. Derouault; P. Granger; *Inorg. Chem.* 21, 2241 (1982)

[241] B. Halle, H. Wennerstrom; *J. Magn. Reson.* 44, 89 (1981)

[242] T.E. Bull; S. Forsen; D.L. Turner; *J. Chem. Phys.* 70, 3106 (1979)

[243] H. Levanon; S. Charbinsky; *J. Chem. Phys.* 53, 3056 (1970)

[244] J. Reyben; Z. Luz; *J. Phys. Chem.* 80, 1357 (1976)

[245] T. Drakenberg; S. Forsen;
in "The multinuclear approach to NMR spectroscopy" ; J.B. Lambert and F.G. Riddell (Eds.), D. Reidel Publishers, Dordrecht, Chap. 14 (1982)

[246] T. Anderson; T. Drakenberg; S. Forsen; E. Thulin; N. Sward; *J. Am. Chem. Soc.* 104, 576 (1982)

[247] P. Westlund; H. Wennerstrom; *J. Magn. Reson.* 50, 451 (1982)

[248] R. Poupko; A. Baram; Z. Luz; *Mol. Phys.* 27, 1345 (1974)

[249] L.G. Werbe Low; A.G. Marshall; *J. Magn. Reson.* 43, 443 (1981)

[250] K.J. Neurohr; T. Drakenberg; S. Forsen; in "NMR of Newly accessible Nuclei" P. Laszlo (ed.) Chap. 8 (1983)

[251] A. Hudson; *Mol. Phys.* 16, 395 (1969)

[252] G.K. Fraenkel; *J. Chem. Phys.* 42, 4275 (1965)

[253] A.D. McLachlan; *Proc. Roy. Soc. London* A280, 271 (1964)

[254] J.W. Akitt; N.N. Greenwood; B.L. Khandelwal; G.D. Lester; *J. Chem. Soc. Dalton* 604 (1972)

[255] J.W. Akitt; A. Farthing; *J. Magn. Reson.* 32, 345 (1978)

[256] J.W. Akitt; A. Farthing, O.W. Howarth; *J. Chem. Soc. Dalton Trans.* 1606 (1981)

[257] J.W. Akitt; A. Farthing; O.W. Howarth; *J. Chem. Soc. Dalton Trans.* 1609 (1981)

[258] J.W. Akitt; A. Farthing; *J. Chem. Soc. Dalton Trans.* 1615 (1981)

[259] J.W. Akitt; A. Farthing; *J. Chem. Soc. Dalton Trans.* 1617 (1981)

[260] J.W. Akitt; A. Farthing; *J. Chem. Soc. Dalton Trans.* 1624 (1981)

[261] J.W. Akitt; in "An introduction to the Fourier Transform Multinuclear Area" Chapman and Hall (Eds.), New York (1983)

[262] D. Mueller; D. Hoebbel; W. Gessner; *Chem. Phys. Letters* 84, 25 (1981)

[263] D. Mueller; W. Gessner; H.J. Behrens; G. Scheler; *Chem. Phys. Letters* 79, 59 (1981)

[264] G. Johansson; G. Lundgren; L.G. Sillen; R. Soderquist; *Acta. Chem. Scand.* 14, 769 (1960)

[265] G. Johansson; *Acta. Chem. Scand.* 14, 771 (1960)

[266] G. Johansson; *Acta. Chem. Scand.* 16, 403 (1962)

[267] J.W. Akitt; R.H. Duncan; *J. Magn. Reson.* 34, 435 (1979)

[268] F.W. Wehrli; S. Wehrli; *J. Magn. Reson.* 44, 197 (1981)

[269] D.E. O'Reilly; *J. Chem. Phys.* 32, 1007 (1960)

[270] H. Noth; R. Rurlander; P. Wolfgardt; *Z. Naturforsch.* 37B, 29 (1982)

[271] F.W. Wehrli; R. Hoerdt; *J. Magn. Reson.* 42, 334 (1981)

[272] S.J. Karlik; G.A. Elgavish; R.P. Pillai; G.L. Eichhorn; *J. Magn. Reson.* 49, 164 (1982)

[273] J.W. Akitt; N.N. Greenwood; G.D. Lester; *J. Chem. Soc.* (A) 2450 (1971)

[274] J.J. Delpuech; M.R. Khaddar; A.A. Peguy; P. Rubini; *J. Chem. Soc. Chem. Comm.* 154 (1974)

[275] J.J. Delpuech; M.R. Khaddar; A.A. Peguy; P.R. Rubini; *J. Am. Chem. Soc.* 97, 3373 (1975)

[276] E.R. Malinowski; *J. Am. Chem. Soc.* 91, 4701 (1969)

[277] G.J. Martin; M.L. Martin; J.P. Govesnard; "^{15}N-NMR Spectroscopy" , NMR Basic Priciples and Progress, Springer-Verlag, Berlin, 18, (1981)

[278] R. Damadian; "NMR in Medicine" NMR Basic Principles and Progress, Springer-Verlag, Berlin, 19, (1981)

[279] R.G. Shulman; "Biological Applications of Magnetic Resonance" , Academic Press, New York, Chapt. 10 and 11, (1979)

[280] R.E. Gordon; P.E. Hanley; D. Shaw; *Prog. NMR Spectrosc.* 15, 1 (1980)

[281] R.A. Itles; A.N. Stevens; J.R. Griffiths; *Prog. NMR Spectrosc.* 15, 49 (1982)

[282] C.T. Burt; T. Glonek; M. Barany; *Science* 195, 145 (1977)

[283] C.F.G.C. Geraldes; M.M.C.A. Castro; *J. Inorg. Biochem.* 28, 319 (1986)

UNIVERSITÉ D'OTTAWA
UNIVERSITY OF OTTAWA